

09/1

7

7

川  
端

# Journal of APPLIED PHYSICS

Volume 62

1 September 1987

Number 1

a publication of the American Institute of Physics

439

# Optical, mechanical, and thermal properties of barium borate

D. Eimerl, L. Davis, and S. Velsko

*Nonlinear Optical Materials Group, Lawrence Livermore National Laboratory, P. O. Box 5508, Livermore, California 94550*

E. K. Graham

*The Pennsylvania State University, University Park, Pennsylvania 16802*

A. Zalkin

*Materials and Molecular Research Division, Lawrence Berkeley Laboratory, Berkeley, California 94720*

(Received 2 March 1987; accepted for publication 27 April 1987)

We report measurements of all the material constants necessary to fully characterize barium borate as a nonlinear optical material. All data was taken on crystals supplied by Professor Chuangtien Chen, Fuzhou, People's Republic of China. We have determined the crystal structure, the optical absorption, the refractive indices from the UV to the near IR, the thermo-optic coefficients, the nonlinear optical coefficients, the resistance to laser damage, the elastic constants, the thermal expansion, thermal conductivity and dielectric constants, and the fracture toughness. This data is used to evaluate barium borate for a variety of applications. We find that, in general, barium borate has a low acceptance angle, and that despite its higher optical nonlinearity, it is therefore not significantly more efficient than other commonly available materials, except in the UV below 250 nm. On the other hand, it has a high damage threshold, it is physically robust, it has good UV and IR transparency, and it has excellent average power capability. It permits deep UV generation, and has great potential for generating tunable visible and IR light as an optical parametric amplifier.

## INTRODUCTION

Barium metaborate ( $\text{BaB}_2\text{O}_4$ ) is a new nonlinear optical material discovered by Professor Chuangtien Chen of the Fujian Institute for Research on the Structure of Matter in Fuzhou, People's Republic of China.<sup>1-7</sup> It is an interesting material characterized by a wide range of transparency in both the ultraviolet and the near infrared. Its large birefringence allows phasematching for many harmonic generation processes, and in particular it has been used to generate the fifth harmonic of Nd:YAG.<sup>2,4</sup> It has a substantial nonlinear coupling. These properties indicate that barium borate is potentially useful for many applications, especially in the ultraviolet region.

However, the utility of a material in applications depends on other properties besides the linear and nonlinear optical constants. These include, for example, the damage threshold, chemical stability, and mechanical strength. At high average power, even weak optical absorption leads to thermal dephasing, and to induced thermal stresses which can fracture the crystal.<sup>8</sup> In the region of transparency, the optical absorption is controlled primarily by trace impurities and consequently crystal quality and the crystal growth process are important factors at high average power. These and other issues associated with average power have been analyzed recently in detail.<sup>8,9</sup> The performance of harmonic generators and other nonlinear optical devices was found to be characterized by four figures of merit. These figures of merit are simple combinations of material constants which determine the crystal shape and size, and the maximum average power density compatible with high conversion efficiency. At this time, complete sets of the relevant material constants are available for only a few materials (KDP,

$\text{LiIO}_3$ ,  $\text{LiNbO}_3$ ,  $\text{KNbO}_3$ ). These are discussed in detail in Refs. 8-10. We have measured all the relevant material constants for barium borate, and calculated figures of merit for many nonlinear optical processes. This paper reports the results of our measurements on the fundamental physical constants of barium borate, and uses this data to discuss the performance of barium borate in various nonlinear optical devices.

## CRYSTAL SAMPLES

The crystals used in this study were grown in Professor Chen's group in Fuzhou, People's Republic of China. The crystals were grown by a top-seeded technique from a high-temperature flux containing oxides of boron, sodium, and barium. Barium and boron oxides are prepared in stoichiometric proportion, and then either sodium oxide or sodium borate is added to the flux, to bring the liquidus below the phase-transition temperature at about 900 °C.

The crystals were typically large,  $10 \times 20 \times 5$  mm, optically clear, and relatively free of strain. One was already cut as a prism for refractive index measurements. All the data reported here was taken on material grown in Fuzhou, People's Republic of China.

## CRYSTAL STRUCTURE

There are two known phases for barium borate.<sup>11</sup> The structure of the quenched high temperature form was determined by Mighell, Perloff, and Block<sup>12</sup> to be  $R\bar{3}c$ . The low-temperature form was given as  $C2/c$  by Hubner,<sup>13</sup> but a subsequent determination by Liebertz and Stahr<sup>14</sup> gave the structure  $R\bar{3}c$ . Frohlich<sup>15</sup> reexamined the low-temperature



phase and confirmed the trigonal structure  $R\bar{3}c$  found by Liebertz and Stahr.

However, Chen<sup>1</sup> and Lu, Ho, and Huang<sup>16</sup> report the crystal structure of the new nonlinear material to be  $R\bar{3}$ . This suggested that the new nonlinear material was in fact a third, hitherto unknown modification of the structure. This is significant because the crystal structure determines which nonlinear coefficients are allowed, and the existence of a third phase impacts the phase diagram and crystal growth techniques. We therefore examined the structure of the crystals provided by Chen using both powder and single-crystal methods. The powder x-ray pattern did not show any of the reflections which would have been allowed in  $R\bar{3}$  but are forbidden by the  $c$  glide in  $R\bar{3}c$ .<sup>17</sup> The independent crystal structure determination was done on a single crystal of dimensions  $0.22 \times 0.17 \times 0.08$  mm<sup>3</sup>. The space group so found was  $R\bar{3}c$  with hexagonal cell dimensions  $a = 12.547(6)$  Å and  $C = 12736(9)$  Å with six formula units in the unit cell.<sup>18</sup> A modified Picker FACS-I diffractometer equipped with a Mo x-ray tube and a graphite monochromator was used to collect 6060 intensities of which 3103 were unique. The data were corrected for absorption,  $\mu = 110.6$  cm<sup>-1</sup>. The resulting structure, which is identical to that reported by Frohlich (see Ref. 15) was refined by least squares, using anisotropic thermal parameters, to an  $R$  factor of 0.035 for 2969 data for which the intensities  $I > \sigma(I)$ . The structure was also refined in space group  $R\bar{3}$ , in which there are 5917 unique data because of the lower symmetry. The structure in  $R\bar{3}$  refined to an  $R$  factor of 0.038 for 5539  $I > \sigma(I)$  data. All of the positional parameters of the pseudo- $c$ -glide-related

atoms were within two standard deviations of their positions in  $R\bar{3}c$ . Since the atomic positions resulting from the refinements in  $R\bar{3}$  are statistically undistinguishable from those in  $R\bar{3}c$ , and half as many parameters are needed in  $R\bar{3}c$  to give about the same statistical agreement between the calculated and observed intensities, it is concluded the  $R\bar{3}c$  is the true space group for this crystal.

The low-temperature form is stable up to about 900°C. The crystal structure is shown in Fig. 1. It consists of nearly planar anionic  $B_3O_6$  ring groups perpendicular to the polar (trigonal) axis. These anionic groups are bonded ionically through the barium ions. There are four anionic groups in each unit cell, which are distributed over two symmetrically independent positions. The four groups are stacked on top of each other and are arranged in two pairs. The upper two rings form one pair, and are oriented parallel to each other. The lower two rings form the other pair, and are also oriented parallel to each other, but 180° relative to the upper pair. The  $c$  glide forces the upper and lower pairs to be exactly 180° apart. If the structure were  $R\bar{3}$  then the two rings in the upper (or lower) pair would not be required to be exactly 180° apart. This occurs in the structure given by Lu.<sup>16</sup> We reexamined the crystal structure carefully to determine the relative orientation of these pairs of rings, as well as any other slight distortion which might remove the  $c$  glide. We found that the structure supports the  $c$  glide to an accuracy corresponding to the uncertainty associated with the estimated standard deviation of the positional parameters. Therefore, we conclude that the crystal structure of the low-temperature phase is indeed  $R\bar{3}c$ , to this accuracy.

The high-temperature phase is also  $R\bar{3}c$ , and is very similar to the low-temperature phase.<sup>12</sup> The only difference between them lies in the oxygen coordination of the barium atoms. In the high-temperature phase there are two Ba sites: one has point symmetry 32 with six oxygen atoms arranged in a trigonal prism, and the other has point symmetry 3 with a ninefold coordination. In the low-temperature phase, the barium atoms all have an irregular eightfold coordination. Powder second harmonic tests on the quenched high-temperature phase gave signals about as large as the low-temperature phase, in basic agreement with the anionic model of the nonlinearity proposed by Chen.<sup>19,20</sup>

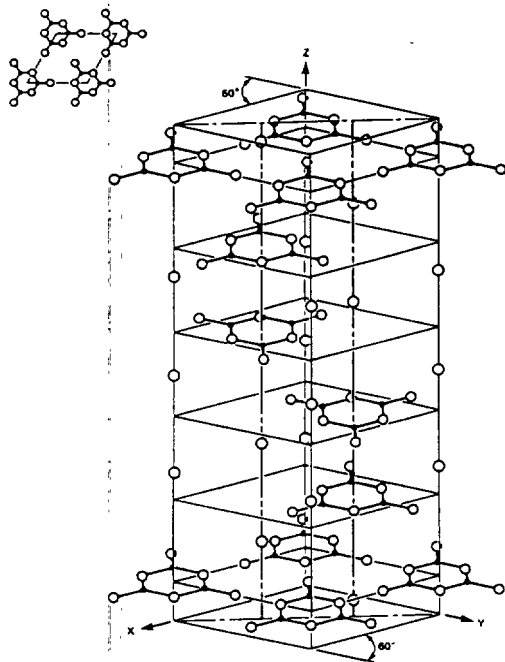


FIG. 1. Crystal structure of barium borate,  $Ba_3(B_3O_6)_2$ , consists of nearly planar  $(B_3O_6)^{-3}$  rings perpendicular to the polar axis, bonded together through the barium atoms. The optical and mechanical properties reflect this structure, which has much in common with the graphite structure. The axes shown refer to the hexagonal cell (see insert).

TABLE I. Refractive indices of  $\beta$ - $BaB_2O_4$ .

$\lambda$	$n_e$	$n_o$
10140	1.543 33	1.656 08
8943.5	1.544 69	1.658 62
8521.2	1.545 42	1.659 69
8189.0	1.545 89	1.660 66
6438.5	1.550 12	1.667 36
5893.0	1.552 47	1.670 49
5790.7	1.552 98	1.671 31
5460.7	1.554 65	1.673 76
5085.8	1.556 91	1.677 22
4799.9	1.559 14	1.680 44
4678.2	1.560 24	1.681 98
4358.3	1.563 76	1.686 79
4046.6	1.567 96	1.692 67

TABLE II. Sellmeier parameters for  $\beta$ -BaB<sub>2</sub>O<sub>4</sub>.

	<i>A</i>	<i>B</i> ( $\mu\text{m}^2$ )	<i>C</i> ( $\mu\text{m}^{-2}$ )	<i>D</i> ( $\mu\text{m}^{-2}$ )	Ref.
<i>n<sub>e</sub></i>	2.3730	0.0128	-0.0156	-0.0044	a
<i>n<sub>o</sub></i>	2.7405	0.0184	-0.0179	-0.0155	a
<i>n<sub>e</sub></i>	2.3785	0.01217	-0.01793	...	b
<i>n<sub>o</sub></i>	2.7462	0.01715	-0.02177	...	b
<i>n<sub>e</sub></i>	2.3753	0.01224	-0.01667	-0.01516	c
<i>n<sub>o</sub></i>	2.7359	0.01878	-0.01822	-0.01354	c

<sup>a</sup> This work.

<sup>b</sup> See Reference 1.

<sup>c</sup> See Reference 4.

## LINEAR OPTICAL CONSTANTS

The refractive indices of barium borate were determined directly in the region 400–1014 nm by the method of minimum deviation. The prism spectrometer is fitted with camera for operation in the near infrared and in the ultraviolet region just beyond the visible. The data are presented in Table I. In order to extend this data to the ultraviolet we measured the phase-matching angles for harmonic generation and fit this data as well as the visible data to a Sellmeier form as follows:

$$n^2 = A + B/(\lambda^2 + C) + D\lambda^2. \quad (1)$$

This fit yields accurate refractive indices in the region 212.8–1064 nm. Table II gives the Sellmeier constants so obtained and also includes the Sellmeier constants of Chen and Kato. Table III gives the refractive indices for the harmonics of Nd:YAG. Our fit gives values which differ only slightly from the formula given by Kato<sup>4</sup> and reproduces the observed phase-matching angles to within the experimental precision.

We also determined the thermo-optic coefficients and their wavelength dispersion. The refractive indices were determined at several temperatures between 20 and 80 °C. The temperature dependence was found to be linear, and a linear least squares fit was made to the data at each of three wavelengths. The resulting thermo-optic coefficients are presented in Table IV. The dispersion of the thermo-optic coefficients is comparable to the precision with which they could be determined. In our subsequent calculations we therefore used the following averaged values:

TABLE III. Refractive indices at Nd YAG harmonics.

$\lambda$ ( $\mu\text{m}$ )	<i>n<sub>o</sub></i>	<i>n<sub>e</sub></i>
1.0642	1.54254	1.65510
0.5321	1.55552	1.67493
0.3541	1.57757	1.70556
0.2660	1.61461	1.75707
0.2128	1.67467	1.84707

TABLE IV. Thermo-optic coefficients for  $\beta$ -BaB<sub>2</sub>O<sub>4</sub>.

$\lambda$ ( $\mu\text{m}$ )	$dn_e/dT \times 10^6/^\circ\text{C}$	$dn_o/dT \times 10^6/^\circ\text{C}$
10140	-9.76	-16.64
5790	-9.42	-16.35
4047	-8.84	-16.83

$$\frac{dn_o}{dT} = -16.6 \times 10^{-6}/^\circ\text{C}, \quad (2)$$

$$\frac{dn_e}{dT} = -9.3 \times 10^{-6}/^\circ\text{C}. \quad (3)$$

The range of transparency was determined in a sample 4 mm thick. The transmission range of this sample was 200–3000 nm, and is shown in Fig. 2(a). In the ultraviolet, the extinction (the combined absorption and scattering) begins at 215 nm and increases slowly as the wavelength decreases. The extinction reaches 100%/cm at about 200 nm. The sample used contained some inclusions and it is possible that higher-quality crystals would show a sharper edge lying deeper into the ultraviolet. Figure 2(b) shows the transmission of the 4 mm sample in the range 150–320 nm.

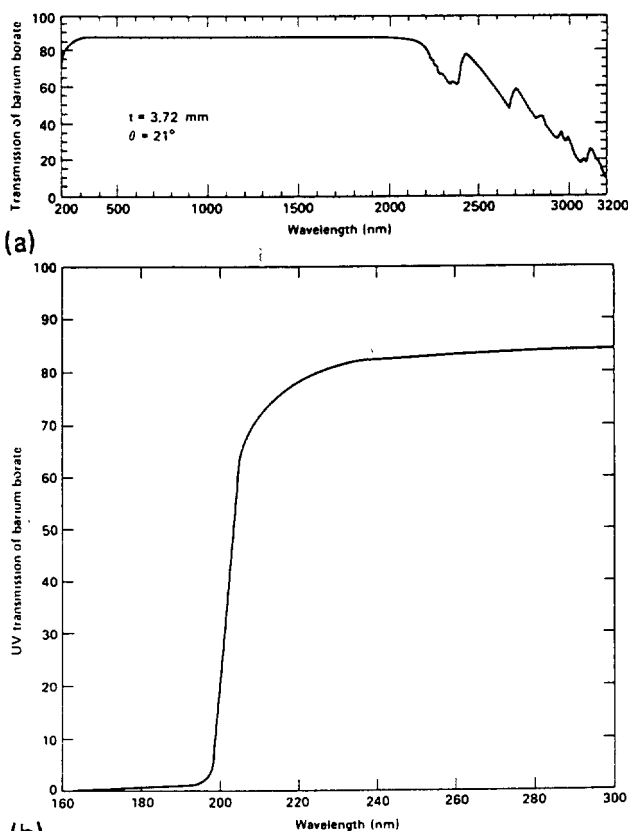


FIG. 2. (a) The transmission of unpolarized light at the type I phase-matched direction through a 3.72-mm sample. The clear transmission range is 200–2000 nm, with infrared structure between 2000 and 3000 nm. (b) The UV edge of the same sample.



## PHASE MATCHING

In the general three-wave mixing experiment, waves at frequencies  $\omega_1$  and  $\omega_2$  are mixed to generate a wave at  $\omega_3 = \omega_1 + \omega_2$ . For low-intensity waves, the simple plane wave theory predicts that the output intensity is

$$I = I_0 \sin^2(\delta), \quad (4)$$

where  $\delta$  is the phase mismatch

$$\delta = (1/2)\Delta k l. \quad (5)$$

Here  $l$  is the crystal thickness and  $\Delta k$  is the wave-vector mismatch

$$\begin{aligned} \Delta k &= k_3 - k_2 - k_1 \\ &= 1/c(n_3\omega_3 - n_2\omega_2 - n_1\omega_1). \end{aligned} \quad (6)$$

The refractive indices depend on the polarization of the waves, and in general there are three different polarization configurations which can lead to a vanishing phase mismatch. In any optical material there are two propagating modes of the electromagnetic field at each frequency. In a birefringent medium they have different velocities, and orthogonal polarizations. One polarization is fast (lower refractive index) and the other is slow (higher refractive index). In biaxial crystals, both velocities depend on the direction of propagation of the wave through the crystal. They are both considered extraordinary waves. However, for uniaxial crystals such as barium borate, only one velocity varies with propagation direction. In negatively birefringent crystals the fast velocity depends on the direction of propagation, whereas in positively birefringent materials, it is the slow velocity which varies with direction. In barium borate, which is negatively birefringent, the fast velocity depends on the propagation direction, and is the extraordinary wave.

With the convention that  $\omega_1 < \omega_2 < \omega_3$ , the three types of phase matching are summarized in Table V. For doubling, type III and type II are the same process, whereas this is not the case for sum frequency generation. Although there are in principle three types of phase matching, only the first two types are usually encountered, because type III requires high birefringence, and is consequently quite rare. In KDP, for example, there is no type III phase matching for mixing 1064 and 532 nm to generate 355 nm, but a very birefringent material such as urea can support type III mixing as well as type II mixing. Because barium borate is a highly birefringent material with a birefringence comparable to urea ( $\Delta n = 0.13$ ), it can support all three types of phase matching for most processes in its range of transparency.

The phase-matching angle  $\theta_m$  for a particular mixing

process at a reference temperature  $T_0$  is given by the following implicit equation:

$$\Delta k(\theta_m, T_0) = 0. \quad (7)$$

For angles near  $\theta_m$  and temperatures near  $T_0$ , the wave-vector mismatch  $\Delta k$  can be expanded as a power series in  $\theta$  and  $T$ ,

$$\Delta k = \beta_\theta(\theta - \theta_m) + \beta_T(T - T_0), \quad (8)$$

where

$$\beta_\theta = \frac{\partial \Delta k}{\partial \theta} \quad (9)$$

and

$$\beta_T = \frac{\partial \Delta k}{\partial T}. \quad (10)$$

For each type of phase-matching expressions for the angular sensitivity  $\beta_\theta$  and the temperature sensitivity  $\beta_T$  are easily derived from Eq. (6). They can then be calculated from the refractive index data. The accuracy of these calculated values depends sensitively on the accuracy with which the refractive indices and the thermo-optic coefficients can be extrapolated or interpolated to the desired wavelengths.

The temperature bandwidth for a crystal of length  $l$  is given by

$$l\Delta T = 4A/\beta_T. \quad (11)$$

If the bandwidth is defined as the temperature range spanned by the first zeros on either side of the peak phase-matched intensity, then  $A = \pi$ . On the other hand, if the bandwidth is defined as the FWHM bandwidth, then  $A = 1.391\,557\,38$ . The angular bandwidth is given by an exactly analogous equation.

## DIRECT DETERMINATION OF THE ANGULAR AND TEMPERATURE BANDWIDTHS FOR HARMONICS OF 1064 nm

In addition to determining the Sellmeier formulas for the refractive indices, we have made direct measurements of the phase-matching angles, and the angular and temperature bandwidths. Our motivation for this was to check the accuracy of the Sellmeier fit as a descriptor of the phase-matching properties. These direct measurements were made on crystals only 1 or 2 mm in size, where direct measurements of the refractive indices are generally too imprecise for phase-matching calculations. The method used is to mount a small crystal on a glass fiber manipulated by a goniometer for accurate orientation. The waves to be mixed are incident on the crystal and the wave generated is detected using wavelength filters and photomultipliers. The intensity of the generated wave can be easily studied as a function of the orientation and temperature of the sample. The technique has been used on samples of other nonlinear materials as small as 0.5 mm in size. A detailed description of the apparatus used to make these measurements has been published elsewhere.<sup>21</sup>

The intensity of the generated wave is a maximum at the zero of the phase mismatch. The locus of points in  $(\theta, T)$  space defined by the relation

$$\Delta k = \beta_\theta(\theta - \theta_m) + \beta_T(T - T_0) = 0 \quad (12)$$

TABLE V. Phase-matching types in  $\beta$ -BaB<sub>2</sub>O<sub>4</sub>. e = extraordinary wave (faster). o = ordinary wave (slower).

Type	$\omega_1$	$\omega_2$	$\omega_3$
I	o	o	e
II	e	o	e
III	o	e	e

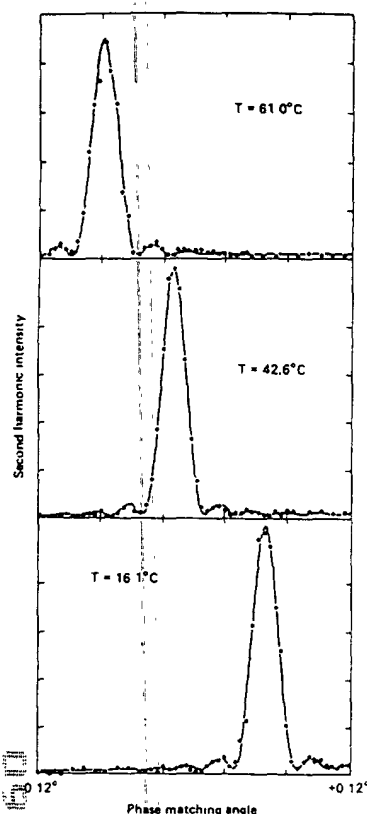


FIG. 3. The method of measuring the thermal bandwidth uses the ratio between  $d\theta_{pm}/dT$  and  $d\Delta k/d\theta$ . These are obtained from measurements of the angle-tuning curve at different temperatures. This technique is much more precise than direct methods.

gives the variation of the phase-matching angle with temperature.

$$\frac{d\theta_m}{dT} = -\frac{\beta_T}{\beta_\theta} \quad (13)$$

This relation was used to determine the temperature sensitivity from the angular sensitivity and the temperature variation of the phase-matching angle. At each temperature, the

TABLE VI. Calculated and observed phase-matching angles.

Process	(Type)	$\theta(\text{Kato})^a$	$\theta(\text{exp})^b$	$\theta(\text{calc})^c$	$\theta(\text{Chen})^d$
$1\omega + 1\omega$	(I)	22.8°	22.7°	22.9°	19.8°
	(II)	32.9°	32.4°	32.6°	28.2°
$1\omega + 2\omega$	(I)	31.3°	31.1°	31.1°	29.3°
	(II)	38.5°	38.4°	38.2°	36.7°
	(III)	59.8°	58.4°	59.8°	56.2°
$2\omega + 2\omega$	(I)	47.5°	47.3°	47.5°	47.4°
	(II)	81.0°		82.6°	81.0°
$1\omega + 3\omega$	(I)	40.2°		40.2°	40.1°
	(II)	46.6°		46.6°	46.5°
$1\omega + 4\omega$	(I)	51.1°		51.1°	53.2°
	(II)	57.2°		57.2°	59.5°
$2\omega + 3\omega$	(I)	69.3°		69.5°	72.7°

<sup>a</sup> Experimental determination, Ref. 4

<sup>b</sup> Experimental data, our laboratory.

<sup>c</sup> Calculated from data in Table III.

<sup>d</sup> Calculated from Chen's Sellmeier data (Table II).

TABLE VII. Angular sensitivity of  $\beta\text{-BaB}_2\text{O}_4$ .

Process	$(\beta_\theta)_{\text{exp}}$ (cm <sup>-1</sup> /rad)	$(\beta_\theta)_{\text{calc}}$ (cm <sup>-1</sup> /rad)
$2\omega\text{I}$	$10600 \pm 200$	10 700
$2\omega\text{II}$	$7000 \pm 170$	7061
$3\omega\text{I}$	$21000 \pm 1300$	21 700
$3\omega\text{II}$	$16100 \pm 500$	16 400
$3\omega\text{III}$	$6400 \pm 500$	7018
$4\omega\text{I}$	$33000 \pm 400$	34 000
$4\omega\text{II}$	...	7400

intensity of the output wave was measured as a function of angle. This data consisted of a series of curves each one slightly displaced in angle from the previous one. Typical results are shown in Fig. 3, in this case for type I doubling of 1064 nm. This data was then used to determine both the angular sensitivity and  $d\theta_m/dT$ . This method of determining the temperature sensitivity was more accurate than a direct measurement of the output intensity as a function of temperature.

Table VI lists calculated and observed phase-matching angles for various processes. For comparison, values from Kato<sup>4</sup> are included, and values using Chen's<sup>1</sup> refractive index formulae. Although not all the sum frequency mixings studied by Kato were also studied by us, the agreement among those common to both is very good.

Experimental and predicted values of the angular and temperature sensitivities are listed in Tables VII and VIII. The temperature sensitivities were calculated using the averaged or dispersionless values for the thermo-optic coefficients, and these differ somewhat from the experimentally determined parameters, especially for processes such as type I doubling of 1064 nm, where cancellations between terms cause the temperature sensitivity to be small. The discrepancies are not great and are reasonably attributable to a combination of experimental errors and the use of dispersionless thermo-optic coefficients.

We conclude from the generally good agreement between observed and measured values for  $\theta_m$ ,  $\beta_\theta$ , and  $\beta_T$  that the refractive index data gives accurate phase-matching properties from the UV edge out to the near IR beyond 1064 nm.

TABLE VIII. Temperature sensitivity of  $\beta\text{-BaB}_2\text{O}_4$ .

Process	$(d\theta/dT)_{\text{exp}}$ (μrad/°C)	$(\beta_T)_{\text{exp}}^a$ (cm <sup>-1</sup> /°C)	$(\beta_T)_{\text{calc}}$ (cm <sup>-1</sup> /°C)
$2\omega\text{I}$	$9.9 \pm 1$	$0.11 \pm 0.10$	0.14
$2\omega\text{II}$	$20.9 \pm 2$	$0.15 \pm 0.10$	0.13
$3\omega\text{I}$	$17.3 \pm 1$	$0.36 \pm 0.08$	0.41
$3\omega\text{II}$	$26.2 \pm 2$	$0.42 \pm 0.08$	0.38
$3\omega\text{III}$	$73.4 \pm 3$	$0.47 \pm 0.09$	0.34
$4\omega\text{I}$	$43.7 \pm 1$	$1.4 \pm 0.03$	1.03
$4\omega\text{II}$	...	...	0.83

<sup>a</sup>  $\beta_T = -\beta_\theta(d\theta/dT)$ .

## PHASE-MATCHING PARAMETERS FOR OTHER PROCESSES

Based on the refractive index data the phase-matching angles have been calculated for several mixing processes. Figures 4–8 show the phase-matching angles for  $1\omega + 1\omega$ ,  $1\omega + 2\omega$ ,  $2\omega + 3\omega$ ,  $1\omega + 3\omega$ ,  $1\omega + 4\omega$ , including all types of polarization configurations which permit phasematching. Figures 9–13 show the corresponding angular sensitivities, and Figs. 14–18 show the temperature sensitivities.

We have also calculated these parameters for optical parametric amplifiers pumped at the second, third and fourth harmonics of 1064 nm. These are shown in Figs. 19–24.

## DAMAGE THRESHOLD

The damage threshold of two samples was measured at 1064 nm and 1 ns pulse width. The first sample was cut at the type I phase-matching angle for doubling 1064 nm, and was about  $10 \times 15 \text{ mm}^2$  in area. Its thickness was 4 mm, and apart from some inclusions of  $\text{Na}_2\text{O}$  it was strain-free and of high optical quality. Thirty sites were irradiated, with each site irradiated once. The one-on-one damage threshold of the inclusion-free areas was about  $13.5 \text{ J/cm}^2$ , and the threshold of the inclusions themselves was about  $4 \text{ J/cm}^2$ .

The second sample was a cube approximately 8 mm on a side cut along the crystallographic (*xyz*) axes. It was of relatively poor optical quality and showed considerable strain-induced birefringence. It was, however, relatively inclusion-free. The relatively small volume and poor quality hindered a good measurement of the damage threshold, but it appeared to be about a factor of 2 lower than the first sample.

## NONLINEAR OPTICAL CONSTANTS AND DEVICE DESIGN

In the space group  $R\bar{3}c$  using the convention that the mirror plane is the two-axis, the only allowed nonlinear coefficients are  $d_{11}$ ,  $d_{31}$ ,  $d_{33}$ ,  $d_{15}$ . The coefficient  $d_{33}$  is irrelevant to (collinear) harmonic generation and Kleinman symme-

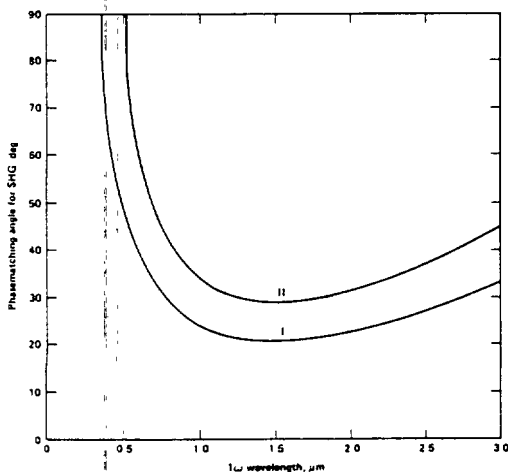


FIG. 4. Phase-matching angles for second harmonic generation.

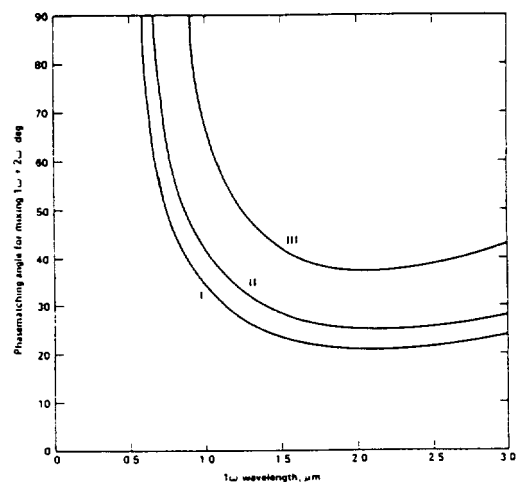


FIG. 5. Phase-matching angles for mixing  $1\omega + 2\omega$ .

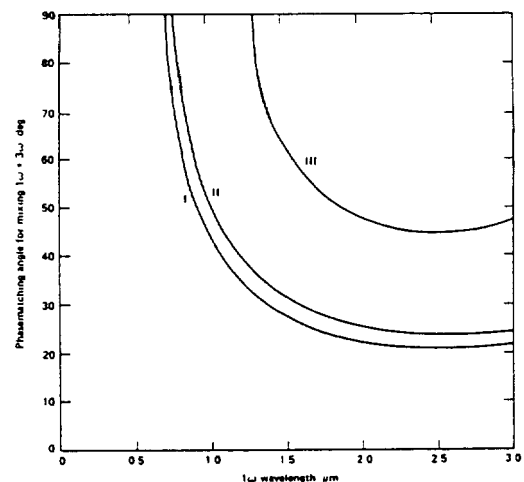


FIG. 6. Phase-matching angles for mixing  $1\omega + 3\omega$ .

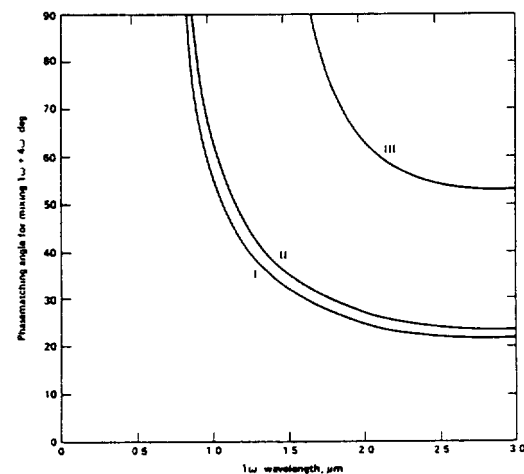


FIG. 7. Phase-matching angles for mixing  $1\omega + 4\omega$ .

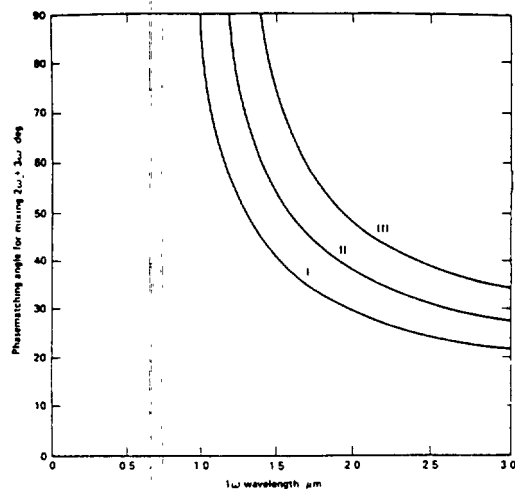


FIG. 8. Phase-matching angles for mixing  $2\omega + 3\omega$ .

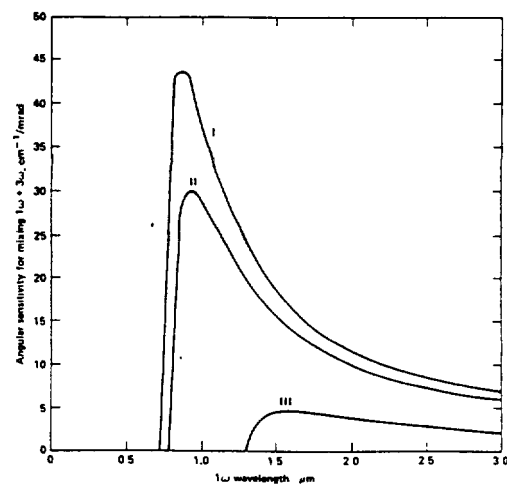


FIG. 11. Angular sensitivity  $d\Delta k / d\theta$  for mixing  $1\omega + 3\omega$ .

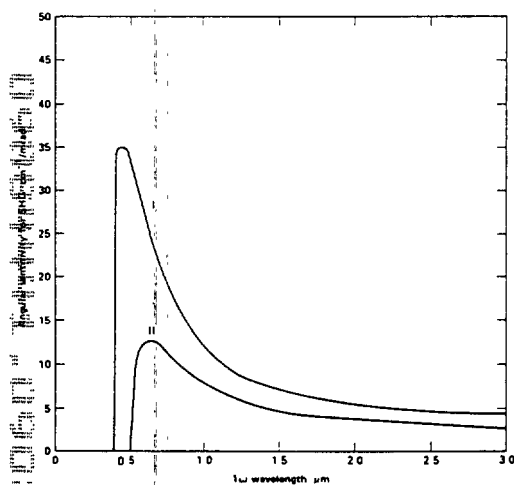


FIG. 9. Angular sensitivity  $d\Delta k / d\theta$  for second harmonic generation.

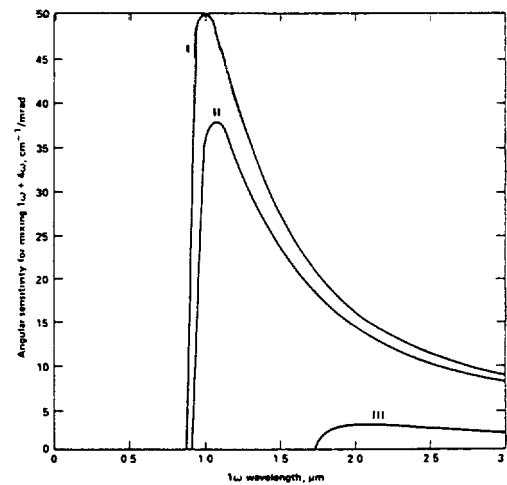


FIG. 12. Angular sensitivity  $d\Delta k / d\theta$  for mixing  $1\omega + 4\omega$ .

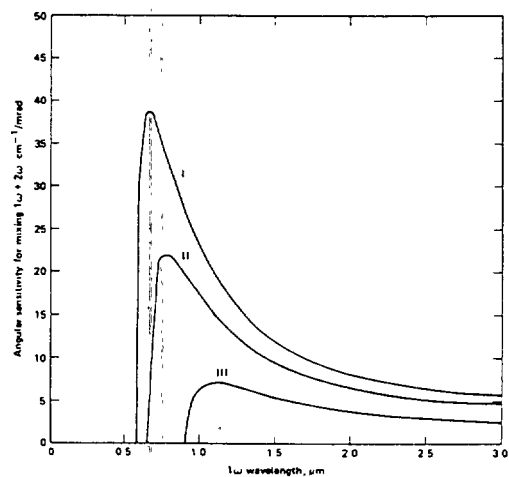


FIG. 10. Angular sensitivity  $d\Delta k / d\theta$  for mixing  $1\omega + 2\omega$ .

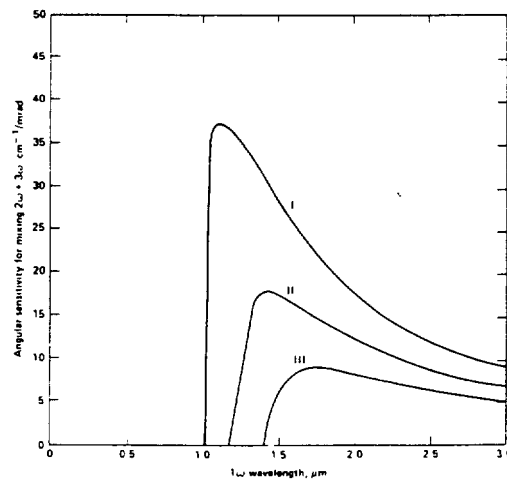


FIG. 13. Angular sensitivity  $d\Delta k / d\theta$  for mixing  $2\omega + 3\omega$ .

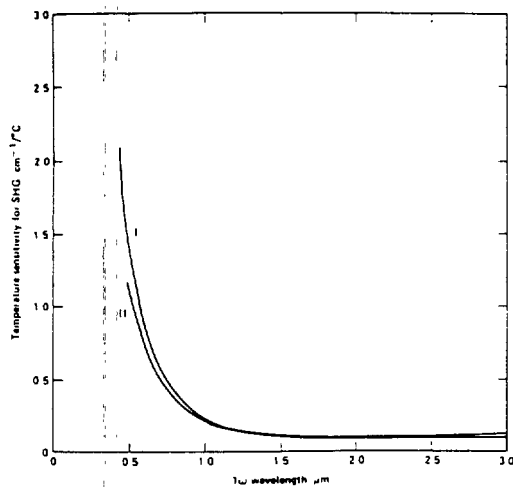


FIG. 14. Temperature sensitivity  $d\Delta k/dT$  for second harmonic generation.

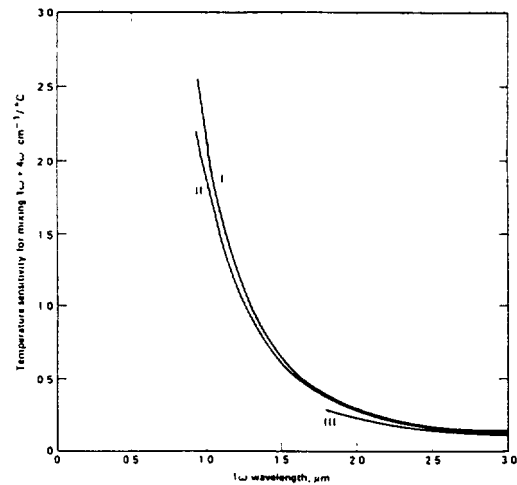


FIG. 17. Temperature sensitivity  $d\Delta k/dT$  for mixing  $1\omega + 4\omega$ .

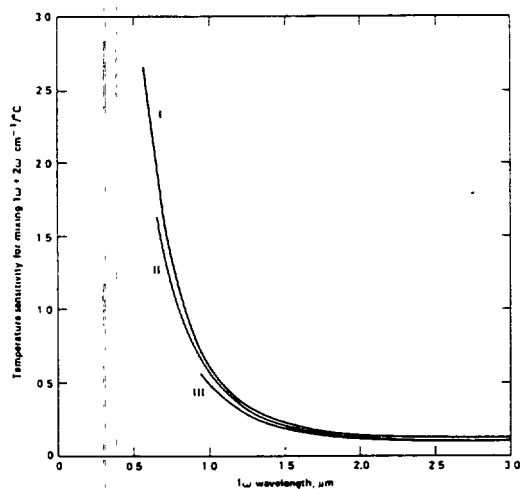


FIG. 15. Temperature sensitivity  $d\Delta k/dT$  for mixing  $1\omega + 2\omega$ .

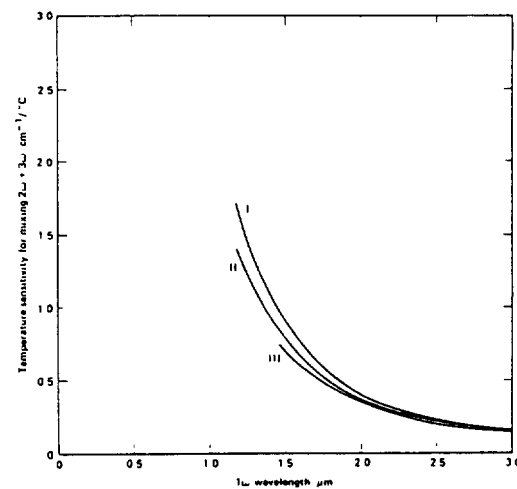


FIG. 18. Temperature sensitivity  $d\Delta k/dT$  for mixing  $2\omega + 3\omega$ .

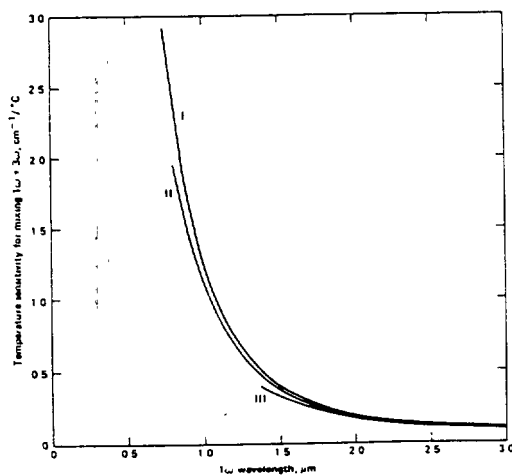


FIG. 16. Temperature sensitivity  $d\Delta k/dT$  for mixing  $1\omega + 3\omega$ .

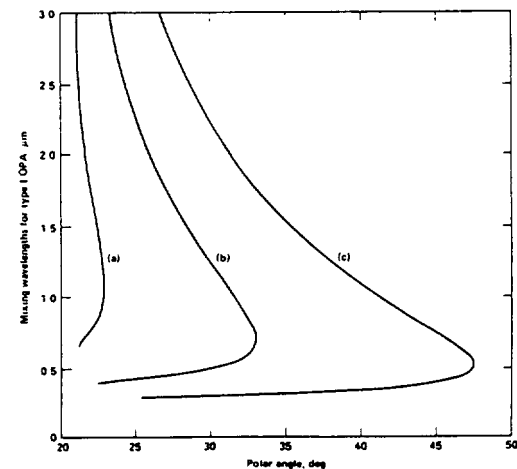


FIG. 19. Signal (idler) wavelength of a type I optical parametric amplifier ( $e \rightarrow o + o$ ) as a function of the polar angle for three pump wavelengths: (a) 532 nm, (b) 355 nm, (c) 266 nm.

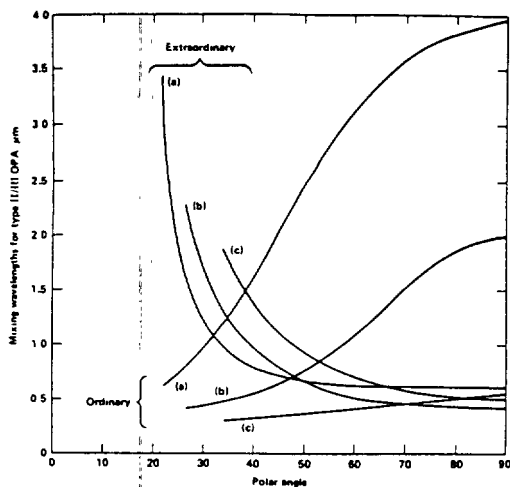


FIG. 20. Signal (idler) wavelength of a type II/III optical parametric amplifier ( $e \rightarrow o + e$ ) as a function of the polar angle for three pump wavelengths: (a) 532 nm, (b) 355 nm, (c) 266 nm.

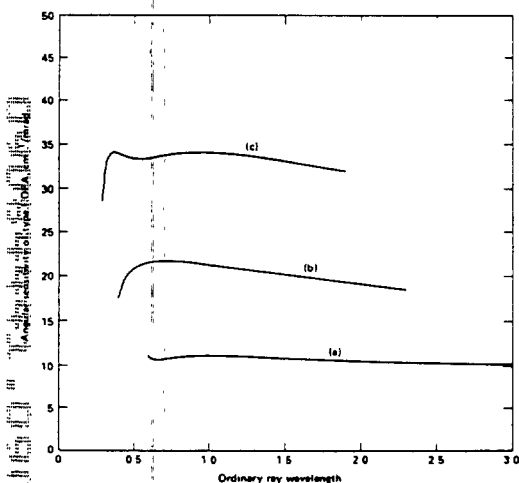


FIG. 21. Angular sensitivity  $d\Delta k/d\theta$  of a type I parametric amplifier as a function of one of the output waves for three different pump wavelengths: (a) 532 nm, (b) 355 nm, (c) 266 nm.

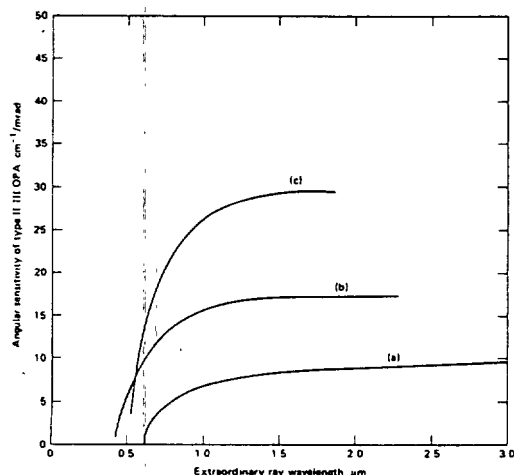


FIG. 22. Angular sensitivity  $d\Delta k/d\theta$  of a type II/III parametric amplifier as a function of the extraordinary output wave for three different pump wavelengths: (a) 532 nm, (b) 355 nm, (c) 266 nm.

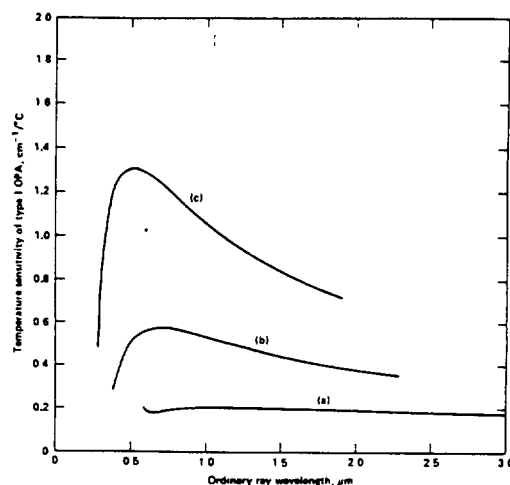


FIG. 23. Temperature sensitivity  $d\Delta k/dT$  of a type I parametric amplifier as a function of one of the output waves for three different pump wavelengths: (a) 532 nm, (b) 355 nm, (c) 266 nm.

try equates  $d_{15}$  and  $d_{31}$ , leaving only two relevant constants. In the space group  $R3$ ,  $d_{22}$  and  $d_{14}$  are also allowed, and Kleinman symmetry requires  $d_{14}$  to vanish, leaving three relevant coefficients. The nonlinear coefficients have been measured relative to  $d_{36}$  (KDP), for second harmonic generation of 1064 nm. They are

$$d_{11} = 1.6 \pm 0.4 \text{ pm/V}, \quad (14)$$

$$\left| \frac{d_{22}}{d_{11}} \right| < 0.05, \quad (15)$$

$$\left| \frac{d_{31}}{d_{11}} \right| < 0.05. \quad (16)$$

In converting our measurements to absolute values we used  $d_{36}(\text{KDP}) = 0.39 \text{ pm/V}$ .<sup>22</sup> The dispersion of the nonlinear coefficients is expected to be weak in the visible and near UV.

For type I processes the nonlinear coupling is

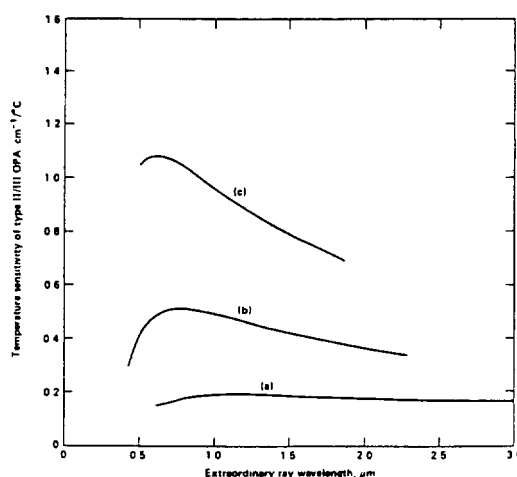


FIG. 24. Temperature sensitivity  $d\Delta k/dT$  of a type II/III parametric amplifier as a function of the extraordinary output wave for three different pump wavelengths: (a) 532 nm, (b) 355 nm, (c) 266 nm.

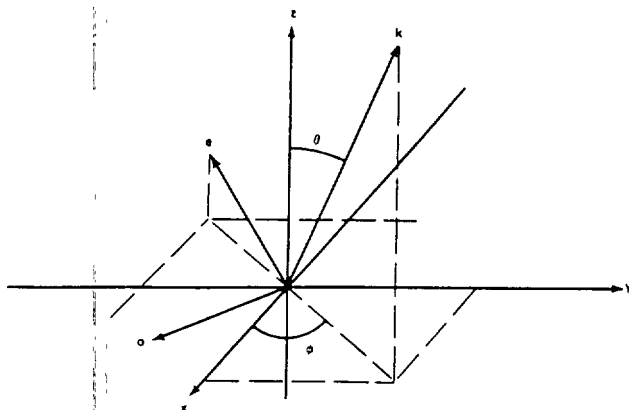


FIG. 25. Polar angle  $\theta$  is defined with respect to the polar axis, and the azimuthal angle  $\phi$  is defined with respect to  $x$  axis, the normal to the crystallographic mirror plane ( $m = y$ ).

$$d_{\text{eff}} = d_{31} \sin \theta - d_{11} \cos \theta \cos 3\phi, \quad (17)$$

and for type II or type III processes it is

$$d_{\text{eff}} = d_{11} \cos^2 \theta \sin 3\phi. \quad (18)$$

The angles are defined in terms of the direction of propagation, as in Fig. 25.

At those wavelengths where the phase-matching angle is  $90^\circ$ , the angular sensitivity vanishes. This condition is called noncritical phase matching, and the wavelengths at which it occurs are tabulated in Table IX. These wavelengths represent the short wavelength limit for each process. From Eqs. (7) and (18), the effective coupling for noncritical phase matching vanishes for type II and type III processes, and for type I, it is proportional to the weak  $d_{31}$  component. Thus, the effective coupling becomes very small at noncritical phase matching, and in practice this may preclude operation within a few nm of the noncritical wavelength.

In frequency conversion devices, the conversion efficiency depends on the intensity of the input waves, and also on the phase mismatch between them. The crystal length is limited by the angular sensitivity of the process and the beam divergence. There is therefore a minimum peak intensity required to achieve efficient conversion. The relevant figure of merit in comparing nonlinear materials is therefore the ratio of the effective coupling to the angular sensitivity. The square of this ratio is expressible as a power which is approxi-

TABLE IX. Noncritical wavelengths\* for  $\beta$ -BaB<sub>2</sub>O<sub>4</sub>.

Process	Type I	Type II	Type III
$1\omega + 1\omega \rightarrow 2\omega$	409.0	527.3	...
$1\omega + 2\omega \rightarrow 3\omega$	587.8	666.6	908.1
$1\omega + 3\omega \rightarrow 4\omega$	737.7	795.6	1299.5
$1\omega + 4\omega \rightarrow 5\omega$	873.0	917.2	1715.6
$2\omega + 3\omega \rightarrow 5\omega$	998.8	1033.2	2180.0
$1\omega + 5\omega \rightarrow 6\omega$	1007.2	1197.0	1434.8

\* Wavelengths given in nm.

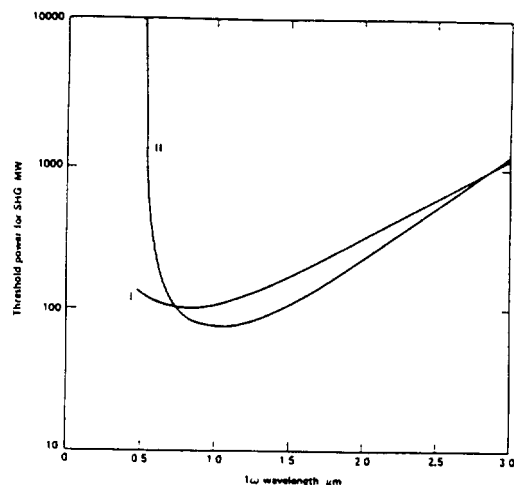


FIG. 26. Threshold power for second harmonic generation.

mately the peak laser power in a diffraction-limited beam which is required for efficient conversion. This ratio is the key figure of merit in designing frequency conversion devices, and is discussed in Refs. 8 and 9. The essential results are summarized in the Appendix.

In Figs. 26–32 the threshold powers of the harmonic generation and parametric amplifier processes discussed above are presented. Note that for harmonic generation devices the peak power of the laser must exceed the threshold power by a significant margin between 1 and 10 (see the Appendix), whereas for parametric amplifiers, it must exceed the threshold power by a larger factor, between 10 and 100. Also the peak power required increases by  $Q^2$ , where  $Q$  is the beam quality, approximately the ratio of the beam divergence to the divergence of a diffraction-limited laser beam.

For comparison, the threshold power of type II doubling of 1064 nm in KDP is about 70 MW. It is therefore apparent that a crystal of barium borate with optimized dimensions will be marginally less efficient than an *optimized*

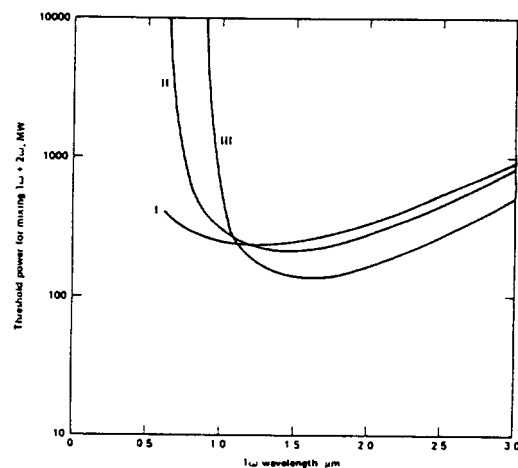


FIG. 27. Threshold power for mixing  $1\omega + 2\omega$ .

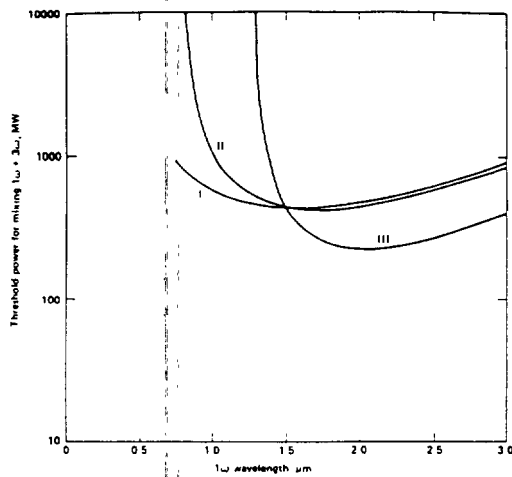


FIG. 28. Threshold power for mixing  $1\omega + 3\omega$

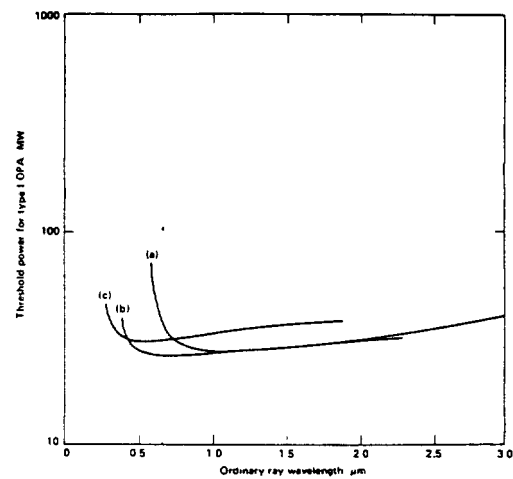


FIG. 31. Threshold power for a type I optical parametric amplifier, for three pump wavelengths: (a) 532 nm, (b) 355 nm, (c) 266 nm.

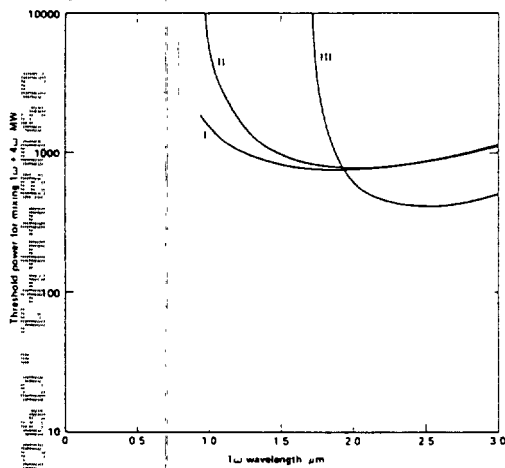


FIG. 29. Threshold power for mixing  $1\omega + 4\omega$ .

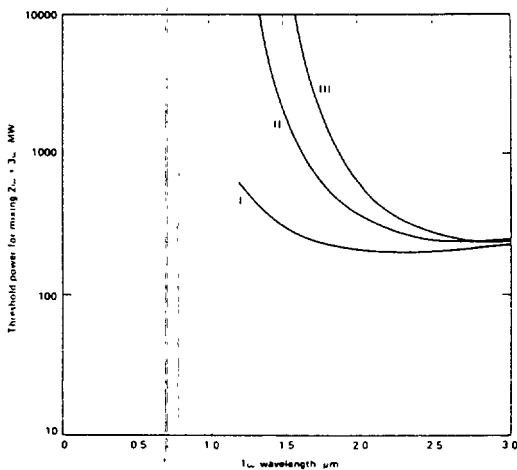


FIG. 30. Threshold power for mixing  $2\omega + 3\omega$

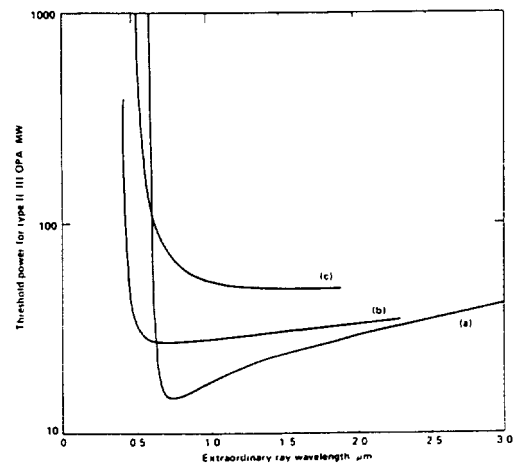


FIG. 32. Threshold power for a type II/III optical parametric amplifier, for three pump wavelengths: (a) 532 nm, (b) 355 nm, (c) 266 nm.

crystal of KDP. On the other hand, it has several advantages. It has higher damage threshold, and lower-temperature sensitivity, and we shall show below that it has also excellent resistance to thermally induced fracture. Moreover, the crystal volume needed is about an order of magnitude smaller than for KDP, and these smaller dimensions reduce the effects of beam walk-off. However, the threshold power is slightly higher, and therefore the optimized conversion efficiency is not significantly different from KDP.

## THERMOMECHANICAL PROPERTIES

Under average power conditions, even a small optical absorption can lead to thermal gradients which cause stress and thermo-optic dephasing. The average power capability of a nonlinear material is therefore limited by its resistance to thermal fracture. We have therefore measured the relevant material constants controlling thermal fracture.



As shown in Ref. 8 the highest average power is reached when the temperature variation in the crystal is minimized. This occurs when the thermal streamlines are shortest, and the heat resulting from optical absorption is removed as close to its point of deposition as possible. The most advantageous geometry for average power applications is therefore the thin plate geometry. For the purposes of characterizing materials, the ideal geometry is an infinite thin plate characterized only by its surface normal and its thickness. In practice, of course, three-dimensional effects must be included to obtain an accurate picture of the thermal behavior of actual devices.

Under the idealized thermal conditions we assume for material characterization, thermal transport is normal to the plate, and the temperature profile in the material is quadratic.<sup>8,10</sup> The temperature profile is characterized by the temperature difference between the plate surfaces and the plane midway between them  $\Delta T$  (Fig. 33). The thermal stresses induced in anisotropic materials of this shape experiencing this temperature profile have been analyzed fully.<sup>8,10</sup> The largest tensile stresses are found in the plate surfaces, and are due to thermal expansion in the interior of the plate in directions parallel to the plate surface. Thermal expansion parallel to the surface normal induces no surface stress. The tensile and shear stresses in the surface are directly proportional to  $\Delta T$ , and do not depend on the plate thickness.<sup>8,10</sup> Thus the surface stresses are given by

$$S_y = \xi_y \Delta T, \quad (19)$$

where  $\xi_y$  depends on the elastic constants and the thermal expansion. In anisotropic materials such as barium borate it also depends on the plate orientation. For a particular plate orientation, there are three surface stresses, two tensile components along orthogonal directions and one shear component. For convenience, the simplest choice of directions in the surface are the optical directions, or the ordinary and extraordinary polarization directions. Thus, there is the ordinary tensile stress, the extraordinary tensile stress and a single shear stress. As  $\Delta T$  increases, these stresses increase linearly and at some value of  $\Delta T$  one of them will exceed the

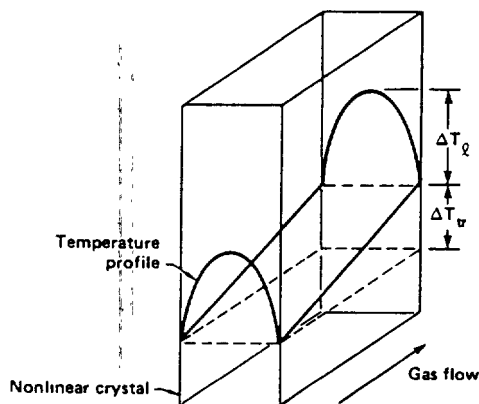


FIG. 33. Thermal profile in a thin plate under conditions of efficient heat removal.

surface strength, and the surface will fracture. In this way, the thermal profile leads to fracture, and to fracture along the weakest direction in the surface. In general, both the fracture strength and the weakest direction in the surface depend on the plate orientation.

Plate surfaces are not perfectly flat, but contain optically invisible defects. The polishing process is an important factor in creating and controlling these (sub-) surface defects. As the surface stress increases, the elastic energy density surrounding the defects increases. When one of the surface stresses exceeds its surface strength, it becomes energetically favorable for one of the defects to increase in size, thereby relieving the stress in the surrounding material. When this happens the surface will become crazed or shatter altogether. The surface strength depends on the size, shape, and orientation of the defect. A standard means of characterizing materials uses the indentation test.<sup>23-25</sup> Under these test conditions the surface strength is

$$S = K_c / a^{1/2}, \quad (20)$$

where  $a$  is the defect size and  $K_c$  is the fracture toughness of the material.

The temperature  $\Delta T$  at which one of the stresses reaches its fracture strength depends on the defect size. The thin plate fracture temperature  $\Delta T_F$  is defined as the temperature difference at which an ideal thin plate with 100  $\mu\text{m}$  defects fractures.  $\Delta T_F$  is a figure of merit which measures the resistance of a material to thermal fracture. It is physically the fracture point for a standard shape and standard defect size. Note that in anisotropic materials both the fracture temperature and the weakest direction depend on the plate orientation.

The fracture temperature depends on the elastic constants, the thermal expansion, and the fracture toughness. These parameters are listed in Table X. The fracture toughness was determined using standard indentation techniques.<sup>23-25</sup> The sample used was the same  $10 \times 15 \times 4 \text{ mm}^3$  plate used for measuring the optical damage threshold.

TABLE X. Thermomechanical constants of  $\beta\text{-BaB}_2\text{O}_4$ .

Elastic constants	$S$ ( $\text{TPa}^{-1}$ )	$C$ (GPa)	$dc/dT$ ( $\text{GPa}/^\circ\text{C}$ )
11	25.63	123.8	-0.02828
12	-14.85	60.3	-0.00904
13	-9.97	49.4	-0.01112
14	-63.97	12.3	-0.00772
33	37.21	53.3	-0.02056
44	331.3	7.8	-0.01363
66	81.0	31.8	-0.00962
Thermal expansion			
11		$4 \times 10^{-6}/\text{K}$	
33		$36 \times 10^{-6}/\text{K}$	
Thermal conductivity			
11		0.08 W/m/K	
33		0.8 W/m/K	
Fracture toughness			150 KPa $\text{m}^{1/2}$

Some anisotropy ( $< 100\%$ ) in the fracture toughness was observed, but there was insufficient material to determine the nature and extent of the anisotropy. The value quoted therefore refers to a plate oriented at the type I phase-matching direction for doubling 1064 nm.

The thermal expansion was determined using high-temperature x-ray methods between room temperature and  $900^\circ\text{C}$ . A series of powder x-ray diffraction patterns was taken at several temperatures ranging from room temperature to  $900^\circ\text{C}$ . Five diffraction lines were measured at four temperatures. The temperatures were determined by measuring the lines from the Pt heater, and using the known thermal expansion of Pt,  $9.1 \times 10^{-6}/^\circ\text{C}$ . A least-squares fit to the five lines gave the hexagonal cell  $a$  and  $c$  dimensions. These data showed that the thermal expansion is uniform over this temperature range, and that it is very anisotropic.

The thermal conductivity was determined using a thermal comparator.<sup>26</sup> It also is highly anisotropic. Both the thermal expansion and conductivity relate to the nonlinear terms in the vibrational energy of the crystal. These terms represent interactions between phonons, which give rise to energy shifts and scattering.<sup>27</sup> The cubic phonon-coupling term is responsible for thermal conductivity, and the quartic term for thermal expansion. The anisotropy indicates that in both terms the coupling increases strongly for phonons which propagate closer to the polar axis. Now, it is apparent from the crystal structure that the barium atoms couple mostly to the  $\text{B}_2\text{O}_6$  rings in the same cell, rather than to barium atoms in neighboring unit cells. Therefore, they participate more in phonons which propagate closer to the polar axis. This suggests that the anisotropy is associated primarily with the barium atoms. This correlates with the existence of the phase transition at  $900^\circ\text{C}$ . The two phases differ only in the location of the barium atoms, indicating that there exists a large temperature-dependent term in the lattice energy, and that this term involves the barium atoms. Thus thermal anisotropies correlate well with the two crystal structures and the existence of a phase transition between them.

## ELASTIC CONSTANTS

The elastic constants were determined from the acoustic velocities (EG). The sample used was a rectangular parallelepiped of approximate dimensions  $7.5 \times 8 \times 9 \text{ mm}^3$ . The edges were oriented perpendicular to the crystallographic ( $xyz$ ) directions. Although it was clear and transparent, there was evidence of internal strain or compositional variation in the form of small bubblelike inclusions and cleavage cracks perpendicular to the  $z$  axis. The density was determined to be  $3.840 \text{ g/cm}^3$  by the mass/volume ratio.

The propagation of a planar elastic wave in a homogeneous crystalline material is described by Christoffel's equation<sup>28</sup>

$$\rho_0 v^2 A_i = C_{ijkl} n_j n_l A_k, \quad (21)$$

where  $\rho_0$  is the ambient density of the crystal,  $v$  is the acoustic wave velocity,  $A_i$  is the wave amplitude components,  $n_i$  is the components of the direction of wave propagation, and  $C_{ijkl}$  is the second-order elastic stiffness coefficients. If one chooses a wave mode (direction and polarization) carefully,

Christoffel's equation reduces to a simple relation between wave velocity and some linear combination of (a few) elastic coefficients.

The trigonal symmetry requires six independent elastic stiffness constants. In the shorthand Voigt<sup>29</sup> notation, these are  $C_{11}$ ,  $C_{33}$ ,  $C_{44}$ ,  $C_{66}$ ,  $C_{14}$ , and  $C_{13}$ . The orientations necessary to define the stiffness in terms of phase velocities via the Christoffel equation have been given by Gieske.<sup>30</sup> All but  $C_{13}$  may be defined by compressional and shear wave mode propagation in the  $x$ ,  $y$ , and  $z$  crystallographic directions. The value of  $C_{13}$  must be determined from wave velocities measured in a direction oblique to  $[001]$  and  $[010]$ , and normal to  $[100]$ .

The ultrasonic pulse superposition method of McSkimin<sup>31</sup> was used to measure the transit-times of compressional (longitudinal) and transverse (shear) waves through the oriented specimen. The technique initially requires the bonding of a piezoelectric transducer onto the crystal specimen.  $X$ -cut quartz transducers are used to generate and detect longitudinal waves and  $AC$ -cut quartz transducers are used for transverse waves. The transducers are generally 0.180 in. in diameter. They resonate at a frequency of 20 MHz. The bonding agent used in all the present measurements is polystyrene fluid.

The principle of ultrasonic pulse superposition is to apply a repetitive sequence of radio-frequency (rf) pulses to the transducer at a rate such that the time for an elastic wave to transit the specimen, reflect from the opposite face, and return to the transducer, precisely equals the arrival time of the next applied rf pulse. The 20-MHz carrier frequency which resonates the transducer is generated by an ultrasonic pulse superposition oscillator. This unit also incorporates a gating circuit which performs two functions. The first is to create an echo window by periodically disabling the rf output to the transducer. Any echoes returning to the transducer can now be observed without being overwhelmed by the applied pulses. The second function is to pulse the rf output, thus producing the requisite ultrasonic pulses. The pulse repetition rate is controlled by a variable rf bridge oscillator. The output from the bridge oscillator is monitored by a frequency counter which gives a direct readout of the period of the repetition rate in microseconds. Critical circuits in the frequency counter are maintained at constant temperature. The bridge oscillator output also provides synchronization for the oscilloscope. The repetition rate is adjusted by the experimenter such that the time delay between applied pulses is exactly equal to an integral multiple of round trips through the specimen. When this condition is achieved, the applied pulses are superimposed upon the return echoes, and we have constructive interference. The echoes now build up sufficient amplitude to be observed in the window produced by gating the sequence of applied pulses from the oscillator. The experimenter now critically adjusts the repetition rate so as to maximize the echo amplitude.

At the condition of constructive interference, provided that bond and applied pulse-rf phase shifts are properly assessed,<sup>32</sup> the repetition rate is identical to the actual round-trip transit time  $t_p$  for the acoustic mode through the specimen. It is then a simple and straightforward matter to find

the wave velocity by using the formula

$$v = 2l / t_p, \quad (22)$$

where  $l$  is the specimen length along the approximate axis of wave propagation. The relevant Christoffel relation can then be applied to determine an elastic stiffness tensor component (or some linear combination of components). As in all acoustic methods, the wave velocity being much greater than the rate of heat flow, adiabatic conditions prevail.

The elastic constants were measured at 25 °C. It was found necessary to control the temperature precisely to obtain reproducible data, due to the temperature dependence of the elastic properties. The experiment was repeated at 50 °C, and the thermoelastic constants were derived. These are tabulated in Table X.

### FRACTURE TEMPERATURE

From the elastic constants the analysis of Ref. 8 was used to calculate the fracture temperature as a function of the plate orientation. The results are presented in Fig. 34. For comparison, the analogous calculation for KDP is presented in Fig. 35. The fracture temperature of barium borate appears to be an order of magnitude greater. The fracture temperature of other nonlinear materials such as  $\text{LiIO}_3$  or  $\text{LiNbO}_3$  is comparable to that of KDP.<sup>10</sup> This data implies that barium borate is about an order of magnitude more fracture resistant than other nonlinear materials.

The slope discontinuities in this figure are related to the weakest direction in the crystal surface. In barium borate, there is no shear stress, although this is not true for nonlinear materials in general. For most plate orientations, the weakest direction in the crystal surface is the ordinary direction, which is perpendicular to the polar axis. However, for some orientations near  $\theta = 45^\circ$ ,  $\phi = 90^\circ$ , the weakest direction is extraordinary. The slope discontinuities represent the points where the weakest direction changes from ordinary to extraordinary.

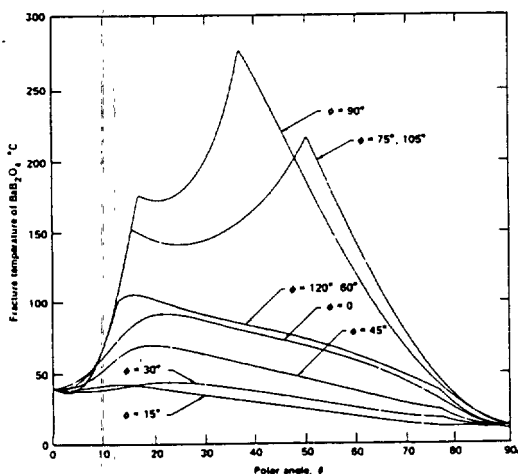


FIG. 34. Thin plate fracture temperature of barium borate. This figure of merit represents the resistance to thermal fracture. Barium borate is about an order of magnitude more resistant than any other nonlinear material for which data exists.

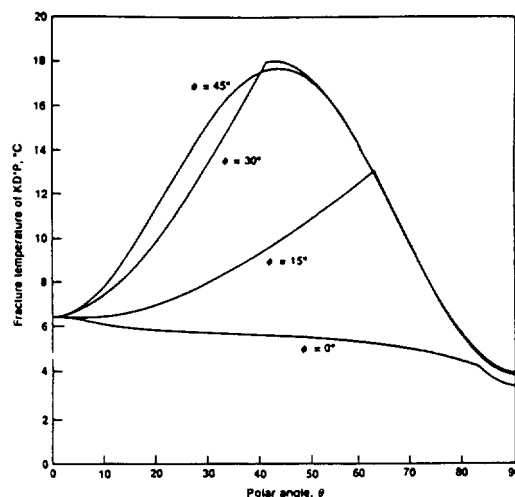


FIG. 35. Thin plate fracture temperature of KDP. Lithium niobate and lithium iodate are similar.

### DIELECTRIC AND ELECTRO-OPTIC PROPERTIES

The dielectric constants were measured as a function of temperature in the range 10–50 °C, and as a function of frequency from 1 to 100 kHz:

$$\begin{aligned} K_{11} &= 6.7, \\ K_{33} &= 8.1, \\ \tan \delta &< 0.001. \end{aligned} \quad (23)$$

No change was seen over the range of temperature and frequency covered. This data may be used to estimate the electro-optic coefficients on the basis of constant Miller's  $\delta$  scaling.<sup>33,34</sup> Such estimates are accurate to within a factor of 2 for other nonlinear optical materials.<sup>22</sup> We obtain

$$\begin{aligned} r_{11} &= 4d_{11} \frac{(K_{11} - 1)}{[\epsilon_0^2(2\omega) - 1]\epsilon_0^4(\omega)} \\ &= 2.7 \text{ pm/V}. \end{aligned} \quad (24)$$

The other electro-optic coefficients are predicted to be an order of magnitude smaller. The corresponding half-wave voltage at 1064 nm is 87 kV.

### SUMMARY

The complete set of material constants required to characterize barium borate as a nonlinear material for frequency conversion has been determined. The crystallographic space group determines the number of independent tensor components. For single pulse conversion, one needs the linear indices as a function of wavelength and temperature, the region of transparency, the nonlinear optical constants and optical damage threshold. From these data the threshold power for any three-wave process can be calculated; this determines whether barium borate can be efficient with the given laser source, and fixes the crystal shape. The crystal size is determined by the damage threshold.<sup>8</sup>

For average power applications, the elastic constants, the thermal expansion and the fracture toughness determine the resistance to thermal fracture, embodied in the thin plate fracture temperature  $\Delta T_F$ . The thermal conductivity is re-

quired to determine the thermal gradients set up as a result of optical absorption. The only parameter which cannot be precisely determined at this time is the optical absorption itself. In the region of transparency, the optical absorption depends on the optical quality, and in particular on the density of inclusions. The absorption of a particular sample is not so much a bulk intrinsic property of the crystal, but is more a function of its crystal growth and history. It seems reasonable that in the region of transparency, the absorption of small samples can be made small, below 0.1%/cm.

The new and exciting features of barium borate compared to existing nonlinear materials are (1) the combination of its range of transparency and its resistance to optical damage, and (2) for average power applications it has a low-temperature sensitivity, and excellent resistance to thermal fracture.

As pointed out in the Appendix, the conversion efficiency depends on two laser system parameters, the total peak power  $P$  and the beam quality  $Q$ . The appropriate figure of merit here is the threshold power; the conversion efficiency is higher for the material with lower threshold power. In general the threshold power of barium borate is not significantly lower than other commonly available materials. Barium borate has a high birefringence, and consequently it has a high angular sensitivity, compared to KDP. The resulting restriction on the crystal length is compensated by the higher nonlinear coupling. In fact, the larger angular sensitivity and the larger nonlinearity almost cancel each other. Barium borate requires high peak powers and high-quality beams to be efficient. On the other hand, it has a high resistance to optical damage, and this leads to smaller crystal size.

The transparency of barium borate in the UV and IR, coupled with its high birefringence, permits phase matching for a variety of optical parametric amplifiers generating tunable radiation in the visible and near IR. However, the peak laser power required for efficient conversion is about the same as for KDP or ADP. Barium borate has the advantage that unlike the KDP isomorphs it is transparent in the near infrared.

Barium borate is one of the few materials capable of fifth harmonic generation of 1064 nm.<sup>1,4</sup> This group includes urea, lithium formate, and potassium pentaborate. However, barium borate has the lowest threshold power and is therefore the most efficient for fifth harmonic generation.

Its most striking advantages occur in average power applications. It is an order of magnitude more resistant to thermal fracture than those other nonlinear materials which have been characterized<sup>10</sup> (LiIO<sub>3</sub>, LiNbO<sub>3</sub>, KDP). It also has a low-temperature sensitivity for doubling 1064 nm and it can be used in a quadrature configuration.<sup>35,36</sup> It is a relatively poor thermal conductor, but this is offset by the wide range of transparency, and in particular by the lack of any intrinsic absorption at 1064, 532, 355, and 266 nm.

Our indirect assessment of its electro-optic properties implies high half-wave voltages and the associated issue of electrical isolation. The operating voltage for transversely excited Pockels cells can be reduced by making the optical path length longer than the transverse dimension. Small ap-

erture Pockels cells using barium borate will require some such voltage reduction technique to be practical. For large aperture switches this consideration may not apply.

In summary, barium borate is a new nonlinear material which brings several new frequency conversion processes closer to general use. This includes fifth harmonic generation, and optical parametric amplifiers generating visible and infrared wavelength. It has excellent average power capabilities and has the potential to make high average power nonlinear optics a practical reality.

## ACKNOWLEDGMENTS

We are pleased to acknowledge our debt to Professor Chuangtien Chen, without whose collaboration this research would not have taken place. All of the data was taken on crystals grown in his laboratory and supplied by him to us. We also gratefully acknowledge the contributions of the following people: R. Gonzales and D. Milam (LLNL, damage threshold), J. Marion (LLNL, fracture toughness), G. Smith and C. Weaver (thermal expansion), D. Smith (PSU, crystal structure), and E. G. Hilbert (PSU, elastic constants). This work was performed under the auspices of the U.S. Department of Energy by Lawrence Livermore National Laboratory under contract W-7405-Eng-48 and the U.S. Department of Defense Advanced Research Projects Agency under ARPA Order No. 5358.

## APPENDIX: THRESHOLD POWER

The threshold power is the key figure of merit in determining the conversion efficiency for critically phase-matched processes. To be efficient the peak power of the laser must exceed the threshold power of the nonlinear material. The peak power required increases rapidly as the beam quality deteriorates. This has been discussed fully in Refs. 8 and 9. Here we summarize the results.

We define the drive and dephasing as follows:

$$\eta_0 = C^2 l^2 I, \quad (A1)$$

$$\delta = (1/2) \Delta k l, \quad (A2)$$

where  $l$  is the crystal length, and  $I$  is the incident total intensity. The nonlinear coupling is

$$C(\text{GW}^{-1/2}) = 5.456 d_{\text{eff}} (\text{pm/V}) / [\lambda_0 (\mu\text{m}) (n_1 n_2 n_3)^{1/2}], \quad (A3)$$

and the phase mismatch is

$$\Delta k = \frac{\partial \Delta k}{\partial \theta} \Delta \theta = \beta_0 \lambda_0 \frac{Q}{D_s}. \quad (A4)$$

Here  $D_s$  is the beam size in the sensitive direction of the crystal (parallel to the extraordinary polarization vector). The beam area is  $D_s D_i$ , where  $D_i$  is the beam dimension in the insensitive direction, and the intensity of the beam is

$$I = P / D_s D_i, \quad (A5)$$

where  $P$  is the incident total power.  $Q$  is the beam quality, or approximately the ratio of the beam divergence in the sensitive direction to the divergence of a diffraction-limited beam. Note that both  $P$  and  $Q$  are unaltered if the beam dimensions are increased using telescopes to expand or contract the

beam aperture. They are paraxial invariants.

The conversion efficiency at low intensity is

$$\eta = \eta_0 \sin^2(\delta), \quad (A6)$$

where  $\sin c(x) = \sin(x)/x$ . The behavior of the conversion efficiency at high intensity where  $\eta_0 > 1$  and the design of frequency conversion devices is discussed fully in Ref. 9 to which the reader is referred for details. Essentially, efficient conversion places a stringent upper limit on the dephasing (0.1–1 rads) and also requires the drive to lie in a range of values between 1 and 10. The crystal length is limited by the requirement of small dephasing. Inserting this limit in the expression for the drive gives a minimum peak power required for efficient conversion.

$$P/Q^2 > P_{th}(\eta_0/4\delta^2)D_i/D_s, \quad (A7)$$

where  $P_{th}$  is the threshold power:

$$P_{th} = (\beta_0 \lambda_0 / C)^2. \quad (A8)$$

The ratio  $\eta_0/\delta^2$  is fixed by the desired conversion efficiency, and the ratio  $D_i/D_s$  is the beam shape factor discussed by Hon.<sup>37</sup> Equation (A7) implies that for efficient conversion of a diffraction limited beam, the threshold power of the crystal must be smaller than the laser peak power. The threshold power required increases rapidly as the beam quality deteriorates.

Because both the peak power and the beam quality are paraxial invariants, it follows that the conversion efficiency is unaffected by telescoping the beam up or down, so long as the crystal dimensions are reoptimized for each beam aperture. In principle, the beam aperture can be chosen to reduce the fluence or intensity to levels compatible with the resistance of the crystal to optical damage.

The threshold power is the relevant figure of merit for comparing the efficiencies of two nonlinear materials.<sup>9</sup> In general, the material with the lower threshold power will be more efficient. It is important to recognize that the process of optimization of a nonlinear material will result in crystal

dimensions which depend on the crystal's parameters, such as its coupling and threshold power. The threshold power determines the efficiency of the optimized system. It is always true that the conversion efficiency of the optimized system increases with the ratio of the peak laser power to the threshold power of the material (Fig. 36).

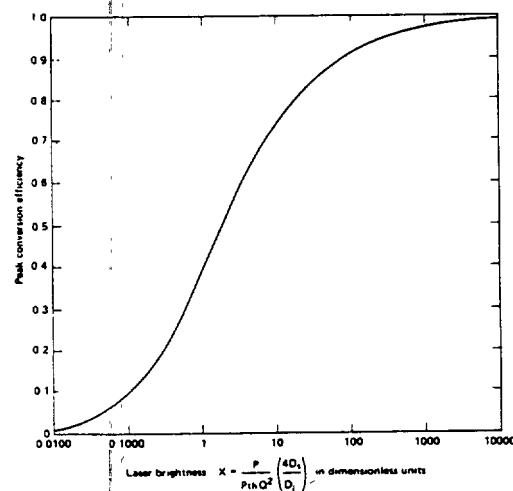


FIG. 36. Peak conversion efficiency for frequency mixing depends only on the paraxial invariant  $P/Q^2$ . For optical parametric amplifiers the curve depends on the small signal gain; it is generally shifted to the right about an order of magnitude in  $P/Q^2$ , relative to this curve.

<sup>1</sup>C. Chen, B. Wu, G. You, and Y. Huang, Digest of Technical Papers of the XIIIth International Quantum Electronics Conference, 1984, paper MCC5 (unpublished).

<sup>2</sup>C. Chen, B. Wu, A. Jiang, and G. You, Sci. Sin. Ser. B 28, 235 (1985).

<sup>3</sup>J.-K. Zhu, B. Zhang, and S.-H. Liu, Society of Professional Instrumentation Engineering Conference on Basic Properties of Optical Materials, Gaithersburg, MD, May 7–9, 1985 (unpublished).

<sup>4</sup>K. Kato, IEEE J. Quantum Electron. QE-22, 1013 (1986).

<sup>5</sup>K. Miyazaki, H. Sakai, and T. Sato, Opt. Lett. 11, 797 (1986).

<sup>6</sup>G. Zhang, C. Jin, F. Lin, C. Chen, and B. Wu, Guangxue Xuebao 4, 513 (1984).

<sup>7</sup>C. Chen, Y. X. Fan, R. C. Eckardt, and R. L. Byer, Society of Photo-Optical Instrumentation Engineering Conference on Lasers, San Diego, CA, July 1986 [Proc. SPIE 684 (to be published)].

<sup>8</sup>D. Eimerl, IEEE J. Quantum Electron. QE-23, 575 (1987).

<sup>9</sup>D. Eimerl, Society of Photo-Optical Instrumentation Engineering Conference on Lasers, San Diego, CA, July 1986 [Proc. SPIE 681 (to be published)].

<sup>10</sup>D. Eimerl, Society of Photo-Optical Instrumentation Engineering Conference on Lasers and Electro-optics, Los Angeles, CA, January 1987 (to be published).

<sup>11</sup>E. M. Levin and H. F. McMurdie, J. Res. Natl. Bur. Stand. 42, 131 (1949).

<sup>12</sup>A. D. Mighell, A. Perloff, S. Block, Acta Crystallogr. 20, 819 (1966).

<sup>13</sup>K. H. Hubner, Neues Jahrb. Mineral. Monatsh., 335 (1969).

<sup>14</sup>J. Liebertz and S. Stahr, Z. Kristallogr. 165, 91 (1983).

<sup>15</sup>R. Frohlich, Z. Kristallogr. 168, 109 (1984).

<sup>16</sup>S. Lu, M. Ho, and J. Huang, Acta Phys. Sin. 31, 948 (1982).

<sup>17</sup>D. Smith, Pennsylvania State University (private communication, 1986).

<sup>18</sup>There seem to be minor, but significant, discrepancies in the cell dimensions reported in the literature. R. Frohlich, Ref. 15:  $a = 12.519(6)$  Å,  $c = 12.723(6)$  Å; Lu *et al.*, Ref. 16:  $a = 12.532$  Å,  $c = 12.717$  Å; Zalkin, this work:  $a = 12.547(6)$  Å,  $c = 12.736(9)$  Å. It is possible that these are due to variations in the samples, or that only one of the above is correct. Due to an insufficient supply of material, we were not able to resolve this question.

<sup>19</sup>R. Li and C. Chen, Acta Phys. Sin. 34, 823 (1985).

<sup>20</sup>C. S. Willand and A. C. Albrecht, Opt. Commun. 57, 146 (1986).

<sup>21</sup>S. Velsko and D. Eimerl, J. Appl. Phys. (to be published).

<sup>22</sup>D. Eimerl, Ferroelectrics 72, 95 (1987).

<sup>23</sup>G. R. Anstis, P. Chantikul, B. R. Lawn, and D. B. Marshall, J. Am. Ceram. Soc. 64, 533 (1981).

<sup>24</sup>P. Chantikul, G. R. Anstis, B. R. Lawn, and D. B. Marshall, J. Am. Ceram. Soc. 64, 539 (1981).

<sup>25</sup>R. F. Cook and B. R. Lawn, J. Am. Ceram. Soc. 66, C-200 (1983).

<sup>26</sup>R. W. Powell and W. T. Clark, J. Sci. Instrum. 39, 545 (1962).

<sup>27</sup>R. E. Peierls, *Quantum Theory of Solids*, Clarendon Laboratory (Oxford University Press, Oxford, 1955), Chap. 1.

<sup>28</sup>H. B. Huntington, *The Elastic Constants of Crystals* (Academic, New York, 1958).

<sup>29</sup>R. F. S. Hearmon, *Landolt Bornstein Series*, Vol. III/II (Springer, Berlin, 1979), p. 2; see also W. Voigt, *Lehrbuch der Kristallphysik* (Teubner, Leipzig, 1928).

<sup>30</sup>J. H. Giekse, Ph.D. thesis, The Pennsylvania State University (1968).

<sup>31</sup>H. J. McSkimin, J. Acoust. Soc. Am. 33, 12 (1961).

<sup>32</sup>J. H. McSkimin and P. Andreatch, J. Acoust. Soc. Am. 34, 609 (1962).

<sup>33</sup>R. C. Miller, Appl. Phys. Lett. 5, 17 (1964).

<sup>34</sup>F. Zernike and J. E. Midwinter, *Applied Nonlinear Optics* (Wiley, New York, 1973).

<sup>35</sup>D. Eimerl, *Proceedings of the International Conference on Lasers 1984*, edited by K. M. Corcoran (STS, McLean, VA, 1984), p. 557.

<sup>36</sup>D. Eimerl, IEEE J. Quantum Electron. (to be published).

<sup>37</sup>D. Hon, *Laser Handbook*, edited by M. L. Stutch (North-Holland, New York, 1979), Vol. 3, Chap. B2, p. 421.

**MBP**

J. T. LIN

*Revised 24 September 1989; revised and accepted 13 February 1990*

```

1 # Importing the libraries
2 import numpy as np
3 import pandas as pd
4
5 # Importing the dataset
6 data = pd.read_csv('Salary_Data.csv')
7
8 # Splitting the dataset into the Training set and Test set
9 from sklearn.cross_validation import train_test_split
10 X = data[['YearsExperience']]
11 y = data['Salary']
12 X_train, X_test, y_train, y_test = train_test_split(X, y, test_size = 0.2,
13                                                     random_state = 0)
14
15 # Feature Scaling
16 from sklearn.preprocessing import StandardScaler
17 sc_X = StandardScaler()
18 X_train = sc_X.fit_transform(X_train)
19 X_test = sc_X.transform(X_test)
20
21 # Fitting the Training set to Linear Regression
22 from sklearn.linear_model import LinearRegression
23 regressor = LinearRegression()
24 regressor.fit(X_train, y_train)
25
26 # Predicting the Test set results
27 y_pred = regressor.predict(X_test)
28
29 # Comparing Actual vs Predicted
30 df = pd.DataFrame({'Actual': y_test, 'Predicted': y_pred})
31
32 # Visualising the Training set results
33 plt.scatter(X_train, y_train)
34 plt.plot(X_train, regressor.predict(X_train))
35 plt.title('Training set results')
36 plt.xlabel('YearsExperience')
37 plt.ylabel('Salary')
38
39 # Visualising the Test set results
40 plt.scatter(X_test, y_test)
41 plt.plot(X_test, regressor.predict(X_test))
42 plt.title('Test set results')
43 plt.xlabel('YearsExperience')
44 plt.ylabel('Salary')
45
46 # Saving the model
47 import pickle
48 with open('model.pkl', 'wb') as f:
49     pickle.dump(regressor, f)
50
51 # Loading the model
52 with open('model.pkl', 'rb') as f:
53     regressor = pickle.load(f)
54
55 # Predicting a new value
56 X_new = np.array([[10]])
57 y_new = regressor.predict(X_new)
58
59 # Evaluating the model
60 from sklearn.metrics import r2_score
61 r2 = r2_score(y_test, y_pred)
62
63 # Conclusion
64 print('The model is trained and tested successfully. The R-squared value is', r2)
65
66 # End of the program
67

```

Advanced solid-state laser technology has been emphasized for applications which require wide wavelength tunability (frequency agility), good efficiency, high average power and beam quality. Tunable solid-state lasers with tuning ranges in the near-infrared (IR) such as alexandrite (710 to 820 nm), Ti:sapphire (660 to 1100 nm) and Cr:Gd<sub>3</sub>Sc<sub>2</sub>Ga<sub>3</sub>O<sub>12</sub> (GSGG) (742 to 842 nm), and in the mid-IR such as Co:MgF<sub>2</sub> (1.5 to 2.3  $\mu$ m) have been studied for wide tunabilities. Diode-pumped systems have been explored for high efficiency and compactness. Phase-conjugate resonators and Raman clean-up systems are attractive for the improvement of beam quality. Non-linear crystals and the associated frequency-conversion techniques, on the other hand, are widely investigated for frequency agility and for the extension of laser spectra not covered by the available direct emissions from the laser host-crystals.

Coherent sources with spectral range of ultraviolet (UV) to IR cover a variety of application areas including research, industry, medicine and military. Specific examples are: (1) laser sources in the 3 to 5 and 8 to 12  $\mu\text{m}$  ranges for military IR countermeasures;

(2) 1.3 to 3.0  $\mu\text{m}$  for remote sensing in lidar systems and medical applications; (3) 1.54  $\mu\text{m}$  for eye-safe radiation used in tactical training systems and communications; (4) tunable visible sources 400 to 700 nm and UV sources (200 to 400 nm) for optical processing, biomedical studies and various military systems; and (5) deep-UV (160 to 200 nm) sources for photochemical and spectroscopy studies.

The recent technology of optical materials growth, both in laser hosts and non-linear crystals, enhances the development of many new coherence sources with tunable spectral regimes which are difficult to achieve or cannot be achieved by conventional lasers and materials. New sources may be generated from various frequency-conversion techniques using non-linear media. For frequency up-conversion, these techniques include second-harmonic generation (SHG), sum-frequency mixing (SFM) and anti-Stokes in stimulated Raman scattering (SRS). On the other hand, for frequency down-conversion, techniques include optical parametric oscillation (OPO), difference-frequency mixing (DFM) and Stokes in SRS.

New non-linear crystals suitable for frequency conversions using the second-order non-linearity have been recently explored for the generation of coherent sources ranging from deep UV to mid-IR [1-6]. In this paper we present a critical review on some important crystals for the generation of tunable sources. In addition to the recent progress, some new results are reported in Sections 3, 4 and 5.

In Section 2 we present schemes for the generation of tunable sources ranging from XUV to IR using various frequency-conversion techniques and the available non-linear crystals and laser systems. In Section 3 we present the features of some new non-linear crystals and their applications for tunable sources. Crystals to be discussed include  $\beta$ -barium-borate (BBO), lithium triborate (LBO), and potassium titanyl phosphate (KTP), potassium niobate (KNbO<sub>3</sub>), MgO-doped lithium niobate (MgO:LiNbO<sub>3</sub>) and the self-frequency-doubling crystal neodymium yttrium aluminium borate (NYAB). The advantages of non-critical phase-matching and several examples are also presented. The figure-of-merit and conversion efficiency are analysed in Section 4. Green source generated from a self-frequency-doubling crystal NYAB is discussed in Section 5. Conclusions are drawn in Section 6.

## 2. Schemes of tunable sources

With the exception of the free-electron laser, the tuning ranges of presently available lasers are either limited by the available lasing materials or are restricted by their operation temperature. Frequency-conversion techniques using the second-order non-linearity in crystals (SHG, SFM, DFM and OPO) or the third-order non-linearity in gases (SRS and three-photon process) provide efficient ways of generating sources with wide spectra. In this section we present the schemes for the generation of UV, visible and IR sources using various non-linear crystals. Greater details of specific schemes with phase-matched tuning curves are given in Section 3.

Fig. 1 illustrates the schemes for the generation of coherence sources ranging in the XUV (38 to 120 nm) and deep-UV (189 to 250 nm) spectral regimes. In these frequency-conversion techniques the new crystals of BBO and LBO are the best candidates for coherent sources limited only by their transparency cutoff at 189 and 160 nm, respectively. Shorter wavelengths may be achieved by third-harmonic generation (using third-order non-linearity) or SFM in gases such as neon and sodium.

Fig. 2 shows tunable sources in the UV and visible regimes generated from SFM and OPO in Nd:Y<sub>3</sub>Al<sub>5</sub>O<sub>12</sub> (YAG) (and its harmonics) and Ti:sapphire lasers. The non-linear

Figure 1 XUV s harmonics of N

crystals suita (LAP) [3, 4].

For tunabl frequency do such as the T be achieved t that BBO cry tuning range 3  $\mu\text{m}$ ), KTP ( of DFM usin for OPO (in

Nd:YA

Figure 2 Tunable harmonics of Nd

# Non-linear crystals for tunable coherent sources

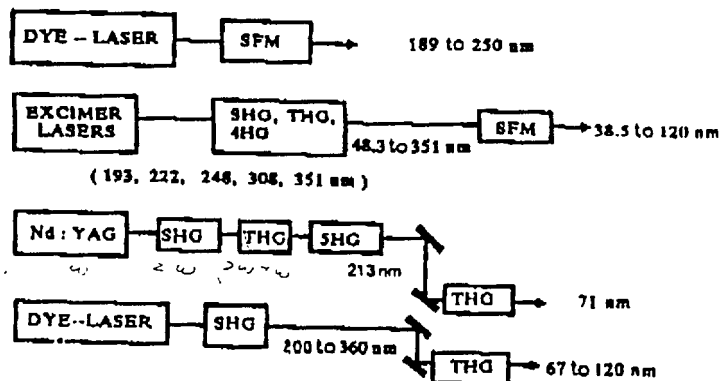


Figure 1 XUV sources generated from SFM and third-harmonic generation (THG) of dye lasers and the harmonics of Nd:YAG and excimer lasers. 4HG, 5HG, Fourth- and fifth-harmonic generation, respectively.

crystals suitable for these applications include BBO, LBO, urea and L-arginine phosphate (LAP) [3, 4].

For tunable IR sources (1 to 8  $\mu\text{m}$ ), OPO and DFM represent the unique techniques for frequency down-conversion (as shown in Fig. 3). Note that using tunable pumping sources such as the Ti:sapphire or the alexandrite laser, rapid beam-steering (in wavelengths) may be achieved by the OPO processes without angle-tuning of the crystal. We discuss below that BBO crystal promises this feature due to this wide tunability (defined as wavelength tuning range per degree of angle-tuning). Crystals suitable for IR sources are BBO (1 to 3  $\mu\text{m}$ ), KTP (1 to 4.5  $\mu\text{m}$ ), KNbO<sub>3</sub>, LiNbO<sub>3</sub>, and lithium iodate (1 to 5  $\mu\text{m}$ ). Tuning curves of DFM using KTP and KNbO<sub>3</sub> are shown in Figs 17 and 18, later. Experimental results for OPO (in KTP) are shown in Section 3.2, where tuning ranges of 1.8 to 2.4  $\mu\text{m}$  are

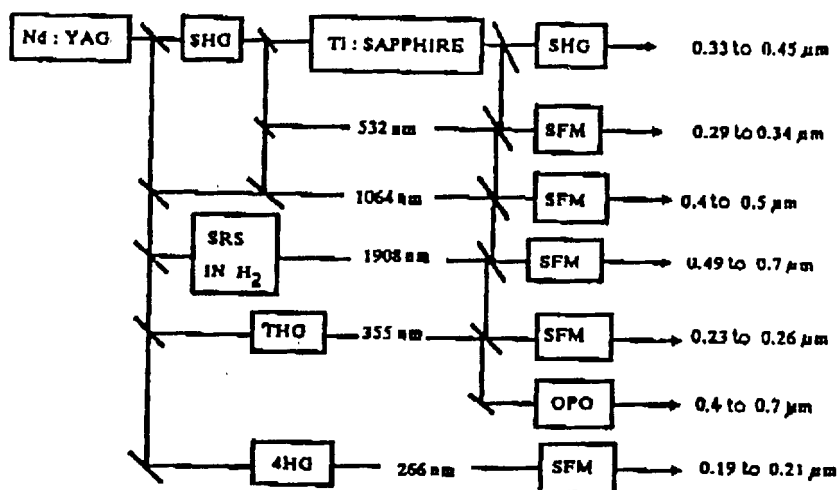


Figure 2 Tunable new lasers in UV and visible spectra generated from SFM of Ti:sapphire laser and harmonics of Nd:YAG laser. THG, 4HG, Third- and fourth harmonic generation, respectively.



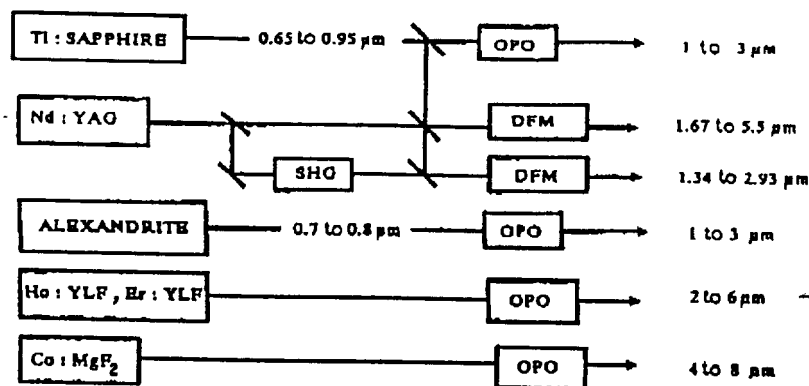


Figure 3 DFM and OPO for new laser sources with tuning ranges of 1 to 8  $\mu\text{m}$ .

demonstrated by using Nd:YAG (1.064  $\mu\text{m}$ ) as the pump [5, 6]. For spectral regimes of 4 to 12  $\mu\text{m}$ , semiconductor crystals such as AgGaSe<sub>2</sub> and thallium arsenic selenide (TAS) with transparency ranges beyond 4  $\mu\text{m}$  are required [7, 8]. Furthermore, using either a CO laser or a doubled-CO<sub>2</sub> laser as the pump, 8 to 12  $\mu\text{m}$  may be achieved from OPO [8].

Frequency mixing of Nd:YAG and dye laser also provides a wide tunable spectral range. We note that shorter wavelengths in the deep-UV (160 to 200 nm) may be achieved by the new crystal of LBO using the SFM scheme. As shown in Fig. 4, the DFM of Nd:YAG and dye laser promises another efficient technique for mid-IR sources, where LiNbO<sub>3</sub> and AgGaS<sub>2</sub> crystals have been demonstrated [10]. For high average-power conversion, crystals of LBO, BBO and deuterated L-arginine phosphate (D-LAP) are suitable for SHG and third-harmonic generation. UV and visible sources generated from the harmonics of a free-electron laser are shown in Fig. 5 for the suitable non-linear crystals, where tunable sources have been identified for potential applications in surgical treatments [11].

Fig. 6 shows the frequency down-conversion of OPO followed by SRS for IR sources beyond 4  $\mu\text{m}$ . Using combinations of BBO, KTP and Raman gases such as H<sub>2</sub>, D<sub>2</sub> and CH<sub>4</sub>, may achieve very wide tuning ranges.

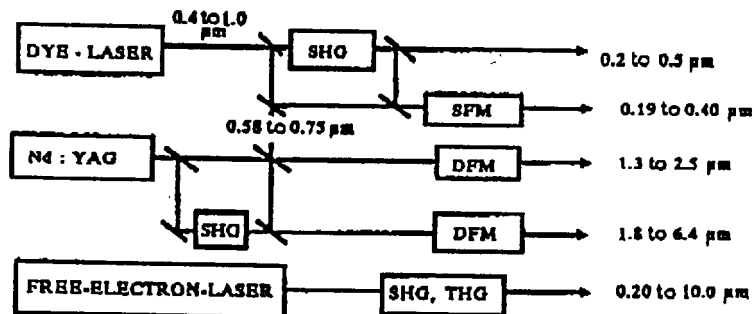


Figure 4 New laser sources in visible and IR regimes using SFM and DFM in dye laser, Nd:YAG and free-electron lasers.

Figure 5 UV and I



Figure 6 Tunable n  
respectively.

Furthermore  
organic crystals  
in diode-laser-p  
ally required in

3. Features  
3.1. BBO and  
Single crystals o  
Institute of Res  
then, BBO has t

## Non-linear crystals for tunable coherent sources

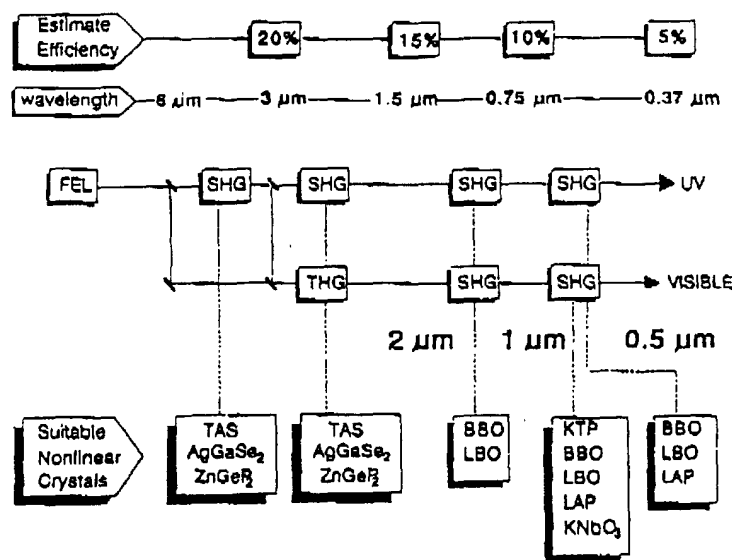


Figure 5 UV and IR sources generated from the harmonics of free-electron laser (FEL).

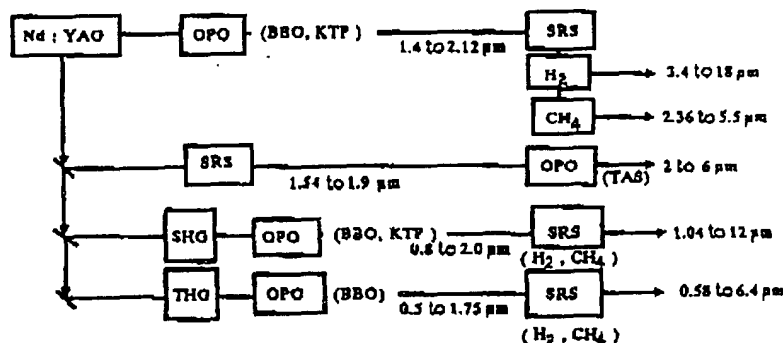


Figure 6 Tunable new laser sources (1 to 18 μm) using OPO and Raman-shift in crystals and gas media, respectively.

Furthermore, high-efficiency non-linear crystals of KTP, MgO:LiNbO<sub>3</sub>, KNbO<sub>3</sub> and organic crystals in both bulk and waveguided forms have been explored for visible sources in diode-laser-pumped systems (Fig. 7). Non-critical phase-matching conditions are generally required in these low-power systems. Greater detail is given in Section 3.

### 3. Features and applications of some non-linear crystals

#### 3.1 BBO and LBO crystals

Single crystals of BBO and LBO were successfully grown and characterized by the Fujian Institute of Research on the Structure of Matter (FIRSM, Fuzhou, China) [12, 13]. Since then, BBO has been widely used for the generation of UV sources from the up-conversion

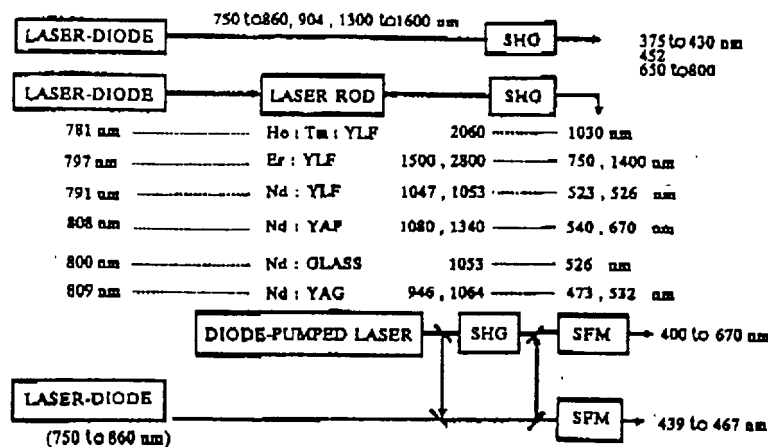


Figure 7 Diode-pumped lasers and their harmonics for visible sources.

of dye lasers and Nd:YAG lasers [14-35]. (Table I gives a list of progress.) BBO has promising features of wide transmission ranges (189 to 3000 nm), high non-linearity (about four times that of KDP, potassium dihydrogen phosphate) and high damage threshold and is phase-matchable within its whole transparency regime. Furthermore, BBO has a very wide tunability in OPO, which makes BBO an excellent crystal for tunable solid-state lasers in the UV, visible and IR regimes [1, 3]. Because of its small group-velocity dispersion ( $105 \text{ fs mm}^{-1}$ ), BBO is a better crystal than KDP for the use of autocorrelation of short pulses (pico- and femtosecond). Large temperature acceptance width (about  $55^\circ \text{C}$ ) also allows BBO to be used in high average power lasers with good conversion stability. However, BBO has a rather small acceptance angle width (only  $0.6$  to  $2 \text{ mrad cm}$ ) and large beam walk-off ( $50$  to  $70 \text{ mrad cm}$ ). Also, its conversion efficiency is limited by the degree of focusing and pump beam quality. To overcome these problems, type II operation with larger acceptance width ( $0.8 \text{ mrad cm}$ ) than that of type I and the cylindrical focusing technique have been explored [3]. The major applications of BBO with the associated phase-matching angles are listed in Table II.

Tunable sources in the UV and visible regimes may be achieved by the SFM of Nd:YAG (1064 nm, 532 nm) and tunable lasers (dye or solid-state). The calculated phase-matching curves are shown in Fig. 8, based on the Sellmeier equations given in [15, 16].

The BBO crystal is a uniaxial crystal with an effective non-linearity given by  $d_{\text{eff}} = d_{22} \cos \theta$  (for type I, optimal value) which represents a vanishing  $d_{\text{eff}}$  when an angle of  $90^\circ$  is achieved. This unfavourable  $90^\circ$  phase-matching of BBO limits its conversion efficiency in deep-UV (189 to 219 nm) sources generation. Fig. 9 shows the cutoff wavelengths of doubling, tripling and mixing of dye lasers, where the shortest wavelength of 189 nm was generated via the mixing of 248.5 and 788 nm [21, 22]. For comparison, the OPO tuning curves of urea, BBO and LBO are shown in Fig. 10. We note that urea crystal may achieve  $90^\circ$  phase-matching with the maximum  $d_{\text{eff}}$  using either 308 nm (excimer laser) or 355 nm (tripled-YAG) as the pump [26]. However, the tunability (wavelength tuning range per degree of crystal angle-tuning) of urea is much narrower than that of BBO. Figs 11-13 show the rapid-tuning OPO curves using BBO crystal, where tunable lasers are required as the pump. For the case of LBO, non-critical phase-matching (NCPM) ( $\theta = 90^\circ$ ,  $\phi = 0^\circ$ ) may

TABLE I Progress

Process

SHG

SHG

SHG

FHG

OPO

THG

SHG

SFM

FHG

OPO

SHG

SHG

OPO

THG

SHG

Q-switch

OPO

SHG

SFM

OPO

FHG, fifth harmonic

be achieved using the degenerate pumped OPO is the may be achieved of 149 to  $200^\circ \text{C}$  temperature tun Nd:YAP laser

LBO has a mu to  $2 \text{ mrad cm}$ ),

# Non-linear crystals for tunable coherent sources

TABLE I Progress of BBO crystal

Process	Output wavelength	Laser used and efficiency	Reference
SHG	204.8 nm	4% from 120 MW cm <sup>-2</sup> , 8 ns dye laser	15, 16
SHG	205 to 310 nm	36% from 423 MW cm <sup>-2</sup> , 18 ns dye laser	17
SHG	532 nm	84% from 120 MW cm <sup>-2</sup> , 1 ns mode-locked YAG	18, 19
FHG	213 nm	11% overall efficiency	18, 19
OPO	940 to 1220 nm	3 mJ from 10 mJ pump (at degeneracy)	18, 19
THG	197.4 nm	20% from tripled dye laser	18, 19
SHG	197.3 nm	low temperature (95 K) doubling dye laser	20
SFM	189 to 197 nm	7% at 193 nm by mixing of excimer laser (248.5 nm) and dye laser (788 to 950 nm)	21, 22
FHG	213, 70.9 nm	FHG of YAG (using BBO) tripled in neon gas 3.7% (for FHG) and 2.4 (at 7 nm <sup>-1</sup> ) out of 2 MW (at 213 nm)	23
OPO	0.45 to 1.68 μm	9.4% pumped by tripled YAG (at 355 nm, 15 mJ)	24
SHG	0.35 to 0.42 μm	31% (105 mJ at 378 nm) SHG of alexandrite laser, 68 ns pulse	25
SHG	532 nm	40% from 10 ns YAG, type I versus type II BBO	9
OPO	0.5 to 0.7 μm	Pumped by excimer (308 nm) and tripled YAG (355 nm)	26-29
THG	351 nm	0.8% from 50 GW cm <sup>-2</sup> , 5 ps Nd: glass laser	30
SHG	215 to 235 nm	5 mW at 225 nm by intracavity doubling of a ring dye laser (Brewster-angle-cut BBO)	31
Q-switch		40 kW peak power (125 ns FWHM)	32
OPO	0.35 to 1.5 μm	51% energy efficiency, pumped by excimer laser of 6.5 mJ	33, 34
SHG	255 nm	0.7% (49 mW) from 8.5 W copper vapour laser, 30 ns pulse	35
SFM	271 nm	0.9% (64 mW) from mixing of 511 and 578 nm	35
OPO	0.35 to 2.37 μm	10% for 454 to 958 nm range, pumped by excimer (308 nm)	36

FHG, fifth harmonic generation; THG, third-harmonic generation; SFM, sum-frequency-mixing.

be achieved using a doubled-YAG (532 nm) as the pump, where the NCPM condition at the degenerate point may also be achieved at high temperature (149°C) (37). Temperature-tuned OPO is therefore promising in LBO crystal, where a tuning-range of 0.9 to 1.3 μm may be achieved by using doubled-YAG (at 532 nm) as the pump and temperature tuning of 149 to 200°C (estimated values based on the calculated phase-matching angles and temperature tuning rate). An NCPM temperature of 112°C was also reported for SHG of Nd: YAP laser (at 1.079 nm) (13, 37).

LBO has a much larger acceptance angle (10 to 60 mrad cm) width than that of BBO (0.6 to 2 mrad cm), therefore higher efficiency may be achieved by using an LBO crystal.

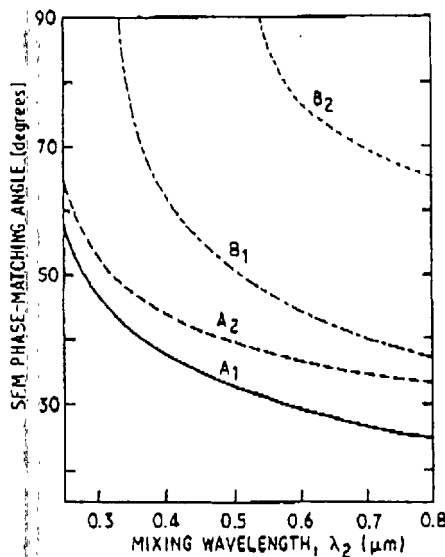


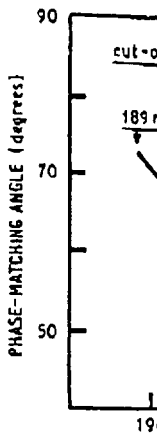
Figure 8. SFM of BBO at mixing wavelengths  $\lambda_1 = 1064$  nm (curves  $A_1$  and  $A_2$ ), 532 nm ( $B_1$  and  $B_2$ ) for type I and II, respectively, where the SFG wavelength  $\lambda_1 < \lambda_2 < \lambda_3$  and polarization directions are in the order of  $(\lambda_1, \lambda_2, \lambda_3)$ . Calculated curves in Figs 8 to 13 are based on the Sellmeier equations given in [15].

Potential applications of LBO should include: (1) NCPM of doubling Nd:YAG, both intra- and external-cavity; (2) NCPM of tunable IR sources (1 to 3  $\mu$ m) by temperature-tuned OPO pumped by 532 or 1064 nm; (3) frequency-doubling of tunable solid-state lasers such as Ti:sapphire and alexandrite laser; (4) deep UV (160 to 250 nm) sources generated from the mixing of dye lasers (200 to 300 nm) and IR lasers (1 to 3  $\mu$ m) [38, 39]. For crystals with large temperature gradients of the wavevector mismatching ( $d(\Delta k)/dT$ ), NCPM may be achieved by temperature tuning of the crystal. We have recently characterized the NCPM temperatures ( $T^*$ ) and temperature bandwidth (FWHM) for various frequency-mixing schemes using LBO. Results are summarized as follows [40]: ( $T^*$ , FWHM) = (149°C, 4°C/cm)

TABLE II Major applications of BBO crystal using type I and type II phase-matching. (Angles are calculated from the Sellmeier equations given in [15])

Phase-match angle, $\theta$ (degrees)		Applications
Type I ( $\phi = 0^\circ$ )	Type II ( $\phi = 30^\circ$ )	
22.8	32.8	SHG of Nd:YAG (both at 1064 and 1320 nm), tunable (600 to 3000 nm) laser pumped by 532 nm in OPO, eye-safe laser (1.54 $\mu$ m) by OPO
31	30	Third-harmonic generation of Nd:YAG, SHG of alexandrite and Ti:sapphire laser
47.6	81	Fourth-harmonic of Nd:YAG, THG of alexandrite and Ti:sapphire laser
51	57.2	Fifth-harmonic of Nd:YAG, SHG of copper vapour laser, SHG of dye laser (470 to 580 nm)
63	*	SHG of dye laser (425 to 480 nm)
80	*	SHG of dye laser (410 to 430 nm), THG and SFM of dye laser for deep-UV sources (189 to 250 nm)

\*Note that the cutoff fundamental wavelengths of BBO are (in nm): 410 and 526 for type I and type II SHG, and 589 and 668 for type I and type II third-harmonic generation.



for SHG of 1064 nm of 1135 nm. (1) of 1064 and 15

The temperature indices by

where  $(d(\Delta k)/dT)$

where  $u_i = \theta_i$ , frequency-mix

The quantities from the Sellmeier

We measured results are shown in Equation 2 be

As shown in Figure of the indices the negative slope doubling of lo +20°C).

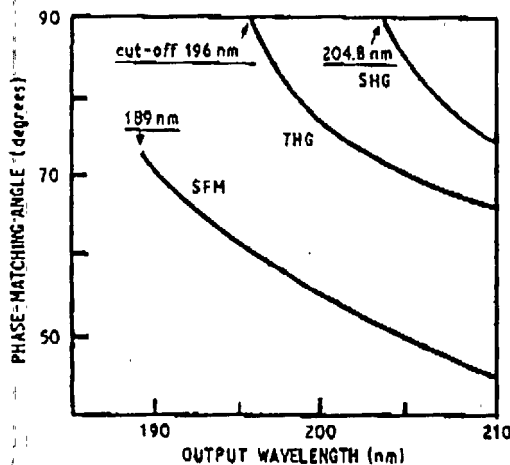


Figure 9 Tunable deep-UV sources generated from SHG, third-harmonic generation (THG) and SFM in dye-laser systems using BBO (type I). Note that 189 nm is generated from the SFM of 248.5 and 788 nm dye lasers. Also shown are the cutoff wavelengths for phase matching.

for SHG of 1064 nm, ( $-9^{\circ}\text{C}$ ,  $9.3^{\circ}\text{C cm}$ ) for SHG of 1319 nm, ( $77^{\circ}\text{C}$ ,  $4.8^{\circ}\text{C cm}$ ) for SHG of 1135 nm, ( $114^{\circ}\text{C}$ ,  $5^{\circ}\text{C cm}$ ) for SFM of 1064 and 1135 nm, ( $12.5^{\circ}\text{C}$ ,  $18^{\circ}\text{C cm}$ ) for SFM of 1064 and 1543 nm, ( $82^{\circ}\text{C}$ ,  $16^{\circ}\text{C cm}$ ) for SFM of 1064 and 1908 nm.

The temperature tuning rate ( $R$ ) is related to the temperature variation of the refractive indices by

$$R = \frac{d\lambda}{dT} = \left( \frac{d(\Delta k)/dT}{d(\Delta k)/d\lambda} \right) \quad (1)$$

where  $(d(\Delta k)/dT)$  may be measured directly or indirectly by using the relationship

$$\frac{d(\Delta k)}{dT} = - \left( \frac{d(\Delta k)}{du} \right) \left( \frac{u_2 - u_1}{T_2 - T_1} \right) \quad (2)$$

where  $u_i = \theta_i, \phi_i$  are the phase-matching angles at temperature  $T_i$  and  $\Delta k$  is given by (for frequency-mixing of  $\lambda_1$  and  $\lambda_2$  with output wavelength  $\lambda_3$ )

$$\Delta k = \frac{n_3}{\lambda_3} - \frac{n_2}{\lambda_2} - \frac{n_1}{\lambda_1} \quad (3)$$

The quantities  $u_i$  and  $T_i$  can be measured experimentally and  $(d(\Delta k)/du)$  can be calculated from the Sellmeier equations [15, 16].

We measured the phase-matching angles of LBO crystal at various temperatures and the results are shown in Fig. 14. For type 1 SHG in the principal  $xy$ -plane (with  $\theta = 90^{\circ}$ ), Equation 2 becomes

$$\left( \frac{dn_{1z}}{dT} - \frac{dn_{2y}}{dT} \right) = - \left( \frac{dn_{1z}}{d\phi} - \frac{dn_{2y}}{d\phi} \right) \left( \frac{\phi_2 - \phi_1}{T_2 - T_1} \right) \quad (4)$$

As shown in Fig. 14, the slope  $(d\phi/dT)$  is not a constant; that is, the temperature variations of the indices difference  $(d(\Delta n)/dT)$  in general are non-linear functions. We note that the negative slope of  $(d\phi/dT)$  also indicates that NCPM may be achieved for frequency-doubling of longer-wavelengths (1.1 to  $1.5 \mu\text{m}$ ) lasers at low temperatures ( $-20$  to  $+20^{\circ}\text{C}$ ).

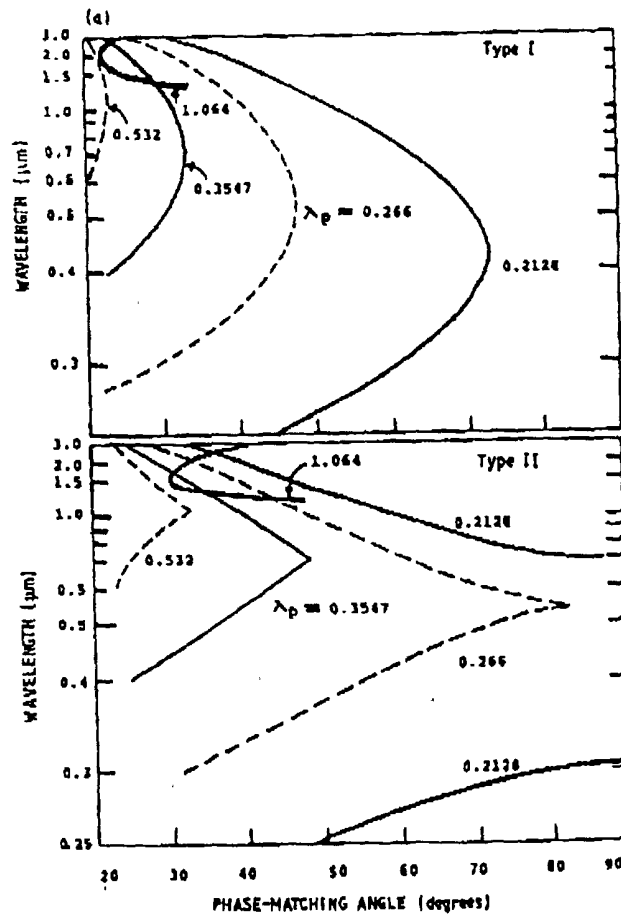


Figure 10 Contin

Figure 10 OPO tuning curves of (a) BBO and (b) urea and LBO at various pumps  $\lambda_p$ . Note that in BBO crystal, type I has smaller phase-matching angle and higher effective non-linearity than that of type II. NCPM may be achieved in urea and LBO.

### 3.2. KTP and KNbO<sub>3</sub> crystals

Mid-IR tunable lasers (1.3 to 4  $\mu\text{m}$ ) may be achieved by OPO in KTP and KNbO<sub>3</sub> (see Figs 15 and 16). KTP, KNbO<sub>3</sub> and LBO all have the same symmetry of mm2. As shown in Table III, non-critical phase-matching may be achieved in these crystals [40]. Using KNbO<sub>3</sub>, efficiencies of 0.27 and 17% have been reported in single-pass and resonant-cavity for frequency-doubling of diode laser at 842 nm. KTP has also been explored for the generation of 459 nm by mixing 809 nm (diode laser) and 1064 nm (diode-pumped Nd:YAG), where room-temperature NCPM is achieved [41, 42]. There are many other potential applications using the room-temperature NCPM in KTP and KNbO<sub>3</sub>, which are discussed in Section 3.3.

S292

Tunable mid or KNbO<sub>3</sub>, wh as the pump [5 15 and 16. Tu Nd:YAG (at (Fig. 17) and k

3.3. OPO in The schematics .xz-plane, the p type II (positiv are linearly pol when the tunin KTP cut at 53°

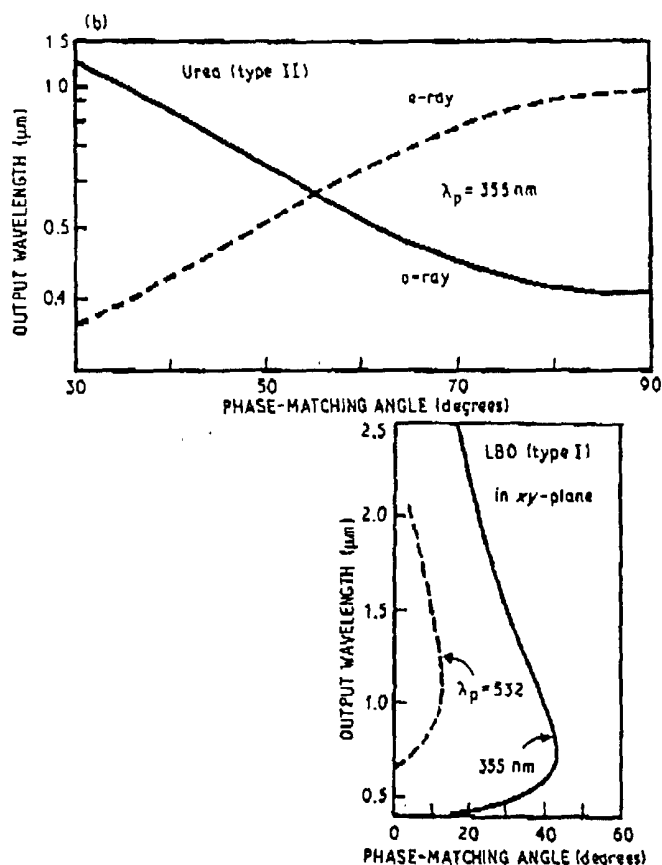


Figure 10 Continued.

Tunable mid-IR (1.5 to 4  $\mu\text{m}$ ) solid-state lasers may be achieved by OPO in either KTP or  $\text{KNbO}_3$ , where either doubled-YAG (at 532 nm) or Nd:YAG (1064 nm) may be used as the pump [5, 6, 43-49]. The OPO tuning curves of KTP and  $\text{KNbO}_3$  are shown in Figs 15 and 16. Tunable mid-IR sources (2 to 5  $\mu\text{m}$ ) may also be generated from DFM of Nd:YAG (at 1064 nm) and Ti:sapphire, dye or diode laser (695 to 877 nm) using KTP (Fig. 17) and  $\text{KNbO}_3$  (Fig. 18).

### 3.3. OPO in KTP crystal

The schematics of the OPO set-up is shown in Fig. 19. For OPO pumped by 1064 nm in the xz-plane, the pump beam was linearly polarized along the 'o-ray' (that is, the y-axis) for the type II (positive crystal) operation (oe-o). We should note that the output signal and idler are linearly polarized in the xz-plane. As shown in Fig. 20, the e-ray switches to the o-ray when the tuning curves cross the degenerate point. We have measured the tuning ranges of KTP cut at 53° (to the z-axis, in the xz-plane). Within our measurement accuracy of  $\pm 0.2^\circ$ ,



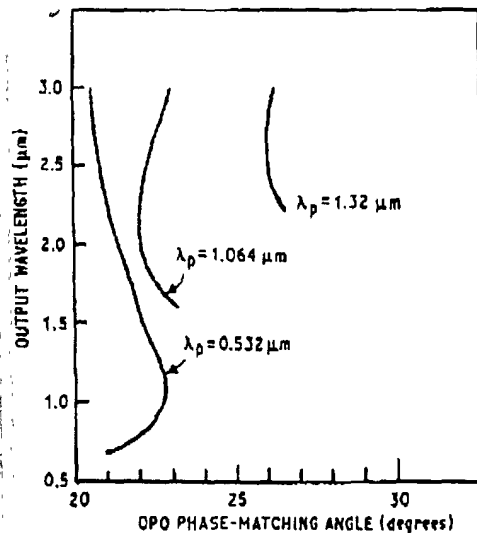


Figure 11 Visible and mid-IR tuning ranges generated from OPO in type 1 BBO crystal. Note that the eye-safe laser at  $1.54 \mu\text{m}$  may be achieved by using either 532 or 1064 nm as the pump. Angle-cut of  $22.8^\circ$  (same angle for SHG of 1064 nm) is appropriate for both OPO processes.

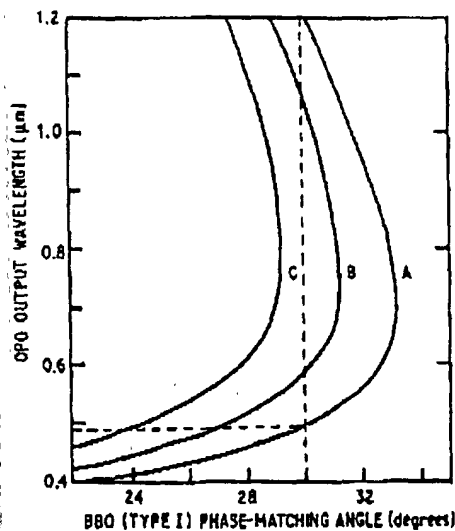


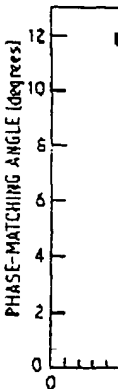
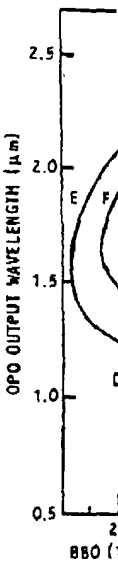
Figure 12 Rapid-tuning OPO ( $0.48$  to  $1.2 \mu\text{m}$ ) in BBO (type I) crystal pumped by tunable sources generated from SHG of alexandrite laser. Note that very wide tunability may be achieved at a fixed crystal angle. Curves A, B and C are for pump wavelengths of 355, 376 and 400 nm, respectively. See text.

the measured data agree very well with the calculated curves based on the Sellmeier equations [16]. A tuning range of  $1.8$  to  $2.4 \mu\text{m}$  was achieved in our experiment. We note that the phase-matching angles of KTP are slightly different in our KTP (grown by the flux method and used in this experiment) from that of the hydrothermally grown KTP in [43–46]. In our experiment, tuning curves were obtained by rotating the crystal about the  $y$ -axis, keeping the angle  $\phi = 0^\circ$ ; that is, in the  $xz$ -plane.

As shown in Figs 21 and 22, we have measured the total output energy of the signal (at  $2.07 \mu\text{m}$ ) and idler (at  $2.2 \mu\text{m}$ ) as a function of the pump energy (at  $1064 \text{ nm}$ ) at various cavity lengths. As expected, a shorter cavity provides a higher efficiency with a lower

S294

Non-linear



threshold. W  
the signal at  
slope efficien  
tance ( $T$ ) of

The effect  
KTP crystal  
 $\text{pm V}^{-1}$ ) =  
(for pump a  
the KTP typ  
type I opera  
 $\theta < \Omega$ , then

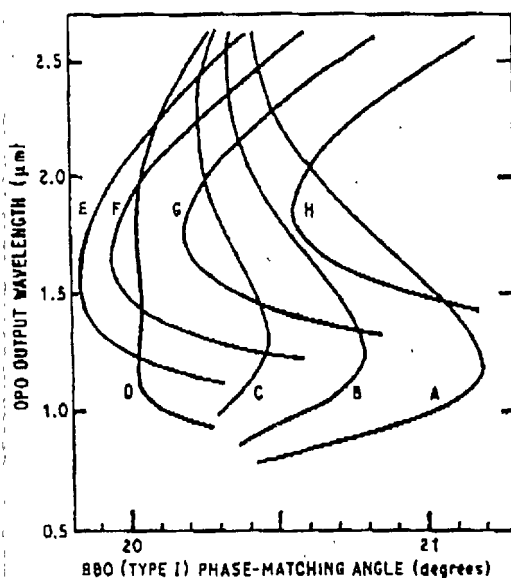


Figure 13 Rapid-tuning OPO in BBO (type I) pumped by tunable dye laser or Ti:sapphire laser at various pump wavelengths (in nm): (A) 600, (B) 625, (C) 650, (D) 700, (E) 776, (F) 825 (G) 875 and (H) 925.

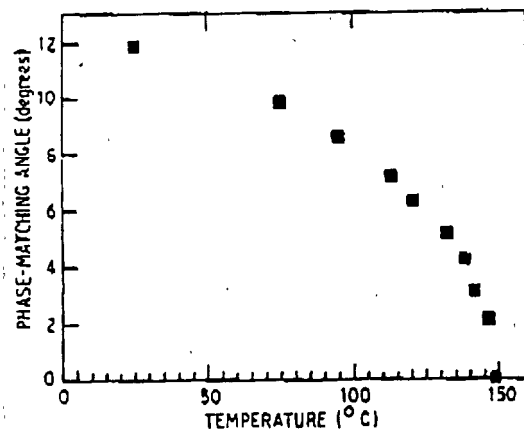


Figure 14 Phase-matching angles at various temperatures for frequency doubling of Nd:YAG (at 1064 nm) using LBO crystal (type I SHG in the  $xy$ -plane).

threshold. We note that a lower threshold may be achieved by using a higher reflectance (at the signal and idler wavelengths) of the out-coupling mirror. On the other hand, a larger slope efficiency (but also a higher threshold) may be achieved by using a higher transmittance ( $T$ ) of the out-coupling mirrors.

The effective non-linear coefficients ( $d_{eff}$ ) for OPO, at the degenerate points, for BBO and KTP crystals at various pumping wavelengths were calculated as follows: for BBO,  $d_{eff}$  (in  $\text{pm V}^{-1}$ ) = 1.64 to 1.65 (for pumping wavelengths of 0.532 to  $1.5 \mu\text{m}$ ); for KTP,  $d_{eff}$  = 7.6 (for pump at 532 nm), 6.15 (at 1064 nm), 6.7 (at  $1.32 \mu\text{m}$ ) and 7.4 (at  $1.54 \mu\text{m}$ ). Note that the KTP type II phase-matching cutoff at about  $1.75 \mu\text{m}$  (for the pump) and  $d_{eff} = 0$  for type I operation in the principal planes of  $xz$ ,  $xy$  and  $yz$ , except when in the  $xz$ -plane and  $\theta < \Omega$ , then  $d_{eff}(I) = d_{32} \sin \theta$  (see Table III).

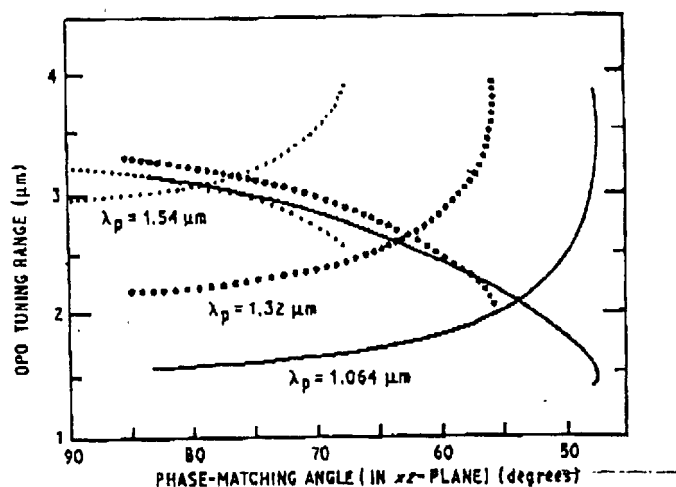


Figure 15 OPO tuning curves of KTP (type II, with angle-tuning in the  $xz$ -plane) at various pumping wavelengths ( $\lambda_p = 1.064, 1.32$  and  $1.54 \mu\text{m}$ ), where the effective non-linear coefficients ( $d_{\text{eff}}$ ) are given in Table III. Curves are calculated based on the Sellmeier equations in [16].

TABLE III Comparison of biaxial crystals with point group of  $mm2$

	KTP	KNbO <sub>3</sub>	LiB <sub>3</sub> O <sub>6</sub>
Symmetry	$mm2$	$mm2$	$mm2$
Optical angle (at 1064 nm) (degrees)	21.9	57.2	54.6
(Crystal type)	(Positive)	(Negative)	(Negative)
Optical axis: ( $x, y, z$ )			
Crystallographic axis	( $a, b, c$ )	( $c, a, b$ )	( $a, c, b$ )
Non-linear coefficients ( $\text{pm V}^{-1}$ )			
$d_{31}, d_{32}, d_{33}$	6.5, 5.0, 13.7	15.8, 18.3, 27.4	1.15, 1.24, 0.063
$d_{15}, d_{24}$	6.1, 7.6	16.5, 17.1	1.15, 1.24
Maximum $d_{\text{eff}}$	Type II	Type I	Type I
Acceptance widths:			
Non-critical ( $\text{mrad cm}^{1/2}$ )	108, 186	30	57
Critical ( $\text{mrad cm}$ )	15, 83	12	9
Temperature width ( $^{\circ}\text{C cm}$ )	25	0.05	9
Non-critical phase-matching	SFM of 809 and 1064 nm (room temperature)	SHG of 860 and 986 nm (room temperature)	SHG of 1064 nm (at $149^{\circ}\text{C}$ ) and 1079 nm (at $112^{\circ}\text{C}$ )
$xz$ -plane ( $\phi = 0^{\circ}$ ):			
$d_{\text{eff}(II)}$ (for $0 < \theta < \Omega$ )	$d_{32} \sin \theta$	$-d_{31} \cos \theta$	$d_{15} \cos^2 \theta + d_{24} \sin^2 \theta$ (II)
$d_{\text{eff}(II)}$ (for $\Omega < \theta < 90^{\circ}$ )	$-d_{24} \sin \theta$	$d_{13} \cos \theta$	$d_{31} \cos^2 \theta + d_{32} \sin^2 \theta$ (I)
$yz$ -plane ( $\phi = 90^{\circ}$ ):			
$d_{\text{eff}(II)}$	0	$-d_{32} \sin^2 \theta - d_{31} \cos^2 \theta$	0
$d_{\text{eff}(II)}$	$-d_{15} \sin \theta$	0	$d_{15} \cos \theta$
$xy$ -plane ( $\theta = 90^{\circ}$ ):			
$d_{\text{eff}(II)}$	0	$-d_{32} \sin \phi$	$d_{32} \cos \phi$
$d_{\text{eff}(II)}$	$-d_{15} \sin^2 \phi - d_{24} \cos^2 \phi$	0	0

Figure 16 OPO tuning curves of KTP (type II, with angle-tuning in the  $xz$ -plane) at various pumping wavelengths ( $\lambda_p = 1.064, 1.32$  and  $1.54 \mu\text{m}$ ), where the effective non-linear coefficients ( $d_{\text{eff}}$ ) are given in Table III. Curves are calculated based on the Sellmeier equations in [16].

In this reflection threshold Within our double-res single-res be achieved generate

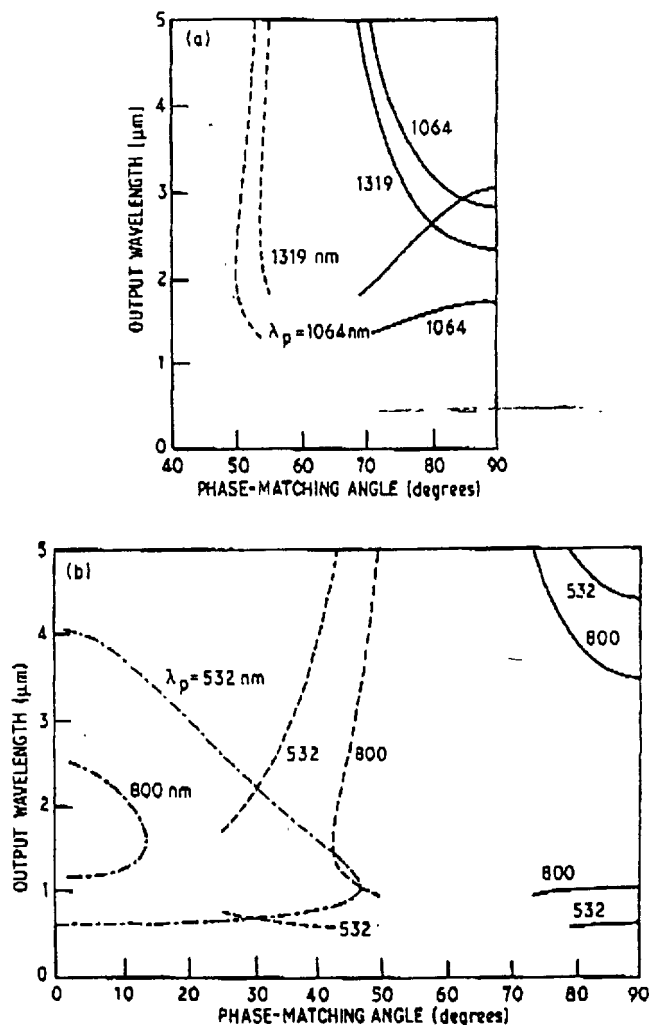


Figure 16 OPO tuning curves of KNbO<sub>3</sub> with angle tuning in the xz-plane for (—) type I, (---) type II and (—) type I (in xy-plane) at various pump wavelengths ( $\lambda_p$ ). Curves are calculated based on the Sellmeier equations in [47-49].

In this experiment the efficiencies achieved were limited by the damage to the anti-reflection-coated mirrors and the uncoated KTP crystal. Furthermore, the tunability and threshold power are limited by the available broadband, high-reflectance entrance mirrors. Within our coating conditions, this experiment was operated at double-pass (for the pump), double-resonance oscillation. The stability of the output power may be improved by single-resonance oscillation coating. Wide tuning ranges of 1.5 to 4.0 μm, in principle, can be achieved when the appropriate coatings are available. By using a pump source at 1.54 μm (generated from SRS in CH<sub>4</sub> gas), it should be possible to achieve the tuning range of 2.5

Nd: YAG  
15 ns, TEM<sub>00</sub>

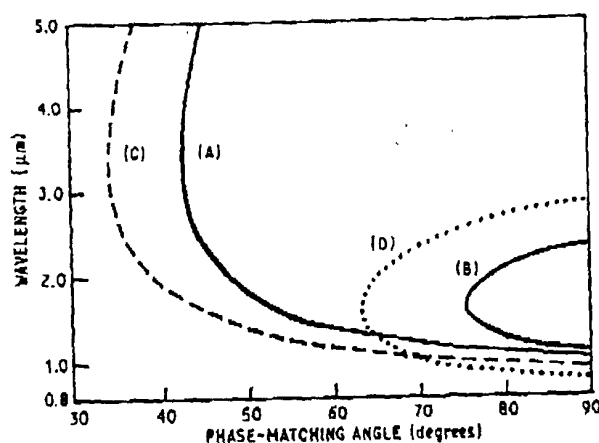


Figure 17 Tunable mid-IR sources (2 to 5 μm) generated from DFM of Nd:YAG (1064 nm) and a Ti:sapphire laser (696 to 877 nm) using KTP with angle-tuning in the xz-plane (curves A and B) and in the yz-plane (curves C and D). Difference polarization configuration (---) (oe-o) and (···) (eo-o) (for 1064 nm, mid-IR Ti:sapphire), respectively, for curves (A, B) and (C, D).

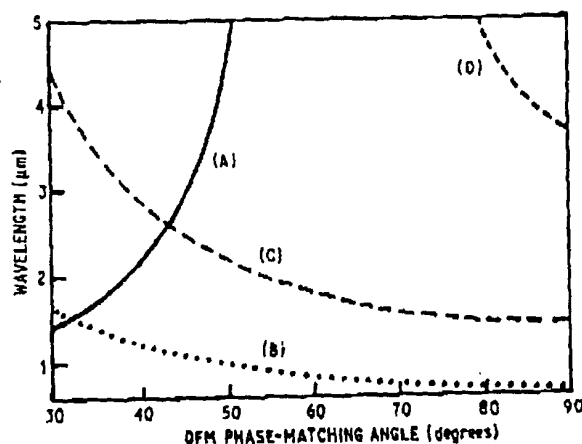
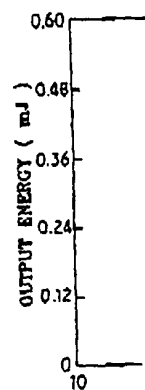
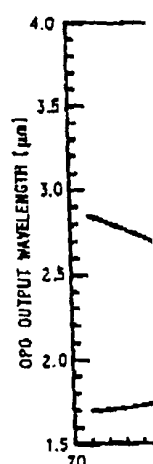
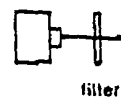


Figure 18 Same as Fig. 17, but for KNbO<sub>3</sub> crystals. The angle tunings are: curve A (type I, in the xz-plane, (oe-e)), B (type I, in the xy-plane, (oe-e)), C (type II, in the xz-plane, (eo-e)), D (same as C but for (oe-e)).

to 3.5 μm easily. Fig. 15 shows the calculated OPO tuning curves of KTP at various pumping wavelengths, where the effective non-linear coefficient, may be found from Table III for a beam propagating in the xz-plane, is also shown. Furthermore, high-efficiency OPO may be achieved via several channels: (1) non-critical phase-matching operated at high temperature; (2) elliptical focusing in the insensitive plane to reduce the walk-off effects; and (3) multiple-resonance of the pump via the appropriate coating of the cavity. We have recently reported the non-critical phase-matching curves for KTP, KNbO<sub>3</sub>, and LBO crystals [36, 50]. We note that the 90° phase-matching is achievable for OPO in



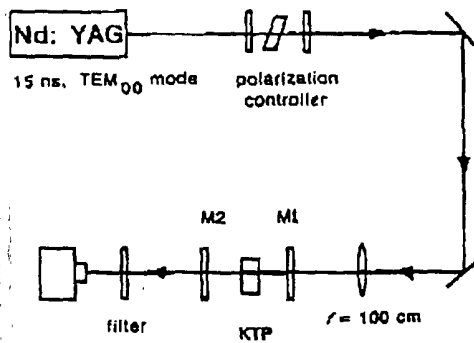


Figure 19 Schematics of the OPO set-up, where the pumping beam was linearly polarized along the y-axis of the crystal angle-tuned about the y-axis in the xz-plane for tunable output.

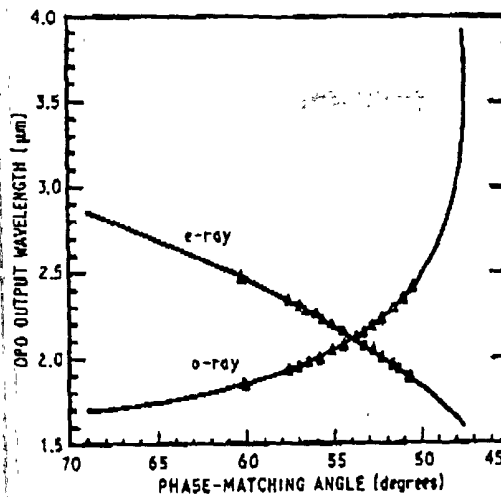


Figure 20 (—) Tuning curves (calculated) of KTP crystal for OPO pumped by YAG lasers (1064 nm) in the xz-plane, where measured tuning ranges of 1.8 to 2.4  $\mu\text{m}$  are also shown ( $\blacktriangle$ ).

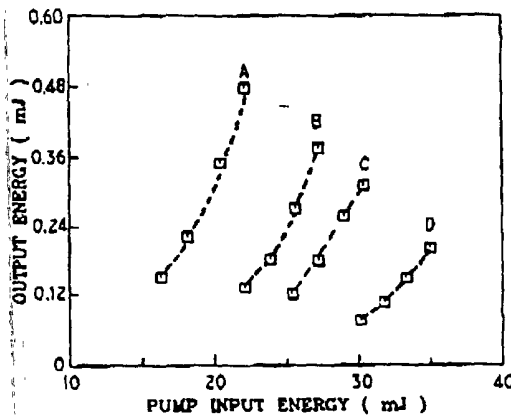


Figure 21 Output energy as a function of pump energy at various cavity lengths (in cm): (A) 2, (B) 3, (C) 4, (D) 4.5 and (E) 5. Output energy was measured at the normal incident with output wavelengths of 2.07 and 2.19  $\mu\text{m}$ , spot sizes were 1.5 mm.

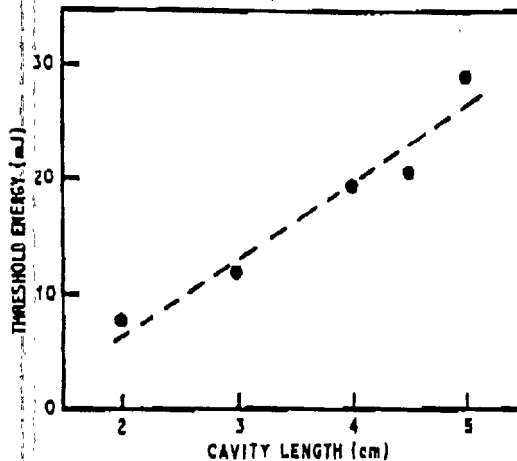


Figure 22 The threshold energy plotted against the cavity lengths, based on the measured data in Fig. 21. (●) Experiment and (---) theory.

KTP using 1064 nm as the pump for the generation of 1.6 and 3.2  $\mu\text{m}$  sources as shown in Fig. 15. This work is in progress.

### 3.4. Non-critical phase-matching (NCPM)

Non-linear crystals operated at the NCPM conditions, particularly at room temperature, are always desirable for high-efficiency frequency conversions. Crystals at the NCPM provide several advantages over that of the critically phase-matched: (1) maximum effective non-linear coefficient ( $d_{\text{eff}}$ ); (2) wide angular, spectral and temperature bandwidths; and (3) no Poynting vector walk-off, where the first-order dispersion of the  $k$ -vector vanishes and only the second-order dispersion contributes to the phase mismatching. We note that under the NCPM conditions it is also possible that  $d_{\text{eff}} = 0$  rather than the maximum, depending on the types of operation (see Table III for greater detail).

KTP crystals operated at the critical-phase-matching (CPM) conditions have been widely used for frequency-doubling of Nd:YAG (1064 nm) laser, where the NCPM usually cannot be temperature-tuned due to the rather small temperature gradient of the refractive indices. High-temperature NCPM operations have been identified in several crystals such as MgO-doped LiNbO<sub>3</sub> and KNbO<sub>3</sub> in doubling Nd:YAG lasers and diode lasers. Angle-tuned CPM in KTP crystal for tunable IR lasers was recently reported [3, 6, 43–46]. In this section we report the room-temperature NCPM using KTP and KNbO<sub>3</sub> for various frequency conversions including SHG, SFM and DFM. These high-efficiency NCPMs operated at room temperature promise potential applications for the generation of coherent sources ranging from the visible to the mid-IR, particularly in the diode-laser-pumped systems.

Depending on the propagation and polarization directions there are, in general, 12 possible configurations for the three-wave-mixing processes in biaxial crystals, where waves (under the NCPM) may propagate along the three principal axes of  $a$ ,  $b$  and  $c$ . These configurations are:

$$[abb] \quad [bba] \quad [acc] \quad [cca] \quad [bcc] \quad [ccb]$$

for type I, and:

$$[aac] \quad [caa] \quad [bbc] \quad [cbb] \quad [aab] \quad [baa]$$

for type II, where the wavelengths of the waves are  $1/\lambda_1$ , where  $w$

In general, the angle  $\theta$ ,  $\phi$  and  $\Omega$ , between the  $c$  axis and the  $a$  and  $b$  principal axes of KNbO<sub>3</sub>,  $d_{\text{eff}}$  is

For KTP (1

For KNbO

From these ex

NCPM has n

Using the c

lished Sellme

NCPM angles

$n_x$  or  $n_z$ . We h

KTP, the  $d_{\text{eff}}$

configurations

IIA[ $bcb$ ] and I

the NCPM an

most of these

reported exper

Nd:YAG (at

angle-tuned v

perature (348

Based on th

of application

temperature l

near-NCPM)

1. Generati

459 nm (from

Nd:YLF), 4

778 and 108

1318 nm), wh

for type II, where  $[a, b, c]$ , etc., represent the directions of the linearly polarized fields with wavelengths of  $[\lambda_1, \lambda_2, \lambda_3]$ , in order. For conservations of energy in SFM,  $1/\lambda_1 + 1/\lambda_2 = 1/\lambda_3$ , where we have assumed that  $\lambda_1 > \lambda_2 > \lambda_3$ .

In general, the effective second-order non-linear coefficient  $d_{\text{eff}}$  is a complicated function of  $\theta$ ,  $\phi$  and  $\Omega$ , where  $\theta$  and  $\phi$  are angles with respect to the  $x$ - and  $z$ -axes and  $\Omega$  is the angle between the optical axis and the  $z$ -axis. For  $mm2$ -orthorhombic crystals of KTP and  $\text{KNbO}_3$ ,  $d_{\text{eff}}$  reduces to a simple form when the mixing waves are propagating along the principal axes. As shown in Table III, the  $d_{\text{eff}}$  are as follows.

For KTP (in the  $xy$ -plane)

$$\begin{aligned} d_{\text{eff}} (\text{type I}) &= 0 \\ d_{\text{eff}} (\text{type II}) &= d_{15} \sin^2 \phi + d_{24} \cos^2 \phi \\ &= d_{15} (\text{along } b\text{-axis, } \phi = 90^\circ, \text{ defined as B-cut}) \\ &= d_{24} (\text{along } a\text{-axis, } \phi = 0^\circ, \text{ defined as A-cut}) \end{aligned} \quad (5)$$

For  $\text{KNbO}_3$  (in the  $yz$ -plane)

$$\begin{aligned} d_{\text{eff}} (\text{type II}) &= 0 \\ d_{\text{eff}} (\text{type I}) &= d_{31} \cos^2 \theta + d_{32} \sin^2 \theta \\ &= d_{31} (\text{along } b\text{-axis, } \theta = 0^\circ, \text{ defined as B-cut}) \\ &= d_{32} (\text{along } a\text{-axis, } \theta = 90^\circ, \text{ defined as A-cut}) \end{aligned} \quad (6)$$

From these expressions we conclude that for principal-axis propagation only type II (I) NCPM has non-vanishing  $d_{\text{eff}}$  in KTP ( $\text{KNbO}_3$ ) crystal.

Using the conventional notations for the refractive indices,  $n_x < n_y < n_z$ , and the published Sellmeier equations for KTP [16] and  $\text{KNbO}_3$  [47-49], we have calculated the NCPM angles that meet the matching conditions of  $n_1/\lambda_1 + n_2/\lambda_2 = n_3/\lambda_3$ , where  $n_i = n_x, n_y$ , or  $n_z$ . We have also calculated the  $d_{\text{eff}}$  for various configurations. It is found that, for KTP, the  $d_{\text{eff}}$  of type I is much smaller than that of type II. Among the six possible configurations, we found that only two meet the NCPM in type II operation. These are IIA[ $bc\bar{b}$ ] and IIB[ $aca$ ] as shown in Fig. 23. We note that the values of  $d_{\text{eff}}$  (of KTP) under the NCPM are 5 to 7  $\text{pm V}^{-1}$ , which are 10- to 15-times that of KDP. We also note that most of these NCPM operations have not been explored experimentally. There is only one reported experiment that used KTP for SFM of diode laser (at 809 nm) and diode-pumped Nd:YAG (at 1064 nm), with extremely wide FWHM of acceptance angle (8 and 18° in angle-tuned with respect to the  $z$ - and  $x$ -axes), acceptance spectrum (3.3 nm) and temperature (348°C) [41, 42].

Based on the NCPM curves shown in Fig. 23 for KTP, we are able to explore a variety of applications which utilize the features of very high  $d_{\text{eff}}$  and very wide angle, spectrum and temperature bandwidth of KTP crystals operated at the room-temperature NCPM (or near-NCPM) conditions. They include the following.

1. Generation of visible sources of 540 nm (from SHG of Nd:YALO at 1080 nm), 459 nm (from SFM of 809 and 1064 nm), 467 nm (from SFM of 842 and 1047 nm, Nd:YLF), 464 nm (from SFM of 830 and 1053 nm, Nd:glass) and 452 nm (from SFM of 778 and 1080 nm, Nd:YALO) and 439 nm (SFM of 818 and 659 nm; that is, tripling of 1318 nm), where YLF and YALO represent laser hosts of LiYF<sub>4</sub> and YALO<sub>3</sub>.



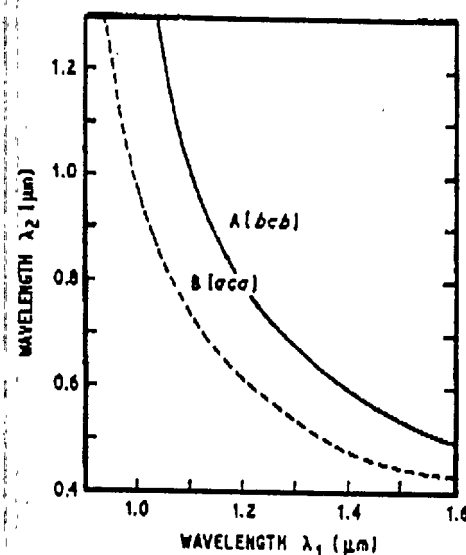


Figure 23 NCPM curves for type II SFM in KTP crystal (at room temperature) [bcb] for curve A represents the polarization directions for  $\lambda_1$ ,  $\lambda_2$  and  $\lambda_3$ , respectively, with  $1/\lambda_3 = 1/\lambda_1 \pm 1/\lambda_2$ . For KTP crystal, (abc) corresponds to the (xyz) axes. An example of curve B is the mixing of 1064 nm (polarization along the a-axis) and 809 nm (polarization along the c-axis) with output of 469 nm (linearly polarized along the a-axis). This is represented as [aca].

2. Generation of tunable sources from SFM of tunable laser-diode (765 to 905 and 1195 to 1330 nm) and the diode-pumped lasers (946, 1047, 1063, 1080, 1320 and 1340 nm). The tuning ranges (at the NCPM conditions) are (in nm): 423 to 463, 442 to 485, 445 to 489, 448 to 492, 484 to 537, 487 to 540, 528 to 553, 558 to 586, 562 to 591, 567 to 596, 627 to 662 and 632 to 667. These tuning ranges cover almost the whole visible spectrum (400 to 700 nm).

We now analyse the NCPM in KNbO<sub>3</sub> crystals. For this crystal we found four configurations that meet the NCPM conditions (at room temperature): IA[bbc], IB[aac] (for type I) and IIA[bcc], IIB[acc] (for type II), where A and B represent the *k*-vector propagation directions along the *a*- and *b*-axis, respectively, with the *E*-fields polarizations along [bbc], etc., for wavelengths of [ $\lambda_1$ ,  $\lambda_2$ ,  $\lambda_3$ ] in order. As discussed above, only type I has a non-vanishing  $d_{xx}$  for propagation along the principal axes. Among these NCPM conditions shown in Fig. 24, there are only few examples that have been explored [47]: (1) SHG of 986 nm (dye laser) using IB[aac]; (2) SFM of 676 nm (krypton laser) and 1064 nm (Nd: YAG laser) using IA[bbc].

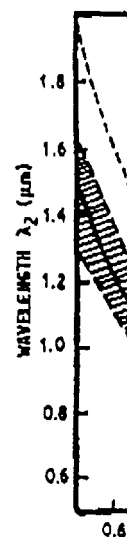
The potential applications based on the NCPM curves shown in Fig. 24 are summarized as follows.

1. A-cut, using  $d_{33}$  of curve A[bbc] for the generation of visible laser of: 414 nm (from SFM of YAG at 1064 nm and excimer at 676 nm), 430 nm (SHG of diode laser at 860 nm), 428 nm (SFM of diode laser at 904 and 815 nm), 447 nm (tripled Nd: YAP at 1340 nm).

2. B-cut, using  $d_{31}$  of curve B[aac] for the generation of: 493 nm (from SHG of dye laser at 986 nm), 490 nm (SFM of 1964 nm and diode laser at 907 nm), 472 nm (SFM of 1320 nm and alexandrite laser at 745 nm), 450 nm (SFM of 1550 nm and dye laser at 635 nm).

3. Tunable visible spectra may be achieved by temperature tuning, where the room-temperature NCPM curves may be up (down) shifted by high (low) temperature operations (as shown in Fig. 24).

Although KNbO<sub>3</sub> has much higher non-linear coefficients than that of KTP, the overall conversion efficiency of KNbO<sub>3</sub> is limited by the rather small acceptance widths.



Furthermore, NCPM curves for tunable microwaves at 809 nm, therefore is possible to pump diodes at 1064 and 809 nm.

3.5. LINB LiNbO<sub>3</sub> crystals have high non-linear coefficients and low refractive index dispersion, or to interact with the signal of length, the signal by a factor of the conversion and by using the crystal. For the case of 23N (for the crystal), the Czochoy growth with reversal in SHG of 189 mW.

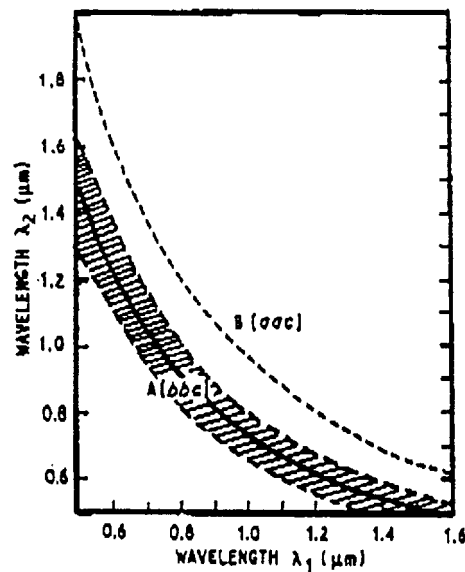


Figure 24 NCPM curves for type I SFM in  $\text{KNbO}_3$  crystal. Note that  $(\delta\delta c)$  corresponds to the  $[yzz]$  axes for this negative crystal, where  $d_{31}$  used in A-cut is larger than  $d_{31}$  used in B-cut. Two special cases of SFM are: A-cut for SHG of 860 nm and B-cut for SHG of 986 nm. Also shown is the shadow regime which may be temperature-tuned for a wider SFM spectrum.

Furthermore, much better temperature control is required in  $\text{KNbO}_3$ . We note that the NCPM curves for SFM, shown in Figs 23 and 24, are also valid for OPO and DFM for tunable mid-IR laser sources. We also note that in the reported experiment of SFM 1064 and 809 nm, the intracavity 1064 nm wave generated from Nd:YAG is randomly polarized and therefore is coupled to 809 nm only by its component polarized in the  $a$ -axis [41, 42]. It is possible to generate a linearly polarized field of 1064 nm by choosing the appropriate pumping diode wavelength. In this case better SFM efficiency may be achieved by coupling 1064 and 809 nm in the  $a$ - and  $c$ -directions [50].

### 3.5. $\text{LiNbO}_3$ and $\text{MgO}:\text{LiNbO}_3$ crystals

$\text{LiNbO}_3$  crystal has recently been developed to meet quasi-phase-matching (QPM) applications and was the first technique suggested by Armstrong *et al.* in 1962 for compensating refractive index dispersion [51]. This technique may be applied to isotropic materials or to interactions which are not phase-matchable in anisotropic materials. By modulating the sign of the non-linear coefficient of the crystal at odd multiples of the coherence length, the periodic stack crystals may achieve QPM with the effective coupling reduced by a factor of  $2/\pi$  in comparison to that of the common phase-matching crystal. However, the conversion efficiency may be largely enhanced by the number of domains in the crystal and by using the highest non-linear coefficient of the crystal such as  $d_{31}$  in  $\text{LiNbO}_3$ . For the case of  $\text{LiNbO}_3$ , an enhancement factor of  $23N^2$  (for periodic domains) and  $23N$  (for random domains) may be achieved, where  $N$  is the number of domains in the crystal [52]. Three methods have been demonstrated for periodically poled  $\text{LiNbO}_3$ : the Czochralski method with dopant gradient of yttrium, the laser-heated pedestal growth with rotating temperature gradient and the titanium-diffusion-induced domain reversal method [53–56]. A conversion efficiency of  $2\text{ W cm}^{-2}$  was recently achieved in SHG of a low-power (2.6 mW) 1064 nm and  $1\text{ }\mu\text{W}$  of 425 nm generated from SHG of 189 mW at 850 nm [41]. Furthermore, direct frequency doubling of a diode laser at

TABLE IV Blue-green lasers from diode- and dye-laser-pumped systems [2]

Laser	Pump source	Conversion technique	Non-linear crystal	Output (nm)
Nd: YAG	Diode laser	SHG(1)	KNbO <sub>3</sub>	473
	Diode laser	SFM(1)	KNbO <sub>3</sub>	436
	Diode laser	SHG(2)	MgO: LiNbO <sub>3</sub>	532
	Diode laser	SHG(3)	MgO: LiNbO <sub>3</sub>	532
	Dye laser	SFM(2)	KTP	459
	Diode laser	SFM(2)	KTP	459
Nd: YLF	Dye laser	SHG(1)	MgO: LiNbO <sub>3</sub>	523.6
Nd: MgO: LN	Dye laser	SHG(self-doubling)		598
Er: YLF	Dye laser	Two-photon process		550
Diode laser		Waveguided	LiNbO <sub>3</sub>	420
Diode laser		DSHG	KNbO <sub>3</sub>	431
Dye laser		DSHG	KNbO <sub>3</sub>	425 to 435
Nd: YAG	Diode laser	SHG(2)	KNbO <sub>3</sub>	532
NYAB	Dye laser	SHG(self-doubling)	NYAB	532
NYAB	Flashlamp	SHG(self-doubling)	NYAB	532
NYAB	Dye/diode laser	SHG(self-doubling)	NYAB	532
Nd: YAG	Diode laser	Quasi-phase-matching	PPLN	532
Diode laser		Quasi-phase-matching	PPLN	525
Diode	(Direct output) from AlGaInP			600, 680

SHG(1), Intracavity SHG; SHG(2), external-cavity SHG; SHG(3), external ring cavity SHG; DSHG, direct SHG of diode laser or dye laser at 840, 842 and 850 to 870 nm; SFM(1), SFM of diode laser (at 809 nm) and diode-pumped Nd: YAG (at 946 nm); SFM(2), SFM of diode laser (at 809 nm) and diode-pumped Nd: YAG (at 1064 nm); NYAB, Nd<sub>2</sub>Y<sub>1-x</sub>Al<sub>x</sub>(BO<sub>3</sub>)<sub>3</sub> and PPLN, periodically poled lithium niobate.

840 nm was reported in waveguided LiNbO<sub>3</sub> using birefringent phase-matching (Cherenkov effect) [57].

MgO-doped LiNbO<sub>3</sub> has two advantages over the undoped-LiNbO<sub>3</sub>: (1) non-critical phase matching for SHG of 1064 nm may be achieved at 105 to 120°C compared with 4°C in undoped LiNbO<sub>3</sub>, and (2) the optical index damage effect (photorefractive) in undoped LiNbO<sub>3</sub> is removed by the dopant when operated at elevated temperatures.

The damage thresholds of 610 and 340 MW cm<sup>-2</sup> were reported for 1064 and 532 nm for the doped LiNbO<sub>3</sub>. These values are 200 to 300 times those of the undoped LiNbO<sub>3</sub> [58, 59]. However, damage thresholds of approximately 30 to 50 MW cm<sup>-2</sup> were also reported due to the two-photon absorption (TPA) process. For applications in OPOs, the IR wavelength (1 to 4 μm) will avoid damage caused by TPA. SHG of diode-pumped Nd: YAG and OPO (using 532 nm as the pump) using MgO: LiNbO<sub>3</sub> have recently been reported [60], where 56% doubling efficiency of a 52.7 mW input at 1064 nm was achieved in an external-cavity-ring resonator. Applications of high-efficiency non-linear crystals for the generation of blue-green diode-pumped lasers are summarized in Table IV.

#### 4. Figure-of-merit and conversion efficiency

##### 4.1. Materials selection rule

The criteria listed below are necessary to achieve the best performance for frequency conversion in non-linear crystals [1]:

- high effective non-linear coefficient;
- high damage threshold;

TABLE V P

Crystal	Transmittance range
KDP	0.2
D-KDP	0.2
CDA	0.27
D-CDA	0.27
D-LAP	0.2
BBO	0.19
LBO	0.16
LiIO <sub>3</sub>	0.3
LiNbO <sub>3</sub>	0.4
KNbO <sub>3</sub>	0.4
KTP	0.35
Urea	0.21

d, Non-linear  
perature acco  
(mrad cm<sup>1/2</sup>);

small  
wide  
wide  
non-c  
large  
chem  
low c  
ease  
high

As show  
LBO, urea  
and KNbO  
regimes an  
AgGaSe<sub>2</sub>

TABLE VI

Material
AgGaS <sub>2</sub>
CdSe
AgGaSe <sub>2</sub>
TAS
CdGeAs <sub>2</sub>
ZnGeP <sub>2</sub>
Tellurium

\*Figure-of-

# Non-linear crystals for tunable coherent sources

TABLE V Properties of some non-linear crystals with transparency ranges of 0.16 to 5  $\mu\text{m}$

Crystal	Transparency range ( $\mu\text{m}$ )	$d/d_K$ (KDP)	Absorption coefficient at 1064 nm ( $\text{cm}^{-1}$ )	$\Delta T, L$ ( $^\circ\text{C cm}$ )	$\Delta A, L$	$\Delta \lambda, L$ (Å cm)	DT (GW $\text{cm}^{-2}$ )	Reference
KDP	0.2 to 1.5	1	0.07	11.5	0.84	106	0.4	70-72
D-KDP	0.2 to 1.5	0.92	0.006	7.4	0.94	32	0.4	70-72
CDA	0.27 to 1.7	0.92	0.04	6	69*		0.3	70-72
D-CDA	0.27 to 1.7	0.92	0.01	6	72*		0.3	70-72
D-LAP	0.2 to 1.9	1.9		1.5	0.53	11	10 to 15	70-72
BBO	0.19 to 3.0	4.4		55	1.5	9.8	3 to 5	18, 19, 70-72
LBO	0.16 to 2.6	2.6 to 2.9		9	(9, 42*)		5 to 10	13
LiIO <sub>3</sub>	0.3 to 5.5	12	0.002	6.9	0.32	3.2	0.01 to 0.05	70-72
LiNbO <sub>3</sub>	0.4 to 5	10		-0.6	47*	2.3	0.01 to 0.04	70-72
KNbO <sub>3</sub>	0.4 to 5.5	37 to 47		0.05	(12, 30*)		0.2 to 0.4	47-49
KTP	0.35 to 4.5	11 to 15	0.001	25	(15, 108*)	5.6	0.5 to 1.0	43-46, 73
Urea	0.21 to 1.4	3		23	0.77	8.3	1 to 2	70-72

$d$ , Non-linear coefficient,  $d_K$  (KDP) =  $1.04 \times 10^{-8}$  esu =  $0.435 \text{ pm V}^{-1}$  [73];  $0.39 \text{ pm V}^{-1}$  [14];  $\Delta T, L$ , temperature acceptance width;  $\Delta A, L$ , angular acceptance width for critical (mrad cm) and/or non-critical\* (mrad  $\text{cm}^{1/2}$ );  $\Delta \lambda, L$ , spectral acceptance width; DT, damage threshold for 10 ns pulse at 1064 nm.

small absorption and scattering loss;  
 wide phase-matching range;  
 wide acceptance widths (angular, spectral and temperature);  
 non-critical phase-matching, if possible;  
 large size with good optical homogeneity;  
 chemical and mechanical stability;  
 low cost (efficiency per dollar);  
 ease of fabrication (cutting, coating and polishing);  
 high thermal conductivity and grown in waveguide on fibre forms.

As shown in Tables V to VII, no known materials meet all of these requirements. BBO, LBO, urea and LAP have very good UV transparency with high damage threshold. KTP and KNbO<sub>3</sub> have high non-linearity but applications are limited by their phase-matchable regimes and the absorption cutoff at about 400 nm. Semiconductor crystals of TAS and AgGaSe<sub>2</sub> are suitable for SHG of 5 to 12  $\mu\text{m}$  lasers; however, they suffer from absorption

TABLE VI Non-linear crystals with transparency ranges 0.5 to 30  $\mu\text{m}$  [1]

Material	Transparency range ( $\mu\text{m}$ )	Absorption at 10.6 $\mu\text{m}$ ( $\text{cm}^{-1}$ )	Damage threshold (MW $\text{cm}^{-2}$ )	Relative figure-of-merit
AgGaS <sub>2</sub>	0.5 to 13	0.09	15	1.0*
CdSe	0.75 to 20	0.016	50	1.6
AgGaSe <sub>2</sub>	0.71 to 18	0.05	12	6.3
TAS	1.26 to 17	0.04	16	6.5
CdGaAs <sub>2</sub>	2.4 to 18	0.23	40	9.2
ZnGeP <sub>2</sub>	0.74 to 12	0.9	3	14.0
Tellurium	3.8 to 32	0.96	45	270

\*Figure-of-merit (evaluated at phase-matching for SHG of 10.6  $\mu\text{m}$ ) of AgGaS<sub>2</sub>,  $14.0 \text{ pm V}^{-1}$  is chosen as 1 unit.

TABLE VII Properties of non-linear organic crystals [1, 74]

Name	Point group	Transparency range ( $\mu\text{m}$ )	Melting point ( $^{\circ}\text{C}$ )	$d$ ( $10^{-9}$ esu)	Figure-of-merit, $d^2/n^3 \text{ pm V}^{-1}$	Damage threshold at $1064 \mu\text{m}$ ( $\text{GW cm}^{-2}$ )
LAP	2	0.2 to 1.9	140	1.9	0.2	10
Urea	42m	0.2 to 1.4		3	0.6	1 to 3
POM	222	0.41 to 2	136	20	15	2
m-NA	mm2	0.5 to 2	113	34	37	0.2
MAP	2	0.5 to 2	81	40	82	3
COANP	mm2	0.48 to 2	71	57	117	
DAN	2	0.43 to 2	167	60	127	
NPP	2	0.5 to 2	117	200	1478	
NPAN	mm2	0.5 to 2	115	200	1478	
MNA	m	0.5 to 2	131	250, (38)	1878, (43)	0.2

and low damage threshold. As shown in Table VII, most of the organic crystals (with the exception of urea and LAP) have absorption cutoff at about 450 nm and have low damage threshold. However, due to their non-linearities, potential applications for low-power lasers (such as diode and diode-pumped lasers) are expected. If the conditions of a good pumping source are met (narrow bandwidth, small divergence, and clear spatial and temporal profiles), then high conversion efficiencies may be achieved if the crystals meet the following conditions:

- low absorption for both the pump and the converted beams;
- phase-matching within large acceptance angles, broad spectral of the spectrum and wide range of temperature;
- large aperture length or small walk-off angle;
- a large figure-of-merit.

Greater detail of the conversion efficiency influenced by the parameters described above is presented in the following.

#### 4.2. Conversion efficiency

The frequency-conversion efficiency depends not only on the properties of the non-linear crystals (acceptance bandwidths, phase-matching angle and non-linearity) but also on the condition of the laser beams (beam quality, beam divergence, spectral width and Poynting vector walk-off). To analyse these effects, we have recently developed a new model that is able to characterize several of these parameters in an analytical expression.

The SHG efficiency with the phase-matched, collimated beam (unfocused) conditions is given by

$$\eta = \tanh^2 X e^{-2\alpha L} \quad (7)$$

where  $X$  is a reduced merit parameter given by the new expression [47]

$$X = 0.1725 d_{\text{eff}} L S \left( \frac{\pi P_0}{4\lambda^2 n_1^2 n_2} \right)^{1/2} \left( \frac{\text{erf } Y}{D^{1/2}} \right) e^{\alpha^2/4D} \quad (8a)$$

$$Y = D^{1/2} (L + \alpha/2D) \quad (8b)$$

where  $d_{\text{eff}}$  is the effective non-linear coefficient ( $\text{pm V}^{-1}$ ),  $L$  is the crystal length (cm),  $P_0$  is the pump power (MW),  $n_{1,2}$  are the index of refraction for the pump (at wavelength  $\lambda$ , in  $\mu\text{m}$ ) and the second harmonics and  $\alpha$  is the absorption constant of the harmonics.

$D$  is a reduced

where  $\beta_j$  are the spot size of  $W_j$  focusing.

The effects of expansion of the

where we have

Some important cancellation of the primary rays may suppress exponential loss and the mechanism via

The effects of efficiency may be given a pump profile, the SHG

$d_1 = \Delta\theta_1/\Delta\theta_2$  for the ideal beam the ratios between acceptance width

$D$  is a reduced main parameter and  $S$  is a spatial overlap function defined as [61]:

$$S = \left(\frac{8}{\pi}\right)^{1/2} \left(\frac{W^2}{W_1 W_2}\right) \quad (9)$$

$$D = c - b^2/a \quad (10)$$

$$g_1 = \frac{2W e_1^2}{W_1^2 a^{1/2}} \quad W \equiv 1 / \sum_{i=1}^3 \left(\frac{e_i}{W_i}\right)^2 \quad (11)$$

$$a \equiv \sum_{i=1}^3 (1/W_i^2) \quad (12)$$

$$b \equiv \sum_{i=1}^3 (\beta_i/W_i^2) \quad (13)$$

$$c \equiv \sum_{i=1}^3 (\beta_i^2/W_i^2) \quad (14)$$

where  $\beta_j$  are the walk-off angles for the pump ( $j = 1, 2$ ) and harmonic ( $j = 3$ ), with beam spot size of  $W_1$  and  $W_2$ ,  $e_j$  is an elliptical focusing parameter with  $e_j = 1$  for spherical focusing.

The effects of beam walk-off on the reduction of efficiency may be easily seen by the expansion of the error function as

$$\eta = 2.97 \times 10^{-2} F_{\text{eff}} P_0 \left(1 - \frac{(DL)^2}{3} + \dots\right) e^{-2\alpha L} \quad (15)$$

where we have defined an effective figure-of-merit

$$F_{\text{eff}} = (d_{\text{eff}} L)^2 / \lambda_1^2 n_1^2 n_2 \quad (16)$$

Some important features may be addressed based on the results of Equations 7 and 15. Cancellation of the walk-off effects may be achieved in type II SHG, where two extraordinary rays may still be coupled when both rays walk-off in the same direction. The efficiency drops exponentially with the total loss factor that consists of the second-harmonic absorption loss and the energy loss due to the walk-off effects. For type I SHG the formal loss mechanism vanishes and  $\cos \beta_1 = 1$ .

The effects of the pump beam quality (divergence, spectral purity, etc.) on the SHG efficiency may be investigated by the Taylor expansion of the phase-mismatching factor. Given a pump with beam divergence and spectral bandwidth governed by a Gaussian profile, the SHG integrated efficiency may be expressed by [61]

$$\eta = \left(\frac{8}{\pi}\right)^{1/2} \left(\frac{8}{d_1 d_2 d_3}\right) \iiint \prod_j \eta_j \times \exp \left[ - \sum_{j=1}^3 \left( \frac{8X_j^2}{\pi^2 d_j} \right) \right] dx_1 dx_2 dx_3 \quad (17)$$

$d_1 = \Delta\theta_L/\Delta\theta_r$ ,  $d_2 = \Delta\phi_L/\Delta\phi_r$  and  $d_3 = \Delta\lambda_L/\Delta\lambda_r$ , where  $\eta_j$  are the SHG efficiency solved for the ideal beam case (that is, when the ratio parameters  $d_j = 0$ ), which are defined by the ratios between the pump beam bandwidths (angle and spectrum) and that of the crystal acceptance widths.

The significant features described by Equations 7 to 17 are discussed as follows.

1. The coupling efficiency may be optimized by maximizing the overlap function  $S$ . For fixed beam radii of  $W_1$  and  $W_2$ , the optimal beam spot of  $W_3^*$  is calculated as

$$W_3^* = \left( \frac{e_1/e_3}{W_1^2} + \frac{e_2/e_3}{W_2^2} \right)^{-1/2} \quad (18)$$

2. The coupling efficiency may be improved by elliptical focusing ( $e_i > 1$ ) in the non-walk-off plane (with  $\beta_i = 0$ ). For example, in the case of type I OPO, the confocal cavity may be designed such as the signal or idler beams ( $j = 1, 2$ ) are focused more tightly than the pump beam ( $j = 3$ ), where only the extraordinary ray (the pump beam) suffers the walk-off ( $\beta_3 \neq 0$ ). Furthermore, the efficiency may be improved by tighter focusing in the insensitive direction (or larger acceptance width) than in the sensitive direction of the crystal. We note that for uniaxial crystals the angular acceptance width is inversely proportional to the walk-off angle. Therefore, the insensitive direction matches the smaller walk-off direction.

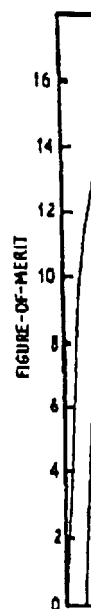
3. The gain reduction parameter  $D$  causes the coupling strength to decrease exponentially as the beams propagating through the non-linear crystal. We notice that this  $D$ -factor is governed by the ratio between the walk-off angle (per unit length) and the beam radius. Therefore, for crystals with large walk-off such as BBO and LiNbO<sub>3</sub>, tight focusing of the extraordinary beam increases the power density but also reduces the effective coupling strength of the crystal.

4. Our numerical solution of Equation 17 shows that the efficiency reduces to 60% of the ideal case (without beam divergence) when the beam divergence is twice the angular acceptance of the crystal.

5. For a multimode beam, in particular, the conversion efficiency is limited by several factors: (a) how tightly the pump beam may be focused; (b) the beam quality, such as divergence within the acceptance angle at the crystal; (c) the ratio of the beam spot size and the total walk-off length referring to Equation 9; and (d) the damage threshold (power density or energy) of the crystal.

6. The minimum peak power required for efficient SHG is governed by the power density desired, the nominal crystal length, the beam divergence and the crystal acceptance widths (in angle and spectrum). Improvement of SHG efficiency may be achieved by elliptical focusing or by optimizing the focusing and crystal length.

Fig. 25 compares crystals of KDP, BBO and urea (both type I and II) based on the effective figure-of-merit (Equation 16) for SHG. Note that the phase-matching curves cut off at  $F_{\text{eff}} = 0$  and the maximum values are achieved when the effects of the phase-matching angle and the wavelength dependence of Equation 16 are optimized. Furthermore, the  $F_{\text{eff}}$  (Equation 16) as a function of the phase-matching angle (for fixed wavelengths and angles) and reveals an excellent candidate for doubling tunable lasers with a spectral range of 410 to 700 nm such as dye laser, Ti:sapphire and alexandrite lasers. However, we also note that BBO type I has a smaller angular acceptance width (0.6 mrad cm, for SHG of 1064 nm) than that of type II (0.8 mrad cm), the SHG efficiency may not be as good as type II, particularly for a pump beam with poor quality as indicated by Equations 9 to 17. In this case the relevant figure-of-merit should be modified by the beam quality effects (see Equation 17). Fig. 25, based on Equation 16, provides the guidance of SHG efficiency for the ideal situation where the pump beam divergence and spectral width are within the



acceptance  
quality

5. Sel  
There a  
Nd: Mg  
MgO: I  
NYA  
0.66 μm  
method  
in opti  
than th  
cross-se  
tively, a  
400 MV  
four tim  
emissio  
matchin  
selectiv  
Gene  
(pulsed  
flashlan  
1064 an

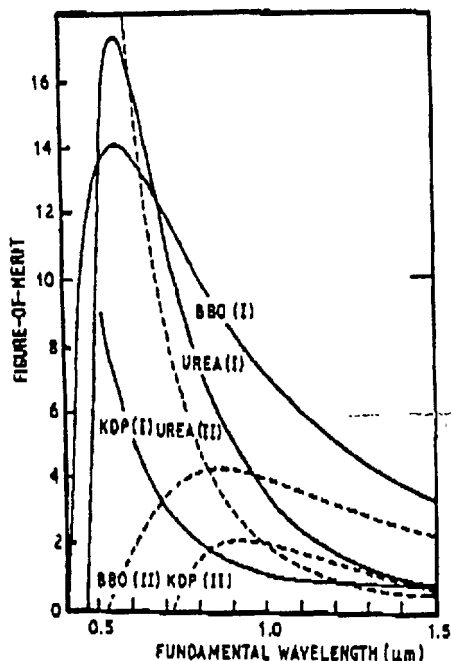


Figure 25 Effective figure-of-merit plotted against the pump wavelengths for various crystals based on Equation 16 for type I and type II operations. Comparisons are based on the same pumping intensity and the typical crystal lengths, 7 mm (for BBO and urea) and 14 mm (for KDP). All of the values are normalized to that of KDP (type I) for SHG of Nd:YAG laser at 1064 nm. See the text for a discussion.

acceptance width of the crystal. Greater details with quantitative results for the beam quality effects are given in [61].

### 5. Self-frequency-doubling crystals

There are two crystals that have been studied recently as self-frequency-doubling materials: Nd:MgO:LiNbO<sub>3</sub> and NYAB [60, 62-67]. There were very few data reported on Nd:MgO:LiNbO<sub>3</sub>. We focus on NYAB in the following discussion.

NYAB was first studied for the generation of 1.32 μm and its second harmonics at 0.66 μm by Dorozhkin *et al.* [62]. This new crystal of NYAB may be grown by the flux method [63, 64] and has several features that are attractive for the generation of green light in optically pumped systems; (1) the active-ion (Nd<sup>3+</sup>) concentration may be much higher than that of Nd:YAG, with rather low luminescence-quenching effects; (2) high effective cross-sections,  $10 \times 10^{-19}$  and  $1.8 \times 10^{-19}$  cm<sup>2</sup> for emission at 1.06 and 1.32 μm, respectively, at  $x = 0.2$  in the composition of Nd<sub>x</sub>Y<sub>1-x</sub>Al<sub>3</sub>(BO<sub>3</sub>)<sub>4</sub>; (3) a damage threshold of 400 MW cm<sup>-2</sup>, which is much higher than that of the non-linear active crystal neodymium-doped LiNbO<sub>3</sub>; (4) it is a self-doubling active crystal with a non-linear coefficient ( $d_{22}$ ) about four times that of  $d_{36}$  in KDP and is comparable with that of BBO; (5) the fundamental emission is highly linearly polarized and may be efficiently doubled using type I phase-matching; and (6) multiple wavelengths of 1.32, 1.06, 0.9, 0.66, 0.532 and 0.45 μm may be selectively achieved via the active-ion concentration level.

Generation of green emission at 532 nm in pulsed operation was reported in a dye-laser (pulsed) pumped NYAB [62]. Recently we reported the pulsed emission at 532 nm in a flashlamp-pumped system [63, 64]. The first demonstration of c.w. laser emission at 1064 and 532 nm in a diode-pumped NYAB was also reported [65]. A comparison of



output power as f

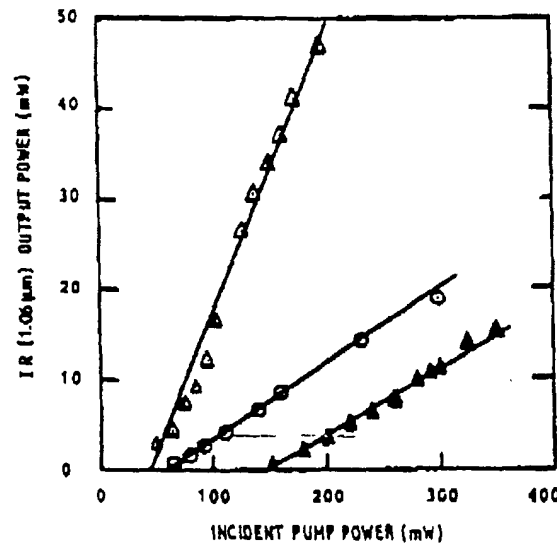


Figure 26 Comparison of diode-pumped ( $\Delta$ ) Nd:YAG and ( $\Delta$ ) NYAB and (O) dye-laser-pumped NYAB for 1.06  $\mu\text{m}$  emission.

diode-pumped Nd:YAG and NYAB is shown in Fig. 26. As shown in Fig. 27, we achieved 9  $\mu\text{W}$  green output power from an input diode laser of 450 mW. Higher efficiency in an acoustic-optics Q-switched system is in progress [66].

The self-frequency-doubling may be described by a simple model that provides the green

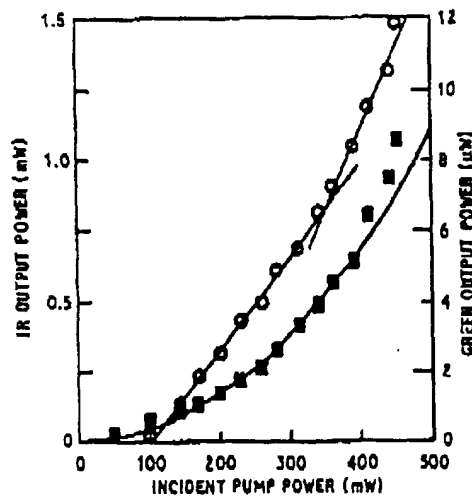


Figure 27 Comparisons of diode-pumped NYAB with emission at (O) 1063 and (■) 632 nm, where the full curves are the theoretical results based on Equation 19. See text.

where  $P_0$ ,  $P_1$  and 1063 nm) and secc and the crystal ler 1064 and 532 nm,

We note that be and 532 nm) are s higher gain (via tl the green,  $\alpha_2$ ). We depending on the more, a better do in the cavity, wher twice that of typ polarized along th by observing the cence emissions ar A better efficiency dopant concentra (a few watts) shou Q-switched opera power of the func

The green effie between the 1063 (only 1.7 pm  $\text{V}^{-1}$ ) non-linearity 20 to priate active ions cross-section and ties of these orga

## 6. Conclusion

In this paper we t OPO and SRS) u tunable coherent ( as BBO, LBO and  $\text{KNbO}_3$  and  $\text{MgO}$  in the visible spect be improved by u devices and NCP) 4, where we shoul by the properties and temporal pro

output power as follows (within the constant-pumped and small-gain approximation) [67]:

$$P_2 \propto (d_{\text{eff}}L)^2(1 - \alpha_2 L/2)P_1^2 \quad (19a)$$

$$\propto (d_{\text{eff}}L)^2(1 - \alpha_2 L/2)(1 - e^{-\alpha_1 L})^2 P_0^2 \quad (19b)$$

$$\alpha_1 = a + bx \quad (20a)$$

$$\alpha_2 = c + dx \quad (20b)$$

where  $P_0$ ,  $P_1$  and  $P_2$  are the powers of the pump (diode laser at 808 nm), fundamental (at 1063 nm) and second harmonic (at 532 nm),  $d_{\text{eff}}$  and  $L$  are the effective non-linear coefficient and the crystal length of NYAB, respectively, with absorption coefficients of  $\alpha_1$  and  $\alpha_2$  (at 1064 and 532 nm, respectively) that depend on the  $\text{Nd}^{3+}$  concentration  $x$ .

We note that both the gain (for emission at 1063 nm) and the absorption losses (at 1063 and 532 nm) are strongly influenced by the  $\text{Nd}^{3+}$  concentration level,  $x$ . A large  $x$  achieves higher gain (via the absorption of 808 nm,  $\alpha_1$ ) but also suffers a larger absorption loss (at the green,  $\alpha_2$ ). We believe that the optimal values of  $x$  should be in the range 0.03 to 0.1, depending on the crystal length used and the beam spot sizes inside the crystal. Furthermore, a better doubling efficiency may be achieved by incorporating a Brewster-cut plate in the cavity, where type I, with effective non-linear coefficient of  $1.4 \text{ pm V}^{-1}$  (which is about twice that of type II), is preferred and requires the fundamental beam to be linearly polarized along the ordinary axis of the crystal. In addition to the green emission at 532 nm, by observing the measured results, we note that NYAB crystal also shows strong fluorescence emissions around 880 to 905 nm, which may be converted to 440 to 452 nm emissions. A better efficiency can be achieved by optimizing parameters including the crystal length, dopant concentration, cavity design and coating. Furthermore, a high-power diode array (a few watts) should be able to produce 100 mW-range green from NYAB. Acoustic-optic Q-switched operation should also generate much higher green emission via the higher peak power of the fundamental (at 1063 nm) [66].

The green efficiency of NYAB is limited by the factors such as poor spatial overlap between the 1063 and 532 nm waves (due to beam walk-off) and the non-linearity of NYAB (only  $1.7 \text{ pm V}^{-1}$ ). Organic non-linear crystals such as COANP, PNP and DAN with non-linearity 20 to  $200 \text{ pm V}^{-1}$  would be the potential candidates providing that the appropriate active ions of neodymium or chromium may be doped and reasonable emission cross-section and fluorescence lifetime are achievable. Modification of the optical properties of these organic crystals by various dopants is in progress [68].

## 6. Conclusion

In this paper we have presented the frequency-conversion techniques (SHG, SFM, DFM, OPO and SRS) using non-linear media (crystals and Raman gases) for the generation of tunable coherent sources. Crystals with high damage thresholds and UV transparency such as BBO, LBO and LAP are suitable for high-power laser applications and for UV lasers. KTP, KNbO<sub>3</sub> and MgO:LiNbO<sub>3</sub> crystals with high non-linear coefficients and good transparency in the visible spectrum are suitable for visible region diode-pumped lasers. The efficiency may be improved by using some novel techniques such as elliptical focusing, QPM, waveguided devices and NCPM. The material selections for non-linear crystals were discussed in Section 4, where we should emphasize that the non-linear conversion efficiency is governed not only by the properties of the crystals, but also by the quality of the radiation such as its spatial and temporal profiles, and angular and spectral bandwidths, as indicated in Section 4.1.

The availability of compact coherent sources in the visible regime will depend on the technology of high-power diode lasers (as the pumping sources) and the development of high-efficiency non-linear crystals (as frequency converters). As a concluding remark, we note that the newly discovered crystal of  $\text{KTiOAsO}_4$  (KTA) with an effective non-linear coefficient 1.6 times that of KTP (for SHG of 1064 nm) [64] and KTP in waveguide and periodically poled forms [75] present the excellent candidates for the generation of visible diode-pumped lasers using either of the SHG or SFM schemes shown Fig. 7. Furthermore nonlinear organic crystals grown in fibre forms were demonstrated as the candidates for high efficiency frequency conversion for low-power lasers [76, 77].

### Acknowledgement

This research was supported by the Florida High Technology and Industrial Council, ONR (Grant No. N00014-88-J-1123) and SUS/DARPA (Grant No. MDA 972-89-J-1006). The referee's constructive comments are appreciated.

### References

1. J. T. LIN and C. CHEN, *Lasers and Optonics* (November 1987) 59.
2. J. T. LIN, *ibid.* (July 1989) 61.
3. *Idem*, in 'Proceedings of Laser '87' (STS Press, Virginia, 1977) p. 404.
4. *Idem*, *SPIE Proc.* 895 (1987) p. 162.
5. J. T. LIN and J. L. MONTGOMERY, *Opt. Commun.* 75 (1990) 351.
6. *Idem*, in Proceedings of the Topical Meeting on Tunable Solid-state Lasers, Cape Cod, Massachusetts, 1-3 May, 1988 (Optical Society of America, Washington, D.C.).
7. R. C. ECKARDT, Y. X. FAN, R. L. BYER, C. L. MARGUARDT, M. E. STORM and L. ESTEROWITZ, *Appl. Phys. Lett.* 49 (1986) 608.
8. J. D. FBICHTNER and G. W. ROLAND, *Appl. Opt.* 11 (1972) 993.
9. R. AUYEUNG, D. ZIELKE and B. FELDMAN, Presented at CLEO '87 (1987) Paper TUH3 (Optical Society of America, Washington, D.C.).
10. D. S. BETHUNE and A. C. LUNTZ, *Appl. Phys.* B40 (1986) 107.
11. S. BENSON, J. MADEY, R. STRAIGHT and B. HOOPER, *J. Laser Appl.* 1 (1989) 49.
12. C. CHEN, B. WU, A. JIANG and G. YOU, *Sci. Sinica B28* (1985) 235.
13. C. CHEN, B. WU, A. JIANG, G. YOU, R. LI and S. LIN, *J. Opt. Soc. Am.* B6 (1989) 616.
14. D. EIMERL, L. DAVIS, S. VELSKE, E. K. GRAHAM and A. ZALKIN, *J. Appl. Phys.* 62 (1987) 1968.
15. K. KATO, *IEEE J. Quantum Electron.* QE-22 (1986) 103.
16. *Idem*, *ibid.* QE-24 (1988) 3.
17. K. MIYAZAKI, H. SAKAI and T. SATO, *Opt. Lett.* 11 (1986) 797.
18. C. CHEN, Y. X. FAN, R. C. ECKARDT and R. L. BYER, *SPIE Proc.* 681 (1986) 12.
19. *Idem*, *IEEE J. Quantum Electron.* 25 (1989) 1196.
20. W. L. OLAB and J. P. MESSLER, *Appl. Opt.* 26 (1987) 3181.
21. P. LOKAI, B. BURGHARDT and W. MUCKENHEIM, *Appl. Phys.* B45 (1988) 245.
22. *Idem*, *ibid.* B45 (1988) 256.
23. A. LAGO, R. WALLENSTEIN, C. CHEN, Y. X. FAN and R. L. BYER, *Opt. Lett.* 13 (1988) 221.
24. L. K. CHENG, W. R. ROSENBERG and C. L. TANG, *Appl. Phys. Lett.* 53 (1988) 175.
25. D. W. CHEN and J. J. YEH, *Opt. Lett.* 13 (1988) 808.
26. M. EBRAHUNZADCH and M. H. DUNN, *Tech. Dig. CLEO '88*, Postdeadline Paper PD30, *Opt. Commun.* 69 (1988) 161.
27. Y. X. FAN, R. C. ECKARDT, R. L. BYER, J. NOTTING and R. WALLENSTEIN, *ibid.* Postdeadline paper PD31.
28. H. KOMINE, *ibid.* Postdeadline Paper PD32.
29. L. K. CHENG, W. R. ROSENBERG, D. C. EDELSTEIN and C. L. TANG, *ibid.* Postdeadline Paper PD33.
30. P. OIU and A. PENZKOFER, *Appl. Phys.* B45 (1988) 225.
31. T. F. JOHNSTON and T. J. JOHNSTON, Presented at CLEO '89 (1989) Paper FE5 (Optical Society of America, Washington, D.C.).
32. C. T. MUELLER and N. D. DUONG, *ibid.* Paper FE4 (Optical Society of America, Washington, D.C.).
33. H. KOMINE, *ibid.*
34. *Idem*, Present of America, V
35. D. W. COUTT, Society of Am
36. J. T. LIN, A. H
37. C. CHEN, A. J of America, V
38. J. T. LIN, C. E
39. J. T. LIN and
40. J. T. LIN, J. L. Lasers (1990)
41. W. P. RISK, J. Phys. Lett. 51
42. W. P. RISK an
43. R. BURNHAM
44. H. VANHERZ
45. J. D. BIERLEI
46. T. Y. FAN, C. Opt. 26 (1987
47. J. C. BAUMEF
48. K. KATO, IEI
49. *Idem*, *ibid.* Q
50. J. T. LIN, SPI
51. J. A. ARMSTE
52. DUAN FENG 37 (1980) 60
53. J. WEBJORN, of America.
54. G. A. MAGE
55. E. L. LIM, M
56. *Idem*, *ibid.* 2
57. G. TOHMON
58. D. A. BRYA
59. J. L. NIGHT
60. W. J. KOZL
61. J. T. LIN an
62. L. M. DORC Tech. Phys.
63. B. LU, J. W.
64. Z. D. LUO.
65. J. T. LIN, *ib*
66. S. C. WANG Society of
67. J. T. LIN a (Optical S
68. W. S. WAN
69. J. D. BIER
70. D. N. NIK
71. Informati
72. D. HON, i
73. R. F. BEL
74. P. V. VID
75. J. D. BIER
76. J. T. LIN.
77. A. HARA Society o

# Non-linear crystals for tunable coherent sources

33. H. KOMINE, *Opt. Lett.* 13 (1988) 643.
34. *Idem*, Presented at Tunable Solid-State Lasers Topical Meeting, 1-3 May 1989, Paper WA1 (Optical Society of America, Washington, D.C.).
35. D. W. COUTTS, M. D. AINSWORTH and J. A. PIPER, Presented at CLEO '89 (1989) Paper FK4 (Optical Society of America, Washington, D.C.).
36. J. T. LIN, A. HORNER and K. KATO, OSA Annual Meeting (1989) Postdeadline paper PD17.
37. C. CHEN, A. JIANG, B. WU, G. YOU and S. LIN, Presented at CLEO '89 (1989) Paper ThQ1 (Optical Society of America, Washington, D.C.).
38. J. T. LIN, C. E. HUANG and J. Q. YAO, *ibid.* Paper ThQ2.
39. J. T. LIN and K. KATO, *SPIE* 1220 (1990), in press.
40. J. T. LIN, J. L. MONTGOMERY, J. R. DeSALVO and A. M. HORNER, in Proceedings, Advances in Solid-State Lasers (1990) (Optical Society of America, Washington, D.C.).
41. W. P. RISK, J. C. BAUMERT, F. M. SCHELLENBERG, W. LENTH, W. P. RISK and G. C. BJORKLUND, *Appl. Phys. Lett.* 51 (1987) 2192.
42. W. P. RISK and W. LENTH, *ibid.* 54 (1989) 789.
43. R. BURNHAM, R. A. STOLZENBERGER and A. PINTO, *IEEE Photon. Lett.* 1 (1989) 27.
44. H. VANHERZEELE, J. D. BIERLEIN and F. C. ZUMSTEG, *Appl. Opt.* 27 (1988) 3314.
45. J. D. BIERLEIN and H. VANHERZEELE, *J. Opt. Soc. Am.* B6 (1989) 622.
46. T. Y. FAN, C. E. HUANG, B. Q. HU, R. C. ECHARDT, Y. X. FAN, R. L. BYER and R. S. FEIGELSON, *Appl. Opt.* 26 (1987) 2390.
47. J. C. BAUMERT, J. HOFFNAGLE and P. GUNTER, *SPIE* 492 (1984) 374.
48. K. KATO, *IEEE J. Quantum Electron.* QE-15 (1979) 410.
49. *Idem*, *ibid.* QE-18 (1982) 451.
50. J. T. LIN, *SPIE* 1040 (1989) 129.
51. J. A. ARMSTRONG, N. BLOEMBERGEN, J. DUCUING and P. S. PERHMAN, *Phys. Rev.* 127 (1962) 1918.
52. DUAN FENG, N. B. NING, J. F. HONG, Y. S. YANG, J. S. ZHU, Z. YANG and Y. N. WANG, *Appl. Phys. Lett.* 37 (1980) 607.
53. J. WEBJORN, F. LAURELL and G. ARVIDSSON, CLEO '89 (1989) Postdeadline Paper PD10 (Optical Society of America, Washington, D.C.).
54. G. A. MAGEL, M. M. FEJER and R. L. BYER, *ibid.* Paper ThQ3.
55. E. L. LIM, M. M. FEJER and R. L. BYER, *Electron. Lett.* 25 (1989) 132.
56. *Idem*, *ibid.* 25 (1989) 175.
57. G. TOHMON, K. YAMAMOTO and T. TANUCHI, *SPIE* 898 (1988) 70.
58. D. A. BRYAN, R. GERSON and H. E. TOMASCHKE, *Appl. Phys. Lett.* 44 (1984) 847.
59. J. L. NIGHTINGALE, W. J. SILVA, G. E. READE and A. RYBICKI, *SPIE* 681 (1986) 20.
60. W. J. KOZLOVSKY, C. D. NABORS and R. L. BYER, *IEEE J. Quantum Electron.* QE-24 (1988) 913.
61. J. T. LIN and S. W. CHONG, *Opt. Commun.*, submitted.
62. L. M. DOROZHUKIN, I. I. KURATOV, N. I. LEONYUK, T. I. TIMUCHENKO and A. V. SHESTAKOV, *Soviet Tech. Phys. Lett.* 7 (1981) 555.
63. B. LU, J. WANG, K. PAN, M. JIANG, E. LIU and X. HOU, *J. Appl. Phys.* 66 (1989) 6052.
64. Z. D. LUO, J. T. LIN, A. D. JIANG, Y. C. HUANG and M. W. QI, *SPIE Proc.* 1104 (1989) 132.
65. J. T. LIN, *ibid.* 1220 (1990), in press.
66. S. C. WANG, R. E. STONE and J. T. LIN, in Proceedings, Advances in Solid-state Lasers (1990) (Optical Society of America, Washington, D.C.).
67. J. T. LIN and S. W. CHONG, *Tech. Dig. OPTICS '89*, 16-20 October 1989, Orlando, Florida, Paper WB5 (Optical Society of America, Washington, D.C.).
68. W. S. WANG and J. T. LIN, *Mater. Res. Bull.* 25 (1990) 71.
69. J. D. BIERLEIN, H. VANHERZEELE and A. A. BALLMAN, *Appl. Phys. Lett.* 54 (1989) 783.
70. D. N. NIKOGOWYAN, *Soviet J. Quantum Electron.* 7 (1977) 1.
71. Information Sheet, Cleveland Technology Inc. (1988).
72. D. HON, in 'Laser Handbook', edited by M. L. Stieh, Vol. 3, B2 (North-Holland, New York, 1979) 421.
73. R. F. BELT, G. GASHUROV and Y. S. LIU, *Laser Focus* (October 1985) 110.
74. P. V. VIDAKOVIC, M. COQUILLAY and F. SALIN, *J. Opt. Soc. Am.* B4 (1987) 998.
75. J. D. BIERLEIN, D. B. LAUBACHER, J. B. BROWN and C. J. VANDER POEL, *Appl. Phys. Lett.* 56 (1990) 1725.
76. J. T. LIN, O. F. HUANG and M. Y. HWANG, *SPIE* 1220 (1990), in press.
77. A. HARADA, Y. OKAZAKI, K. KAMIYAMA and S. UMEGAKI, *Tech. Dig. CLEO '90*, paper CFE2 (Optical Society of America, Washington, D.C.).

## GENERATION OF TUNABLE PICOSECOND PULSES IN THE ULTRAVIOLET REGION DOWN TO 197 nm

Yuichi TANAKA, Hiroto KURODA and Shigeo SHIONOYA  
The Institute for Solid State Physics, The University of Tokyo  
Roppongi, Minato-ku, Tokyo 106, Japan

Received 2 February 1982

Revised manuscript reserved 16 March 1982

Tunable picosecond pulses in the ultraviolet region down to 197 nm with  $> 20$  kW peak power are generated by the sum frequency mixing of fourth or third harmonic pulses of a mode-locked YAG laser with tunable pulses produced by a  $\text{LiNbO}_3$  parametric oscillator pumped by second harmonic pulses of the YAG laser by using a KB5 or KDP crystal.

Previously we reported [1] the development of a temperature-controlled  $\text{LiNbO}_3$  parametric oscillator system pumped by second harmonic pulses of a repetitively mode-locked YAG:  $\text{Nd}^{3+}$  laser. It was shown that picosecond pulses tunable in the spectral region from 240 nm to  $3.6 \mu\text{m}$  can be generated continuously with this system by the use of techniques of second harmonic generation and sum and difference frequency mixing. The shortest wavelength of 240 nm was achieved by mixing second harmonic of the output pulses of the parametric oscillator with the fundamental pulses of the YAG laser. This tunable picosecond laser system has been used successfully by us to investigate dynamics of ultrafast processes in direct-gap semiconductors [2-4].

In the present letter we report the extension of the tunable range in the ultraviolet region down to 197 nm. This was performed by the sum frequency mixing of parametric output pulses with fourth or third harmonic pulses of the YAG laser by using a KB5 (potassium pentaborate tetrahydrate) or KDP-type I crystal. The shortest wavelength of 196.7 nm was attained by mixing 775 nm parametric pulses with fourth harmonics by using the KB5 crystal.

It is known that KB5 crystal is transparent in the spectral range down to 180 nm [5], has large anisotropy and is useful as a nonlinear crystal to be used in the ultraviolet region [6,7]. With regard to the genera-

tion of tunable pulses using KB5, Kato [8] demonstrated that nanosecond pulses tunable in the range down to 196.6 nm are produced by mixing fourth harmonic pulses of a Q-switched YAG laser with near-infrared pulses of a dye laser pumped by second harmonics of the YAG laser. Stickel and Dunning [5,9] reported the generation of nanosecond pulses tunable in wavelengths extending to 185 nm attained by mixing the outputs of two dye lasers, one operating in the infrared and the other in the ultraviolet. The generation of picosecond pulses tunable in these short wavelengths by using KB5 seems not reported yet according to the authors' knowledge.

In our experiments a mode-locked YAG laser system including three amplifiers was used, which produces a train of  $1.064 \mu\text{m}$  pulses separated by 7 ns. The average peak power of pulses is  $\sim 1$  GW and the duration is  $\sim 20$  ps.

Fig. 1 shows the experimental set-up in the case when parametric output pulses are mixed with fourth harmonics of the YAG laser by using a KB5 crystal. The output of the YAG laser is converted to the second harmonic of  $\sim 100$  MW peak power by a KDP type-I crystal. Second harmonic pulses pump a parametric oscillator composed of a  $90^\circ$  Z-cut  $\text{LiNbO}_3$  crystal ( $10 \times 10 \times 20 \text{ mm}^3$ ) and a resonator cavity. The length of the cavity is adjusted so as to be the same as that of the YAG laser oscillator. The  $\text{LiNbO}_3$

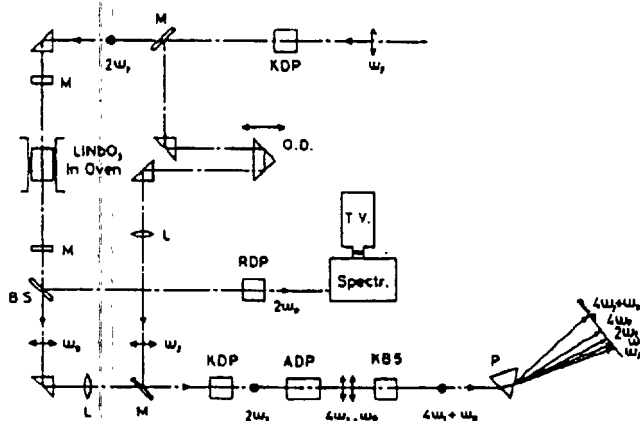


Fig. 1. Experimental set-up to generate tunable pulses by the sum frequency mixing of output pulses of a  $\text{LiNbO}_3$  parametric oscillator (frequency:  $\omega_p$ ) with fourth harmonic pulses of a mode-locked YAG laser (output frequency:  $\omega_1$ ).

crystal is located in an oven. By changing the temperature of the crystal between 50 and  $450^\circ\text{C}$  parametric pulses ( $\omega_p$ ) tunable in the ranges of 630–900 nm and 1.29– $3.6\ \mu\text{m}$  are generated. The peak power is  $\sim 10\ \text{MW}$  in the vicinity of 750 nm. In the case of generating pulses in the range of 900 nm– $1.29\ \mu\text{m}$ , the oven is replaced by a Peltier element and the crystal is cooled down to  $0^\circ\text{C}$ . The output pulse of  $1.064\ \mu\text{m}$  at the degenerate point is produced at  $0^\circ\text{C}$ . By precisely adjusting the cavity length of the oscillator, the duration of output pulses could be made as short as 8–9 ps. The wavelength of parametric output pulses was monitored by a spectrograph and a multi-channel analyzer using a TV camera after conversion to second harmonic pulses by an RDP crystal, as shown in the figure. The spectral width of the pulses is less than 0.2 nm in the wavelength below 400 nm, while it is 0.8 nm at about 500 nm corresponding to the  $1.064\ \mu\text{m}$  degenerate point.

After the generation of second harmonic pulses fundamental laser pulses ( $\omega_1$ ) with  $\sim 600\ \text{MW}$  peak power are split, made to pass through an optical delay and then made to join parametric pulses, as shown in fig. 1. These two kinds of pulses were carefully adjusted so as to coincide with each other in time as well as in space. Fundamental pulses are then converted to second harmonic pulses by a KDP type-I crystal and further to fourth harmonic pulses with  $\sim 10\ \text{MW}$  peak power by an ADP type-I crystal ( $10 \times 10 \times 20\ \text{mm}^3$ ). Then, by a KB5 crystal ( $7 \times 7 \times 7\ \text{mm}^3$ ) para-

metric and fourth harmonic pulses are mixed to generate sum-frequency pulses ( $4\omega_1 + \omega_p$ ) by means of angle-phase-matching. The KB5 crystal is cut and polished in order that the normal direction of the entrance plane may have the condition of  $\theta = 65^\circ$  and  $\phi = 90^\circ$ , where  $\theta$  is the angle between the direction of light propagation and the z-axis, and  $\phi$  is the azimuth angle measured from the x-axis [10]. The generation of mixed pulses was confirmed by a fluorescent screen after dispersion by a quartz prism.

The  $4\omega_1 + \omega_p$  pulses are tunable from 196.7 nm to 217 nm, as shown in fig. 2, with using parametric pulses from 755 nm to  $1.09\ \mu\text{m}$ . The peak power for the shortest wavelength of 196.7 nm is about 20 kW. The spectral width was not measured, but it is sure that the width is nearly the same as or less than that of the  $2\omega_p$  pulses mentioned above. The shortest wavelength limit originates from the phase-matching condition of the KB5 crystal for the case of the mixing with  $4\omega_1$  pulses. The longest wavelength limit is due to the fact that the infrared absorption of KB5 starts from  $1.1\ \mu\text{m}$  [5], so that parametric pulses with wave-

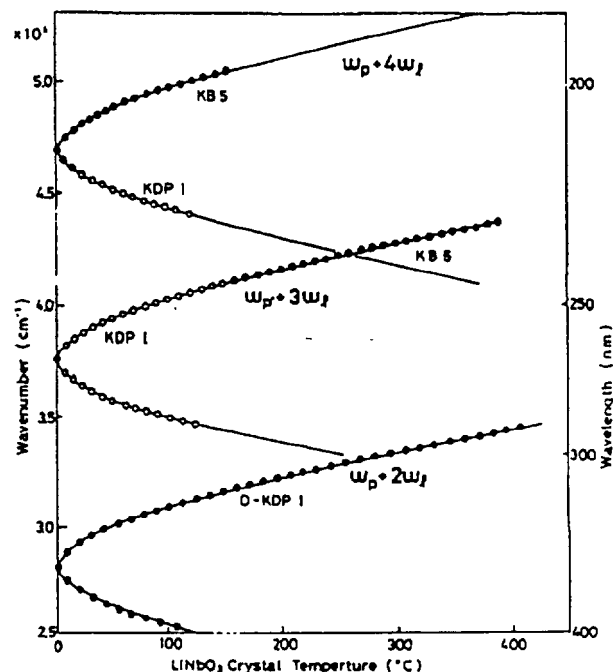


Fig. 2. Wavelengths of tunable pulses generated by mixing parametric pulses ( $\omega_p$ ) with fourth, third or second harmonic pulses ( $4\omega_1$ ,  $3\omega_1$  or  $2\omega_1$ ) of a YAG laser as a function of the  $\text{LiNbO}_3$  crystal temperature

length longer than  $1.1 \mu\text{m}$  are absorbed.

Tunable pulses in the range longer than 217 nm are obtained by replacing the KB5 crystal with a KDP type-I crystal ( $15 \times 15 \times 15 \text{ mm}^3$ , cut so as to be  $\theta = 60^\circ$ ), as shown in fig. 2. The longest wave-length limit of 226 nm in this case is due to the absorption of parametric pulses by the KDP crystal, in which infrared adsorption starts from  $1.5 \mu\text{m}$ .

The generation of the 212.8 nm fifth harmonic pulses of the YAG laser by mixing  $\omega_1$  and  $4\omega_1$  pulses was also performed using the KB5 crystal with the same configuration as in fig. 1. The  $5\omega_1$  pulse of  $\sim 5$  MW peak power was obtained for the condition of the  $\omega_1$ ,  $2\omega_1$  and  $4\omega_1$  pulses with peak powers of 1 GW, 300 MW and 30 MW, respectively.

In the case of the mixing of parametric pulses with third harmonic pulses, the ADP crystal in fig. 1 was replaced by a D-KDP type-II crystal, and  $3\omega_1$  pulses with  $\sim 20$  MW peak power was produced by mixing  $\omega_1$  and  $2\omega_1$  pulses. Then, parametric pulses were mixed with  $3\omega_1$  pulses by either the KB5 or KDP crystal. With the former, pulses tunable in 225–269 nm, while with the latter those in 269–287 nm are generated, as shown in fig. 2, with  $\sim 100$  kW peak power. The shortest wavelength limit of 225 nm comes from the wavelength limit of parametric pulses, while

the longest wavelength limits of 269 and 287 nm are due to the absorption of parametric pulses by each crystal.

The mixing of parametric pulses with second harmonic pulses was also performed by using a D-KDP type-I crystal, and pulses tunable in 288–393 nm were obtained as shown in fig. 2.

## References

- [1] Y. Tanaka, T. Kushida and S. Shionoya, *Optics Comm.* 25 (1978) 273; Erratum, *Optics Comm.* 41 (1982) 459.
- [2] Y. Masumoto, S. Shionoya and Y. Tanaka, *Solid State Comm.* 27 (1978) 1117.
- [3] Y. Masumoto, Y. Unuma, Y. Tanaka and S. Shionoya, *J. Phys. Soc. Japan* 47 (1979) 1844.
- [4] H. Yoshida, H. Salto and S. Shionoya, *Phys. Stat. Sol. (b)* 104 (1981) 331.
- [5] R.E. Stickel, Jr. and F.B. Dunning, *Appl. Optics* 17 (1978) 981.
- [6] C.F. Dewey, Jr., W.R. Cook, Jr., R.T. Hodgson and J.J. Wynne, *Appl. Phys. Lett.* 26 (1975) 714.
- [7] H.J. Dewey, *IEEE J. Quantum Electron.* QE-12 (1976) 303.
- [8] K. Kato, *Appl. Phys. Lett.* 30 (1977) 583.
- [9] F.B. Dunning and R.E. Stickel, Jr., *Appl. Optics* 15 (1976) 3131.
- [10] K. Kato, *Appl. Phys. Lett.* 29 (1976) 562.

BS-RO(7-87)

ISSN 1040-0136

A678

0268

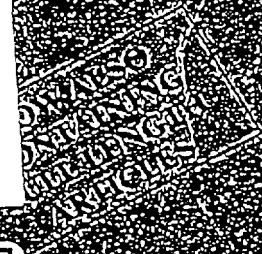
# OPTICS COMMUNICATIONS

A journal devoted to the publication of original research papers in the field of optics and optical communications.

VOLUME 80

NUMBER 2

DECEMBER 1991



F0082

OPTICS COMMUNICATIONS

1991 VOLUME 80 ISSUE 2

SISAC

331



00000327282085

OPTICS



0030-0018(1991)80:2-M

REF: A678BA0

14851369

80(2)



記事  
連番 0013

# Temperature-tuned noncritically phase-matched frequency conversion in $\text{LiB}_3\text{O}_5$ crystal

J.T. Lin, J.L. Montgomery

Center for Research in Electro-Optics and Lasers (CREOL) and Department of Physics,  
University of Central Florida, 12424 Research Pky, Orlando, FL 32826, USA

and

K. Kato

Second Research Center, Japan Defense Agency, Ikejiri 1-2-24, Setagaya, Tokyo, Japan

Received 17 April 1990; revised manuscript received 24 June 1990

The new nonlinear crystal of lithium triborate,  $\text{LiB}_3\text{O}_5$  (LBO), was investigated for frequency doubling and mixing of 1064 nm, 1135 nm and 1908 nm operated at the noncritically phase-matched (NCPM) temperatures of 149°C (for doubling 1064 nm), 77.4°C (for doubling 1135 nm), 112°C (mixing 1064 and 1135 nm) and 81°C (mixing 1064 and 1908 nm). The temperature tuning curves (from 0°C to 150°C), angular and temperature bandwidths are measured and compared with the calculated values.

## 1. Introduction

The newly discovered nonlinear crystal of lithium triborate,  $\text{LiB}_3\text{O}_5$  (LBO), has several advantages over another borate family,  $\beta\text{-BaB}_2\text{O}_4$  [1-5]. These include nonhygroscopic, wide transparency (0.16-2.6  $\mu\text{m}$ ), high damage threshold and may be temperature-tuned for noncritical phase-matching (NCPM). Under this NCPM condition, frequency conversion efficiency may be greatly improved by the large angular acceptance widths and by the absence of beam walk-off. Examples of this NCPM for frequency mixing using LBO, KTP and  $\text{KNbO}_3$  crystals were reported [5,6]. We note that all of these crystals of KTP,  $\text{KNbO}_3$  and LBO have the same point symmetry of  $mm2$  and that they are biaxial crystals which may be noncritically phase-matched for the input beam propagating along one of the principal axes. The features of these crystals are compared in table 1.

LBO crystal belongs to the orthorhombic,  $mm2$  symmetry and the principal axes  $x$ ,  $y$  and  $z$  are found to be parallel to the crystallographic axes of  $a$ ,  $c$  and

$b$ , respectively, with  $n_z > n_y > n_x$  [1]. The calculated optic angle is 54.6° at 0.532  $\mu\text{m}$  which defines LBO as a negative crystal [7]. From the Sellmeier equations for the refractive indices, we have obtained the phase-matching angles of 11.8° (type-I, to the  $x$  axis, in the  $xy$  plane) and 22.7° (type-II, to the  $z$  axis, in the  $yz$  plane) for SHG of 1064 nm. Furthermore, the room temperature NCPM may be achieved in SHG of 1200 nm (calculated value). It is therefore desirable to investigate the possibility of temperature-tuned NCPM particularly for the type-I operation whose matching angle is not too far away from the  $a$ -axis of LBO.

In this paper, we report the first demonstration of NCPM using LBO (temperature-tuned) for the second harmonic generation (SHG) and sum frequency mixing (SFM) of Nd:YAG laser and YAG-laser-pumped Raman cell in  $\text{H}_2$  gas. The temperature and angular bandwidths operated at this NCPM condition are measured and compared with the calculated values. The SHG efficiency, angular bandwidths and the tuning rates ( $d\phi/dT$ ) are measured at various wavelengths of 1064 nm, 1135 nm and

Table 1  
Comparison of biaxial crystals with point group of  $mm2$

	KTP	KNbO <sub>3</sub>	LiB <sub>3</sub> O <sub>3</sub>
symmetry:	$mm2$	$mm2$	$mm2$
optical angle (at 1064 nm): (crystal type)	21.9° (positive)	57.2° (negative)	54.6° (negative)
optical axis: ( $x, y, z$ ) crystallographic axis:	( $a, b, c$ )	( $c, a, b$ )	( $a, c, b$ )
nonlinear coefficients: (pm/V) $d_{31}, d_{32}, d_{33}$ $d_{13}, d_{24}$	6.5, 5.0, 13.7 6.1, 7.6	15.8, 18.3, 27.4 16.5, 17.1	1.15, 1.24, 0.063 1.15, 1.24
max. $d_{eff}$ :	type II	type I	type I
acceptance widths: noncritical (mrad. cm <sup>1/2</sup> ): critical (mrad. cm):	108, 186 15, 83	30 12	57 9
temperature width (°C cm):	25	0.05	4.2
noncritical phase- matching:	SFM of 809 & 1064 nm (room temp.)	SHG of 860, 986 nm (room temp.)	SHG of 1064 nm (at 149°C) 1079 nm (at 112°C)
$xz$ plane ( $\phi=0^\circ$ ): $d_{eff(I)}$ (for $0 < \theta < \Omega$ ) $d_{eff(II)}$ (for $\Omega < \theta < 90^\circ$ )	$d_{32} \sin \theta$ $-d_{24} \sin \theta$	$-d_{31} \cos \theta$ $d_{13} \cos \theta$	$d_{13} \cos^2 \theta + d_{24} \sin^2 \theta$ (II) $d_{31} \cos^2 \theta + d_{32} \sin^2 \theta$ (I)
$yz$ plane ( $\phi=90^\circ$ ): $d_{eff(I)}$ $d_{eff(II)}$	0 $-d_{13} \sin \theta$	$-d_{32} \sin^2 \theta - d_{31} \cos^2 \theta$ 0	0 $d_{13} \cos \theta$
$xy$ plane ( $\theta=90^\circ$ ): $d_{eff(I)}$ $d_{eff(II)}$	0 $-d_{13} \sin^2 \phi - d_{24} \cos^2 \phi$	$-d_{32} \sin \phi$ 0	$d_{32} \cos \phi$ 0

1908 nm. We note that the data obtained in this work deviates from that of the earlier work in refs. [1] and [4] due to the difference in the growth of the LBO crystals, where slight differences of the indices of refraction were found [8].

## 2. Experiment

In this experiment, we have used two LBO crystals with the lengths of 12.5 mm and 4.7 mm for the efficiency and bandwidths measurements, respectively. Note that a shorter crystal provides larger

acceptance widths and hence better reading accuracy. The entrance faces, of size  $3 \times 3$  mm, were polished, uncoated and normal to the  $x$  axis of the crystal. To achieve the type-I NCPM condition, the pump beam was propagated long the  $x$  axis and linearly polarized along the  $z$  axis in the  $xz$  plane. A Quantel laser (model 580) of 10 ns, 10 Hz, TEM<sub>00</sub> transverse mode, beam spot of 4 mm, divergence of 0.7 mrad and output energy up to 50 mJ was used as the pump source.

Four experiments were conducted: (A) SHG of 1064 nm, (B) SHG of 1135 nm, (C) SFM of 1064 nm and 1135 nm, and (D) SFM of 1064 nm and

1908 nm, where the 1135 nm and 1908 nm radiations were generated from the rotational and vibrational first-Stokes in  $H_2$  Raman cell (pumped by 1064 nm). The results are summarized as follows: (for angular and temperature bandwidths measurement, a crystal length of 4.7 mm was used).

(A) SHG of 1064 nm: The NCPM temperature was measured to be 149°C with fwhm of 4.0°C cm. Angular bandwidths of  $\Delta\theta/l^{1/2} = 1.9$  degree-cm<sup>1/2</sup> and  $\Delta\phi/l^{1/2} = 2.3$  cm<sup>1/2</sup> were measured. 60% energy efficiency was achieved at input energy of 40 mJ, where the pump beam was focused into a 1 mm spot size. LBO crystal with a length of 12.5 mm was used for achieving 60% efficiency. We note that the LBO crystals used in this work were uncoated and surface damage was found at an input energy of (45–50 mJ), depending upon the crystal quality. The accurate surface and bulk damage thresholds still need to be investigated.

(B) SHG of 1135 nm: A lower NCPM temperature of 77.4°C was measured with fwhm of 4.7°C cm. Angular bandwidths were comparable to that of SHG of 1064 nm.

(C) SFM of 1064 and 1135 nm: NCPM temperature of 112°C was measured with fwhm of 5°C cm. Angular bandwidths were not accurately measured due to the unstable output energy of the Raman emission.

(D) SFM of 1064 and 1908 nm: NCPM temperature of 81°C were measured with fwhm of 7.4°C cm.

Temperature profiles of the above measurements are shown in fig. 1.

As shown in fig. 2, the temperature variations of the phase-matching angles are measured for SHG of 1064 nm, 1135 nm and SFM of 1064 nm with 1135 and 1908 nm. Fig. 2 shows the noncritical phase-matching (NCPM) temperatures at 149°C, 77.4°C and 81°C, respectively. We note that these curves have increasing slopes of  $\partial\phi/\partial T$  when the phase-matching angles approach the NCPM condition. We have also measured the temperature bandwidths ( $\Delta T/l$ ) at the various regimes of these curves. Our data shows a slightly decreasing function of ( $\Delta T/l$ ) versus  $T$ , i.e., a narrower temperature bandwidth was found at the NCPM compared with that of the critical phase-matching at room temperature.

The angular bandwidths ( $\Delta\phi/l$ ) are, however, an

increasing function of temperature when it approaches the NCPM temperature. The measured results are shown in fig. 3 where maximum bandwidth ( $\Delta\phi/l$ ) may be achieved when the phase-matching angle approaches the NCPM (angle-tuned), i.e. along one of the principal axes of the crystal,  $\phi, \theta = 0^\circ$  or  $90^\circ$ . Fig. 2 shows the temperature-tuned NCPM which is expected to have a trend similar to that of the angle-tuned NCPM, where maximal angle bandwidth may be achieved when the NCPM condition is met either by temperature tuning or angle tuning for a particular fundamental wavelength. We note that near or at NCPM, the first-order derivative of the wave-vector mismatching vanishes and the second-order derivative is required to obtain accurate bandwidths which will be shown in the next section. We have also measured the angle bandwidths for various processes at room temperature (external bandwidths, mrad) using LBO crystal with 4.7 mm in length,  $(\Delta\phi, \Delta\theta) = (5.3, 112)$  for SHG of 1064 nm;  $(23.9, 122)$  for SHG of 1135 nm;  $(17.8, 118)$  for SFM of 1064 nm and 1135 nm;  $(50, 199)$  for SFM of 1064 nm and 1908 nm. These angular bandwidths in the sensitive ( $\Delta\phi$ , tuning in  $xy$  plane) and insensitive ( $\Delta\theta$ , tuning in  $xz$  plane) directions will be analyzed as follows.

### 3. Analyses

In order to analyze the above measured data, we have calculated the internal angular acceptance widths (fwhm) in the principal planes for type-I SFM of  $1/\lambda_1 + 1/\lambda_2 = 1/\lambda_3$ , where  $\lambda_1 \geq \lambda_2 > \lambda_3$ , as follows. Details of the derivations of the following expressions will be published elsewhere [9].

(A) In  $xy$  plane ( $\theta = 90^\circ$ ), first-order (for critical phase-matching),

$$\Delta\phi/l = \frac{\lambda_1}{11.29} [n_3^3(\phi) (n_{3x}^{-2} - n_{3y}^{-2}) \sin 2\phi]^{-1},$$

$$n_3(\phi) = (n_{3x}^{-2} \sin^2 \phi + n_{3y}^{-2} \cos^2 \phi)^{-1/2}. \quad (1)$$

(B) In  $xy$  plane, second-order (for NCPM with  $\phi = 0^\circ$  and  $\theta = 90^\circ$ ),

$$\Delta\phi/l^{1/2} = 9.4 \left( \frac{\lambda_1}{n_{3y}^3 (n_{3x}^{-2} - n_{3y}^{-2})} \right)^{1/2}. \quad (2)$$

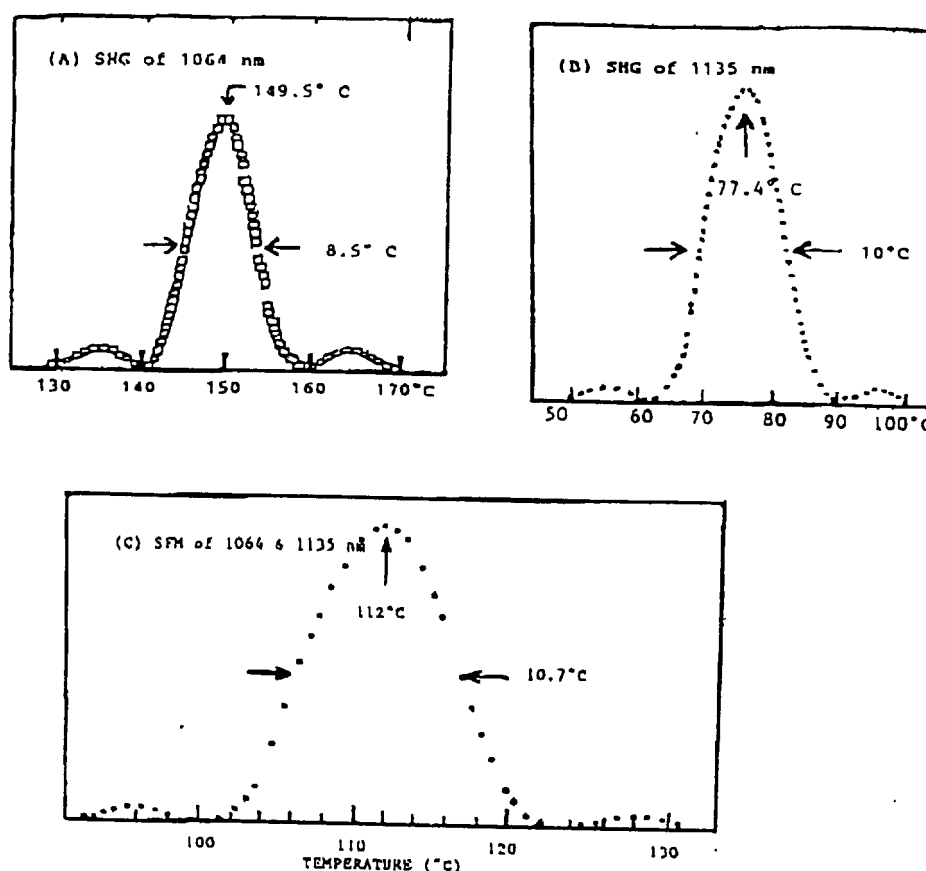


Fig. 1. Temperature profiles of LBO crystal for frequency doubling and mixing: (A) SHG of 1064 nm, (B) SHG of 1135 nm, and (C) SFM of 1064 and 1135 nm. LBO length of 4.7 mm was used in this experiment.

(C) In  $xy$  plane, second-order (for NCPM),

$$\Delta\phi l^{1/2} = 9.4 (N_1 + N_2), \quad (3a)$$

$$N_j = \left( \frac{\lambda_j}{n_{jy}^3 (n_{jx}^{-2} - n_{jy}^{-2})} \right)^{1/2}. \quad (3b)$$

In eqs. (1)–(3), the units used are: wavelength ( $\lambda_i$ ) in  $\mu\text{m}$  and angle bandwidths in mrad cm (for critical, first-order) and mrad  $\text{cm}^{1/2}$  (for noncritical, second-order).

Based on the Sellmeier equations [7] and above derived expressions, we have calculated the angular bandwidths for various processes. The calculated data are in good agreement with those measured values shown in fig. 3. We note that the LBO crystals used in this work were grown by the Research Institute of Synthetic Crystals (Beijing, China) which had slight differences in the refractive indices when compared with that of the crystals grown by Fujian Institute of

Research in the Structure of Matter (China) due to the different fluxes used in crystal growth [8]. Data obtained in this work therefore deviate from that of refs. [1] and [4]. Examples are (measured data): SHG of 1064 nm shows a phase-matching angle (at room temperature) of  $11.8^\circ$  (this work) and  $12.5^\circ$  (Chen's work); NCPM temperatures for SHG of 1064 nm are  $149^\circ\text{C}$  (this work) and  $133^\circ\text{C}$  (Chen's) [4,8]. We also found some mistakes (typing errors) in refs. [1] and [4]. We should also note that the analyses described above are valid for phase-matching either in the principal planes or along the  $x$ -axis. In the general case, both the first- and second-order contributions of the Taylor expansion of the dephasing wavevector should be included in the calculation. The analytic expressions of the general case are quite complicated and will be presented elsewhere [7]. In fig. 4, we show the calculated acceptance width  $\Delta\phi$  (with crystal length of 1 cm), where

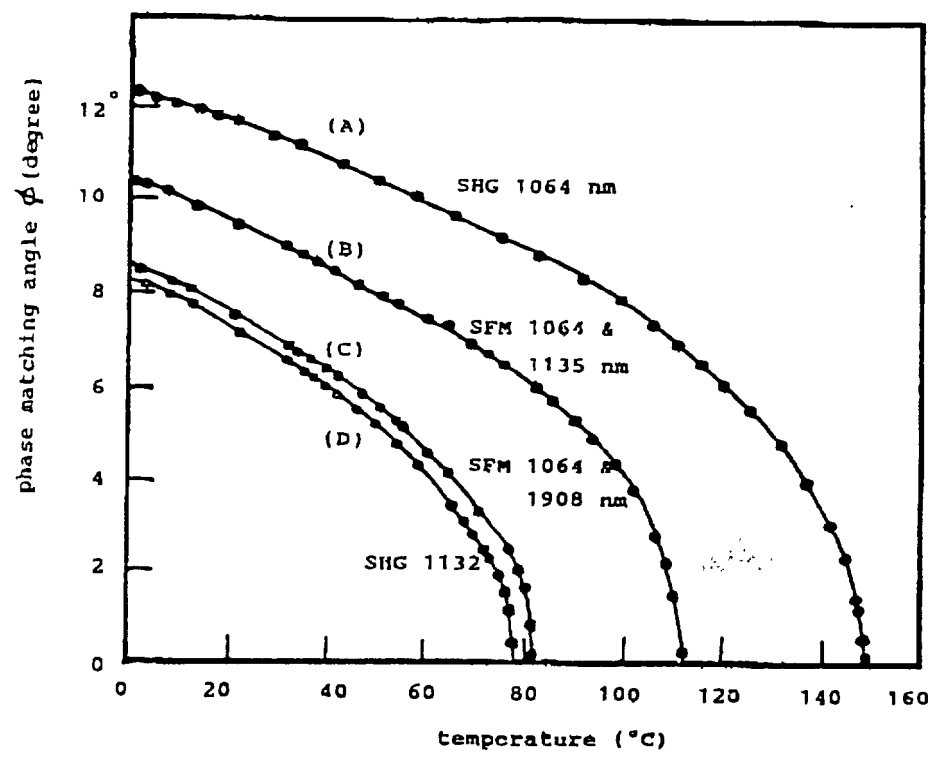


Fig. 2. Temperature tuning curves of LBO for various processes: (A) SHG of 1064 nm, (B) SFM of 1064 and 1135 nm, (C) SFM of 1064 and 1908 nm and (D) SHG of 1135 nm, where angles are tuned in the  $xy$  plane (type-I operation) and have been converted into internal angles.

the dashed-curve shows the first-order results based on eq. (1) and the solid-curve shows the exact solution based on a quadratic equation of  $\Delta\phi$ :

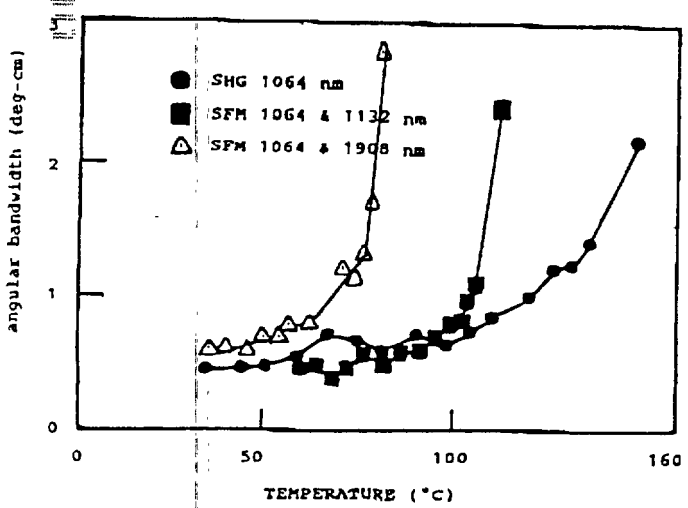


Fig. 3. Measured angular bandwidth ( $\Delta\phi/l$ ) of LBO versus temperature tuning for various processes as described in fig. 2.

$$0.001 K'' l (\Delta u)^2 + 2K' l (\Delta u) - 1.1132 = 0, \quad (4)$$

where  $K'$  and  $K''$  are the first and second derivatives of the dephasing vector  $\Delta k$ ,  $l$  is the crystal length (in cm) and  $\Delta u$  (fwhm) =  $\Delta\phi$  or  $\Delta\theta$  (in mrad). Other constants are derived for wavelengths in  $\mu\text{m}$ . We note that near the NCPM points ( $\phi=0^\circ$  or  $90^\circ$ ) the second-order term in eq. (2) is dominant.

Given the Sellmeier equations of the indices of refraction, we should be able to calculate the temperature bandwidths expressed by (for NCPM SHG along  $a$ -axis):

$$\Delta T l = \frac{\lambda_1}{2.26} \left( \frac{\partial(n_1^2 - n_2^2)}{\partial T} \right)^{-1}, \quad (5)$$

where  $l$  and  $\kappa_1$  both are in the units of cm and  $\partial n / \partial T$  may be measured or calculated from  $\partial n / \partial T = (\partial n / \partial \lambda) (\partial \lambda / \partial T)$ . By measuring the wavelength tuning rate ( $\partial \lambda / \partial T$ ) and calculating ( $\partial n / \partial \lambda$ ) from the Sellmeier equations, the temperature bandwidths may be calculated. In our experiment, we are limited by the available laser wavelengths and measured values are

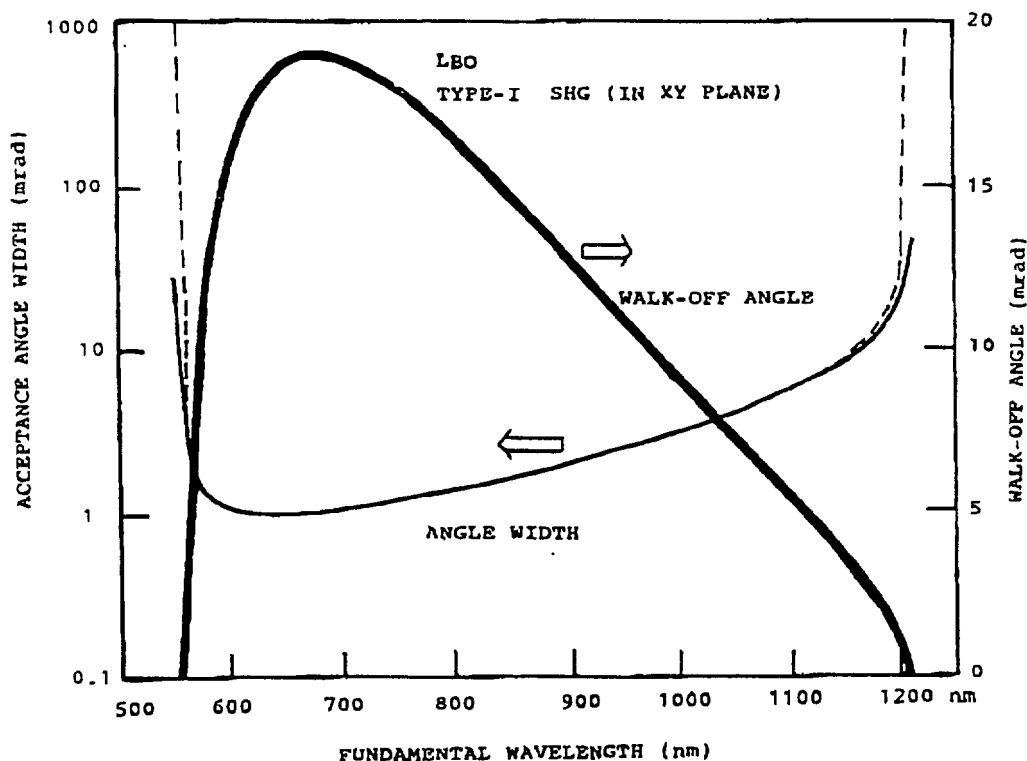


Fig. 4. Calculated angular bandwidths for SHG (type-I in  $xy$  plane) using LBO, where solid-curve shows the exact solution of  $\Delta\phi$  and dashed-curve shows the first-order approximation. Also shown are the calculated walk-off angles; noting that beam walk-off vanishes at the noncritical points of  $\phi=0^\circ$  and  $90^\circ$ , where the second-order solution for the angular bandwidth is required.

not sufficient to define a continuous curve of  $(\partial\lambda/\partial T)$ . Therefore, an alternative evaluation of  $\partial n/\partial T$  is described as follows. The temperature variation of the refractive index difference,  $\partial(\Delta n)/\partial T$ , may be found by Taylor expansion of the wave-vector mismatch  $\Delta k=2\pi\Delta n$  as follows:

$$\frac{\partial\Delta n_1}{\partial T} - \frac{\partial\Delta n_2}{\partial T} = \left[ \left( \frac{\partial\Delta n_1}{\partial\phi} \right)_{\phi_1} - \left( \frac{\partial\Delta n_2}{\partial\phi} \right)_{\phi_2} \right] \left( \frac{\phi_2 - \phi_1}{T_2 - T_1} \right), \quad (6)$$

where  $\phi_{1,2}$  are the phase-matching angles at two temperatures  $T_{1,2}$ ,  $\Delta n_{1,2}$  are the dephasing factor evaluated at  $\phi_{1,2}$ . For type-I SHG in the principal plane of  $xy$ , we have

$$\Delta n_{1,2} = -\frac{1}{2} [n_x^2(\phi)(n_{2x}^{-2} - n_{2y}^{-2}) \sin 2\phi]_{\phi=\phi_{1,2}}, \quad (7)$$

$$n_2(\phi) = (n_{2x}^{-2} \sin^2 \phi + n_{2y}^{-2} \cos^2 \phi)^{-1/2}, \quad (8)$$

where the indices of refraction are evaluated at the wavelength of the second harmonic. As shown in fig.

2, the measured slopes,  $(\partial\phi/\partial T)$ , may be combined in eq. (4) with the calculated values of  $(\partial\Delta n/\partial\phi)$  and allow us to evaluate the values of  $(\partial\Delta n/\partial T)$ . Our results show the similar trends of the temperature gradients of  $(\partial\Delta n/\partial T)$  and  $(\partial\phi/\partial T)$ , where high sensitivity (or large slope) is found when the NCPM is achieved. These features limit the applications of LBO to a well-controlled temperature, however, they also provide a large temperature tuning rate in optical parametric oscillation (OPO) near the degenerate point when NCPM is achieved.

#### 4. Conclusion

In conclusion, we have demonstrated the NCPM experiment in LBO crystals for SHG of 1064 nm and 1135 nm and the mixing of 1064, 1135 and 1908 nm. The broad angular bandwidth with no beam walk-off effects (when operated at NCPM) make LBO an excellent crystal for high-efficiency frequency conversion. The deep-UV transmission (as short as 160

nm) of LBO also provides the potential use for the generation of coherent sources with the spectral regime of (160–188 nm) which can not be achieved by other crystals such as BBO [10]. Furthermore, tunable radiation (0.9–1.3  $\mu\text{m}$ ) may be generated from optical parametric oscillation (OPO), where doubled-YAG (at 532 nm) may be used as the pump to meet the temperature tuned NCPM for various output wavelengths in the near-IR spectral range. We have recently achieved a tuning range of (0.9–1.3  $\mu\text{m}$ ) using 532 nm as the pump, where LBO crystal was temperature tuned from 135°C to 150°C. This work is in progress and will be published elsewhere [11].

#### Acknowledgements

We would like to thank R. DeSalvo, A. Horner and M.Y. Hwang for their assistance in the experiment. This research is supported by DARPA/SUS (grant

No. MDA 972-89-J-1006), Florida High Technology Industrial Council and the AFSC SBIR program.

#### References

- [1] C. Chen, Y. Wu, A. Jiang, B. Wu, G. You, R. Li and S. Lin, *J. Opt. Soc. Am. B* 6 (1989) 616.
- [2] C. Chen, A. Jinag, B. Wu, G. You and S. Lin, in *Digest of CLEO'89*, paper ThQ1.
- [3] J.T. Lin, C.E. Huang and J.Q. Yao, in *Digest of CLEO'89*, paper ThQ2.
- [4] B. Wu, N. Chen, C. Chen, D. Deng and Z. Xu, *Optics Lett.* 14 (1989) 1080.
- [5] J.T. Lin and A. Horner, in *Technical Digest of OSA Annual Meeting* (Oct. 15-20, 1989), post-deadline paper PD 17.
- [6] J.T. Lin, in: *Proc. SPIE* 1040 (1989) 129.
- [7] J.T. Lin, K. Kato and S.W. Chong, to be published.
- [8] C. Chen, private communication.
- [9] J.T. Lin and S.W. Chong, in: *Laser hosts and nonlinear crystals*, ed. J.T. Lin (Springer Verlag, NY), in press (1991).
- [10] J.T. Lin and K. Kato, *Proc. SPIE* 1120 (1990), in press.
- [11] J.T. Lin and J.L. Montgomery, *Optics Lett.*, submitted.

## 9

Professor of Clinical Ophthalmology,  
Columbia University College of Physicians and Surgeons,  
New York, New York

[illegible]

**Tone drawings by Virginia Cantarella**

ST. LOUIS · BALTIMORE · TORONTO 1989





9

*Editor:* Eugenia A. Klein  
*Assistant editor:* Constance C. Spasser  
*Senior secretary:* Robin O. Sutter  
*Project manager:* Kathleen L. Teal  
*Manuscript editor:* Judith Bange  
*Design:* John Rokusek  
*Production:* Ginny Douglas, Judith Bange, Teresa Breckwoldt

THIRD EDITION

Copyright © 1989 by The C.V. Mosby Company

All rights reserved. No part of this publication may be reproduced, stored in a retrieval system, or transmitted, in any form or by any means, electronic, mechanical, photocopying, recording, or otherwise, without prior written permission from the publisher.

Previous editions copyrighted 1975 and 1983

Printed in the United States of America

The C.V. Mosby Company  
11830 Westline Industrial Drive, St. Louis, Missouri 63146

**Library of Congress Cataloging in Publication Data**

L'Esperance, Francis A., 1932-  
Ophthalmic lasers.

Bibliography: p.

Includes index.

1. Laser coagulation. 2. Eye—Diseases and defects—Radiotherapy. I. Title. [DNLM: 1. Eye—surgery—atlases. 2. Lasers—therapeutic use—atlases. WW 17 L637o]

RE992.P5L47 1989 617.7'1 88-23131

ISBN 0-8016-2965-9

GW/MV/MV 9 8 7 6 5 4 3 2

## Corneal Laser Surgery

OLIVIA N. SERDAREVIC

Advances in laser technology hold the promise for exciting new developments in corneal surgery. Cutting imprecision, lack of predictability, and absence of reproducibility have been major limiting factors in the accuracy of standard corneal surgical techniques using mechanical cutting devices. Distortion of corneal topography has been unavoidable with currently available instruments that require corneal applanation with pressure or suction. Incomplete visualization during surgery has led to poor positioning and inadequate centration. The inability to cut almost infinitely thin sections, to control tissue removal at the submicron level, and to cut with almost no damage to adjacent tissue has been an obstacle in achieving optimal visual results. In an effort to find the ideal corneal cutting device, newly available laser systems capable of corneal vaporization and ablation have been investigated over the past few years.

This chapter reviews the development of laser applications in corneal surgery, the current status of experimental and clinical investigations, and possible future laser corneal surgical applications, problems, and solutions.

---

### TYPES OF LASERS

Several lasers have been investigated for their corneal cutting potential. These lasers have been selected on the basis of corneal absorption characteristics; they emit radiation in either the infrared range absorbed primarily by corneal water or the ultraviolet range absorbed principally by corneal solids. The infrared lasers, including the carbon dioxide (CO<sub>2</sub>) laser, the hydrogen fluoride (HF) laser, and the erbium: yttrium-aluminum-garnet (Er:YAG) laser, interact with the cornea by photovaporization with thermal effects. The ultraviolet lasers, including the excimer laser and the neodymium:YAG (Nd:YAG) laser of the fifth harmonic, interact with the cornea by photochemical ablation with or without thermal effects, depending on the wavelength and energy used. These tissue interactions are discussed in earlier chapters.



**Fig. 24-1.** Light micrograph of human eye bank cornea incised with a Q-switched CO<sub>2</sub> laser. Smallest scale division is equal to 5  $\mu$ m. (Hematoxylin and eosin;  $\times 100$ .) (From Keates RH and others: *Ophthalmic Surg* 12(2):117, 1981.)

## Historical Background

### Infrared Lasers

The continuous-wave (CW) CO<sub>2</sub> laser emitting radiation at 10.6  $\mu$ m was the first laser explored for corneal surgery by Fine and others<sup>1</sup> in 1967. This laser was shown to be capable of vaporizing corneal tissue, but the amount of energy required to create corneal incisions led to very significant charring and burning of adjacent tissue. Beckman and associates<sup>2</sup> obtained less thermal destruction by pulsing the exposure, thereby causing less heat dissipation. In 1981 Keates and associates<sup>3</sup> further decreased the total energy exposure by using a Q-switched CO<sub>2</sub> laser and reduced the amount of charring at the incision site to a zone 25 to 30  $\mu$ m wide (Fig. 24-1). Over the past several years, however, investigators have abandoned the CO<sub>2</sub> laser for corneal cutting in favor of other infrared lasers, such as the HF laser and the Er:YAG laser, that emit radiation in the 2.7- to 3.0- $\mu$ m peak water absorption range, allowing for increased corneal absorption and decreased thermal damage to adjacent tissue. Esterowitz and others<sup>4</sup> reported the first use of the Er:YAG laser (2.95  $\mu$ m) for corneal ablation in 1986. In that same year Loertscher and others<sup>5</sup> and Seiler and others<sup>6</sup> demonstrated the ability of the pulsed HF laser (2.7 to 3.0  $\mu$ m) to vaporize corneal tissue and to produce sharp incisions with a 1- to 15- $\mu$ m-wide zone of thermal damage (Fig. 24-2).

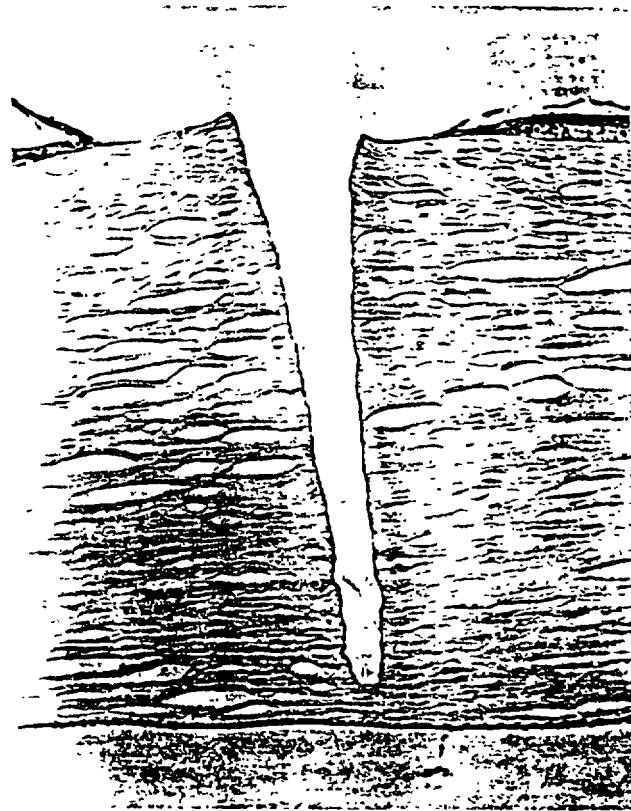


Fig. 24-2. Light micrograph of human eye bank cornea incised with a pulsed HF laser. The corneal epithelium was removed before irradiation (Hematoxylin and eosin.) (Courtesy Hanspeter Loertscher, M.S., Miami, Fla.)

#### Ultraviolet Lasers

Of all the lasers that have been evaluated recently, pulsed far-ultraviolet lasers appear to have the most potential for increasing the accuracy of standard corneal surgical procedures and for expanding the corneal surgeon's armamentarium of techniques. The excimer laser-corneal interaction was investigated for the first time in 1981 by Tabadda and others,<sup>15</sup> who studied the response of the corneal epithelium to the krypton fluoride (KrF) excimer laser (248 nm). In 1983 Trokel and associates<sup>121</sup> achieved precise, sharply controlled cutting with the argon fluoride (ArF) excimer laser (193 nm). Krueger and others<sup>31,32</sup> demonstrated the possibility of determining ArF excimer laser cutting width and depth to sub-micron accuracy according to pulse energy, pulse frequency, pulse numbers, and fluence. Each pulse has been shown to remove 0.1 to 0.5  $\mu\text{m}$  of tissue. Comparative histologic and ultrastructural studies of the ArF and KrF excimer laser outputs demonstrated the superiority of the ArF laser for corneal surgery.<sup>24,32,70,88</sup> The ArF excimer laser, as opposed to the KrF excimer laser, produced corneal photochemical ablation without thermal effects within a broad range of fluences (Fig. 24-3).<sup>\*</sup> All investigators have commented on the highly localized

\*References 4, 21, 52, 68-70, 88, 105, 107, 110

tissue interaction, the preservation of the normal lamellar structure of stromal collagen, and the minimal alteration of adjacent tissue obtained with the ArF excimer laser.\* The ablated corneal tissue has been shown to be ejected at supersonic velocities,<sup>10</sup> but deposition of electron-dense material at the wound edge has been noted in an extremely narrow zone (0.02 to 0.3  $\mu\text{m}$  wide)<sup>69, 70, 98, 108</sup>

\*References 3-6, 10, 19, 21, 24, 25, 30, 34, 38-40, 48, 51, 52, 55, 56, 68-70, 74, 75, 79, 86, 88-90, 102, 105, 107, 108, 110, 115, 121, 129



**Fig. 24-3.** Transmission electron micrograph of a human cornea 4 months after lamellar keratectomy with an ArF excimer laser. Note the elongated basal cells of the epithelium (*top*), the prominent basal lamina, and the electron-lucent vacuoles (*arrows*). Some amorphous granular ground substance can be noted above the area of ablated stromal tissue (*arrowhead*). (Copyright © Taunton Technologies, Inc., 1988.)

The presence of discontinuously distributed deposits appeared to depend on the orientation of collagen lamellae at the time of irradiation<sup>108</sup> (Fig. 24-4). Remnants of incompletely ablated epithelial cells or keratocytes have been shown occasionally to impart a more continuous, pseudomembrane appearance to the wound edge<sup>70, 78, 108</sup> (Fig. 24-5).

The Nd:YAG laser of the fifth harmonic (212 nm), another far-ultraviolet laser, has also been reported to produce smooth corneal cutting, but most experimental and clinical investigations of laser corneal surgery have been pursued with the ArF excimer laser. Although ultraviolet-induced mutagenesis was an initial concern regarding the use of far-ultraviolet lasers, no mutagenesis has been detected in ArF excimer studies measuring anaplastic transformation in fibroblast tissue cultures<sup>29</sup> and unscheduled nucleic acid synthesis in regenerating corneas.<sup>80</sup>

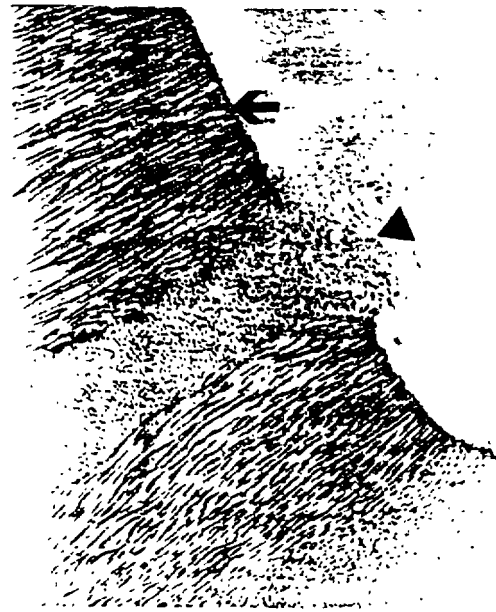


**Fig. 24-4.** Transmission electron micrograph of rabbit cornea incised with an ArF excimer laser. Note the fluffy deposits (*arrow*) in a zone 0.02 to 0.08  $\mu\text{m}$  wide at the edge of stromal lamellae that are cut perpendicular to their direction. There is a dispersion of collagen fibrils (*arrowhead*) without deposits when the lamellae are cut parallel to their direction. (Original magnification,  $\times 10,200$ .) (From Serdarevic ON and others: Published courtesy of Ophthalmology [1988; 95:493-505].)



**Fig. 24-5.** Transmission electron micrograph of rabbit cornea incised with an ArF excimer laser. Remnants of an incompletely ablated keratocyte (arrow) impart a more continuous, pseudomembrane appearance to the wound edge. (Original magnification,  $\times 8,300$ ) (Photograph jointly produced with Yves Pouliquen, M.D., and Michele Savoldelli, M.S., Paris, France.)

## CORNEAL SURGICAL APPLICATIONS

### Penetrating Keratoplasty

Astigmatism is a significant problem after penetrating keratoplasty. Although corneal surgeons are becoming increasingly successful in maintaining clear grafts, high and irregular astigmatism precludes satisfactory visual acuity in up to 10% of postkeratoplasty patients.<sup>77</sup> Despite advances in mechanical trephine design and suturing techniques, mean postoperative astigmatism is reported to be between 3 and 5 diopters in large keratoplasty series.<sup>12, 42, 77, 81, 123</sup> Imprecise trephination is considered a major factor in postkeratoplasty astigmatism.\* Currently available mechanical trephines cause varying amounts of disparity between donor button and recipient wound configuration. This disparity results from irregular cutting, corneal topographic distortion, and poor centration.

\*References 12, 42, 77, 81, 82, 84, 123

### Experimental Studies

In 1971 Beckman and associates<sup>7</sup> were the first to apply a laser experimentally for noncontact trephining in penetrating keratoplasty. They used a rapid-pulsed CO<sub>2</sub> laser combined with a diverging prismatic axicon lens and a focusing lens (Fig. 24-6). The optical system converted each laser pulse into an annulus, the diameter of which depended on the focal length used. They were able to obtain perforation within 1 sec using a pulse energy of 0.4 J at a repetition rate of 60 pulses per second. High-speed cinematography demonstrated that the anterior layers of the cornea were being lasered more rapidly than the posterior layers, resulting in a pyramid-shaped button with a smaller anterior than posterior portion. Optical system refinements to create more parallel sides were not pursued at that time, since the CO<sub>2</sub> laser produced significant corneal thermal damage, resulting in poorer quality cutting than that obtained mechanically.

The recent availability of laser systems permitting more precise cutting with less thermal damage led to renewed interest in laser trephination. In 1987 Loertscher and associates,<sup>8</sup> working with the pulsed HF laser, and my associates and I,<sup>9</sup> working with the ArF excimer laser, reinvestigated the feasibility of laser corneal trephination.

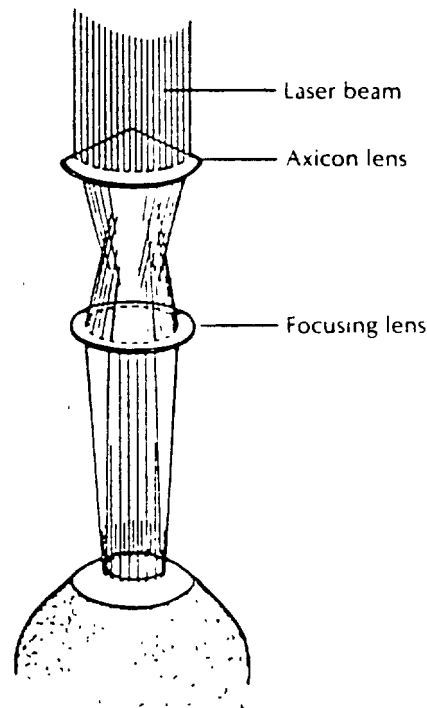


**Fig. 24-6.** Schematic diagram of the delivery system for pulsed CO<sub>2</sub> laser corneal trephination. The "core" of laser energy acts as an "optical trephine" and removes a circular area of the cornea. (From Beckman H and others. *Am J Ophthalmol* 71:1277-1283, 1971. Published with permission from The American Journal of Ophthalmology. Copyright by The Ophthalmic Publishing Company.)



The "no-touch" trephine system used by Loertscher and associates consisted of a pulsed HF laser and optical system incorporating a modified axicon lens (Fig. 24-7). The diameter of trephination could be varied from 5 to 7 mm by altering the position of the axicon lens. Corneal trephination (Fig. 24-8) with focal perforation was achieved in eye bank eyes in 7 to 9 sec using a laser output energy of 100 mJ per pulse at a frequency of 10 Hz. Shadow photogrammetric analysis of buttons trephined with the HF laser demonstrated that the edges were more vertical and parallel when compared with those of buttons trephined with some mechanical devices (Fig. 24-9). The laser induced less disparity between tissue and trephine size than did suction and motorized trephines.<sup>26</sup> Histologically, the wound edges compared favorably with those obtained by mechanical trephination; there was a 10- $\mu$ m zone of thermal coagulation and a 100- $\mu$ m zone of stromal lamellar disorganization (Fig. 24-10). The width of the excised annulus was 100 to 150  $\mu$ m.

Using the ArF excimer laser, my associates and I achieved noncontact corneal trephination that was distinctly more precise than that obtainable by mechanical devices.<sup>27</sup> The delivery system included rotating circular slits that allowed for the projection of a hollow circular beam onto the cornea (Fig. 24-11). Depending on the thickness of the cornea and the stability of the eye, the exposure time until perforation in one area (with the rest of the cornea trephined down to Descemet's membrane) varied from 30 sec to a few minutes when the fluence was 110 mJ/cm<sup>2</sup>. Pulse energies at the cornea were between 4 and 6.6 mJ, and the repetition rates were 15 and 20 Hz. The trephination diameter could be varied from 4 to 8 mm, depending on the distance of the cornea from the spherical lens. Complete visualization during trephination allowed for perfect centration with the helium-neon (HeNe) aiming beam. On microscopic examination (Fig. 24-12), the excimer laser created a much more sharply defined, regularly cut edge in eye bank eyes and in animal eyes *in vivo* than even the Hanna suction trephine, which is reported to create the most regular mechanical trephination.<sup>27</sup> Thinner trephination sections were possible with less disruption of tissue when the corneas were trephined with the laser rather than manually. Irradiated incisions as thin as 10  $\mu$ m were possible, but eye movements sometimes led to wider sections. There was minimal alteration of surrounding tissue; deposition of electron-dense material was sometimes evident at the wound edges in an area only 0.02 to 0.08  $\mu$ m wide. Scanning electron microscopic examination demonstrated less endothelial cell loss and damage at the edge of Descemet's membrane after excimer laser trephination than after manual trephination. On morphologic examination at 6 hours to 3 months after penetrating keratoplasty in an animal autograft model, there was no evidence of any latency or adverse alteration of wound healing processes, including cellular migration, proliferation, and production of new tissue (Fig. 24-13).

### Future Directions

Laser trephination has not yet been evaluated clinically. Although improvement in trephination precision theoretically should decrease postkeratoplasty astigmatism, studies are necessary to assess postoperative corneal curvatures in primates.

*Text continued on p. 934*

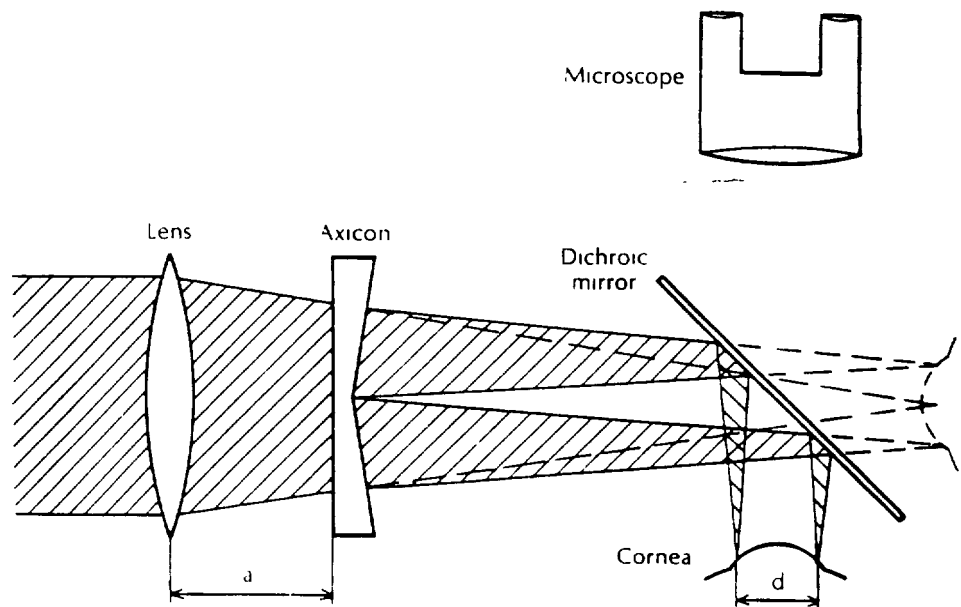


**Fig. 24-7.** Schematic diagram of the delivery system for pulsed HF laser corneal trephination. An axicon placed between a focusing lens and its focal plane converts each laser pulse into an annulus, which is focused on the cornea. The diameter of the annulus ( $d$ ) can be varied by adjusting the distance between the axicon and the lens ( $a$ ). (From Loertscher H and others. *Am J Ophthalmol* 104:471-475, 1987. Published with permission from The American Journal of Ophthalmology. Copyright by The Ophthalmic Publishing Company.)

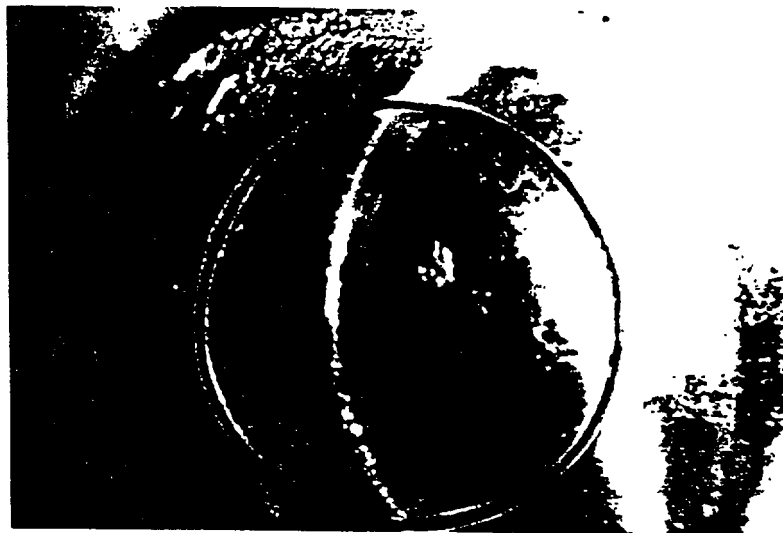


**Fig. 24-8.** Slit lamp photograph of a 6.5-mm diameter trephination produced in an eye bank eye using the HF laser trephine system. (From Loertscher H and others: *Am J Ophthalmol* 104:471-475, 1987. Published with permission from The American Journal of Ophthalmology. Copyright by The Ophthalmic Publishing Company.)

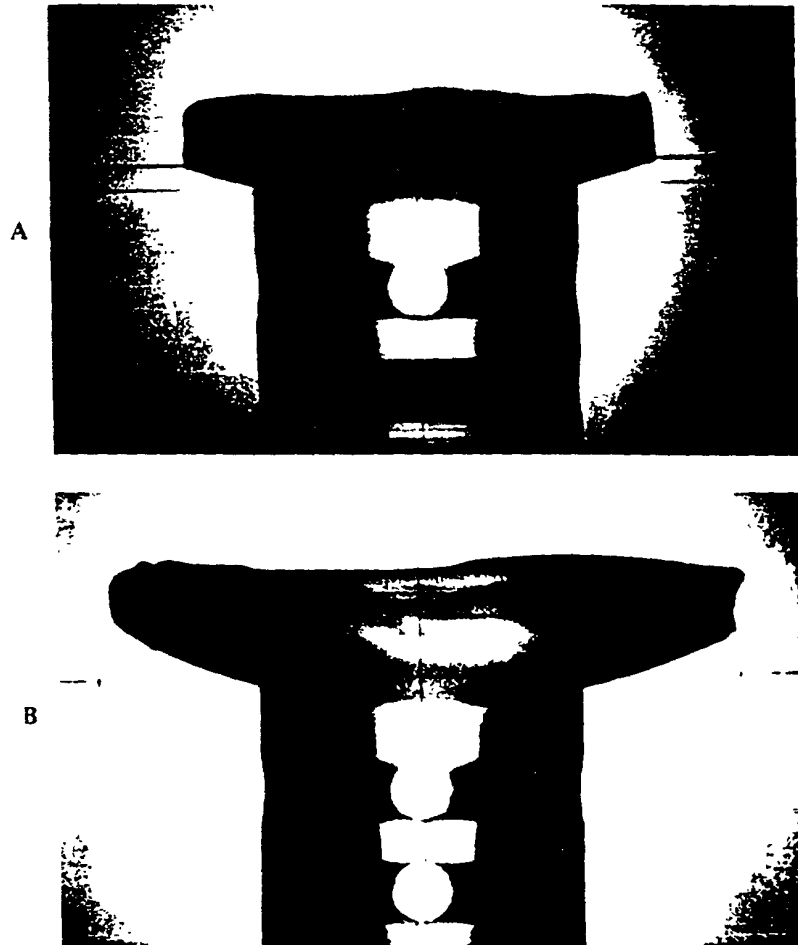


**Fig. 24-9.** Shadow photographs of eye bank corneal buttons trephined with a HF laser (A) and a Hessburg-Barron suction trephine (B). The laser produces more vertical and parallel edges. (Courtesy Hanspeter Loertscher, M.D., and D.B. Denham, Miami, Fla.)

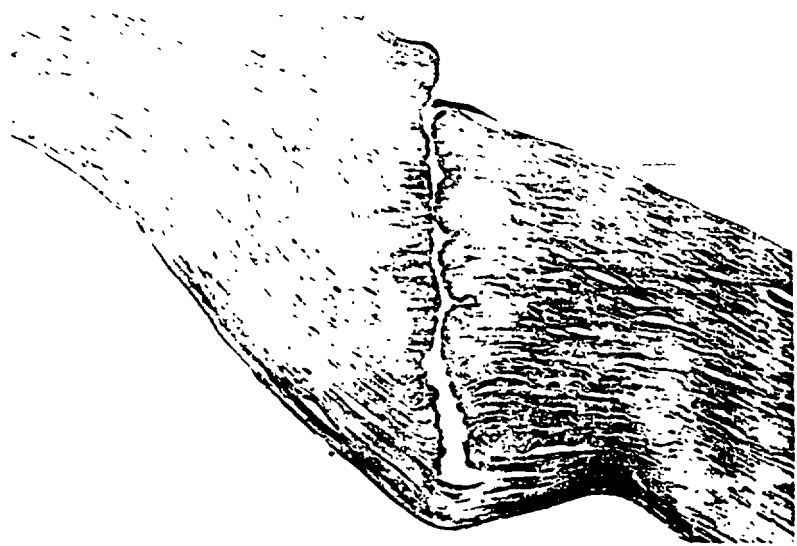


**Fig. 24-10.** Light micrograph of HF laser-trephined cornea in an eye bank eye. There is a 10- $\mu$ m zone of thermal damage along the edges and a 100- $\mu$ m zone of disorganization of the lamellar structure of the stroma. The endothelium is present. The epithelium was removed before irradiation (Hematoxylin and eosin.) (From Loertscher H and others: Am J Ophthalmol 104 471-475, 1987. Published with permission from The American Journal of Ophthalmology. Copyright by The Ophthalmic Publishing Company.)

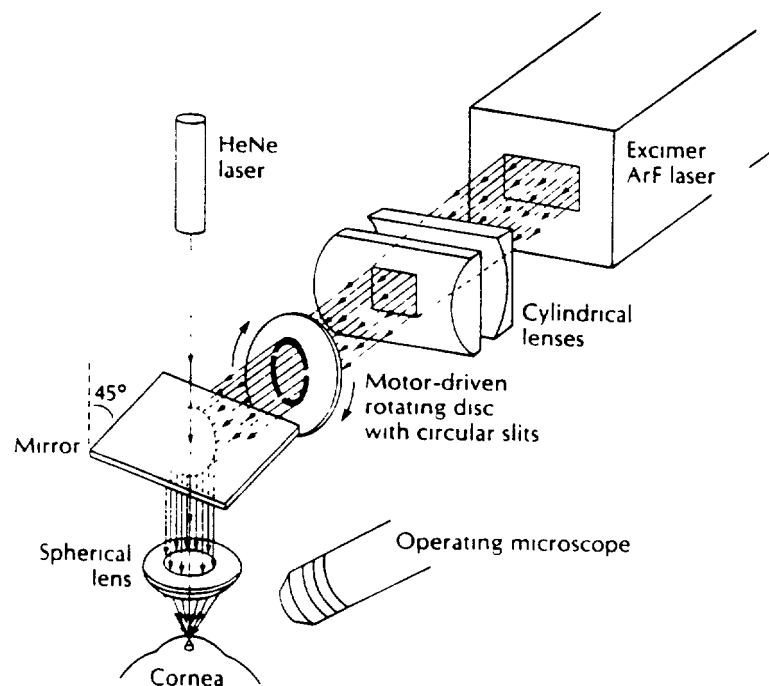


**Fig. 24-11.** Schematic diagram of the rotating-slit delivery system for ArF excimer laser corneal trephination. (From Serdarevic ON and others. Published courtesy of Ophthalmology, [1988; 95 493-505].)

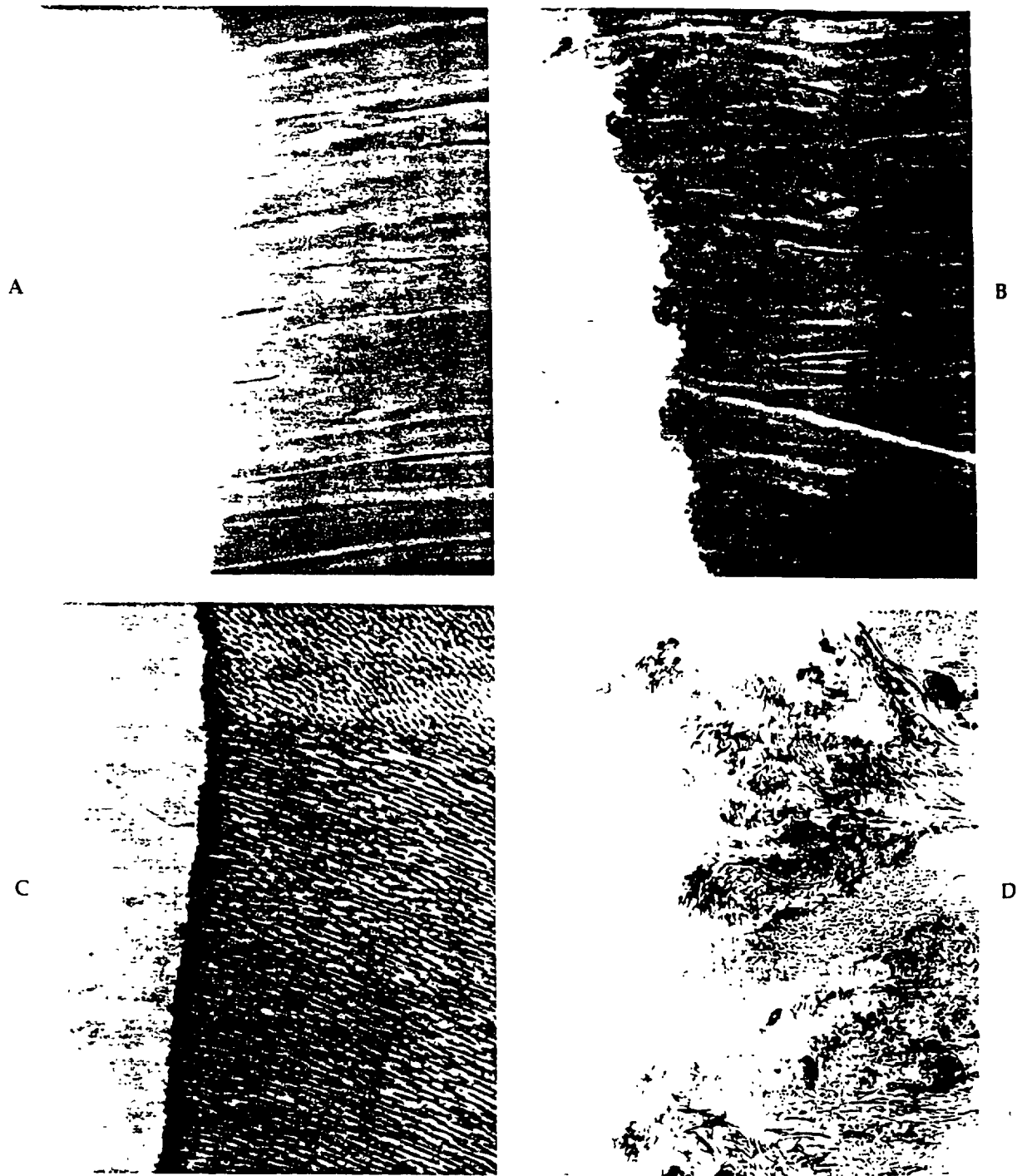


**Fig. 24-12.** Light micrographs of the corneal stromal edge in human eye bank eyes after trephination with an ArF excimer laser (A) and a Hanna suction trephine (B). Note the more regularly cut edge obtained with the laser. (Toluidine blue; original magnification,  $\times 40$ .) C, Transmission electron micrograph of human corneal stroma after ArF excimer laser trephination. The normal structure of stromal collagen is preserved. ( $\times 18,800$ .) D, Transmission electron micrograph of human corneal stroma after manual trephination. There is significant disruption of stromal lamellae ( $\times 12,100$ .) (From Serdarevic ON and others. Published courtesy of Ophthalmology [1988 95:493-505].)

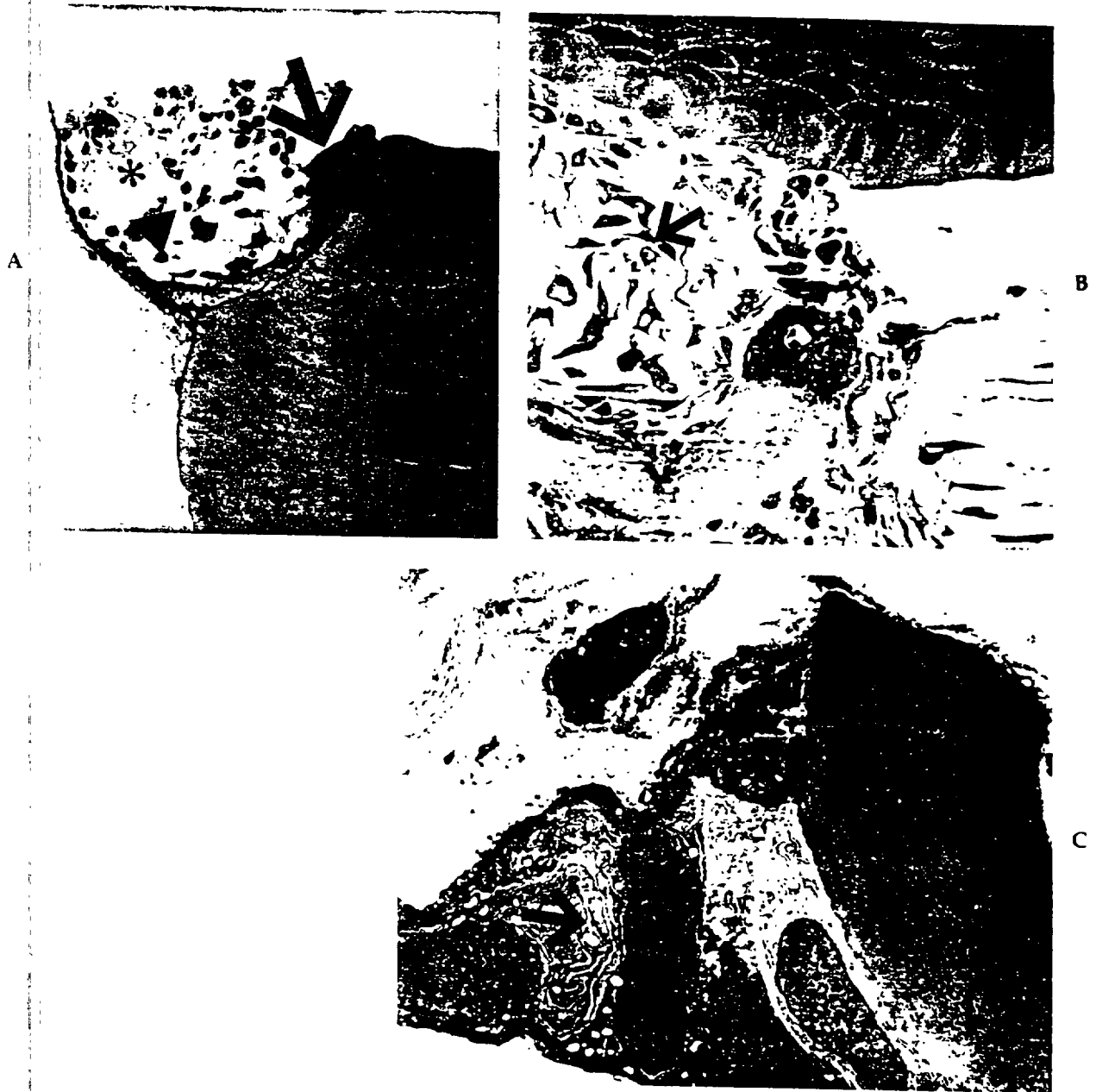


**Fig. 24-13.** Representative micrographs of rabbit corneas after trephination with the excimer laser and resuturing of the circular keratectomy. **A**, Light micrograph of the anterior portion of the wound 6 hours postoperatively showing epithelium (*arrow*) that is starting to slide over the wound edge. Fibrin (*asterisk*) and inflammatory cells (*arrowhead*) are seen at the wound margin. (Toluidine blue; original magnification,  $\times 40$ .) **B**, Light micrograph showing that epithelium (*E*) covers the wound 5 days postoperatively. There is marked cellular proliferation in the wound site. Active fibroblasts (*arrow*) are haphazardly arranged and are producing new collagen. (Toluidine blue; original magnification,  $\times 40$ .) **C**, Transmission electron micrograph of the posterior aspect of a wound that has been reendothelialized 5 days postoperatively. Abundant rough endoplasmic reticulum (*arrow*) is seen in the active endothelium that is synthesizing new Descemet's membrane. (Original magnification,  $\times 4780$ .) (From Sordano et al., and others. Published courtesy of Ophthalmology [1988; 95:493-505].)

*Continued.*



**Fig. 24-13, cont'd.** **D**, Light micrograph showing good scar formation 2 weeks postoperatively with fibroblasts (*arrow*) in the mid-stroma starting to reorient themselves parallel to the corneal surface. (Toluidine blue, original magnification,  $\times 40$ .) **E**, Transmission electron micrograph of multilayered endothelium producing new Descemet's membrane (*DM*) 2 weeks postoperatively. Normal interdigitating lateral cell boundaries (*arrow*), apical junctions (*circle*), and apical folds (*asterisk*) are seen in the posterior endothelial layer (*E*). (Original magnification,  $\times 6800$ .) **F**, Light micrograph of anterior stroma 2 months postoperatively in which fibroblasts (*arrow*) are oriented parallel to the corneal surface. There is decreased cellularity, and the fibroblasts are flatter, resembling keratocytes. (Toluidine blue, original magnification,  $\times 40$ .) **G**, Transmission electron micrograph showing hemidesmosomes (*circle*) and almost complete basal lamina (*arrow*) 3 months postoperatively. (Original magnification,  $\times 30,700$ .)



Fig. 24-13, cont'd. For legend see opposite page.  
Continued





Fig. 24-13, cont'd. H, Light micrograph of posterior cornea 3 months postoperatively showing small cellular infiltrate (*arrow*) anterior to Descemet's membrane (*D*), which has increased to almost normal thickness. (Toluidine blue; original magnification,  $\times 40$ .)

It is not clear at the present time which delivery approach would be optimal. Both delivery systems that have been developed could be used with the same type of laser and allow for almost simultaneous 360° corneal irradiation. A system that could rotate a single point source 360° would not be feasible, because exposure time would be too prolonged and corneal topography would be altered by incising one portion of the cornea before another. Both existing delivery systems, nevertheless, require technical refinements. A device to achieve micron stabilization of the eye or an optical tracking system to allow the laser to follow ocular movements would increase trephination accuracy with thinner, more uniform incision widths and shorter exposure times. Improving the homogeneity of the laser beam and removing lens irregularities would further increase the uniformity of trephination depth.

The advantages of using a far-ultraviolet laser versus a mid-infrared laser for corneal trephination in penetrating keratoplasty are still theoretic. A possible advantage of the HF laser is its faster trephination rate. Even with increases in the repetition rate that could decrease exposure time for ArF excimer laser trephination and still allow for excellent-quality cutting, the speed of excimer laser trephination would be slower than that of HF laser trephination. If an effective ocular stabilization device or optical tracking system were to be developed, this exposure time differential might prove to be insignificant. Some researchers have voiced concerns that the smoothness of the ArF excimer laser incisions might lead to latency in the early phases of wound healing and that the condensed material at the irradiated wound edge might impede diffusion of chemical markers and inflammatory cells,<sup>10,11</sup> but morphologic studies of wound healing after

ArF excimer laser corneal cutting did not demonstrate any adverse alteration of wound healing processes.<sup>108,119</sup> In addition, preliminary animal studies did not show statistically significant differences in the strength of wounds 3 weeks after incisions with a metal blade, the HF laser, and the ArF excimer laser.<sup>3</sup>

Of all laser and mechanical systems evaluated to date, the ArF excimer laser creates the most precise and regular trephined edges, the thinnest incisions, the least distortion of corneal tissue, and the least endothelial cell damage; this fact suggests that it should be the laser of choice for corneal trephination.

Decreased donor-recipient size and shape mismatch with the resulting improved donor-recipient wound approximation should aid the corneal surgeon in obtaining better postkeratoplasty visual results, but trephination imprecision, although a major factor, is not the only one causing postkeratoplasty astigmatism. Recipient corneal disease affecting curvature, thickness, and elasticity is another important factor. Advances in corneal imaging and modeling systems now offer the possibility for real-time analytic evaluation of corneal structure<sup>37,49</sup> (Fig. 24-14). Technologic developments using holographic interferometry enable calculation of stress lines within the cornea.<sup>1,109</sup> High-precision analysis of recipient corneal parameters would facilitate intraoperative determination of the ideal donor button shape and size to correct for preexisting astigmatism. A distinct advantage of laser versus mechanical trephination would be in allowing for precise, noncircular trephination of any shape to match these desired parameters.

If the objective of intraoperative correction of astigmatism were to be realized, the problems of suture-induced astigmatism and irregular wound healing also would need to be addressed. Pharmacologic agents, such as growth factors, are being investigated for their ability to accelerate wound healing processes and to allow for earlier suture removal and less wound healing variability.<sup>71,45,93,127</sup> Ideally, such pharmacologic agents would be combined with a corneal adhesive that would obviate the need for sutures and eliminate suture placement and tightening errors.

## Lamellar Keratectomy and Keratoplasty

Lamellar keratectomy and keratoplasty are performed for optical, therapeutic, and tectonic purposes. Optical indications for lamellar surgical techniques include central opacification and surface irregularities resulting from anterior corneal dystrophies, Salzmann's nodular degeneration, spheroid degeneration, band keratopathy, posttraumatic scars, and postinfectious leukomas.<sup>2,20,28,42</sup> Therapeutic lamellar keratectomy with or without a lamellar graft is useful in the management of pterygium, squamous cell carcinoma, epithelioma, and Mooren's ulcer.<sup>2,20,28</sup> In fungal keratitis unresponsive to medical therapy, lamellar keratectomy can be helpful as a debulking procedure to remove fungal plaques or infiltrates and allows for deeper penetration of topical antimycotic medications.<sup>67</sup> Lamellar keratoplasty usually is contraindicated in corneal infections, since the extent of corneal involvement is difficult to ascertain and a lamellar graft could prevent adequate penetration of topical antimicrobial therapy for eradication of underlying residual organisms.<sup>67</sup> Tectonic lamellar grafts are used to repair areas of corneal thinning or peripheral corneal perforations.<sup>2,20,28</sup>

Lamellar keratoplasty has been used with decreasing frequency over the past few decades, since meticulous stromal dissection is required to prevent irregularities and scarring.<sup>2,20,28,42</sup> Even when corneal disease does not involve the

endothelium, penetrating keratoplasty often is performed instead of lamellar keratoplasty, because many surgeons attain better visual results with the former procedure.<sup>18,20,28-32</sup> Lamellar keratectomy and keratoplasty generally are performed using traditional techniques consisting of mechanical trephination and stromal lamellar dissection with a blade or spatula. Control of dissection can be challenging in heavily scarred, necrotic, or vascularized corneas. In skilled hands, an electromechanical microkeratome allows for a smoother, more regular keratectomy surface.<sup>31,32</sup> However, loss of suction or imperfect positioning of the microkeratome or perilimbal suction ring results in an irregular keratectomy and possible corneal perforation. Moreover, the microkeratome follows the irregularity of an astigmatic corneal contour and, in such cases, causes the keratectomy surface to be astigmatic.<sup>32</sup>

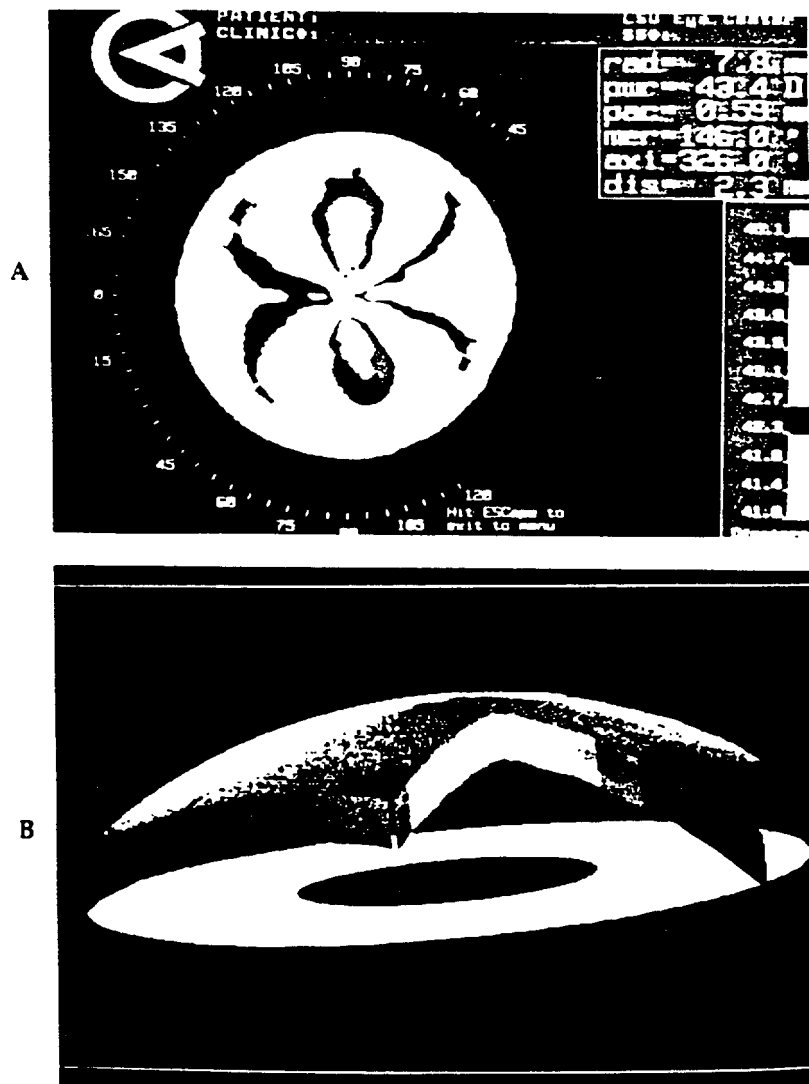


**Fig. 24-14.** A, Dioptric map of a normal cornea from the apex to the limbus. B, Topographic model of a normal cornea with multiple cross sections to show pachymetry. (From Gormley DJ and others. Corneal modeling. *Cornea* 7(1):30, 1988.)

### Experimental Studies

In 1984 my associates and I<sup>107</sup> were the first to apply the ArF excimer laser for therapeutic lamellar keratectomy. We chose an experimental fungal keratitis model to evaluate the potential of the excimer laser for creating a precise, controlled lamellar keratectomy in an inflamed, necrotic cornea. Rabbit corneas with *Candida albicans* fungal lesions 2 to 5 mm in diameter were irradiated with the excimer laser at energy densities varying from 300 to 330 mJ/cm<sup>2</sup>. Both ArF and KrF laser outputs were evaluated at pulse rates of 10 and 20 Hz, respectively. The laser beam was focused through circular slits and masks, and the exposure time ranged from 30 to 90 sec, depending on the depth (between one half to nearly the full thickness of the cornea) required to remove all clinically visible infiltration (Fig. 24-15). The ArF excimer laser treatment achieved sterilization on culture examination and histopathologically in all corneas, whereas the KrF excimer laser treatment was not successful in eradicating infection compared with untreated controls. The ArF excimer laser was effective, probably because infected tissue was removed totally by photochemical ablation. The precise lamellar keratectomy obtained with the ArF excimer laser was shown to heal with minimal scarring that became less visible with time, so that the cornea was almost completely clear after 4 months (Fig. 24-16).

The fact that the cornea healed without surface irregularities and with almost no scarring after ArF excimer laser deep lamellar keratectomy for fungal keratitis led to intensive investigation of this unique lamellar procedure.\* Ultrastructural studies in eye bank eyes confirmed the smoothness of the ArF excimer laser keratectomy beds that had perturbations of less than 1  $\mu$ m as compared with the rough undulations greater than 10  $\mu$ m observed in the uneven and distorted

\*References 10, 19, 25, 30, 34, 38-40, 48, 55, 56, 56a, 56b, 65, 68, 74, 75, 79, 86, 90, 124, 129.

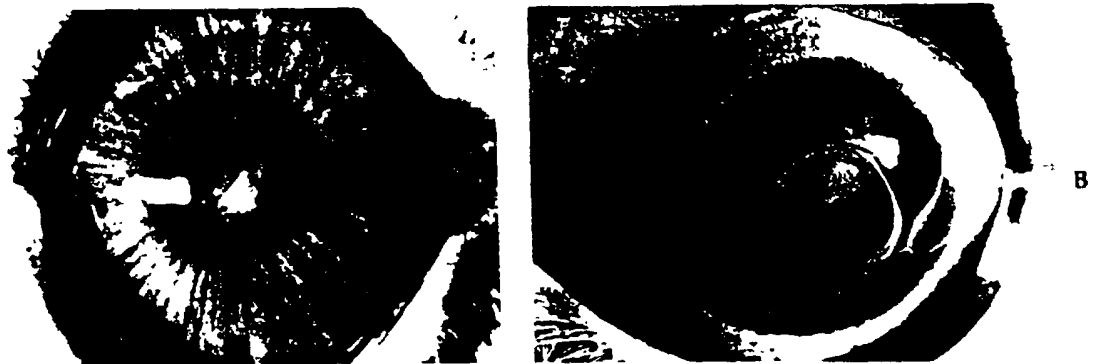


**Fig. 24-15.** A, *Candida albicans* keratitis 2 days after inoculation. B, Cornea immediately after treatment with an ArF excimer laser. (From Serdarevic ON and others: Am J Ophthalmol 99:534-538, 1985. Published with permission from The American Journal of Ophthalmology. Copyright by The Ophthalmic Publishing Company.)

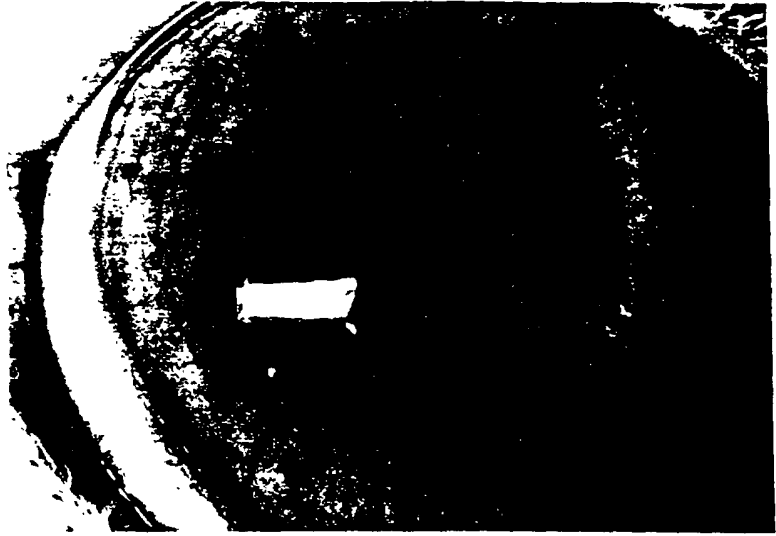


Fig. 24-16. Rabbit cornea that is almost transparent 4 months after treatment with an ArF excimer laser for fungal keratitis. (From Serdarevic ON and others: *Am J Ophthalmol* 99:534-538, 1985. Published with permission from The American Journal of Ophthalmology Copyright by The Ophthalmic Publishing Company.)

keratectomy beds obtained by freehand dissection.<sup>48</sup> No significant endothelial damage occurred when corneal ablations were performed more than 40  $\mu\text{m}$  away from Descemet's membrane.<sup>68</sup> Wound-healing studies in nonhuman primates demonstrated that, despite the ablation of Bowman's membrane, smooth epithelial resurfacing of the keratectomy bed occurred with the production of normal-appearing epithelial attachment complexes.<sup>69</sup> There was minimal alteration of the anterior cornea stroma at low fluences; superficial stromal vacuoles containing remnants of degenerating collagen fibers were observed within and between lamellae extending 10 to 15  $\mu\text{m}$  beneath the basal membrane of epithelial cells in the keratectomy beds. Stromal reorganization and eventual disappearance of the vacuoles were noted during the healing process. The corneas were clear on slit lamp examination, and the anterior stroma was well structured microscopically at 8 months following keratectomy.<sup>68</sup> The degree of corneal scarring has been noted to be related to the uniformity of energy distribution in the treatment beam.<sup>65, 124</sup>

### Clinical Studies

Successful ArF excimer laser clinical treatment of corneal ulcers in France was reported in 1987, but published data are not yet available. Seiler has used the ArF excimer laser in Germany to smooth the corneal surface after pterygium excision by irradiating through an appropriate-size slit in a polymethylmethacrylate mask that was held in place over the eye by a suction ring. A thin layer of viscous fluid was applied to fill the corneal "valleys" and allow the laser beam to ablate progressively the corneal "peaks" to the level of the liquid until a smooth surface was obtained.<sup>10</sup>

### Future Directions

On the basis of studies to date, it seems feasible to use the ArF excimer laser for lamellar keratectomy for all the indications for which conventional surgical keratectomy is performed presently. Nevertheless, this laser's exact clinical role remains to be determined. Better and more predictable visual results would expand the application of lamellar keratoplasty in cases of anterior corneal disease where penetrating keratoplasty is performed currently, so that the higher rejection rate of penetrating graft and the complications of intraocular surgery could be avoided. The corneal clarity and lack of surface irregularities achieved with ArF excimer laser keratectomy suggest the possibility of performing only a keratectomy in cases where, with conventional techniques, both a lamellar keratectomy and graft are necessary in order to retain Bowman's membrane. If a lamellar graft were needed because of structural weakening of the cornea, it could be prepared with the ArF excimer laser. The tremendous advantage of preparing either the lamellar keratectomy bed or lamellar graft with the ArF excimer laser is that this laser not only could produce a very precisely controlled, smooth surface, but also could sculpt the cornea to directly change the corneal contour and correct refractive errors. The potential of performing nonuniform lamellar keratectomies for refractive indications has engendered enormous interest; therefore most recent experimental and clinical studies of ArF excimer laser large-area corneal ablation have been undertaken with the nonuniform rather than the uniform lamellar keratectomy model.

### Nonuniform Lamellar Refractive Keratectomy and Keratoplasty

Although lamellar refractive surgery has been performed since the 1960s and has been modified with improved results over the past three decades, its clinical indications and acceptance remain limited because of variable visual results, slow visual rehabilitation, corneal complications, or technical difficulty.\* Auto-

\*References 14-16, 53, 98, 99, 111-114, 125, 130

plastic lamellar procedures in which the anterior portion of a patient's cornea is removed, reshaped, and then replaced in the corneal bed include keratomileusis (KM) and planar lamellar retractive keratoplasty (PLRK). Homoplastic lamellar procedures in which a donor cornea is reshaped and either sutured onto the front surface of the patient's deepithelialized or keratectomized cornea or placed intrastromally include KM, PLRK, keratophakia (KF), and epikeratophakia. In alloplastic lamellar keratophakia a synthetic lenticule is placed into an intrastromal pocket or between the patient's excised anterior cornea and keratectomized bed and modifies the cornea's refractive power either by altering the anterior corneal curvature, as in other lamellar procedures, or by increasing the stromal refractive index.

Lamellar retractive surgery generally is indicated only for high myopia, high hyperopia, aphakia, and keratoconus; but, whenever possible, these conditions first are treated nonsurgically with spectacles or contact lenses or, in the case of aphakia, surgically with intraocular lenses. Lamellar retractive procedures require a high degree of accuracy in corneal carving. However, with current cryolathing techniques, the ability to precarve lenticules that result in the desired refraction in KM and KF is still not at the level of contact lenses or intraocular lenses; the accuracy usually is within  $\pm 2$  diopters.<sup>112-125</sup> There is a 1-diopter change in refraction for every 10- $\mu$ m change in thickness. In autoplasmic procedures intraoperative cryolathing can lead to lathing errors of the order of microns that cause greater inaccuracy or possible perforation of the lenticule, necessitating donor tissue. The microkeratome used for lamellar dissection in KM, PLRK, and KF and for preparation of the lenticule in PLRK is less precise than the cryolathe.<sup>111-125</sup> The microkeratome often produces too thin, too thick, or irregular sections, thus contributing to inaccuracy in dioptric power and producing irregular astigmatism and interface scarring.<sup>99, 111-114, 125</sup>

Corneal freezing or lyophilization in KM, KF, and epikeratophakia induces fractures of Bowman's membrane, kills keratocytes, and alters collagen interfibrillar distance and fiber structure<sup>11, 16, 98, 130</sup>; this damage often results in slow visual recovery and corneal complications due to prolonged or incomplete healing. Although PLRK eliminates freeze-induced damage, the accuracy of this technique may not match that of cryolathing,<sup>10, 53, 113</sup> and retention of cellular viability in donor tissue may contribute to rejection. The recent introduction of Moist-Pak storage, rather than lyophilization, of epikeratophakia lenticules allows for retention of stromal glycosaminoglycans, faster repopulation of keratocytes, and less tissue swelling and may lead to faster corneal clearing and fewer epithelial problems.

Alloplastic lamellar procedures avoid the complications associated with donor tissue but are still investigational. Thin thermoplastic materials are easy to implant into an intrastromal pocket but are water impermeable and cause nutritional problems.<sup>72</sup> Thicker hydrogel implants are highly water permeable but require a microkeratome resection for insertion and, because of their compressibility, may result in unpredictable results.<sup>72</sup>

Attachment problems are another source of inaccuracy in lamellar procedures. Suturing is necessary in all these procedures and can lead to twisting and bending of the lenticule or anterior lamella. Direct mechanical reshaping of the corneal surface to avoid problems related to donor and synthetic lenticules and lenticule attachment has been attempted but has not been pursued because of inadequate control of tissue removal with mechanical devices.<sup>7,43</sup>

### Experimental Studies

**Direct nonuniform lamellar refractive keratectomy.** In the course of their studies of uniform lamellar ArF excimer laser keratectomies, Marshall and others<sup>44</sup> noted significant photokeratoscopic changes even after very shallow ablations and suggested correcting refractive errors by varying the energy distribution in the laser beam for precisely controlled removal of a thin layer of corneal tissue on a microtopographic basis.

In 1987 McDonald and others,<sup>45</sup> Hanna and others,<sup>46</sup> and Renard and others<sup>40</sup> were the first to report results of nonuniform lamellar keratectomies performed for myopic correction by two different prototype ArF excimer lasers. Both systems were designed to decrease central corneal curvature and thus to decrease central corneal refractive power by ablating the most tissue centrally and progressively tapering the ablation to zero toward the edge. The amount and shape of tissue ablation required for correction of myopia has been determined on the basis of mathematic analyses<sup>47</sup> (Fig. 24-17).

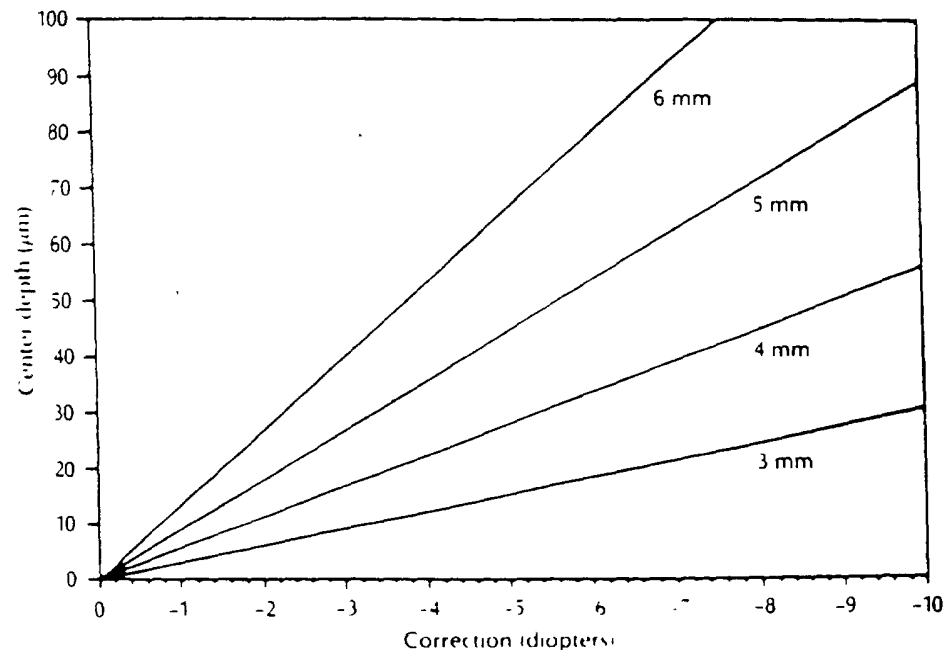


**Fig. 24-17.** Maximum depth of a cut calculated from an equation for myopic correction. Each line represents the depth of the cut on the optical axis for a given-size treatment zone. (From Munnerlyn CR, Koons SJ, and Marshall LF. *Cataract Refract Surg* 14:46, 1988.)



In the delivery system evaluated by McDonald and others<sup>73</sup> the laser beam was shaped by a diaphragm that progressively closed across the cornea based on a computer program to vary energy distribution in time, rather than in the laser beam itself, as suggested by Marshall and others.<sup>74</sup> Initially the diaphragm was controlled manually to create multiple stepped lesions. Better wound healing was noted when smaller steps and less sharp edges were produced, since, as several investigators have observed, irregularities and steep steps at the surface induced epithelial healing in multiple layers of varying thickness and marked subepithelial infiltration.<sup>74-75</sup> As the homogeneity of laser energy distribution was increased and as computer control allowed for increased smoothness and rapidity of diaphragm closing, improved optical clarity and dioptric correction were attained.<sup>73</sup> In the initial nonhuman primate series, there was significant corneal scarring and no significant dioptric change in refraction; but after refinements in the delivery system, all corneas were reported to remain clear postoperatively and significant dioptric corrections were achieved without regression over a 6-month period. McDonald and others<sup>75</sup> have noted, though, that even the scarring observed initially in the early studies cleared with time as the stroma remodeled.

Hanna and others<sup>76-79</sup> developed a rotating-slit delivery system (Fig. 24-18) for nonuniform lamellar keratectomies that could be used for the correction of

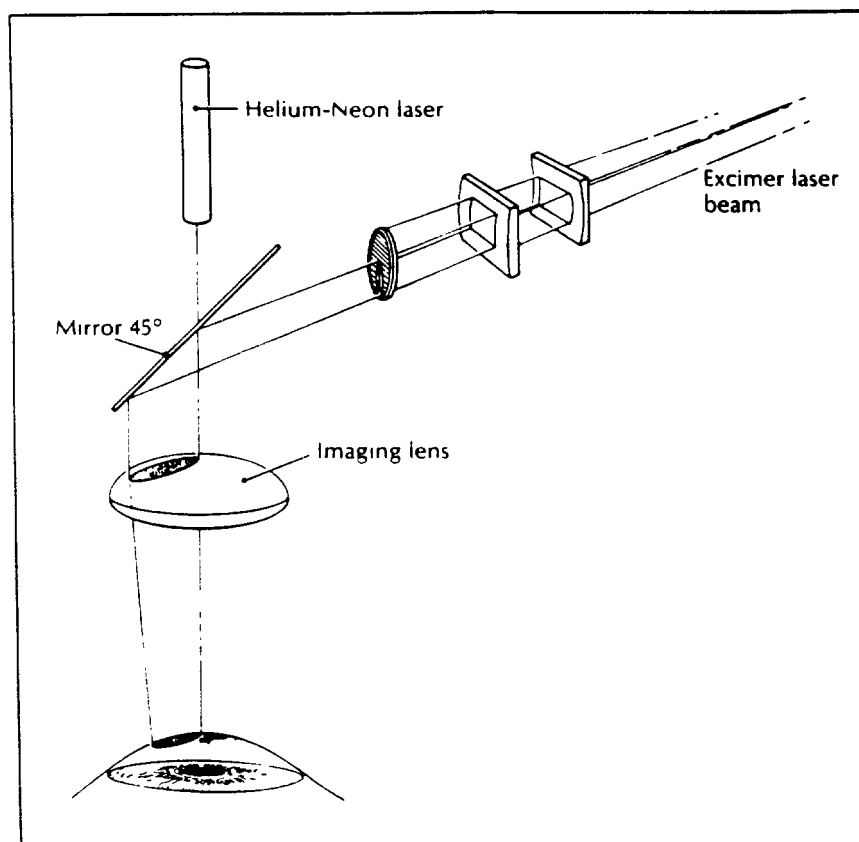


**Fig. 24-18.** Schematic diagram of the rotating-slit delivery system for ArF excimer laser nonuniform lamellar keratectomy for myopic correction. (From Hanna KD and others: Arch Ophthalmol 106:245, 1988. Copyright 1988 American Medical Association.)

myopia, hyperopia, and myopic and hyperopic astigmatism. They attempted to improve surface regularity by avoiding damage, possibly due to shock waves, that can occur when too many laser pulses are delivered at a high repetition rate to the same area too rapidly. The laser beam was shaped by a slit rotating at 0.033 Hz that, because each pulse was of 23-ns duration, was effectively stationary during each pulse but shifted to another area with subsequent pulses, thereby allowing less energy to dissipate from the corneal surface between pulses. The shape of the slit was determined mathematically so that, for myopic correction, the central part of the ablated zone would be deeper than the peripheral part (Fig. 24-19) and, for hyperopic correction, the peripheral part of the ablated zone would be deeper than the central part. The slit was rotated many times to produce a smooth ablation profile with 4.5 mJ per pulse delivered to the cornea at a repetition rate of 20 Hz. The fluence at the cornea was about 200 mJ/cm<sup>2</sup>. Astigmatic correction could be obtained by varying the laser rep-

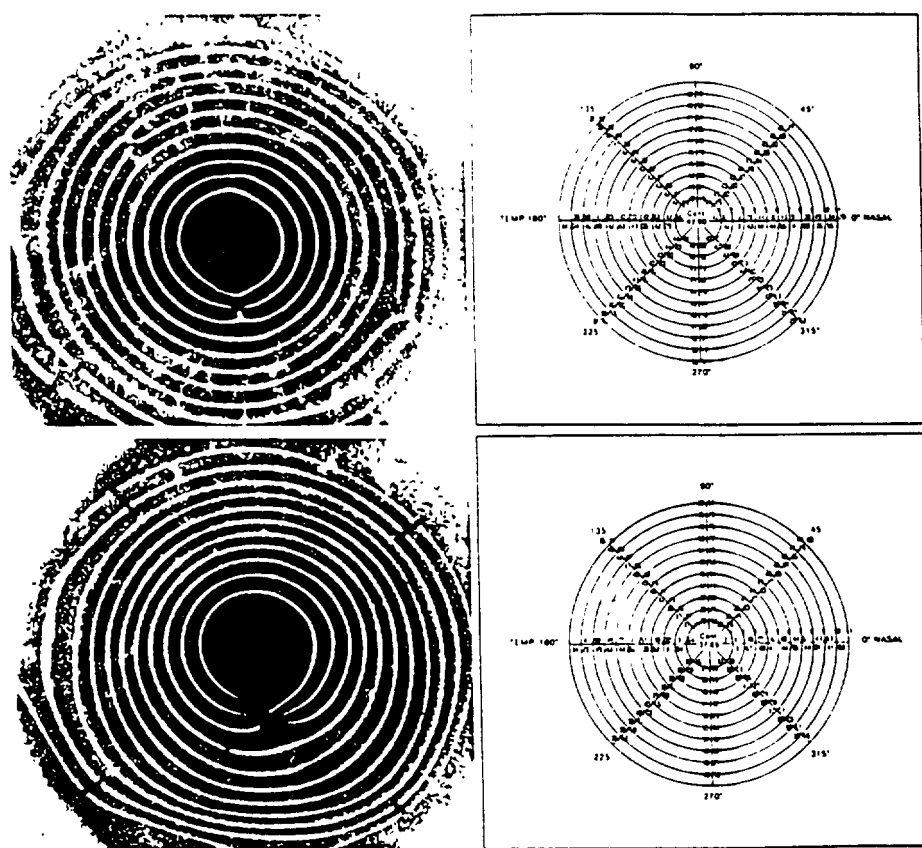


**Fig. 24-19.** Keratographs before and after nonuniform lamellar keratectomy for myopic correction with an ArF excimer laser. *Top left.* Before treatment, central mires are reasonably regular and round. *Top right.* Image analysis of the keratograph before treatment gives the surface power of the cornea, with an average central reading of 42.90 diopters and a gradual decrease of about 10 diopters. *Bottom left.* Keratograph after treatment shows larger-diameter circles centrally because of flatter cornea. Irregularity in rings 1 through 3 inferiorly is surface artifact. *Bottom right.* Image analysis of the keratograph after treatment demonstrates a surface power centrally of 37.85 diopters with general steepening in the outer rings. (From Hanna KD and others. Arch Ophthalmol 106:245, 1988. Copyright 1988, American Medical Association.)

etion rate with the angular position of the slit so that the ablation profile could vary with the meridian. Recent modifications of the system have allowed for computerized calculation and control of ablation.<sup>21</sup>

On light microscopic and ultrastructural examination of human eye bank corneas, Renard and others<sup>22</sup> and Hanna and others<sup>23,24</sup> noted the smoothly sloping surface produced during ablation using the profile for myopic correction (Fig. 24-20). Because epithelial cell nuclei were observed to resist ablation more than the cytoplasm (Fig. 24-21), and because the epithelium required more laser energy than the stroma, the epithelium subsequently was removed routinely before laser treatment. Following laser ablation, most of the rabbit corneas remained clear, but slight scarring became visible on slit lamp examination in a

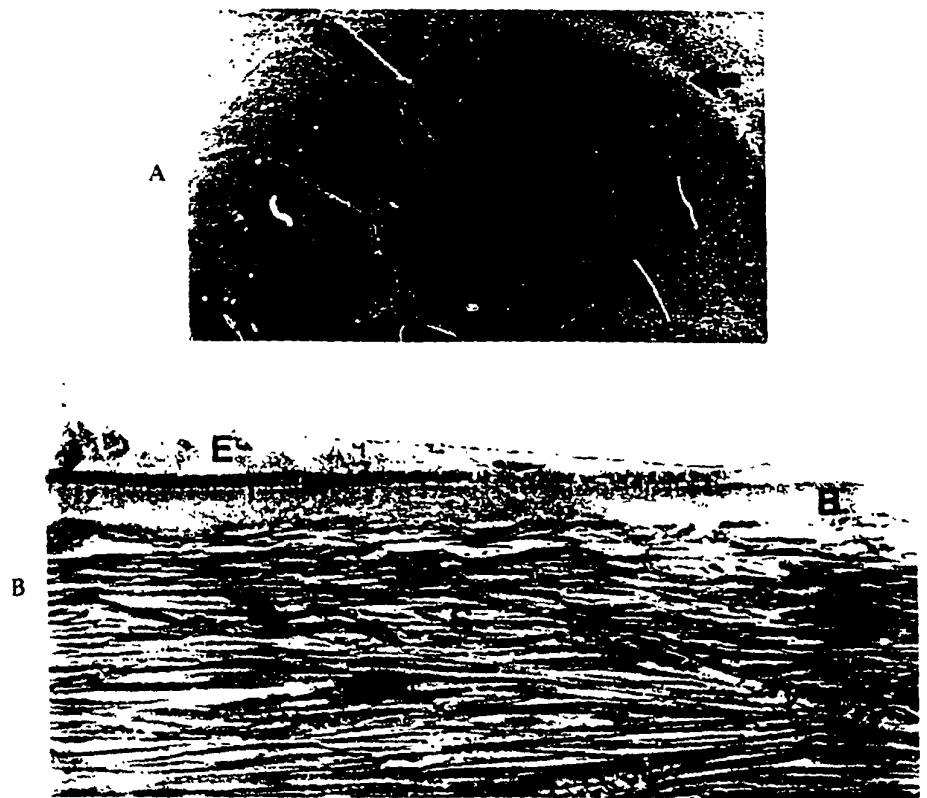


**Fig. 24-20.** A, Scanning electron micrograph of cornea with full-thickness ablation using a profile for myopic correction shows an edge of cut epithelium (upper arrow) and the concave slope surface leading to the central endothelial perforation (lower arrow). (Original magnification,  $\times 20$ .) B, Light micrograph of human cornea after nonuniform lamellar keratectomy for myopic correction, demonstrating the gradually sloping surface that extends from the epithelium (E) through Bowman's membrane (B) down toward the stroma (S). (Toluidine blue; original magnification,  $\times 130$ ). (A from Hanna KD and others: Arch Ophthalmol 106:245, 1988, courtesy Gilles Renard, M.D., Paris, France. Copyright 1988, American Medical Association. B and C courtesy Gilles Renard, M.D., and Michèle Savoldelli, M.S., Paris, France.)



**Fig. 24-20, cont'd. C.** Transmission electron micrograph of ablated human corneal stroma (S). Note the minimal disruption of collagen fibrils. A thin, discontinuous, electron-dense layer is slightly detached from the stroma (arrow). (Original magnification,  $\times 14,500$ .)

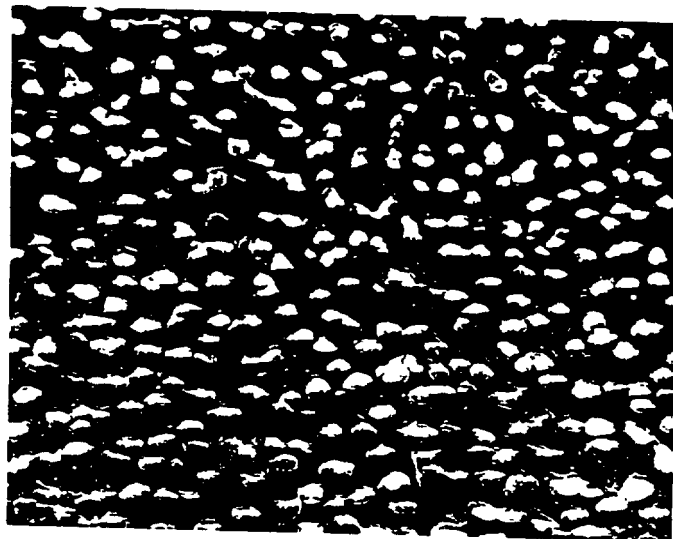


**Fig. 24-21.** Scanning electron micrograph of ArF excimer laser-ablated human corneal epithelium showing the rounded, protuberant appearance of the nuclei that resisted ablation more than the cytoplasm. (Original magnification,  $\times 400$ .) (From Hanna KD and others: Arch Ophthalmol 106:245, 1988; courtesy Gilles Renard, M.D., Paris, France. Copyright 1988, American Medical Association.)

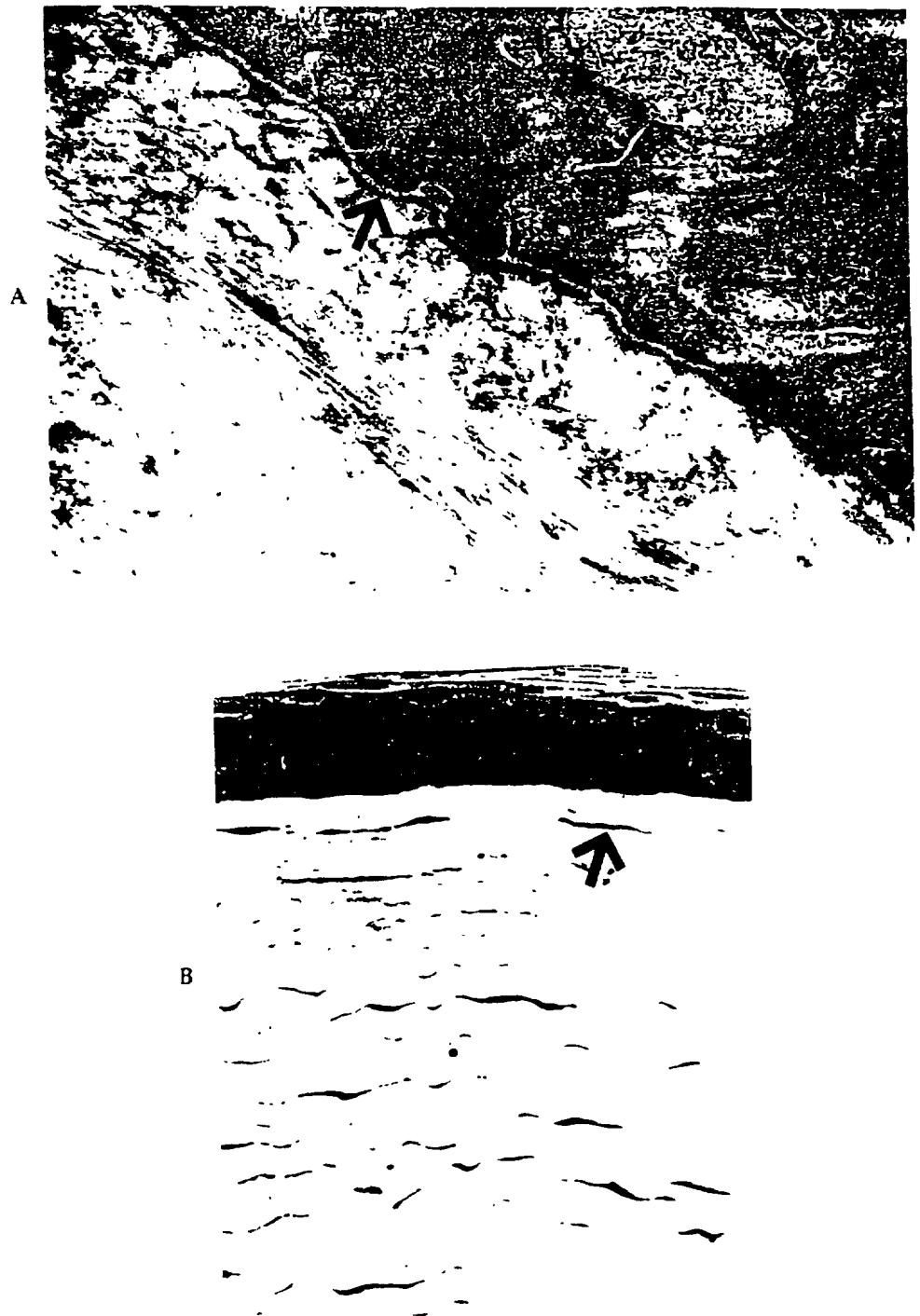


**Fig. 24-22.** A, Transmission electron micrograph of rabbit cornea 3 months after Ar: excimer laser nonuniform lamellar keratectomy for myopic correction, demonstrating normal hemidesmosomes (boxed) and basal lamina (arrow). B, Light micrograph of rabbit cornea that remained clear for 3 months after surface ablation. The epithelium (E) is layered normally. The stromal keratocytes (arrow) are normal in number and appearance. (Toluidine blue; original magnification  $\times 400$ ). Courtesy Yves Pouliquen, M.D., and Michèle Savoldelli, M.S., Paris, France.

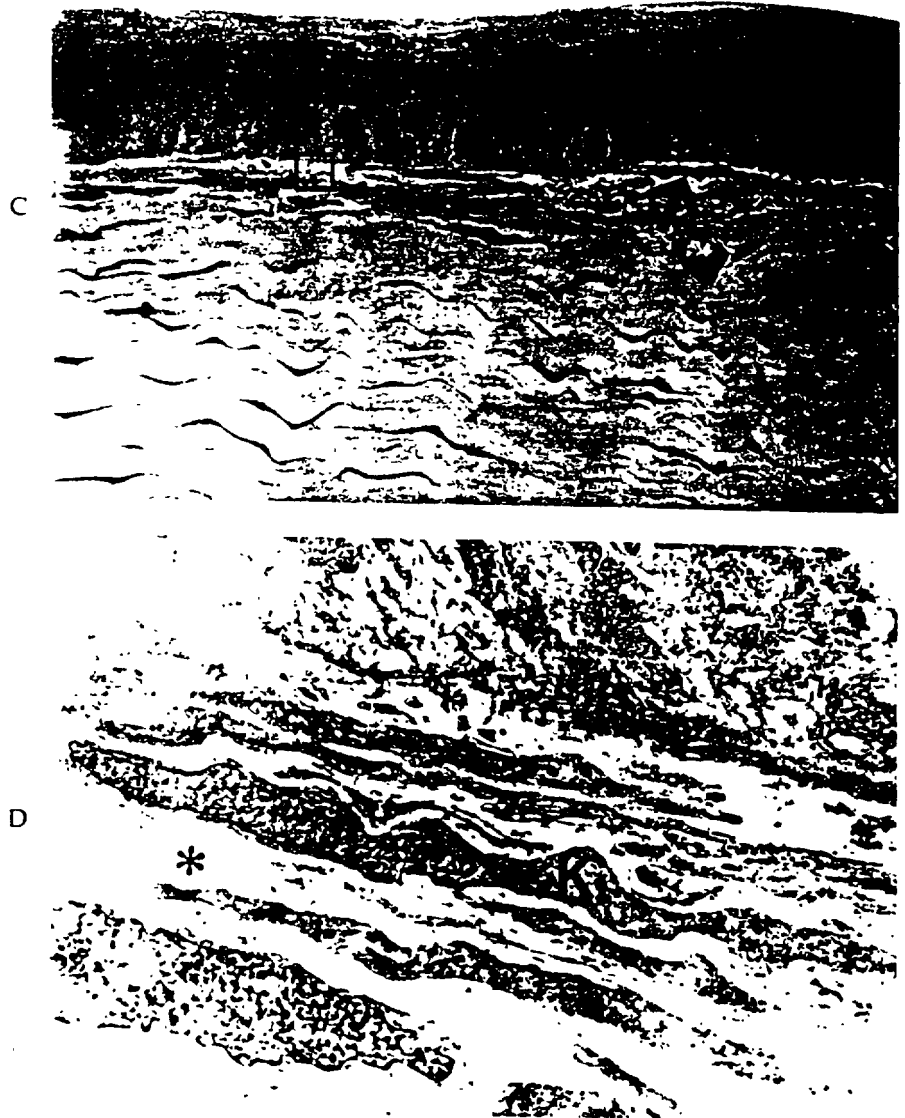


**Fig. 24-22, cont'd.** C, Light micrograph of rabbit cornea that demonstrated some corneal scarring on slit lamp examination 3 months after surface ablation. Note the increased number of keratocytes (*arrow*) and disorganized stromal collagen (*boxed*) (Toluidine blue; original magnification,  $\times 40$ .) D, Transmission electron micrograph of slightly scarred rabbit cornea 3 months postoperatively showing active subepithelial keratocytes (*K*) and disorganized new collagen (*asterisk*)

few cases. Corneas that remained clear demonstrated normal hemidesmosome and basal lamina formation and minimal fibroblastic proliferation and activity<sup>86</sup> (Fig. 24-22, A and B). Although fibroblasts were noted to show signs of activity at all layers of the stroma for 3 months postoperatively, there was no evidence of fibroblast secretory products or new collagen deposition. In the corneas that developed some scarring, however, there was reduplication of basal lamina and fibroblastic activity with new collagen production<sup>87</sup> (Fig. 24-22, C and D).

Short-term endothelial cell alterations, probably due to acoustic or shock waves, have been observed.<sup>86, 129</sup> Poulighen has noted that following laser ablation of the stroma to any depth, endothelial cells developed vacuoles within the first 24 hours that persisted for up to 3 days; endothelial cells also showed signs of activity with early accumulation of electron-dense material in intercellular spaces and at the edge of the endothelial side of Descemet's membrane (Fig. 24-23, A). Although gap and tight junctions appeared intact, this material may have resulted from cytoplasmic exudation following small cellular junction rupture or from hyperactive endothelial cell secretions during the early postoperative period.<sup>87</sup> Poulighen,<sup>86</sup> Burstein,<sup>130</sup> and Gaster and others<sup>14</sup> have observed anterior migration of this material with time (Fig. 24-23, B). The rabbit corneal endothelium is known to be much more reactive than human endothelium; therefore the clinical significance of these findings remains to be determined.

Other ArF excimer laser prototypes for nonuniform lamellar refractive keratectomies have been developed more recently using apertures on a rotating disc for myopic, hyperopic, and astigmatic correction<sup>15, 30, 30a, 30b</sup> and axicon lenses for hyperopic correction.<sup>131</sup>

**Preparation of lenticules for lamellar refractive surgery.** In 1987 Lieurance and others<sup>37</sup> and Hanna and others<sup>38, 40</sup> evaluated the feasibility of using the ArF excimer laser for preparation of lenticules from nontrozen tissue for lamellar refractive surgery.

Lieurance and associates<sup>37</sup> cut epikeratophakia lenticules from human eye bank corneas that had been stored in McCarey-Kautman medium. The convex epithelial surface of the donor cornea was held by capillary attraction against the concave surface of a sintered glass mold that had been shaped to produce a lenticule of the desired dioptric power. The ArF excimer laser was focused along the horizontal base of the mold, which was rotated on a turntable at 5 rpm to ablate all corneal tissue outside the concave surface of the mold. The energy levels were 15 to 30 J/cm<sup>2</sup>, and the exposure time varied from 2.5 to 4 min. The cut surface of the lenticule was smoother on scanning electron microscopic examination than that obtained by cryolathing (Fig. 24-24). Light and transmission electron microscopic examination demonstrated intact epithelium, Bowman's membrane, keratocytes, and stromal collagen (Fig. 24-25). The lenticules that were grafted onto rabbit eyes were clear in the first week after surgery, and there were no epithelial abnormalities or haze at the graft-host interface.

Hanna and associates,<sup>38, 40</sup> in a keratomileusis-like procedure, reshaped with the ArF excimer laser, instead of with the cryolathe, the stromal surface of the anterior portion of a fresh eye bank cornea that had been resected with the microkeratome. The resected disc was placed on a concave suction punch block, and the stromal surface was ablated more centrally than peripherally, in a myopic profile, by the ArF excimer laser beam, which was shaped by a rotating slit as already described. The energy parameters were the same as those used for direct

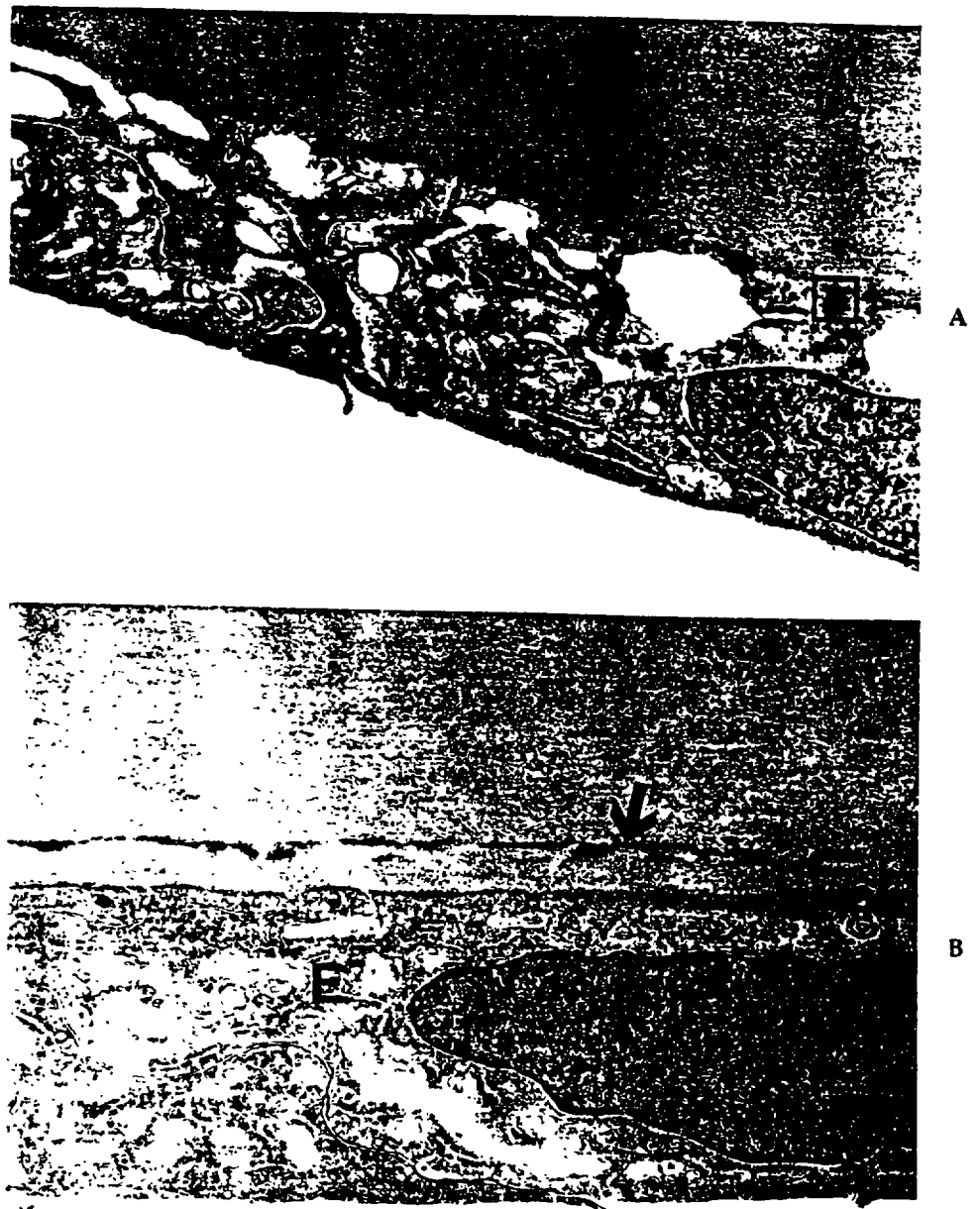


**Fig. 24-23.** A, Transmission electron micrograph of active endothelium beneath an area of rabbit cornea that had undergone ArF excimer laser nonuniform lamellar keratectomy 24 hours earlier. The rough endoplasmic reticulum is dilated (*arrow*). There is an accumulation of electron-dense material (*boxed*) at the edge of Descemet's membrane. B, Transmission electron micrograph of normal-appearing endothelium (*E*) 7 days post-operatively. Note the electron-dense material (*arrow*) that has migrated anteriorly through Descemet's membrane. (Courtesy Yves Pouliquen, M.D., and Michele Savoldelli, M.S., Paris, France.)



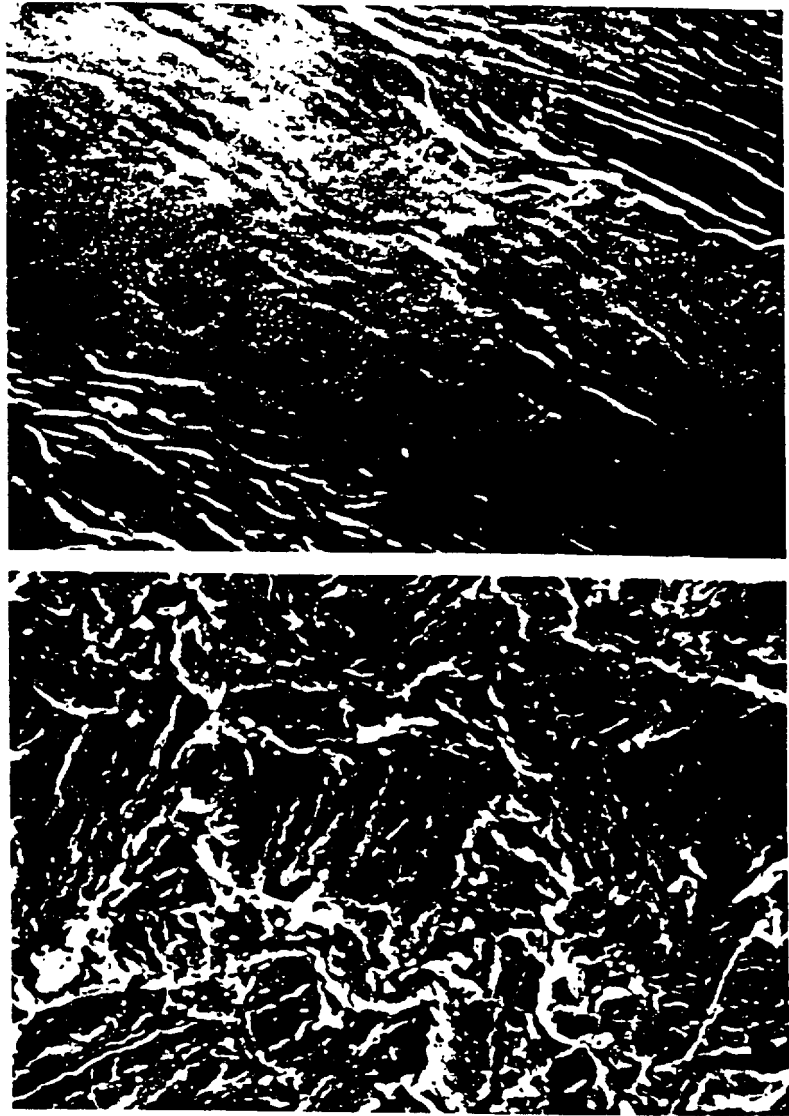


**Fig. 24-24.** Scanning electron micrographs of human epikeratophakia lenticles obtained by ArF excimer laser (*top*) and cryolathing (*bottom*). The posterior surface of the laser-cut lenticule is much smoother. ( $\times 80,000$ ) (From Lieurance RC and others: *Am J Ophthalmol* 103:475-476, 1987; courtesy David Schanzlin, M.D., St. Louis, Mo. Published with permission from The American Journal of Ophthalmology. Copyright by The Ophthalmic Publishing Company.)

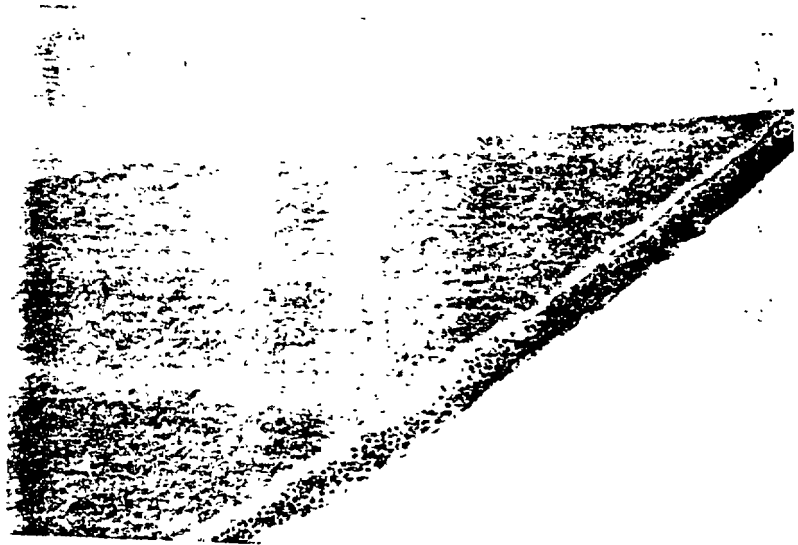
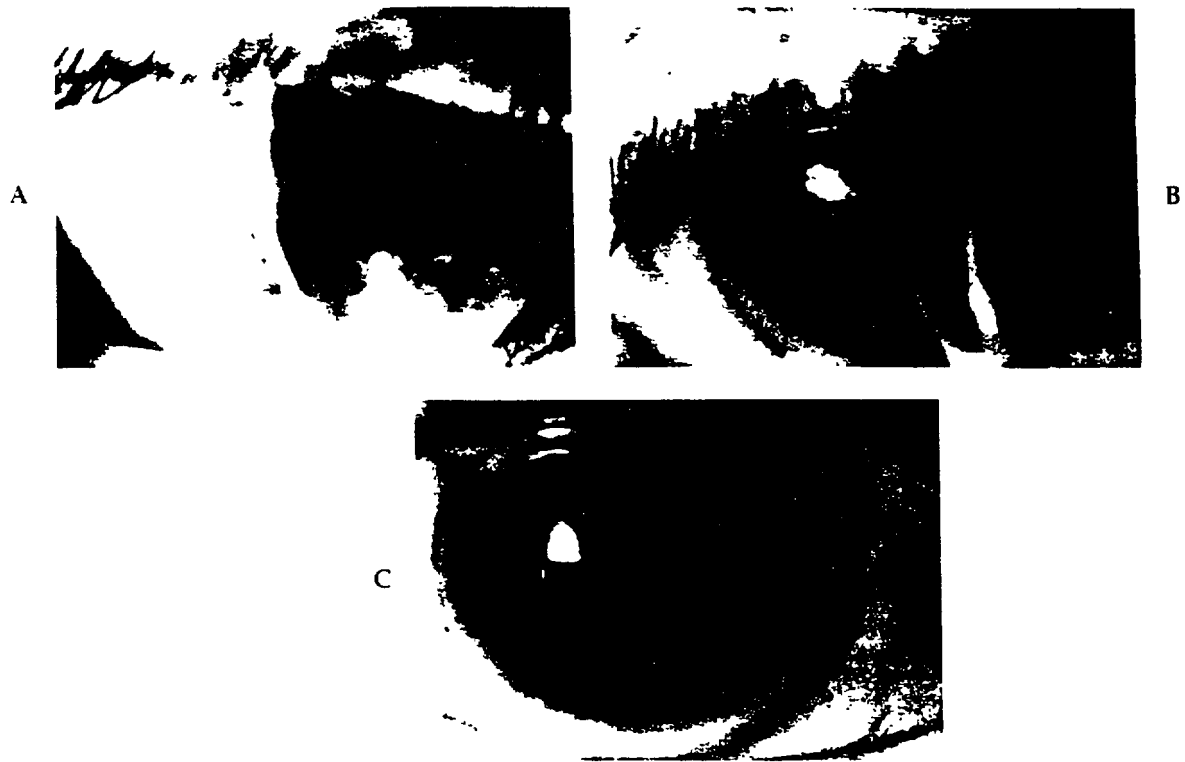


Fig. 24-25. Light micrograph of an ArF excimer laser-cut human, high-powered lenticule. The epithelium and Bowman's membrane are intact. The cut stromal edge is smooth and minimally disturbed. (Hematoxylin and eosin:  $\times 24$ .) (From Lieurance RC and others: *Am J Ophthalmol* 103:475-476, 1987; courtesy David Schanzlin, M.D., St. Louis, Mo. Published with permission from The American Journal of Ophthalmology. Copyright by The Ophthalmic Publishing Company.)

myopic laser lamellar keratectomy. The exposure time was 5 min. The sloping stromal edge had a smooth, regular appearance similar to that obtained in the direct surface ablation.

#### Clinical Studies

L'Esperance and associates<sup>25, 26, 27</sup> were the first to perform uniform and nonuniform lamellar retractive keratectomy (or *photokeratoglyphery*, as they have termed the procedure) in human eyes scheduled for enucleation. Central corneal flattening was achieved in eyes that were lasered for myopic correction to depths ranging from 40 to 130  $\mu\text{m}$ . The corneas were clear immediately postoperatively, but a slight fibrillar haze that sometimes decreased with time was noted to develop at 4 to 6 weeks postoperatively (Fig. 24-26). Wound healing was followed for time periods varying from a few days to 12 months, but in all cases, normal epithelial resurfacing was observed. Histologic and ultrastructural studies by Del Pero and others<sup>28</sup> demonstrated normal hemidesmosome and basal lamina formation and subepithelial fibroblast activity with some new collagen production 4 months postoperatively (Fig. 24-27).



**Fig. 24-26.** A, Slit lamp photograph of the *seventh* human eye to be treated with the ArF excimer laser before nonuniform lamellar keratectomy for myopic correction. B, Slit lamp photograph 4 months postoperatively demonstrating central corneal flattening. C, Four months postoperatively, the cornea appears clear with direct illumination. Slight subepithelial fibrillar haze is visible only on slit beam examination. (Copyright © Taunton Technologies, Inc., courtesy Daniel M. Taylor, M.D., New Britain, Conn.)

### Future Directions

The ArF excimer laser holds great promise for bringing about important advancements in refractive surgery. Results to date suggest that direct nonuniform lamellar refractive surgery with the ArF excimer laser may prove to be clinically effective. This procedure appears to allow for optical clarity and good wound healing without Bowman's membrane, if the laser-ablated surface is smooth enough, without sharp edges, and with a gradual enough change in curvature. However, further study of the interactions between the tear film, corneal epithelium, and keratocytes during wound healing after surface ablation is necessary. If refinements in the optical system were to be insufficient for reproducibly preventing all but an optically insignificant amount of subepithelial keratocyte response and fibrosis, as well as of epithelial hyperplasia, pharmacologic agents to modify wound healing would need to be investigated. Collagen shields that have been found to accelerate epithelial wound healing with concomitant decreased stromal edema and decreased fibroblastic reaction after diamond knife incisions<sup>1</sup> may be a first step in this approach. Fibronectin and growth factors

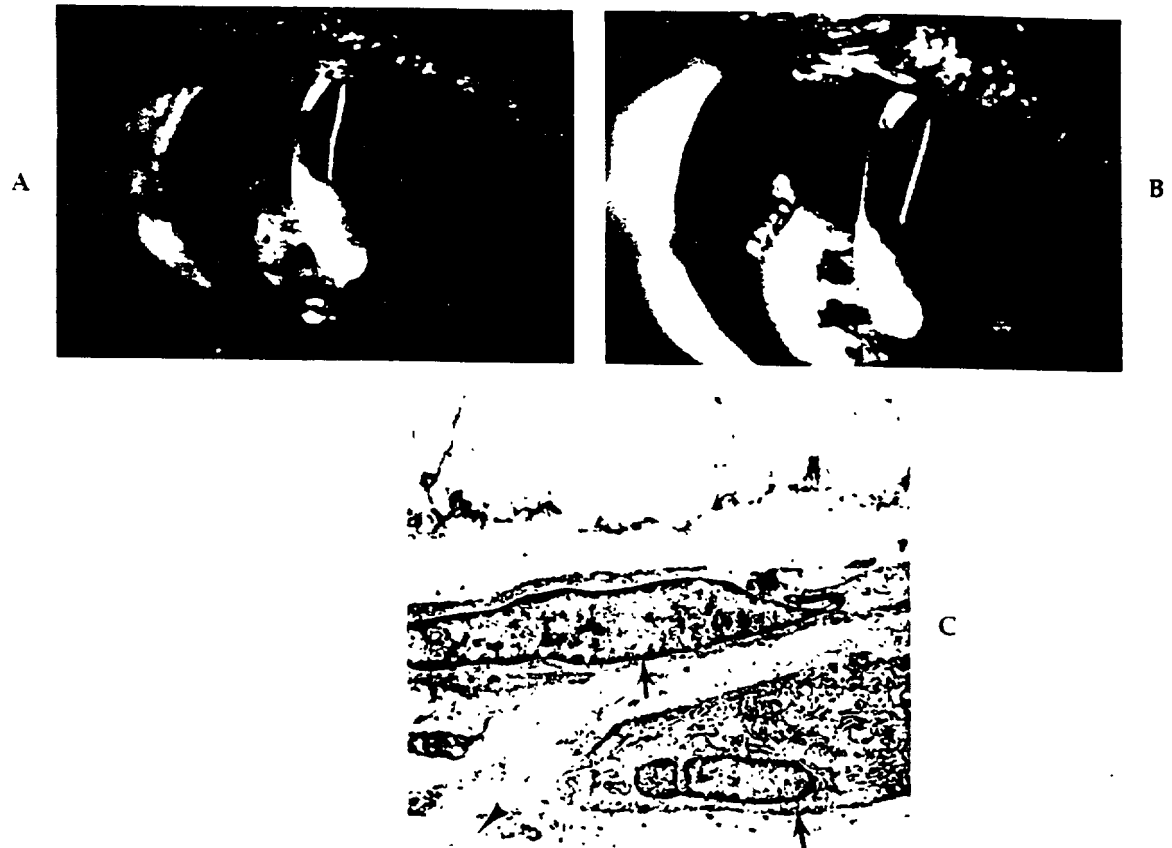


**Fig. 24-27.** A, Preoperative slit lamp photograph of a human eye with corneal leukoma. B, Slit lamp photograph showing corneal flattening 4 weeks after ArF excimer laser nonuniform lamellar keratectomy performed superior to the leukoma. There is a trace fibrillar haze at the epithelial-stromal interface. C, Transmission electron micrograph of the cornea with slight haze 4 months postoperatively. Note the active subepithelial keratocytes (arrows) and disorganized collagen (arrowhead). (Copyright © Taunton Technologies, Inc.; A and B also courtesy Daniel M. Taylor, M.D., New Britain, Conn.)

that would accelerate epithelial resurfacing and thereby decrease the exposure of keratocytes to inflammatory stimuli in the tear film also may be beneficial in decreasing subepithelial scarring if the degree to which these agents themselves would activate keratocytes proves to be minimal. The effect of antiinflammatory agents also remains to be determined.

Technical refinements are necessary to improve the uniformity of laser energy ablation. According to Munnerlyn and others,<sup>20</sup> there are three primary laser beam characteristics that should be considered: the total beam energy, the accuracy of the beam profile, and the level of high-frequency spatial irregularity. Munnerlyn and others<sup>21</sup> suggested that approaches to enhance ablation uniformity include spatially averaging by rotating the laser beam between pulses and decreasing the repetition rate. The optimal fluence for refractive surgery is still not known. Recent work has shown that surface smoothness can be improved by increasing the fluence above currently employed levels.<sup>20</sup>

If the patient is to benefit from the ArF excimer laser's cutting precision of  $0.1\text{ }\mu\text{m}$ , a better laser-eye coupling system, such as optical tracking, would need to be used rather than the currently employed suction ring.

Although advanced corneal imaging and modeling systems that integrate photokeratoscopy and slit lamp image analysis could be used in laser procedures such as trephination, modifications in these systems or alternative methods of intraoperative, real-time corneal structure measurement and analysis would be necessary for direct laser lamellar procedures because of strong light scattering from the laser-ablated surface. Gormley<sup>36</sup> has suggested placing viscoelastic fluid over the ablated surface to reduce light scattering. This modification would allow postkeratectomy measurement but would not permit real-time evaluation during ablation. The success of direct laser ablation for refractive purposes would be contingent on accurate calculation of refractive results after wound healing. Therefore advances in computer corneal modeling, as proposed by McCarey and Hanna,<sup>37</sup> would be required for determination of surgical results by pre-operative surgical simulation.

If these requirements were to be realized, safe, precise, predictable, and reliable laser correction of an extended range of refractive errors would be possible. Although preliminary results of studies in nonhuman primates using a very homogeneous beam have shown stability of dioptric correction up to 6 months postoperatively,<sup>38</sup> further studies are necessary to verify long-term stability. However, even then, some patients with too-thin corneas, as in keratoconus, would be unable to profit from the direct nonuniform lamellar refractive keratectomy technique. In these cases, until a time when synthetic epikeratophakic lenticles that could be attached with an adhesive would be available, the ArF excimer laser could be used for more precise preparation of donor lenticles.

### Refractive Keratotomy and Keratectomy (Noncentral Incisional and Excisional Techniques)

Refractive keratotomy and keratectomy procedures that are performed in the midperipheral and peripheral cornea have been designed to correct myopia, hyperopia, or astigmatism by alteration of the central corneal curvature. These techniques consist of various patterns, numbers, lengths, and depths of radial, parallel, transverse, and arcuate incisions and excisions. Sutures sometimes are used to compensate for or to enhance the effects of corneal relaxing incisions or to approximate wound edges after corneal excision. Radial keratotomy for the correction of mild and moderate myopia is the most frequently performed refractive procedure. Depending on the amount of correction desired, four or more deep radial incisions are made from the edge of the optical zone, which is between 3 and 4.5 mm in diameter, to the limbus. The radial incisions cause the midperipheral and peripheral cornea to weaken and bulge outward, thereby flattening the central optical zone and relatively steepening the midperipheral zone.<sup>39-41</sup> Hexagonal keratotomy has been recommended for the correction of mild hyperopia. It has been theorized that a  $360^\circ$  uninterrupted circumferential incision in the midperiphery destabilizes the central cornea, thus causing it to bow forward and steepen.<sup>42</sup>

In all keratotomy procedures for the correction of astigmatism, the cornea is incised in the steepest meridian. Multiple parallel or grouped radial incisions

extending from a central optical zone have been advocated for the correction of mild myopic astigmatism, since midperipheral corneal bulging in one meridian leads to a greater central corneal flattening in that meridian than in other meridians.<sup>11</sup> Symmetric transverse midperipheral incisions are performed to correct mild and moderate astigmatism. Transverse incisions transect corneal collagen bundles, leading to meridional corneal flattening.<sup>11-43,59</sup> Increased astigmatic correction has been achieved with multiple transverse incisions<sup>11,59</sup> or arcuate incisions.<sup>47-52,48</sup> The amount of spherical equivalent correction after these procedures has been shown to be related to the length of the transverse or arcuate incision because of a coupling effect; incising the steeper meridian circumferentially not only causes it to flatten, but also causes the flatter meridian 90° away to steepen. Therefore myopic or hyperopic astigmatism can be corrected, depending on the chosen incisions and optical zone.<sup>13,59</sup> For moderate and high astigmatism, transverse incisions have been combined with radial incisions, as in trapezoidal keratotomy procedures, to increase astigmatic correction and to reduce the coupling effect.<sup>7,43,59,76,117</sup> Corneal wedge resection is performed for correction of very high degrees of astigmatism. Removal of a peripheral crescentic wedge of tissue that is centered on the flattest meridian and suturing of the wound result in central corneal steepening with peripheral corneal flattening in the area of the resection.<sup>78,59</sup>

Refractive keratotomy and keratectomy procedures are constantly evolving. Over the past several years, widespread interest in these techniques has necessitated and generated numerous experimental and clinical studies that have increased the corneal surgeon's understanding of refractive procedures and have led to many technical refinements. Although many intraoperative and postoperative complications have been reported,<sup>13,22</sup> the incidence of severe complications is low, and recent improvements in surgical design and instrumentation have led to decreased complications rates.<sup>13,22,44,66</sup> Significant changes in surgical technique, including the abandonment of intersecting radial and transverse or arcuate incisions, the execution of radial incisions toward the corneal periphery but not across the limbus, fewer radial incisions, less incision redeepening, and fewer repeat operations, as well as improved pachymeters and high-quality, calibrated gem knives, have rendered these procedures relatively safe.

Nevertheless, these techniques do not allow for retention of best-corrected visual acuity in all cases. In the Prospective Evaluation of Radial Keratotomy (PERK) Study, a multicenter clinical trial, 1.5% of eyes had a decrease of two or more lines in best-corrected acuity at 4 years after surgery.<sup>61</sup> Although few patients develop a permanent decrease in best-corrected vision, visual impairment is common because of glare, distortion, monocular diplopia, or fluctuating vision.<sup>13,22</sup> Despite the fact that many refractive incisional and excisional procedures have been shown to reduce refractive errors, the unpredictability and instability of these techniques are major concerns.<sup>13,22,44,62,63</sup> The PERK Study demonstrated that, at 4 years after radial keratotomy, uncorrected visual acuity was 20/20 or better in only 50% of eyes and 20/40 or better in 75% of eyes, and cycloplegic refractive error was within 1.00 diopter of emmetropia in only 54% of eyes. The total change in refractive error between 1 and 4 years after radial keratotomy was noted to be greater than 1.00 diopter in 17% of eyes, with 14% having a change in the direction of a continued effect of surgery.<sup>61</sup>

There has been no multicenter prospective clinical trial of keratotomy or ker-

atectomy procedures for the correction of hyperopia and astigmatism; clinical observations of multiple researchers, however, have not yet demonstrated predictable and stable results with any of these techniques.\*

There are several factors relating to surgical technique and response of the operated eye that affect the predictability and stability of these procedures. With current instrumentation, the depth of the incision is the most difficult surgical factor to control.<sup>62-126</sup> When incisions are performed with metal knives and thickness is measured by optical pachymetry, the depth of cuts has been reported to range from 30% to 100% of corneal thickness.<sup>45,46,96</sup> When incisions are created by diamond knives and thickness is measured by ultrasonic pachymetry, the predictability of incision depth is improved, but variations in incision depth of 61% to 98% of corneal thickness have been found.<sup>97</sup> It has been calculated that keratotomy incisions require an accuracy of within 20  $\mu\text{m}$  between desired and attained cutting depth.<sup>44</sup> Freehand corneal cutting does not allow for this precision. However, even with high-quality, micrometer-calibrated knives, accurate depths are inconsistently attained. Tilting of the blade to the side or in the forward-backward direction, variation in pressure exerted on the knife or in the speed with which the incisions are executed, and poor eye fixation causes differences in incision depth.<sup>44,66-126</sup> Even if gem knives are used, microscopic defects of the cutting edge, micrometer inaccuracy, and faulty foot plate design can lead to significant errors.<sup>44</sup>

### Experimental Studies

**Radial keratectomy.** In 1985 Cotliar and others<sup>21</sup> were the first to evaluate the ArF excimer laser in human cadaver eyes for use in radial keratotomy or *radial keratectomy*, as the procedure should be termed, since ArF excimer laser photobleaching always involves removal of tissue. The laser beam was focused to produce a rectangular beam 70  $\mu\text{m}$  wide on the corneal surface that was shielded with a contact lens to spare the central 3.5-mm optical zone and allow for two 3.5-mm excisions of the peripheral cornea. Two additional excisions were performed on the cornea by reexposing the surface after 90° rotation of the laser beam. The laser output was 100 mJ per pulse at a frequency of 10 Hz. Depending on the depth desired, the exposure time was varied from 10 to 45 sec. The edges of the excision sites were extremely smooth. Corneal flattening ranging from 0.12 to 5.35 diopters was obtained. The depth of the corneal excisions and the degree of central corneal flattening were found to correlate with the energy delivered (Fig. 24-28).

Steinert and Puliafito<sup>110</sup> used a slit lamp-delivered excimer beam to perform radial keratectomies one at a time in a rabbit in vivo. Photokeratoscopy 1 day after laser exposure confirmed central corneal flattening and midperipheral steepening at each of the excision sites.

### Clinical Studies

**Radial keratectomy.** In 1987 Aron-Rosa and others<sup>111</sup> and Tenner and others<sup>112</sup> investigated ArF excimer laser radial keratectomies in blind eyes.

In the slit lamp delivery system used by Aron-Rosa and associates,<sup>111</sup> the laser beam was directed by prisms through an articulated arm to be coaxial with the

\*References 43, 50, 54, 58, 59, 64, 76, 118, 122

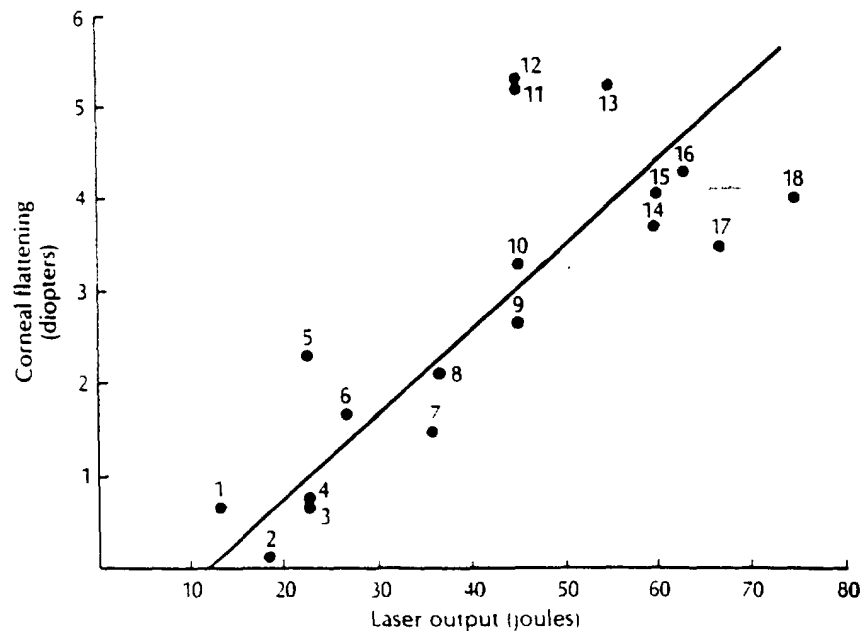


**Fig. 24-28.** Amount of central corneal flattening as a function of ArF excimer laser output after four-incision radial keratectomy in human eye bank eyes. (From Cotliar AM and others: Published courtesy of *Ophthalmology* (1985; 92:206-208) )

slit lamp illumination and HeNe aiming beam and was transmitted through an adjustable slit that could be rotated 360°. The size of the slit could be varied from 50 to 500  $\mu\text{m}$  in width and up to 5 mm in length. The fluence was 370 mJ/cm<sup>2</sup> with a frequency of 20 Hz. The total number of pulses was computer controlled and was determined by the desired excision depth. The slit was set for a width of 70  $\mu\text{m}$ , and the depth was programmed for either 50% or 90% of corneal thickness. The patient's eye was stabilized by retrobulbar anesthesia. A metal blocking mask with a 70-mm-wide slit was placed on the cornea to further control the size of the excision, but patient movement sometimes led to step-shaped edges. The excision depth was determined histologically and by slit lamp examination to be 85% or less of the programmed depth. The relatively shallow depths were attributed to poor beam quality, poor eye stability, and the presence of ejected photoablation remnants that might have acted as a shield when pulses were directed repeatedly at the same area. Corneal flattening measured by pachymetry at 1 day postoperatively was reported to be stable when remeasured 3 weeks later. Wound healing was followed for as long as 3 weeks postoperatively. Light and electron microscopy demonstrated good wound healing (Fig. 24-29).

Schroder and associates<sup>110</sup> developed a delivery system with special design features to decrease eye motion artifacts and improve cutting precision (Fig. 24-30). The laser was encased underneath a bed, allowing the patient to remain supine during laser beam delivery through an articulated arm. To further minimize errors due to eye movement, a plastic suction mask incorporating a metal



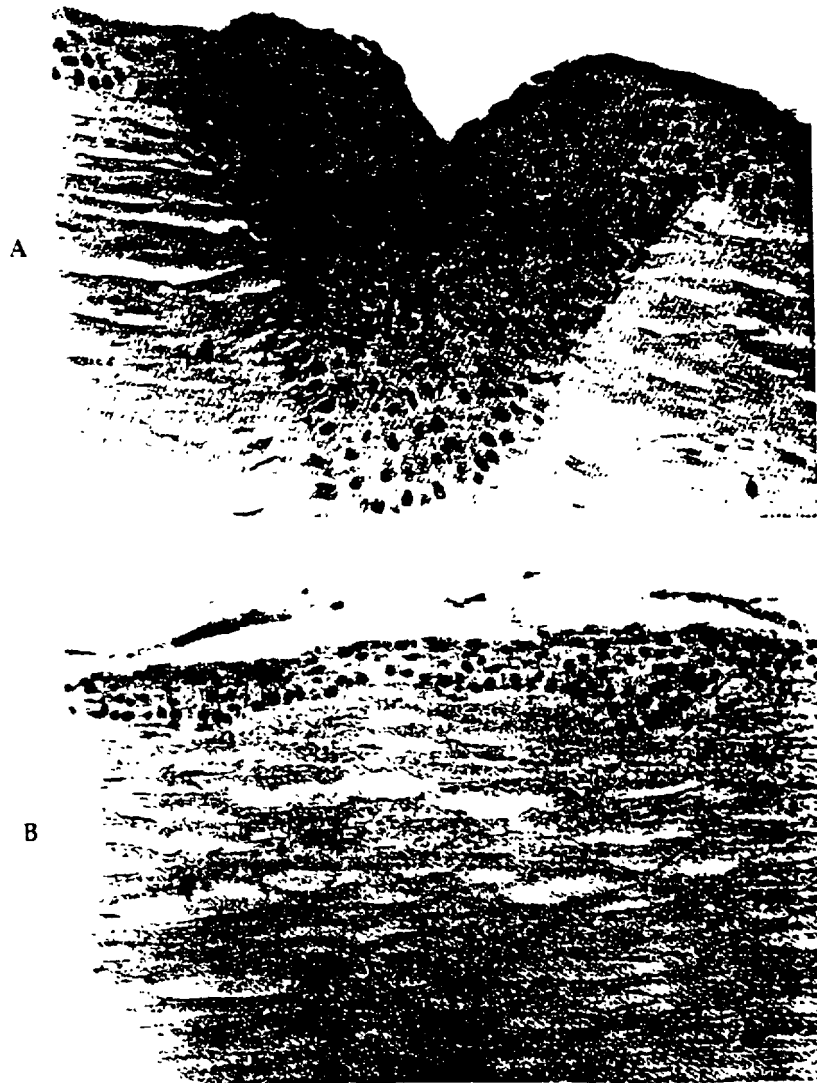


**Fig. 24-29.** A, Light micrograph of human cornea 14 days after 70- $\mu$ m-wide ArF excimer laser radial keratectomy. Note the v-shaped epithelial plug. (Hematoxylin, eosin, and safran.) B, Light micrograph of human cornea 21 days after 70- $\mu$ m-wide excimer laser radial keratectomy. The epithelial plug is smaller than at 14 days. (Hematoxylin, eosin, and safran.) (From Aron-Rosa DS and others. *J Cataract Refract Surg* 14:173, 1988.)

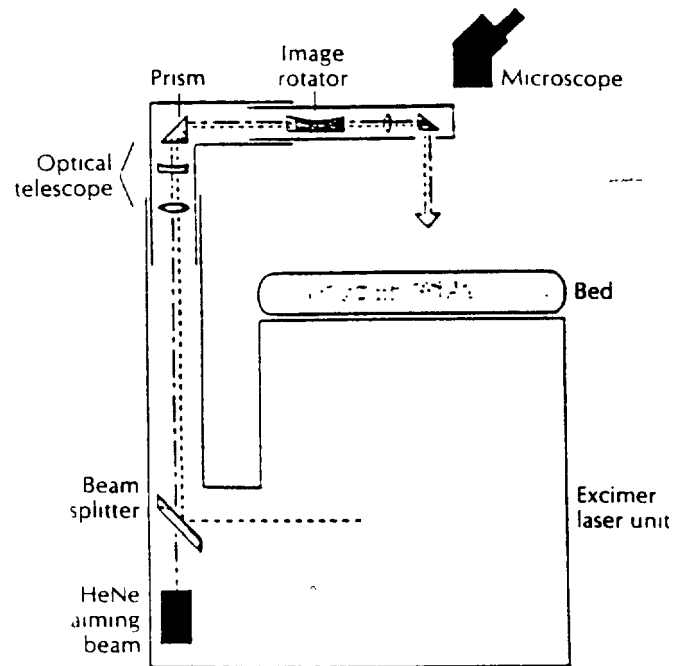


**Fig. 24-30.** Schematic diagram of the delivery system for ArF excimer laser radial keratectomy. (From Schroder E and others: *Am J Ophthalmol* 103:472-473, 1987. Published with permission from The American Journal of Ophthalmology. Copyright by The Ophthalmic Publishing Company.)

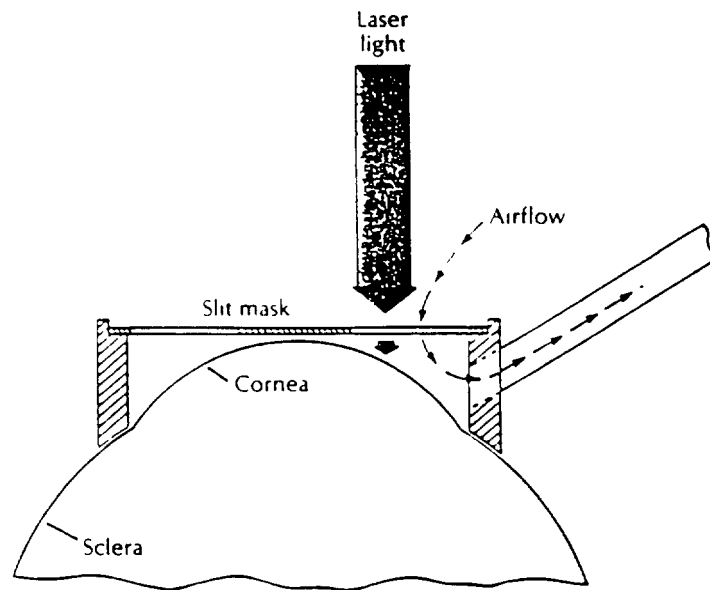


**Fig. 24-31.** Schematic diagram of a suction mask with slits for ArF excimer laser radial keratectomy. (From Schroder E and others: *Am J Ophthalmol* 103:472-473, 1987. Published with permission from The American Journal of Ophthalmology. Copyright by The Ophthalmic Publishing Company.)

plate with 70- $\mu\text{m}$ -wide slits, was held to the eye by a slight vacuum (Fig. 24-31). Constant airflow within the mask cooled the mask and removed molecular remnants to improve laser absorption. Increasing the depth of field of the image also allowed for more constant absorption over the entire excision site.

Tenner and others<sup>110</sup> reported on radial keratectomies performed with this laser on blind eyes. The number of pulses required to attain a desired depth was calculated based on measured corneal thickness and an assumed ablation depth of 2  $\mu\text{m}$  per pulse. To ensure safety, the depth was preset for only 60% of corneal thickness. Completion of eight radial excisions that were performed one at a time required 5 to 7 min. On slit lamp examination, the excisions appeared smooth and straight (Fig. 24-32) and were estimated by several observers to extend through 60% of corneal thickness. The degree of corneal flattening attained compared favorably with that achieved by radial keratotomy procedures using diamond knives and the same parameters; 6-month follow-up of two patients, though, did not demonstrate regression of initial effect, as has been observed with conventional techniques. The excision sites healed without any notable infiltrate or reaction and with less-visible scars than those produced by diamond and steel blade incisions (Fig. 24-33). Clinical trials using this laser in sighted eyes currently are underway in Europe.

**Transverse and arcuate keratectomy.** Seiler and associates<sup>102,104</sup> were the first to perform transverse (Fig. 24-34) and arcuate keratectomies with the ArF excimer laser in blind eyes and sighted eyes with astigmatic errors. They used a system incorporating the ArF excimer laser coupled to an operating microscope that provided for coaxial laser delivery at a fluence of 165  $\text{mJ}/\text{cm}^2$  and a repetition rate of 30 Hz. The beam was shaped by two 150- $\mu\text{m}$ -wide transverse or arcuate slits in a polymethylmethacrylate contact lens that was coated with a metal foil to reflect ultraviolet radiation. The posterior surface of the contact lens contained grooves to minimize capillary forces, thereby allowing for the maintenance of a dry corneal surface and preventing excision site accumulation of tear fluid that has been shown to decrease tissue absorption of laser energy and to decrease excision depth predictability. The procedure was performed with the patient supine. After instillation of topical anesthesia, the contact lens was centered on the cornea and the eye was stabilized with a Thornton ring. Each slit was irradiated separately for less than 1 minute. The number of pulses was precalculated and microprocessor controlled. Although excision depth correlated in a linear fashion to the total number of pulses,<sup>105</sup> the ablation depth obtained per pulse in the epithelium was approximately twice that obtained in the stroma.<sup>104,105</sup> Therefore the ablation rate and desired ablation depth of both the epithelium and stroma were considered during calculation of pulse number. The ultrasonically measured central corneal thickness was multiplied by 1.18 before determination of desired incision depth in order to correct for increased peripheral corneal thickness and for nonperpendicular alignment of the laser beam at the irradiated surface.



**Fig. 24-32.** A, Photograph taken through a surgical microscope of a human eye immediately after ArF excimer laser radial keratectomy with a 5-mm optical clear zone. Incision length, 3 mm; incision width, 70  $\mu$ m; incision depth, 300  $\mu$ m, corresponding to 60% of the corneal thickness. B, Slit lamp photograph 30 min postoperatively. (From Tenner A and others: J Refract Surg 4:5, 1988.)

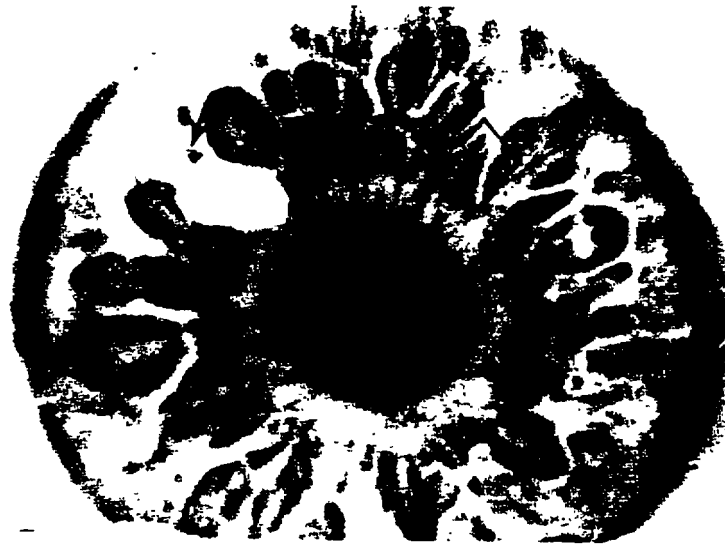


**Fig. 24-33.** Slit lamp photograph of the same eye as in Fig. 24-32 several weeks postoperatively. There was 2 diopters of central corneal flattening. Arrows identify some of the incisions. (From Tenner A and others: J Refract Surg 4:5, 1988.)

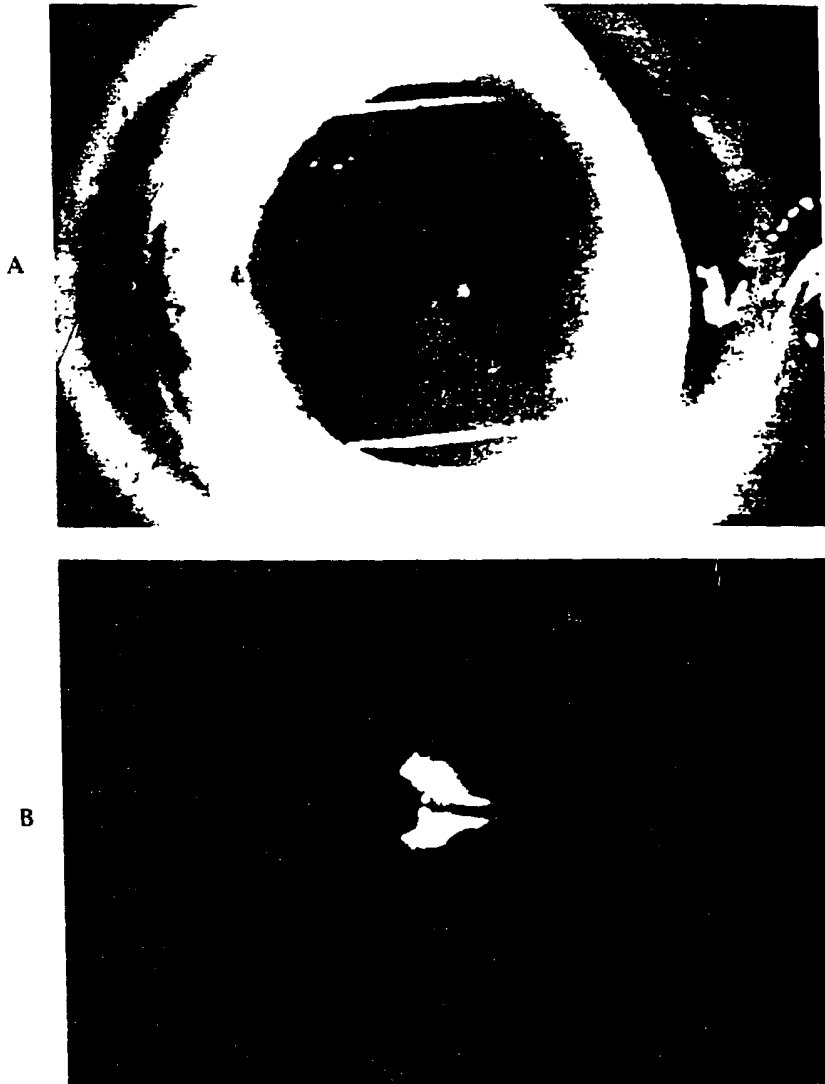


**Fig. 24-34.** A, Slit lamp photograph of a human eye after ArF excimer laser transverse keratectomy. B, Slit lamp photograph 5 weeks postoperatively. The excision depth was estimated to be  $90\% \pm 8\%$  of the corneal thickness. (From Seiler T and others: *Am J Ophthalmol* 105:117-124, 1988. Published with permission from The American Journal of Ophthalmology. Copyright by The Ophthalmic Publishing Company.)

As compared with conventional techniques, the ArF excimer laser led to less deviation between intended and attained excision depth. Histologic examination of the enucleated eyes demonstrated that the depth was within  $\pm 5\%$  of the intended value. Analysis of slit lamp micrographs revealed attainment of accurate depths within the measurement error of  $\pm 8\%$ . According to Seiler and Wollensak's biomechanical model,<sup>106</sup> astigmatic changes were predicted to be very dependent on incision depth. The clinical results obtained with ArF excimer laser transverse keratectomy correlated well with the theoretic curve (Fig. 24-35), although actual total astigmatic changes were slightly greater than predicted. Following transverse keratectomy, steepening of the flat meridian was greater than flattening of the steep meridian, thereby inducing a myopic shift. Biconcave arcuate excisions were found to produce astigmatic changes similar to those obtained with transverse excisions, but with no change in the spherical equivalent. Biconvex arcuate excisions have been suggested by Seiler<sup>102</sup> to be the method of choice to correct high hyperopic astigmatism; this procedure caused a myopic shift similar to that produced with transverse excisions but created a one- to sixfold higher astigmatic shift.

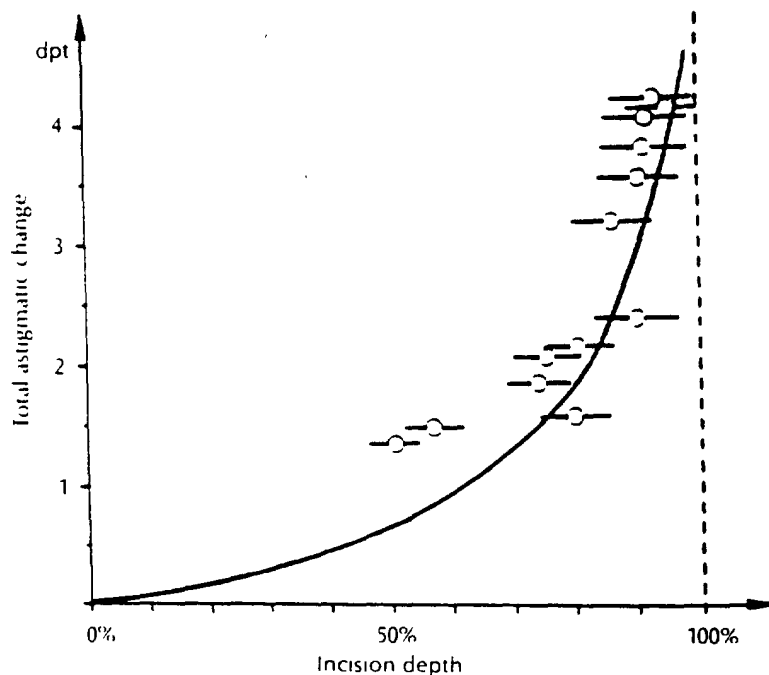


**Fig. 24-35.** Total astigmatic changes after ArF excimer laser transverse keratectomy as a function of excision depth compared with a theoretic curve (From Seiler T and others: *Am J Ophthalmol* 105:117-124, 1988. Published with permission from The American Journal of Ophthalmology. Copyright by The Ophthalmic Publishing Company.)

Following laser keratectomy, large fluctuations in astigmatism were noted during the first few days and were attributed to stromal edema.<sup>104</sup> Stabilization was achieved within approximately 2 weeks, and no regression was noted over the 6-month follow-up period. Patients complained of foreign body sensations and photophobia during the first week postoperatively. These symptoms generally resolved by the following week. Glare persisting for up to 2 months was noted by some patients. Rapid reepithelialization over the first few days was found biomicroscopically and histologically (Fig. 24-36). Epithelial plugs persisted for variable time periods.



**Fig. 24-36.** Light micrograph of human cornea 4 days after 150- $\mu$ m-wide ArF excimer laser transverse keratectomy. Epithelium covers the surface of the excision. (From Seiler T and others: *Am J Ophthalmol* 105 117-124, 1988. Published with permission from The American Journal of Ophthalmology. Copyright by The Ophthalmic Publishing Company.)

### Future Directions

Recent refinements in ArF excimer laser systems offer precise control of excisional depth, a major factor in the accuracy of noncentral incisional and excisional retractive procedures. Therefore the use of the laser, instead of steel or gem knives, theoretically should improve predictability of refractive error correction. However, the effects of laser keratectomies need to be studied much more extensively. Although not shown to date, it has been speculated that the wider excisions produced by the laser should lead to greater retractive change for the same depth.

It is not yet known whether wider laser excisions will cause greater instability of the eye and provoke increased glare and fluctuation of visual acuity. The answers to these questions will determine whether these relatively wide excisions should continue to be performed or whether systems producing thinner excisions should be investigated. The use of an ocular tracking device would obviate the need for masks and would allow for thinner excisions and, if combined with a corneal imaging and modeling system, for real-time analysis of corneal contour.

The degree to which cutting precision and corneal healing responses contribute to variability in retractive results has not been determined. Unsutured incisions or excisions render the cornea unstable. Morphologic studies<sup>23, 128</sup> have demonstrated that wound healing is incomplete for up to 47 months following conventional radial keratotomy. These studies showing persistence of epithelium within the wound, abnormal surface epithelium, and continued fibroblastic activity correlate with clinical findings<sup>91</sup> of fluctuation in vision and change in refractive error for up to 4 years postoperatively. Although complete wound healing has been reported<sup>17</sup> at 66 and 70 months after radial keratotomy performed with a diamond knife, the long-term course of laser keratectomy wound healing is not yet known.

Pharmacologic agents may prove to be beneficial in decreasing wound healing variability. Growth factors and fibronectin are being investigated for their ability to accelerate wound healing and stabilization of refractive results. Enhancement of epithelial and stromal healing responses may, however, negate a large degree of surgical effect. Collagen bandage lenses have been demonstrated to cause more rapid reepithelialization of diamond knife keratotomy wounds with decreased fibroblastic response.<sup>1</sup> Antimetabolites and collagen cross-linkage inhibitors to reduce scar formation have not yet been proven effective. Even if an agent that could weaken corneal wounds successfully were found, there probably would be poor patient acceptance of such an approach requiring long-term usage.

The ArF excimer laser probably will enable the corneal surgeon to perform more precise and predictable noncentral excisional retractive surgery with an infinite possibility of linear and nonlinear patterns to alter corneal topography. However, reliability problems due to wound healing and corneal instability may cause these procedures to be replaced in the future by other laser techniques such as nonuniform lamellar keratectomies.



## REFERENCES

1. Aquavella JV and others: The effect of a collagen bandage lens on corneal wound healing: a preliminary report. *Ophthalmic Surg* 18(8):570, 1987
2. Arentsen JJ Lamellar grating. In Brightbill FS, editor: *Corneal surgery: theory, technique, and tissue*. St Louis, 1986, The CV Mosby Co.
3. Aron-Rosa DS: Discussion at the International Cornea Laser Society Meeting, Dallas, Nov 1987.
4. Aron-Rosa D and others: Keratorefractive surgery with the excimer laser. *Am J Ophthalmol* 100:741, 1985
5. Aron-Rosa DS and others: Corneal wound healing after excimer laser keratotomy in a human eye. *Am J Ophthalmol* 103:454, 1987
6. Aron-Rosa DS and others: Wound healing following excimer laser radial keratotomy. *J Cataract Refract Surg* 14:173, 1988.
7. Arrowsmith P: Astigmatism correction by paired quantitative T-incisions. In Brightbill FS, editor: *Corneal surgery: theory, technique, and tissue*. St Louis, 1986, The CV Mosby Co.
8. Barraquer E and others: Comparative corneal wound healing between metal blade and two cutting lasers. *Invest Ophthalmol Vis Sci* 29:390, 1988.
9. Beckman H and others: Limbectomies, keratectomies, and keratostomies performed with a rapid-pulsed carbon dioxide laser. *Am J Ophthalmol* 71:1277, 1971
10. Berlin M, Bende T, and Seiler T: Corneal resurfacing by excimer laser photoablation. *Invest Ophthalmol Vis Sci* 29:310, 1988.
11. Bille JF and others: 3-D corneal imaging using the laser tomographic scanner. *Invest Ophthalmic Vis Sci* 28:223, 1987
12. Binder PS: Selective suture removal can reduce postkeratoplasty astigmatism. *Ophthalmology* 92:1412, 1985
13. Binder PS: Radial keratotomy in the United States. *Arch Ophthalmol* 105:37, 1987
14. Binder PS, Baumgartner SD, and Zavala EY: Why do some epikeratoplasty cases fail? *Arch Ophthalmol* 105:63, 1987
15. Binder PS, Krumeich J, and Zavala EY: Laboratory study of freeze and non-freeze lamellar retractive keratoplasty. *Arch Ophthalmol* 105:1125, 1987.
16. Binder PS and others: Combined morphologic effects of lathing and Ivophylization on epikeratoplasty lenticules. *Arch Ophthalmol* 104:671, 1986.
17. Binder PS and others: An ultrastructural and histochemical study of long-term wound healing after radial keratotomy. *Am J Ophthalmol* 103:432, 1987.
18. Boruchoff SA: Therapeutic keratoplasty. In Smolin G and Thoft RA, editors: *The cornea: scientific foundations and clinical practice*. Boston, 1983, Little, Brown and Co.
19. Burstein N: Corneal epithelial, stromal and endothelial response to excimer laser ablation. Paper presented at the Laser Symposium, CLAO-ISRK Annual Meeting, Las Vegas, Jan 16, 1988
20. Casey T: The lamellar graft. In Casey T and Mayer D, editors: *Corneal grafting: principles and practice*. Philadelphia, 1984, WB Saunders Co.
21. Cotliar AM and others: Excimer laser radial keratotomy. *Ophthalmology* 92:206, 1985.
22. Cross WO and Head WJ III: Complications of radial keratotomy. In Sanders DR, Hofmann RF, and Salz JJ, editors: *Refractive corneal surgery*. Thorofare, NJ, 1986, Slack, Inc.
23. Deg JK, Zavala EY, and Binder PS: Delayed corneal wound healing following radial keratotomy. *Ophthalmology* 92:734, 1985.
24. Dehm EJ and others: Corneal endothelial injury in rabbits following excimer laser ablation at 193 and 248 nm. *Arch Ophthalmol* 104:1364, 1986.
25. Del Pero RA, and others: Human excimer laser lamellar retractive keratectomy: a clinical study. *Invest Ophthalmol Vis Sci* 29:281, 1988.
26. Denham DB and others: Evaluation of manual, motorized and laser trephines by shadow photogrammetric analysis. *Invest Ophthalmic Vis Sci* 29:452, 1988
27. Duttev RJ and others: Quantification of paired arcuate keratotomy in human cadaver eye. *Invest Ophthalmol Vis Sci* 29:392, 1988.
28. Erlich MI and others: Techniques of lamellar keratoplasty. *Int Ophthalmol Clin* 28(1):24, 1988

29. Esterowitz L and others: Advantages of the 2.94 micron wavelength for medical laser applications. Paper presented at the Conference on Lasers and Electro-Optics, San Francisco, June 9-13, 1986.
30. Fantes F and others: Excimer radiant exposure and quality of surface ablations, *Invest Ophthalmol Vis Sci* 29:309, 1988.
31. Fine BS and others: Preliminary observations on ocular effects of high power continuous CO<sub>2</sub> laser irradiation, *Am J Ophthalmol* 64:209, 1967.
32. Forstot SL: Modified relaxing incision technique for postkeratoplasty astigmatism, *Cornea* 7(2):133, 1988.
33. Frantz JM and others: Moist-Pak storage of epikeratophakia tissue lenses, *Invest Ophthalmol Vis Sci* 29:282, 1988.
34. Gaster and others: Excimer laser ablation and wound healing of superficial cornea in rabbits and primates, *Invest Ophthalmol Vis Sci* 29:309, 1988.
35. Gilbert ML and others: Hexagonal keratotomy in human cadaver eyes, *J Refract Surg* 4:12, 1988.
36. Gormley DJ: Personal communication, 1988.
37. Gormley DJ and others: Corneal modeling, *Cornea* 7(1):30, 1988.
38. Hanna K and others: A rotating-slit delivery system for excimer laser refractive keratoplasty, *Am J Ophthalmol* 103:474, 1987.
39. Hanna K and others: Corneal wound healing after excimer laser keratomileusis in rabbits, *Invest Ophthalmol Vis Sci* 29:390, 1988.
40. Hanna KD and others: Excimer laser keratectomy for myopia with a rotating-slit delivery system, *Arch Ophthalmol* 106:245, 1988.
41. Hays JC and Rowsey JJ: Corneal topography. In Brightbill FS, editor: *Corneal surgery: theory, technique, and tissue*. St Louis, 1986. The CV Mosby Co.
42. Heidemann DG and others: Over-sized donor grafts in penetrating keratoplasty: a randomized trial, *Arch Ophthalmol* 103:1807, 1985.
43. Hofmann RF: The surgical correction of idiopathic astigmatism. In Sanders DR, Hofmann RF, and Salz JJ, editors: *Refractive corneal surgery*. Thorofare, NJ, 1986. Slack, Inc.
44. Hofmann RF and Lindstrom RL: Sources of error in keratotomy knife incision, *J Refract Surg* 3(6):215, 1987.
45. Jester JV and others: Radial keratotomy in non-human primate eyes, *Am J Ophthalmol* 92:153, 1981.
46. Jester JV and others: A statistical analysis of radial keratotomy in human cadaver eyes, *Am J Ophthalmol* 92:172, 1981.
47. Keates RH and others: Carbon dioxide laser beam control for corneal surgery, *Ophthalmic Surg* 12(2):117, 1981.
48. Kerr-Muir MG and others: Ultrastructural comparison of conventional surgical and argon fluoride excimer laser keratectomy, *Am J Ophthalmol* 103:448, 1987.
49. Kivce SD: Computer-assisted corneal topography: high resolution graphic presentation and analysis of keratotomy, *Invest Ophthalmol Vis Sci* 25(1):426, 1984.
50. Krachmer JH and Fenzl RE: Surgical correction of high postkeratoplasty astigmatism, relaxing incisions vs. wedge resection, *Arch Ophthalmol* 98:1400, 1980.
51. Krueger RR and Trokel SL: Quantitation of corneal ablation by ultraviolet light, *Arch Ophthalmol* 103:1741, 1985.
52. Krueger RR, Trokel SL, and Schubert HD: Interaction of ultraviolet laser light with the cornea, *Invest Ophthalmol Vis Sci* 26:1455, 1985.
53. Krumeich JH and Swinger CA: Non-freeze epikeratophakia for the correction of myopia, *Am J Ophthalmol* 103:397, 1987.
54. Lavery GW and others: The surgical management of corneal astigmatism after penetrating keratoplasty, *Ophthalmic Surg* 16:165, 1985.
55. L'Esperance FA Jr, Taylor DM, and Warner JW: Human excimer laser keratectomy: short term histopathology, *J Refract Surg* 4:118, 1988.
56. L'Esperance FA Jr and others: Human excimer laser corneal surgery: preliminary report. Presented at the American Ophthalmological Society Meeting, Hot Springs, May 22-25, 1988. *Trans Am Ophthalmol Soc* (in press).
- 56a. L'Esperance FA Jr and others: Excimer laser instrumentation and technique for human corneal surgery, *Arch Ophthalmol* 1988 (in press).

- 56b. L'Esperance FA Jr and others: Human excimer laser corneal surgery: clinical and histopathological results. Manuscript submitted for publication, 1988.
57. Lieurance RC and others: Excimer laser cut lenticles for epikeratophakia. *Am J Ophthalmol* 103:475, 1987.
58. Lindstrom RL and Lavery QW: Correction of postkeratoplasty astigmatism. In Sanders DR, Hofmann RF, and Salz JJ, editors: *Refractive corneal surgery*. Thorotare, NJ, 1986, Slack, Inc.
59. Lindstrom RL and Lindquist TD: Surgical correction of postoperative astigmatism. *Cornea* 7(2):138, 1988.
60. Loertscher H and others: Preliminary report on corneal incisions created by a hydrogen fluoride laser. *Am J Ophthalmol* 102:217, 1986.
61. Loertscher H and others: Noncontact trephination of the cornea using a pulsed hydrogen fluoride laser. *Am J Ophthalmol* 104:471, 1987.
62. Lynn MJ and others: Factors affecting outcome and predictability of radial keratotomy in the PERK study. *Arch Ophthalmol* 105:42, 1987.
63. Lynn M and others: Prospective evaluation of radial keratotomy (PERK) study: results four years after surgery. *Invest Ophthalmol Vis Sci* 29:310, 1988.
64. Mandel MR, Shapiro MB, and Krachmer JH: Relaxing incisions with augmentation sutures for the correction of post keratoplasty stigmatism. *Am J Ophthalmol* 103:441, 1987.
65. Mandel ER and others: Excimer laser large area ablation of the cornea. *Invest Ophthalmol Vis Sci* 28:275, 1987.
66. Mandelbaum S and Lynn MJ: Theory, case selection, and major variables in success or failure of radial keratotomy. In Brightbill FS, editor: *Corneal surgery: theory, technique, and tissue*. St Louis, 1986, The CV Mosby Co.
67. Mandelbaum S and Udel II: Corneal perforations associated with infectious agents. In Abbott RL, editor: *Surgical intervention in corneal and external diseases*. New York, 1987, Grune & Stratton, Inc.
68. Marshall J, Trokel S, and Rothery S: Photoablative reprofiling of the cornea using an excimer laser: photorefractive keratectomy. *Lasers Ophthalmol* 1:21, 1986.
69. Marshall J and others: An ultrastructural study of corneal incisions induced by an excimer laser at 193 nm. *Ophthalmology* 92:749, 1985.
70. Marshall J and others: A comparative study of corneal incisions induced by diamond and steel knives and two ultraviolet radiations from an excimer laser. *Br J Ophthalmol* 70:482, 1986.
71. Mathers WD and Jester JV: Full thickness corneal wound strength enhancement by epidermal growth factor. *Invest Ophthalmol Vis Sci* 29:312, 1988.
72. McCarey BE: Synthetic keratophakia: theory and major variables in success or failure. In Brightbill FS, editor: *Corneal surgery: theory, technique, and tissue*. St Louis, 1986, The CV Mosby Co.
73. McCarey BE and Hanna K: Corneal modeling. Paper presented at the American Academy of Ophthalmology Annual Meeting, Dallas, Nov 8-12, 1987.
74. McDonald MB and others: Refractive surgery with the excimer laser. *Am J Ophthalmol* 103:469, 1987.
75. McDonald M and others: Excimer laser surface shaping of the primate cornea for the correction of myopia. *Invest Ophthalmol Vis Sci* 29:310, 1988.
76. Merch MP, Williams PA, and Lindstrom RL: Trapezoidal keratotomy: a vector analysis. *Ophthalmology* 93:719, 1986.
77. Moro-Besson J: *Astigmatisme post-kératoplastie transfixiante: intérêt de l'utilisation du micro-kérato-trépan*. thèse, Paris, 1987. Dactvlo-Sorbonne.
78. Mueller FO and O'Neill P: Some experiments on corneal grinding. *Exp Eye Res* 6:42, 1967.
79. Munnerlyn CR, Koons SJ, and Marshall J: Photorefractive keratectomy: a technique for laser refractive surgery. *J Cataract Refract Surg* 14:46, 1988.
80. Nuss RC, Puliafito CA, and Dehm E: Unscheduled DNA synthesis following excimer laser ablation of the cornea in vivo. *Invest Ophthalmol Vis Sci* 28:287, 1987.
81. Olson RJ: Corneal curvature change associated with penetrating keratoplasty: a mathematical model. *Ophthalmic Surg* 11:838, 1980.
82. Olson RJ: Prevention of astigmatism in corneal transplant surgery. *Int Ophthalmol Clin* 28(1):37, 1988.

83. Olson RI, Kautman HE, and Rhein-  
strom SD: Reshaping the cat corneal  
anterior surface using a high-speed  
diamond fraise. *Ophthalmic Surg*  
11:784, 1980.
84. Perlman EM: An analysis and inter-  
pretation of refractive errors after pen-  
etrating keratoplasty. *Ophthalmology*  
88:39, 1981.
85. Petrousos G, Sebag J, and Courtois Y:  
Epidermal growth factor increases  
tensile strength during wound heal-  
ing. *Ophthalmic Res* 18:299, 1986.
86. Pouliquen Y: Wound healing after ex-  
cimer laser keratomileusis. Paper pre-  
sented at the International Cornea La-  
ser Society Meeting, Dallas, Nov 7,  
1987.
87. Pouliquen Y. Personal communica-  
tion, 1988.
88. Puliafito CA and others: Excimer laser  
ablation of the cornea and lens: ex-  
perimental studies. *Ophthalmology*  
92:741, 1985.
89. Puliafito CA and others: High-speed  
photography of excimer laser ablation  
of the cornea. *Arch Ophthalmol*  
105:1255, 1987.
90. Renard G and others: Excimer laser  
experimental keratectomy: an ultra-  
structural study. *Cornea* 6(4):269,  
1987.
91. Rich LF: A technique for preparing  
corneal lamellar donor tissue using  
simplified keratomileusis. *Ophthal-  
mic Surg* 11:606, 1980.
92. Rich LF, MacRae SM, and Frauntelder  
FT: An improved method for lamellar  
keratoplasty. *CLAO J* 14(1):42, 1988.
93. Rich LF and others: Stimulation of cor-  
neal wound healing with mesodermal  
growth factor. *Arch Ophthalmol*  
97:1326, 1979.
94. Rowsey JJ and others: Prospective  
evaluation of radial keratotomy: pho-  
tokeratometer corneal topography.  
*Ophthalmology* 95:322, 1988.
95. Rubinstein JB, Merck MD, and Keys  
CL: Transverse versus arcuate kera-  
totomy for reduction of astigmatism.  
*Invest Ophthalmol Vis Sci* 29:392,  
1988.
96. Salz JJ and others: Radial keratotomy  
in fresh human cadaver eyes. *Oph-  
thalmology* 88:742, 1981.
97. Salz JJ and others: Analysis of incision  
depth following experimental radial  
keratotomy. *Ophthalmology* 90:655,  
1983.
98. Schanzlin DJ, Jester IV and Kay ED:  
Cryolathe corneal injury. *Cornea* 2:57,  
1983.
99. Schanzlin DJ and Nesburn AB: Re-  
fractive keratoplasty. In Smolin G and  
Thoft RA, editors: *The cornea: scien-  
tific foundations and clinical practice*.  
Boston, 1983, Little, Brown and Co.
100. Schroder E and others: An ophthalmic  
excimer laser for corneal surgery. *Am  
J Ophthalmol* 103:472, 1987.
101. Seiler T: Personal communication,  
1988.
102. Seiler T: Clinical aspects of laser ker-  
atectomy, linear and elliptical inci-  
sions in the cornea. Paper presented  
at the Laser Symposium. CLAO-ISRK  
Annual Meeting, Las Vegas, Jan 16,  
1988.
103. Seiler T and others: The potential of  
an infrared hydrogen fluoride (HF) (3  
microns) for corneal surgery. *Lasers  
Ophthalmol* 1:49, 1986.
104. Seiler T and others: Excimer laser ker-  
atectomy for correction of astigmat-  
ism. *Am J Ophthalmol* 105:117, 1988.
105. Seiler T and Wollensak J: In vivo ex-  
periments with the excimer laser:  
technical parameters and healing pro-  
cesses. *Ophthalmologica* 192:65, 1986.
106. Seiler T and Wollensak J: Zur theorie  
der T-inzision der kornea. *Klin Mon-  
atsbl Augenheilkd* 191:120, 1987.
107. Serdarevic O and others: Excimer la-  
ser therapy for experimental *Candida*  
keratitis. *Am J Ophthalmol* 99:534,  
1985.
108. Serdarevic ON and others: Excimer la-  
ser trephination in penetrating kera-  
toplasty: morphologic features and  
wound healing. *Ophthalmology*  
95:493, 1988.
109. Smolek MK: Real-time holographic in-  
terferometry of bovine eyes. *Invest  
Ophthalmol Vis Sci* 29:389, 1988.
110. Steinert RF and Puliafito CA: Corneal  
incisions with the excimer laser. In  
Sanders DR, Hofmann RF, and Salz  
JJ, editors: *Refractive corneal surgery*.  
Thorofare, NJ, 1986, Slack, Inc.
111. Swinger CA: Keratomileusis for my-  
opia. In Sanders DR, Hofmann RF,  
and Salz JJ, editors: *Refractive corneal  
surgery*. Thorofare, NJ, 1986, Slack,  
Inc.
112. Swinger CA: Keratophakia and kera-  
tomileusis for hyperopia. In Sanders  
DR, Hofmann RF, and Salz JJ, editors:

- Refractive corneal surgery, Thorofare, NJ, 1986, Slack, Inc.
113. Swinger CA, Krumeich JH, and Casiday D: Planar lamellar refractive keratoplasty. *J Refract Surg* 2:17, 1986.
  114. Swinger CA and Villasenor RA: Myopic keratomileusis: evaluation of published results. In Brightbill FS, editor: *Corneal surgery: theory, technique, and tissue*, St Louis, 1986, The CV Mosby Co.
  115. Taboada J, Mikesell GW, and Reed RD: Response of the corneal epithelium to KrF excimer laser pulses. *Health Phys* 40:677, 1981.
  116. Tenner A and others: Excimer laser radial keratotomy in the living human eye: a preliminary report. *J Refract Surg* 4:5, 1988.
  117. Terry MA and Rowsey JJ: Dynamic shifts in corneal topography during the modified Ruiz procedure for astigmatism. *Arch Ophthalmol* 104:1611, 1986.
  118. Terry MA and Rowsey JJ: Clinical applications of the modified Ruiz procedure for astigmatism. *Invest Ophthalmol Vis Sci* 29:392, 1988.
  119. Thompson KP, Barraquer E, and Loertcher H: New collagen production and wound morphology following corneal laser excision. *Invest Ophthalmol Vis Sci* 29:310, 1988.
  120. Trentacorte J and others: Mutagenic potential of a 193-nm excimer laser on fibroblasts in tissue culture. *Ophthalmology* 94:125, 1987.
  121. Trokel SL, Srinivasan R, and Bransen B: Excimer laser surgery of the cornea. *Am J Ophthalmol* 96:710, 1983.
  122. Troutman RC and Swinger C: Relaxing incision for control of postoperative astigmatism following keratoplasty. *Ophthalmic Surg* 11:117, 1980.
  123. Troutman RC, Swinger CA, and Belmont S: Selective positioning of the donor cornea in penetrating keratoplasty for keratoconus: postoperative astigmatism. *Cornea* 3:135, 1984.
  124. Tuft S, Zabel R, and Marshall J: Corneal remodeling following anterior keratectomy. *Invest Ophthalmol Vis Sci* 29:310, 1988.
  125. Villasenor RA: Homoplastic keratomileusis for myopia. In Sanders DR, Hofmann RF, and Salz JJ, editors: *Refractive corneal surgery*, Thorofare, NJ, 1986, Slack, Inc.
  126. Villasenor RA and others: Changes in corneal thickness during radial keratotomy. *Ophthalmic Surg* 12:341, 1981.
  127. Woost PG and others: Effect of growth factors with dexamethasone on healing of rabbit corneal stromal incisions. *Exp Eye Res* 40:47, 1985.
  128. Yamaguchi and others: Long-term histologic evaluation of wound healing after anterior radial keratotomy in rabbits. *Invest Ophthalmol Vis Sci* 29:391, 1988.
  129. Zabel R, Tuft S, and Marshall J: Excimer laser photorefractive keratectomy: endothelial morphology following area ablation of the cornea. *Invest Ophthalmol Vis Sci* 29:390, 1988.
  130. Zavala EY and others: Refractive keratoplasty: lathing and cryopreservation. *CLAO J* 11:155, 1985.

# EUROPEAN PATENT APPLICATION

21 Application number: 88401607.2

51 Int. Cl.4: A 61 F 9/00

22 Date of filing: 24.06.88

30 Priority: 25.06.87 FR 8708963

43 Date of publication of application:  
28.12.88 Bulletin 88/52

64 Designated Contracting States: DE FR GB

71 Applicant: Hanna, Khalil  
19, rue Las Cases  
F-75007 Paris (FR)

64 Designated Contracting States: DE FR GB

71 Applicant: Compagnie IBM FRANCE  
5 Place Vendôme  
F-75000 Paris 1er (FR)

64 Designated Contracting States: FR

71 Applicant: International Business Machines Corporation  
Old Orchard Road  
Armonk, N.Y. 10504 (US)

64 Designated Contracting States: DE GB

72 Inventor: Khalil, Hanna  
19, rue Las Cases  
FR-75007 Paris (FR)

Asfar, Louis  
8, Square de Brettaville  
FR-78150 Le Chesnay (FR)

Chastang, Jean-Claude  
68, Hatfield Road - Box 354  
R.F.D. 1 - Mahopac New York 10541 (US)

74 Representative: Martin, Jean-Jacques et al  
Cabinet REGIMBEAU 26, Avenue Kléber  
F-75116 Paris (FR)

54 Device for correcting the shape of an object by laser treatment.

57 The invention concerns a device for correcting the shape of an object by laser treatment.

The device comprises means (1) for emitting a laser beam (FL) and means (2) for generating a treatment laser beam (FLT) comprising at least one lobe of elongate cross-section. Means (3) enable focussing of the image of the lobe or lobes of the treatment laser beam on the area of the object (OE) to be corrected and means (4) enable displacement of the image of the lobe of the treatment laser beam in translation or in rotation over the area of the object to be corrected. The total correction or ablation is effected by the summation of a plurality of elementary discrete ablations.

Application to refractive surgery in the case of keratomileusis for myopia, hypermetropia or astigmatism, and to shaping contact lenses and intra-ocular implants.

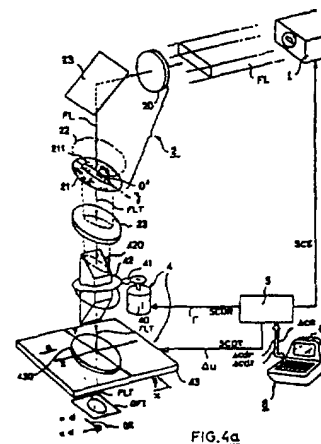


FIG. 4a

## Description

## DEVICE FOR CORRECTING THE SHAPE OF AN OBJECT BY LASER TREATMENT

The present invention relates to a device for performing surgery on the cornea of the eye. The purpose of such modifications of the shape of the cornea is to correct ametropia by correcting dimensional optical characteristics of the cornea and principally its radius of curvature. At the present time such modifications, known as keratomileusis, are achieved by actually machining a disk removed from the cornea. The disk is made rigid by freezing it and then machined by the Barraquer process or applied to a template with the appropriate radius of curvature and recut using the Barraquer-Krumeich technique.

This type of operation has the major disadvantage of necessitating first removal of the disk of corneal material and then treatment of the aforementioned disk, which has to be reimplanted on the eyeball of the patient after treatment.

However, recent work has shown the very precise ablative properties of excimer laser radiation when this radiation is applied to the corneal tissue. The radiation emitted by an excimer laser, with a wavelength substantially equal to 193 nm, may be used to eliminate corneal material by photodecomposition. Generally speaking, a round light spot (an image of the laser beam) is formed on the cornea, the spot being substantially centered on the optical axis of the eyeball. The spot has a substantially circular or annular shape or a symmetrical shape relative to the optical axis of the eyeball and may be moved and/or the radius size changed, the exposure time for a particular area depending on the thickness of the cornea to be eliminated.

Although such devices enable direct operation on the eyeball of the patient, enabling better centering through avoiding the aforementioned problem of cutting out, and reimplanting after correction, a piece of the cornea, they do not make it possible to implement a precise treatment method in that, although the exposure time can be defined with good precision, the effects and in particular the thickness of the cornea subjected to photodecomposition vary with the size of the light spot and the energy density of the laser beam used. Moreover, the surface state of the cornea after treatment and undesirable side effects due to thermal or shockwave phenomena vary significantly with the energy level delivered by each pulse and the repetition frequency with which the same area is successively irradiated.

An object of the device in accordance with the present invention for performing surgery on the cornea of the eye using laser radiation is to remedy the aforementioned disadvantages through the use of a device enabling an ablation process to be carried out by successive discrete ablations, the total ablation resulting from the summation of numerous discrete ablations, while avoiding irradiating the same area with two or more consecutive pulses and limiting the surface area irradiated by each pulse.

Another object of the present invention is the use of a device in which each elementary discrete ablation is optimised both from the point of view of the extent of the area over which the discrete ablation is effected and the irradiation time for the area to carry out the aforementioned discrete ablation, the surface state of the area over which the discrete ablation has been effected featuring a minimum degree of roughness and the corrected area, the summation of the areas over which one or more discrete ablations have been effected, having a minimum degree of roughness, the reduction of undesirable side effects such as shockwave and thermal effects making it possible to preserve and respect the integrity of surrounding tissue.

Another object of the present invention is the use of a refractive surgery device for laser treatment of the cornea of the eye enabling direct operation on the eyeball of the patient, the operation being computer- or microcomputer-assisted.

The refractive surgical device for laser treatment of the cornea of the eye in accordance with the present invention comprises means for emitting a pulsed laser beam. It is characterised in that it comprises means for generating a treatment laser beam comprising at least one lobe of elongate cross-section, means for focussing the image of said lobe or lobes of the treatment laser beam onto the area of the eye to be corrected, and means for synchronising displacement of the image of said lobe or lobes of the treatment laser beam, complete correction or ablation being effected as the summation of a plurality of elementary discrete ablations.

The device in accordance with the invention finds an application in any surgical operation on the cornea of the eye intended to correct ametropia by keratomileusis in the case of myopia, hypermetropia and astigmatism, by epikeratophakia, by radiating incisions, bar-shaped incisions or circular incisions for corneal grafting, uniform deep ablation for lamellar grafting.

The invention will be better understood on reading the following description and referring to the drawings in which:

- figure 1 shows a graph plotting the depth of a discrete elementary ablation by one laser emission pulse as a function of the radiation energy density,
- figure 2a shows a plan view of the cornea of an eye with the corresponding definition of parameters defining the surface to be treated,
- figure 2b shows a view in cross-section on the line A-A in figure 2a with the corresponding definition of parameters defining the surface treated and the area removed by photodecomposition,
- figure 3a shows a block diagram of the device in accordance with the invention in the case where the image of the treatment laser beam is moved in rotation,
- figure 3b shows a particularly advantageous object slit enabling treatment by keratomileusis of

myopia in the case of the embodiment of the device from figure 3a,

- figure 3c shows a particularly advantageous object slit enabling treatment by keratomileusis of hypermetropia in the case of the embodiment of the device from figure 3a,

- figure 3d shows in a non-limiting way one embodiment of an object slit with multiple lobes enabling treatment of myopia by keratomileusis in the same way as in the case of figure 3b,

- figures 3e and 3f respectively represent in an advantageous, non-limiting way an embodiment of an auxiliary slit of the circular sector type, enabling, when associated with an object slit such as that shown in figure 3b or figure 3c, treatment by keratomileusis of astigmatism of the eyeball and the cornea, in the case of the embodiment of the device from figure 3a and a circular incision for trepanation and for correction of astigmatism by partial and localised incisions,

- figure 4a shows a non-limiting alternative embodiment of the device in accordance with the invention shown in figure 3a in the case where the image of the treatment laser beam is moved either in rotation or in translation,

- figure 4b shows a particularly advantageous object slit enabling treatment of myopia by keratomileusis in the case of the embodiment of the device from figures 3a and 4a, the image of the laser beam being moved in translation,

- figure 4c shows a particularly advantageous object slit enabling treatment of hypermetropia by keratomileusis in the case of the embodiment of the device from figure 4a, the image of the laser beam being moved in translation,

- figure 4d shows in a non-limiting way an alternative embodiment of an object slit with multiple lobes enabling treatment of myopia by keratomileusis in the same way as in the case of figure 3a,

- figure 4e shows a particularly advantageous embodiment in which at least one edge of the slit is adjustable to enable compensation of irregular distribution of the energy of the laser beam,

- figure 5a shows in the case of use of the device from figure 4a with the image of the laser beam moved in translation the area of the cornea subjected to irradiation in two elementary areas extending in two directions OX, OY, the areas defined by movement in translation of the laser beam in the corresponding direction OX or OY being concurrent,

- figure 5b shows a profile characteristic of total ablation of a cornea subjected to treatment for myopia by keratomileusis,

- figure 5c shows a profile characteristic of total ablation of a cornea subject to treatment for hypermetropia by keratomileusis,

- figures 6a and 6b show a non-limiting embodiment of a diaphragm enabling improved focussing of images of the slits onto the cornea and figures 6c through 6e show a particularly advantageous embodiment of a diaphragm the slit in which is moved in rotation, enabling discontinuity between the corrected and non-corrected areas of the cornea to be avoided,

- figure 7 shows an advantageous alternative embodiment of the device in accordance with the invention.

Prior to the description proper of the device for refractive surgical laser treatment of the cornea of the eye in accordance with the invention, there follow preliminary remarks summarising the effects of excimer laser light irradiation at a wavelength of 193 nanometres when such radiation is applied to the corneal tissue.

Figure 1 shows a curve of ablation on which the values of the depth of discrete elementary ablations are plotted on the ordinate axis, this axis being graduated in micrometres, as a function of the energy density per laser illumination pulse, the abscissa axis being graduated in millijoules/cm<sup>2</sup>.

The discrete elementary ablation curve is characterised by the presence of a threshold, that is to say a value of the energy density below which no ablation occurs. Generally speaking, the curve is strongly non-linear and the depth of ablation increases only very slowly with the energy density. It will in fact be noted that the depth of each discrete elementary ablation is small, lying between 0.25 and 1  $\mu$ m.

The refractive eye surgery device in accordance with the invention is, in its essentials, advantageously based on a discrete ablation process, a large number of discrete elementary ablations being employed to obtain a total resulting ablation. Although the discrete elementary ablation caused by a laser illumination pulse features the previously mentioned non-linearity with regards to its depth as a function of the energy density, it is assumed (providing that the energy density is constant from one pulse to another) that the resulting total ablation at a fixed point for a given number n of consecutive pulses is equal to n times the average ablation corresponding to a single pulse. Thus the discrete elementary ablation corresponding to the aforementioned average ablation is denoted:

$$\bar{a}(e) \quad (1)$$

This average ablation corresponds substantially for a laser illumination pulse with an energy density in the order of 200 millijoules/cm<sup>2</sup> to a depth of ablation corresponding to the step in the curve shown in figures 1, and in practice to a depth of ablation between 0.5 and 0.8  $\mu$ m.

A more detailed description of the operations to be carried out to correct ametropia by correcting dimensional optical characteristics of the cornea and principally its radius of curvature will be given with reference to figures 2a and 2b. To simplify the description of the device in accordance with the invention, the principal operations aforementioned will be limited to keratomileusis for treating myopia, hypermetropia and myopic astigmatism.

Figure 2a shows a plan view of the eyeball designated OE. The aforementioned plan view is seen along the



optical axis of the eye designated OZ in figure 2a, the aforementioned optical axis being centered on the cornea designated COR and the pupil of the iris, not shown in this figure. In the following explanation it will be considered that the optical axis and the visual axis of the eye are substantially coincident. Reference directions are denoted OX and OY, the frame of reference OX, OY being an orthogonal frame of reference. The distance

from a given point on the corneal surface to the optical axis OZ is designated  $h$ . Figure 2b shows a cross-section on the line A-A in figure 2a. In figure 2b the radius of curvature of the cornea COR before treatment, the cornea before treatment being shown in figure 2b in dashed outline, is designated  $r_0$  while  $r$  designates the radius of curvature of the cornea COR after treatment using the device in accordance with the invention. Generally speaking, R designates the radius of the optical area on the cornea for operating on and correcting the latter. Of course, the value of this parameter R and the area of the cornea over which the operation will be carried out are defined by the practitioner, following a clinical analysis carried out by him or her. Finally, A(h) designates the ablation function, that is to say the thickness (in the direction OZ of the optical axis of the eye) to be removed by photodecomposition to a distance h from the optical axis OZ of the eye to alter the cornea from the initial radius of curvature  $r_0$  to the final radius of curvature  $r$ , after the aforementioned operation.

In the case of keratomileusis for myopia, the object of the corresponding operation is to increase the radius of curvature of the cornea. The initial radius of curvature  $r_0$  is increased to a value  $r > r_0$  after the operation. This effect is obtained by ablation with a substantially parabolic profile of revolution and the ablation function is, using the notation from figures 2a and 2b:

$$A(h) = A_0 \left( 1 - \frac{h^2}{R^2} \right); \quad 0 \leq h \leq R \quad (2)$$

In the case of keratomileusis for hypermetropia, the object of the operation is to reduce the radius of curvature of the cornea, the initial radius  $r_0$  being reduced to a value of  $r < r_0$ . In this case ablation is still on a surface of revolution about the optical axis OZ of the eye, there being no ablation at the centre O, for  $h = 0$ , and maximum ablation for a particular value  $h = v$ . The ablation of the corneal profile between  $h = v$  and R then constitutes a merging area defined by purely mechanical considerations: no sudden transition with the optical area proper ( $h < v$ ) or with the rest of the cornea ( $h > R$ ). The ablation function A(h) satisfies the equation:

$$A(h) = A_0 \frac{h^2}{R^2} \quad \text{where } 0 \leq h \leq v \quad (3)$$

For values of  $h$  greater than  $v$  and less than R, the ablation function A(h) is a polynomial in  $h$  defining the aforementioned merging area according to previously mentioned mechanical considerations.

In equations (2) and (3) above,  $A_0$  represents, of course, the extent of ablation for  $h = 0$ , that is the thickness of ablation at the optical axis OZ of the eye itself:

$$A_0 = \frac{R^2}{2} \left( \frac{1}{r_0} - \frac{1}{r} \right)$$

In the case of keratomileusis for myopic astigmatism, the ablation is no longer on a surface of revolution. It will be remembered that in cases of corneal astigmatism the principal astigmatism directions are defined by orthogonal planes in which it is possible to define a maximum radius of curvature and a minimum radius of curvature for the optical surface in question, in this instance the cornea. In this case, and by way of simplification, and in line with what the practitioner will have to do in any event to carry out the operation using the device in accordance with the invention, it is advantageous to take as the reference directions OX and OY the principal astigmatism directions as previously defined. The aforementioned directions OX and OY are then contained in the aforementioned astigmatism planes. The radius of curvature of the cornea COR is in this case a

function of the azimuth angle denoted  $\beta$ , the radius of curvature  $r$  of the cornea after the operation for example satisfying the equation:

$$r(\beta) = r_x \cos \beta + r_y \sin \beta \quad (4)$$

In equation (4),  $\beta$  represents the azimuth angle of any plane containing the optical axis OZ, the azimuth angle being for example the dihedral angle formed by the aforementioned any plane and the plane OZ, OX. The values  $r_x$  and  $r_y$  are the corresponding values of the radius of curvature  $r$  for  $\beta = 0$  and  $\beta = \pi/2$ , respectively.

In the case of keratomileusis for myopic astigmatism, research has shown that the ablation profile may be written (the OX and OY axes having been determined as previously described):

$$A(X, Y) = A_0 \left( 1 - \frac{X^2}{R_x^2} - \frac{Y^2}{R_y^2} \right) \quad (5)$$

In equation (5), the quantities  $A_0$ ,  $R_x$  and  $R_y$  are defined by:

$$A_0 = \frac{A_0^x + A_0^y}{2}, \quad R_x = R \sqrt{\frac{A_0}{A_0^x}}, \quad \text{and} \quad R_y = R \sqrt{\frac{A_0}{A_0^y}} \quad (6)$$

The terms  $A_0^x$  and  $A_0^y$  are themselves defined as functions of the parameters  $R$ ,  $r_x$  and  $r_y$  by equations (7) and (8) below:

$$A_0^x = \frac{R^2}{2} \left( \frac{1}{r_x} - \frac{1}{r} \right) \quad (7)$$

$$A_0^y = \frac{R^2}{2} \left( \frac{1}{r_y} - \frac{1}{r} \right) \quad (8)$$

Generally speaking, iso-ablation curves are ellipses.

A more detailed description of the device in accordance with the invention for performing refractive surgery on the eye by laser treatment of the cornea will now be given with reference to figure 3a.

Referring to the aforementioned figure, the device in accordance with the invention comprises means 1 for emitting a laser beam denoted FL. The laser beam FL is a pulsed laser beam.

The means for emitting the laser beam FL are preferably an excimer laser emitting radiation at a wavelength of 193 nanometres. The emission means 1 preferably emit laser pulses with an energy level of the laser beam FL in the order of 180 millijoules per pulse, the repetition frequency of the laser pulses being in the order of 20 Hz. The duration of each pulse is in the order of 10 nanoseconds and the instantaneous power of each pulse reaches high values, in the order of 10 MW.

As further seen in figure 3a, the device in accordance with the invention comprises means 2 for generating a treatment laser beam denoted FLT comprising at least one lobe denoted L1 through L6 of elongate cross-section. In figure 3a the image of the treatment laser beam FLT has been shown to a larger scale, it being possible to show this image on a screen, for example, not shown in figure 3a.

The device in accordance with the invention also comprises means 3 for focussing the image of the lobe or lobes L1 through L6 of the treatment laser beam FLT on the area of the eye OE to be corrected, on the cornea of the latter. Of course, the means 2 for generating the treatment laser beam FLT and the means 3 for

focussing the image cause a loss of energy of the laser pulses of the laser beam FL, but the energy delivered to the cornea COR is in the order of 5 millijoules per pulse. The energy density on the image of the lobes of the laser beam generated by the means 3 for focussing the image of the aforementioned lobes is in the order of 200 millijoules/cm<sup>2</sup> as previously explained.

According to an advantageous aspect of the device in accordance with the invention, means 4 for moving the image of the lobe or lobes of the treatment laser beam FLT are provided for moving the aforementioned image over the area of the eye OE to be corrected.

Means 5 for synchronising the displacement of the image of the lobe or lobes of the treatment laser beam FLT over the area of the eye to be corrected are provided to ensure synchronisation with the pulses of the treatment laser beam.

Although the precise mechanism of the ablation process is still the subject of research, in some aspects it may be regarded as similar to a micro-explosion causing by photodecomposition a discrete elementary ablation by each laser pulse. The total correction or ablation resulting from implementation of the method in accordance with the invention is effected by summation of a plurality of elementary discrete ablations.

According to another advantageous characteristic of the device in accordance with the invention shown in figure 3a, the means 3 for focussing the image of the lobe or lobes L1 through L6 of the treatment laser beam FLT make it possible to focus the aforementioned image in such a way that the generatrix of an end of the lobe or lobes or the axis of longitudinal symmetry of the aforementioned lobe or lobes of the treatment laser beam are coincident with the optical axis OZ of the eye to be treated. Of course, as shown in figure 3a, the device in accordance with the invention may advantageously comprise an alignment device denoted 6 consisting, for example, of an auxiliary laser emission device such as a low-power helium-neon laser enabling the practitioner to carry out the appropriate adjustments of the focussing means 3 relative to the optical axis OZ of the eye OE of the patient.

According to another advantageous characteristic of the device in accordance with the invention, the means 4 for displacing the image of the lobe or lobes of the treatment laser beam over the area of the eye to be corrected make it possible to displace the image of the aforementioned lobes L1 through L6 in rotation about the previously mentioned end generatrix or the longitudinal axis of symmetry of the lobe or lobes of the treatment laser beam FLT.

According to an advantageous aspect of the device in accordance with the invention, the latter enables the aforementioned rotation by increments of the angle of rotation denoted  $\Gamma$ .

In one specific embodiment of the device in accordance with the invention shown in figure 3a, the means 2 for generating the treatment laser beam FLT may advantageously comprise a focussing optical system 20. The focussing optical system 20 may consist of a Galilean telescope producing from the laser emission means 1 a laser beam FL of regular (for example cylindrical) cross-section.

According to another particularly advantageous aspect of the device in accordance with the invention, the means 4 for displacing the image of the lobe or lobes of the treatment laser beam in rotation may comprise, as shown in figure 3a, a mask or diaphragm 21 incorporating an object slit denoted 211. Of course, the object slit 211 is of elongate shape and illuminated, for example in parallel light, by the laser beam FL. One end of the object slit 211 is disposed, for example, at the centre of the diaphragm 21 and generates the aforementioned end generatrix of the treatment laser beam FLT or the longitudinal axis of symmetry of the lobes L1 through L6 of the treatment laser beam FLT.

The object slit 211 and the image of this object slit are rotated by drive means 40, 41 for rotating the mask or diaphragm 21.

Of course, but not in any limiting way, the diaphragm 21 may be a circular shape diaphragm and the drive means for the diaphragm 21 advantageously comprise a toothed ring denoted 210 disposed at the periphery of the diaphragm and a stepper motor 40 the drive shaft of which is fitted with at least one toothed wheel 41 meshing with the toothed ring 210.

To focus the image of the lobe or lobes of the treatment laser beam FLT, the focussing means 3 advantageously comprise a semi-reflecting mirror 30 consisting of a prism or the like, for example, serving by total reflection to transmit the treatment laser beam FLT and the alignment beam delivered by the alignment means 6, together with a focussing lens 31 constituting the objective lens of the device. The combination of the semi-reflecting mirror 30 and the focussing lens 31 serves to form the image of the treatment laser beam FLT on the area of the cornea to be treated, of course.

In a conventional way, all of the device in accordance with the invention and in particular the means 2 for generating the treatment laser beam FLT and the laser emission means are mounted on an optical bench and the focussing means 3 are mounted on a barrel that can be oriented by the practitioner for correct aiming onto the area of the eye to be treated. The corresponding mountings for the aforementioned component parts as a whole will not be described as they constitute part of the prior art in the field of high-precision optical instruments.

A more detailed description of the diaphragm enabling operations as previously described herein by means of the image of the laser beam lobe moved in rotation over the area of the eye to be treated will now be given with reference to figures 3b, 3c, 3d and 3e.

One embodiment of the object slit 211 of the diaphragm 21 will be described first in connection with treatment or operation by keratomileusis for myopia, the image of the lobe or lobes of the treatment laser beam FLT being rotated about the optical axis OZ of the eye to be treated.

Referring to the aforementioned figure 3b, the object slit 211 of the diaphragm 21 has a profile satisfying the equation:

$$\Theta(\rho) = \Gamma \frac{A_0}{\bar{a}(e)} \left(1 - \frac{\rho^2}{R^2}\right) = \Theta(0) \left(1 - \frac{\rho^2}{R^2}\right) \quad (9)$$

In the aforementioned equation,  $\theta(\rho)$  represents the aperture angle of the slit defined as the angle at the centre of a circle with its centre at the end of the object slit, for generating the end generatrix or the axis of symmetry of the treatment laser beam FLT with for radius the corresponding value  $\rho$  of the distance from a point on the edge of the slit or lip of the object slit or of the lobe of the laser beam to the aforementioned centre.

In figure 3b it will be noted that the object slit 211 has convex lips or edges, the aperture angle  $\theta(0)$  of the slit at the origin, that is to say at the centre  $O'$  at the end of the slit being maximum.

$\Gamma$  represents the increment of angular rotation as previously mentioned. It will be noted that equation (9) represents the equation in polar coordinates of one of the lips of the slit, the other being deducible by considerations of symmetry.

Another example of an embodiment of an object slit 211 of the diaphragm 21 for treatment of hypermetropia by keratomileusis in the case where the operation is conducted by rotating the image of the lobe or lobes of the treatment laser beam FLT will also be described with reference to figure 3c.

In this case, as shown in the aforementioned figure, the profile of the slit 211 satisfies the equation:

$$\Theta(\rho) = \Gamma \frac{A_0}{\bar{a}(e)} \frac{\rho^2}{R^2}, \quad \rho \in [0, v], \quad v < R \quad (10)$$

$$= \theta_{\max} \frac{\rho^2}{R^2} \quad \text{where} \quad \theta_{\max} = \Gamma \frac{A_0}{\bar{a}(e)}$$

In equation (10) the parameters are defined according to the definitions previously given. It will be noted that the lips of the slit 211 in the case of figure 3c are substantially concave up to a particular value of the radius  $\rho$ , this particular value being denoted  $v$ . It will be noted that the corresponding lip then has a point of inflection, the curvature of the latter becoming convex and decreasing regularly up to the end of the slit corresponding to the maximum longitudinal dimension of the latter. This continuous decrease in the aperture angle  $\theta$  beyond the value of the radius  $\rho = v$  advantageously serves to prevent excessive discontinuity at the periphery of the resulting total ablation. In a non-limiting way and by way of example only, the particular value of  $v$  is substantially equal to 2/3 of the maximum longitudinal dimension of the slit.

Of course, as shown in figure 3d in particular, the diaphragm 21 may advantageously comprise a plurality of elementary object slits denoted 211<sub>1</sub>, 211<sub>2</sub> through 211<sub>n</sub> in the aforementioned figure. Each elementary object slit generates a corresponding lobe of the treatment laser beam FLT, of course. The number of slits in the same diaphragm 21 is limited only by the maximum aperture  $\theta_{\max}$  of the object slit in question, the aperture angle at the origin  $\theta(0)$  of each slit in the case of figure 3d and  $\theta(R)$  in the case of figure 3c, for treatment of hypermetropia by keratomileusis.

It will be noted, of course, that increasing the number of object slits on the diaphragm provides for a commensurate decrease in the total operation time, since the summation of the successive elementary ablations achieved on the area to be treated by rotating the diaphragm and the object slit is added to the spatial summation due to the corresponding distribution of the various object slits on the diaphragm. It will be noted that in the case of multiple slits they may be regularly distributed over the diaphragm and all meet at their common end situated of the axis of rotation. Each of the slits generates in this way one lobe of the treatment laser beam FLT. In the case of slits used for treatment of myopia by keratomileusis, adjacent slits tangential to the centre have a surface area exactly equal to one-half the surface area of the disk within which the slits are inscribed.

It will be noted that the choice of the angular rotation increment  $\Gamma$  actually determines the surface area of the object slit or slits used and vice versa. The choice of the angular increment  $\Gamma$  and the maximum aperture angle

$\theta_{\max}$  are governed by the following considerations:

A narrow slit corresponding to a small angular increment  $\Gamma$  enables use of a small part of the laser beam FL with the possibility of choosing the most homogeneous part of the latter, use of a low-power laser and also irradiation of a small part of the cornea by each pulse. Furthermore, increasing the number ND of slit images that are totally separated or at worst tangential, the number of images ND being denoted ND<sub>1</sub> in the case of treatment of myopia by keratomileusis and ND<sub>2</sub> in the case of treatment of hypermetropia by keratomileusis, means that the sequence of positions of the irradiated slits can be programmed to minimise heating of the cornea.

On the other hand, too small a rotation increment  $\Gamma$  can lengthen the correction or treatment period.

In practice it is more advantageous to have a limited set of slits and to vary the rotation increment  $\Gamma$  as appropriate to the required correction.

Thus a slit is totally defined by:

- its length which defines the radius of the corrected area, that is to say the parameter R defined by the practitioner,

- the type of correction or operation carried out, that is to say keratomileusis for myopia or hypermetropia, - the maximum aperture angle  $\theta_{\max}$  appropriate to the type of correction or operation carried out.

For optimum performance of the operation, the device in accordance with the invention comprises means 8 for calculating the angular rotation increment  $\Gamma$  which, for a given object slit (the slit having been chosen beforehand by the practitioner, of course) satisfies the equation:

$$\Gamma = \theta_{\max} \frac{\bar{a}(e)}{A_0} \quad (11)$$

The calculation means 8 are then used to determine the number of laser emission pulses NI, this number of laser pulses being denoted NI<sub>1</sub> in the case of treatment of myopia by keratomileusis. The number NI<sub>1</sub> of laser emission pulses satisfies the equation:

$$N_{I1} = \frac{2\pi}{\Gamma} = N_{D1} \frac{A_0}{\bar{a}(e)} \quad (12)$$

In the aforementioned equation ND<sub>1</sub> represents the number of separate or adjacent slit images that can be formed on the area of the cornea COR to be treated.

The calculation means 8 are also used to calculate the minimum total irradiation time denoted T<sub>min</sub> or T<sub>1min</sub> in the case of treatment of myopia by keratomileusis. In this case, the minimum total irradiation time satisfies the equation:

$$T_{lmin} = N_{I1} \frac{\tau(e)}{N_{D1}} = \tau(e) \frac{A_0}{\bar{a}(e)} \quad (13)$$

In this equation,  $\tau(e)$  represents the minimum time interval between two successive irradiations of the same point on the cornea. The value of  $\tau(e)$  is established experimentally and is the threshold beyond which heating of the cornea may occur. The value T<sub>1min</sub> depends of course on the energy flux but does not depend on the rotation increment  $\Gamma$ . This is because all of the ND<sub>1</sub> separate slits can be irradiated in the aforementioned interval  $\tau(e)$ . In practice, the type of laser used to produce the laser pulses and the maximum speed of displacement of the slit may limit the frequency at which the pulses can be delivered.

The refractive eye surgery device using laser illumination in accordance with the invention may also be used to correct astigmatism of the cornea COR or of the eyeball.

In a case like this the ablation profile varies with the meridian in question of the eyeball, this meridian consisting of the intersection with the surface of the cornea of a plane containing the optical axis OZ of the eyeball oriented at an angle  $\beta$  in azimuth relative to a plane containing the previously defined reference

direction OX. In the case where, as previously defined, the reference directions OX and OY correspond to the principal directions of astigmatism, and in the case of myopic astigmatism, the ablation function satisfies the equation:

$$A(h, \beta) = A_0(\beta) \left(1 - \frac{h^2}{R^2}\right) \quad (14)$$

In this equation,  $A_0(\beta)$  is equal to:

$$A_0(\beta) = \frac{1}{2} R^2 \left( \frac{1}{r(\beta)} - \frac{1}{r} \right) \quad (15)$$

$$r(\beta) = r_x \cos \beta + r_y \sin \beta$$

From the equations (6), (7) and (8) previously given in this description, it is possible to compensate for the variations in  $A_0(\beta)$  by varying the rotation increment  $\Gamma$  as a function of  $\beta$ .

In this way it is possible to correct astigmatism of the eyeball with slits identical to those previously described with reference to figures 3a, 3b, 3c, 3d by modulating the angular rotation increment  $\Gamma$  as a function of the angle  $\beta$  defining the meridian of the cornea of the eyeball.

To this end, the device in accordance with the invention comprises means for modulating the angular rotation increment  $\Gamma$  as a function of the angle  $\beta$ , this angle rotation increment  $\Gamma$  as a function of the angle  $\beta$  satisfying the equation:

$$\Gamma(\beta) = \Theta \frac{\bar{a}(e)}{\max A_0(\beta)} \quad (16)$$

In this equation,  $A_0(\beta)$  represents the ablation at the origin near the optical axis OZ of the eyeball in the direction with azimuth angle  $\beta$ .

However, in the case of myopic astigmatism, the ablation at the centre is not constant and varies with the meridian. To establish circular symmetry of the cornea the device in accordance with the invention may comprise as shown in figure 3e at least one auxiliary diaphragm 21 provided with an object slit 211 of circular sector shape the equation for which in polar coordinates is  $\theta(\rho) = k$  where  $k$  is a constant. The aforementioned auxiliary slit 211 enables such correction by means of supplementary irradiation and rotational displacement by the rotation increment  $\Gamma(\beta)$  modulated as a function of the azimuth angle  $\beta$  to establish a constant ablation at the origin 0 without modifying the radius of curvature of the cornea, however. The residual ablation to be effected during such supplementary irradiation using the slit 211 shown in figure 3e satisfies the equation:

$$\delta A(\beta) = A_0(0) - A_0(\beta)$$

$$\text{with } A_0(0) = \frac{R^2}{2} \left( \frac{1}{\min(r_x, r_y)} - \frac{1}{r} \right)$$

in which equation  $\min(r_x, r_y)$  represents the smaller of the values  $r_x$  and  $r_y$ .

The residual ablation effected during the supplementary irradiation is then obtained by modulating the angular rotation increment  $\Gamma$  as a function of the azimuth angle  $\beta$ , the rotation increment  $\Gamma$  satisfying the equation:

$$\Gamma(\beta) = \Theta(0) \frac{\bar{a}(\epsilon)}{\delta A(\beta)} \quad (18)$$

It should be noted that this method introduces a discontinuity at the periphery of the resulting total ablation, this discontinuity being null for  $\beta = 0$ , that is in the OX direction, and maximal for  $\beta = \pi/2$ , that is in the OY direction. The maximal value of this discontinuity is equal to:

$$\frac{R^2}{2} \left( \frac{1}{r_Y} - \frac{1}{r_X} \right) \quad (19)$$

with  $r_X < r_Y$ .

This discontinuity can be resolved, as will be explained later in this description.

In an alternative embodiment of the device shown in figure 3a, for the purpose of compensating by correction astigmatism of the eyeball and of the cornea, the device may comprise upstream of the focussing means 3, on the path of the treatment laser beam FLT, an anamorphic optical system 9 in which the magnification depends on the azimuth angle  $\beta$ . In this case, the iso-ablation curves on the cornea are ellipses. Correction of astigmatism implies that the total resulting ablation as a function of the azimuth angle  $\beta$  is not constant. Anamorphic systems are systems in which the magnification depends on the aforementioned azimuth angle  $\beta$ . Generally speaking, and with the orientation of the axes OX and OY previously defined relative to the eyeball in figure 2a, an anamorphic system having a corresponding magnification denoted  $M_X$  and  $M_Y$  at an elementary surface  $dS$  of the object, that is to say of the object slit 211, corresponds to an elementary surface  $dS' = M_X M_Y dS$  of the image given by the anamorphic system. Under these conditions, the image of a circle obtained by means of the rotating slit or by some other equivalent means is an ellipse. Thus the iso-energy curves in the object plane of the anamorphic system, that is to say of the object slit 211, are circles and the images of these circles given by the anamorphic system are ellipses. Given that the total resulting ablation at a given point on the cornea is proportional to the energy received at that point, the iso-ablation curves are consequently ellipses.  $R_X$  and  $R_Y$  being the half major axes of these ellipses, the magnifications  $M_X$  and  $M_Y$  of the anamorphic system 9 must be in the same ratio as the aforementioned half major axes. The anamorphic system 9 may consequently comprise two cylindrical lenses the longitudinal axes of which are orthogonal and respectively oriented to define the corresponding directions OX and OY, the lenses having respective magnifications  $M_X$  and  $M_Y$ . These anamorphic optical systems as such are prior art and because of this they will not be described in more detail in this description.

Of course, to facilitate the work of the practitioner the device in accordance with the invention may be provided with an auxiliary diaphragm 21 having an object slit 211 of circular arc shape with a particular radius of curvature. This type of object slit is shown in figure 3f by way of non-limiting example. It is used to make circular incisions for arc-shaped corneal grafts, for example.

Also, the object slit as shown in figure 3e may also be used to correct astigmatism as previously described by modulating the rotation increment as a function of the azimuth angle  $\beta$ , to carry out such operations as removal of a locally parallel faced meniscus for epikeratohakia, or removal of a parallel surface corneal disc from a donor or removal of a surface to be modified by the laser for correcting myopia or hypermetropia, with a view to carrying out lamellar grafting. The lamellar grafting operations may then be carried out with constant rotation increments  $\Gamma$ , the ablation obtained during this operation corresponding to that of a locally parallel faced meniscus the edges of which are substantially rectilinear.

An alternative embodiment of the device in accordance with the invention more particularly adapted to operations such as those previously described will be described with reference to figure 4a.

In the embodiment shown in the aforementioned figure, but in a non-limiting way, the means 4 for displacing the image of the lobe or lobes of the treatment laser beam FLT over the area of the line to be treated provide for displacement in translation in a direction  $d$  substantially perpendicular to the largest dimension denoted Oz of the lobe of the treatment laser beam FLT. In this case, as will be described in more detail later in this description, the treatment laser beam FLT may be advantageously comprise two lobes or component parts of a single lobe symmetrical relative to a centre of symmetry denoted O".

According to an advantageous characteristic of the device in accordance with the invention shown in figure 4a, the displacement in translation is advantageously effected by means of displacement increments denoted  $\Delta u$ . The displacement in translation is defined relative to the two reference directions OX, OY with  $u = X$  or  $u = Y$ , these directions defining a plane tangential to the cornea at the point O on the optical axis of the eyeball as defined previously in figure 2a.

The means 4 for displacement in translation of the image of the lobe or lobes of the treatment laser beam FLT advantageously provide for displacement in translation of the latter in the orthogonal directions OX and OY.

As shown by way of non-limiting example in figure 4a, the means 4 for displacing the image of the lobe or lobes of the treatment laser beam FLT in translation may comprise in succession along the path of the laser beam FL: a fixed diaphragm denoted 21 comprising at least one object slit 211 of elongate shape. This object slit is illuminated with parallel light. As shown in a non-limiting way in figure 4a, the laser beam FL may be generated by the means 1 previously described in relation to figure 3a, the laser beam FL possibly having a rectangular cross-section obtained in the classical way by passing the emitted laser beam through suitable diaphragms. Of course, as shown in figure 4a, a lens 20, a direction-changing mirror 21 such as a semi-reflecting mirror enabling under conditions analogous to those of figure 3a transmission of an auxiliary alignment laser beam not shown in this figure and a field lens 22 are used to conduct the parallel light laser beam FL to the slit 211 in the diaphragm 21.

Moreover, as also shown in figure 4a, a first lens 23 is placed relative to the object slit 211 and to the diaphragm 21 so that the object slit 211 is in the object focal plane of the lens 23 to generate the lobe or lobes of the beam imaging the object slit in parallel light.

A rotating prism 420 is provided whereby rotation of the prism in question through an angle  $\alpha$  rotates the emergent light beam, i.e. the treatment laser beam FLT, through an angle  $2\alpha$ .

Also, a second focussing lens 430 serving as an objective lens is movable in translation in the previously mentioned directions OX and OY.

It will be understood that the embodiment of the device in accordance with the invention shown in figure 4a is particularly advantageous in that it enables two methods to be used: in the first the treatment laser beam FLT is scanned in rotation, the focussing lens 430 being held in a fixed position and centred on the optical axis OZ of the eye, of course, the prism 420 then being rotated to obtain the corresponding scanning of the treatment laser beam; in the second method, with the prism 420 fixed in position, the treatment laser beam emerging from the prism 420 is directed along the optical axis OZ of the eye and the focussing lens 430 produces corresponding movement in translation of the treatment laser beam FLT by corresponding defocussing due to movement of the lens 430 in translation in direction X or in direction Y.

The rotator prism 420 may advantageously be a Dove or Wollaston prism. Also, a diaphragm denoted DFI may be provided between the lens 430 and the eye of the patient to limit the luminous intensity received by the eye OE of the patient. It may be disposed in the vicinity of or on the eye. Of course, other direction-changing mirrors can be provided on the path of the laser beam FL to obtain an appropriate optical path to enable unrestricted circulation of persons in the environment of the apparatus and the practitioner.

The device in accordance with the invention in figure 4a is particularly advantageous in that, over and above any possible operation by scanning the area of the eye to be treated in rotation, it also makes it possible to carry out this operation by scanning the laser beam over the area of the eye to be treated in translation, in particular in the previously mentioned two directions OX and OY. The lobe or lobes of the laser beam and the beam direction Oz being oriented in the OY direction, the scanning in one direction (the OX direction, for example) is obtained by means of the rotator prism 420. This orients the aforementioned direction Oz with the OX direction for subsequent movement of the treatment laser beam FLT in the direction perpendicular to the new orientation of the Oz axis, i.e. the direction OY. The displacement in translation is effected by displacing the lens 430 in the corresponding directions.

A more detailed description of an object slit 211 profile specifically used in the case where displacement in translation of the image of the object slit 211 is brought about to carry out the treatment or operation as aforementioned will be given with reference to figures 4b, 4c, 4d.

Referring to figure 4b, the object slit 211 of the diaphragm 21 and consequently the image of the lobe or lobes of the treatment laser beam FLT for treatment and correction by keratomileusis of myopia and astigmatism has a substantially parabolic profile. The profile defined by one 1/2 of the slit satisfies the equation:

$$E(z) = 2 E_{\max} \left( \frac{1}{2} - \frac{z^2}{R^2} \right) \quad (20)$$

It will be noted for convenience that the slit 211 has a longitudinal axis denoted O"x.

In the above equation, the various parameters are defined as follows:

E(z) represents the transverse dimension of the object slit or of the lobe of the treatment laser beam at the abscissa z on the longitudinal reference axis oriented relative to the slit. The abscissa is referenced relative to an origin point O".

E<sub>max</sub> represents the maximal transverse dimension of the object slit 211.

While carrying out the aforementioned operation, the practitioner is required to displace the image of the object slit 211 in translation along a direction at least perpendicular to the longitudinal axis O"z of the object



slit 211. Of course, the image of the object slit 211 is then oriented in such a way that the longitudinal axis  $O''z$  of the latter is oriented in one of the directions OX or OY of figure 2a. Thus for a direction  $u$  of orientation of the slit 211 or of its longitudinal axis  $O''z$  in the direction OX or OY, the equation relating the aperture of the slit  $E(u)$  and the translation displacement increment denoted  $\Delta u$ , this displacement being in the direction perpendicular to the orientation direction  $u$  of the slit, is of the form:

$$E(u) = \Delta u \frac{A_0}{\bar{a}(e)} \left( \frac{1}{2} - \frac{u^2}{R^2} \right) \quad (21)$$

In this equation:

$u$  represents the abscissa or position of the edge of the slit on the longitudinal axis of reference  $O''z$ , the slit itself being oriented in the direction  $u$  corresponds to the direction OX or to the direction OY,

$\Delta u$  represents the translation displacement increment in the direction orthogonal to the aforementioned alignment direction  $u$ , i.e. in the direction OY or in the direction OX,

$A_0$  represents the thickness of ablation or correction at the centre of the area of the cornea to be corrected at the time of displacement in translation of the object slit 211 or of the lobe of the treatment laser beam in the direction OY or in the direction OZ.

A description of an object slit 211 for treatment and correction of the cornea by keratomileusis for hypermetropia and hypermetropic astigmatism will also be given with reference to figure 4c.

In the case of the aforementioned operation, the object slit 211 and the corresponding lobe or lobes of the treatment laser beam FLT have a substantially parabolic profile satisfying the equation:

$$E(z) = E_{\max} \left( \frac{z^2}{R^2} \right) \quad (22)$$

As in figure 4b the orientation of the longitudinal axis  $O''z$  of the object slit 211 in the direction OX or in the direction OY serves to establish the relationship defining the connection between the displacement increment  $\Delta u$  in the direction perpendicular to the orientation direction and the aperture  $E(u)$  of the slit 211, this relationship being of the form:

$$E(u) = \Delta u \frac{A_0}{\bar{a}(e)} \left( \frac{u^2}{R^2} \right) \quad (23)$$

In the above equations (22) and (23), the same notation designates the same parameters as in the previous equations (20) and (21).

In an analogous manner to an operation carried out by scanning the image of the object slit 211 in rotation, in the case of scanning in translation the values of the displacement increment in the direction perpendicular to the alignment direction of the axis  $O''z$  of the object slit 211 and the irradiation times satisfy similar equations.

Consequently, in the figure 4a embodiment, the device in accordance with the invention comprises calculation means denoted 8 for calculating the translation displacement increment  $\Delta u$  in the direction OY or OX for an orientation  $u$  in the direction OX, OY, the increment for a given object slit satisfying the equation:

$$\Delta u = E_{\max} \frac{\bar{a}(e)}{A_0} \quad (24)$$

In this equation the parameters  $\bar{a}(e)$  and  $A_0^u$  correspond of course to the definitions given previously in this description.

Also, in the embodiment shown in figure 4a, the device in accordance with the invention also comprises means 8 for calculating the number of laser emission pulses denoted  $NI_2$  and the number of translation displacements increments  $\Delta u$  in the direction OY, OX. The number  $NI_2$  of pulses satisfies the equation:

$$NI_2 = \frac{2\pi}{\Delta u} = ND_2 \frac{A_0^u}{\bar{a}(e)} \quad (25)$$

In this equation  $ND_2$  represents the number of totally separate or adjacent images that can be formed on the cornea.

In the same way as in the case of treatment or correction by an object slit or object slit image performing a rotating scan, in the figure 4a embodiment the calculation means 8 may also be used to calculate the minimum total radiation time denoted  $T_{2min}$ . This satisfies the equation:

$$T_{2min} = NI_2 \frac{\tau(e)}{ND_2} = \tau(e) \frac{A_0^u}{\bar{a}(e)} \quad (26)$$

In this equation,  $\tau(e)$  represents the minimum time interval between two successive irradiations of the same point on the cornea.

As will be noted from figures 3b, 3c, 3d, 3e, 4b, 4c and 4d in particular, the object slits 211, whether used during an operation to effect scanning in rotation or in translation of the area of the cornea to be treated, are symmetrical with respect to their longitudinal axis O'z or O''z. This corresponds to a particularly advantageous, non-limiting embodiment in which, without departing from the scope of the present invention, the slits may be asymmetrical with respect to the longitudinal axis O'z or O''z provided that the corresponding width of the slit at a given point z is substantially the same.

As will be noted in figure 4c, in the case of an object slit 211 used for treatment of hypermetropia by scanning in translation the object slits, whether they generate one or more lobes of the treatment laser beam FLT scanned in rotation or in translation, may advantageously comprise a curvilinear shape edge denoted C at the end. This edge at the end is, as shown to a larger scale in figure 4c, symmetrical with respect to the longitudinal axis O''z. The curvilinear shape departs from the variation law  $p = \text{constant}$ , representing a circular arc in polar coordinates, to eliminate edge effects from the resulting profile of the total ablation obtained.

As will be noted in figure 4c, in a non-limiting way, the curvilinear shape C may be concave and convex with a point of inflection. Likewise, provided that the curvilinear shape C departs from the variation law  $p = \text{constant}$ , the edge at the end may equally well be continuously concave, as shown in dashed outline in the enlarged view of figure 4c.

A curvilinear character of this kind for the edge of the slits at the end improves the continuity of the curvature in transitions between corrected and uncorrected areas. Thus any slit of which an edge at the end has a non-zero width or aperture could comprise the aforementioned curvilinear slit C. The curvilinear shape C, in the absence of any point of inflection, provides for transitions between corrected and uncorrected areas at which there is a discontinuity in the curvature.

Of course, in an analogous way to the embodiment of the object slits in figure 3e in the case of rotational scanning for a plurality of object slits 211 on the same diaphragm 21, in the case of treatment by scanning in translation it is also possible to use a plurality of object slits 211 on the same diaphragm. A diaphragm of this kind is shown in figure 4d, in which three slits 211<sub>1</sub>, 211<sub>2</sub> and 211<sub>3</sub> have been shown by way of non-limiting example. The various object slits are spaced in a direction perpendicular to their longitudinal axes O'z by a distance at least equal to the widest aperture  $E_{max}$  thereof.

A prototype of the device in accordance with the invention was manufactured with the object slits 211 as described previously with reference to figures 3b, 3c, 3d, 4b, 4c and 4d.

To give a non-limiting example, in the case of an object slit such as that shown in figure 3b, the object slit 211 had a length substantially equal to 3.2 mm, its length being measured along the longitudinal axis O'z, and a width or maximal dimension in the direction perpendicular to the aforementioned longitudinal axis substantially equal to 0.8 mm.

An object slit 211 as shown in figure 3c had a length substantially equal to 3.2 mm and a maximal width in the

order of 1.4 mm.

In the case of an object slit 211 as shown in figure 4b the length of the slit along the longitudinal axis O"z was in the order of 6 mm and its maximal width in the order of 1 mm.

Of course, the foregoing dimensions of the object slits 211 are given by way of non-limiting example only, since it is to be understood that these dimensions vary according to the total magnification of the optical system of the device in accordance with the invention. The latter may of course and advantageously be provided with an optical system offering variable magnification so that from a particular design of object slit the practitioner is in a position to choose the final dimension of the image of the lobe or lobes of the treatment laser beam FLT given by the aforementioned object slits.

In accordance with another advantageous characteristic of the device in accordance with the invention, with particular reference to the figure 4a embodiment in which the diaphragm 21 is fixed, each slit may advantageously have a variable profile to provide for compensation for any irregular distribution of the light energy over the cross-section of a lobe of the treatment laser beam FLT.

As will be noted in figure 4e, the variable slit 211 may comprise at least one edge made up of mobile strips denoted 2110, these strips being movable in translation in a direction perpendicular to the longitudinal axis O"z of the slit. The mobile strips 2110 may of course be disposed to slide relative to each other, each being adapted to be driven by the intermediary of a motor or like means 2111. It will be understood of course that in the case of the figure 4e embodiment the dimensions of the object slit 211 may be increased to facilitate implementation of the movable strips, the magnification of the optical system of the device in accordance with the invention being adjusted accordingly.

One example of an operation for treatment of myopic astigmatism by keratomileusis using the device in accordance with the invention shown in figure 4a and scanning of the area to be treated in translation will now be described with reference to figure 5a.

The total resulting ablation is in this instance obtained by means of a slit such as that shown in figure 4d, for example, the image of the slit or the lobe of the treatment laser beam FLT being displaced in a direction perpendicular to the longitudinal axis O"z in consecutive elementary increments. The elementary displacement increments being equal, the effect of the treatment is to produce a channel of uniform parabolic profile. The length of the channel is of course equal to the distance over which the slit is displaced and its width is equal to the length of the slit.

In a particularly advantageous method of working, two operations are effected along two perpendicular axes to achieve complete correction of the cornea COR.

In the case of myopia, this method of working has the following advantages:

- It eliminates the problem of precisely focussing the end or the image of the slit on the rotation axis in the case of scanning in rotation, and

- it enables all types of astigmatism to be corrected.

The longitudinal axis O"z of the slit being oriented in the direction OX, for example, in figure 2a, irradiation of the object slit 211 in successive positions spaced by a constant translation increment  $\Delta Y$  in the direction OY in figure 2a within a range of displacement ranging between  $-R/\sqrt{2}$  and  $+R/\sqrt{2}$  serves to obtain with respect to the axis OX an ablation profile B(X) defined by the equation:

$$B(X) = \bar{a}(e) \left[ \frac{E(X)}{\Delta x_Y} \right], \quad \forall X \in \left[ \frac{-R}{\sqrt{2}}, \frac{R}{\sqrt{2}} \right] \quad (27)$$

In this equation:

- E(X) represents, of course, the profile of the slit at the abscissa X and  $\Delta x_Y$  represents the constant translation displacement increment in the direction Y, the slit being oriented in the direction X,

- R is the radius of the area to be corrected centered at O".

As previously mentioned in this description, when the axes OX and OY from figure 2a correspond to the principal directions of the meridians corresponding to the ends of the curves at the centre of the cornea, the principal astigmatism directions, the ablation profile to be obtained is expressed by the equation:

$$A(X, Y) = A_0^x \left( \frac{1}{2} - \frac{X^2}{R^2} \right) + A_0^y \left( \frac{1}{2} - \frac{Y^2}{R^2} \right) \quad (28)$$

In equation (28) the parameters  $A_0^x$  and  $A_0^y$  satisfies the equations:

$$A_0^x = \frac{R^2}{2} \left( \frac{1}{r_x} - \frac{1}{r} \right) \quad (29)$$

$$A_0^y = \frac{R^2}{2} \left( \frac{1}{r_y} - \frac{1}{r} \right) \quad (30)$$

The ablation function may be regarded as the result of summing two ablation functions, one a function of X only and the other a function of Y only. In equations (29) and (30),  $r_x$  represents the radius of curvature of the cornea in the direction OX and  $r_y$  represents the radius of curvature in the direction OY,  $r$  representing the radius of curvature of the cornea in a meridian direction at the azimuth angle  $\beta$  previously mentioned.

Adopting the following notation:

$$A_0 = \frac{A_0^x + A_0^y}{2} \quad (31)$$

$$R_x = R \sqrt{\frac{A_0}{A_0^x}} \quad (32)$$

$$R_y = R \sqrt{\frac{A_0}{A_0^y}} \quad (33)$$

the equation for the resulting total ablation function may be written:

$$A(X, Y) = A_0 \left( 1 - \frac{X^2}{R_x^2} - \frac{Y^2}{R_y^2} \right) \quad (34)$$

The iso-ablation curves are therefore ellipses in the general case and the equation for the ellipse which delimits the ablation contour is:

$$\frac{X^2}{R_x^2} + \frac{Y^2}{R_y^2} = 1 \quad (35)$$

As shown in figure 5a, theory indicates that the resultant ablation should extend from  $-R_x$  to  $+R_x$  on the OX axis and from  $-R_y$  to  $+R_y$  on the OY axis. The ablation profile is thus contained within two orthogonal rectangles with respective lengths  $2R_x$  and  $2R_y$  and the same width  $R/\sqrt{2}$  and whose common area is square inscribed in the circle  $C_0$  of radius  $R$  centered at O. The ablation profile obtained is perfect within the square where they intersect although a satisfactory approximation of the ablation profile is nevertheless obtained outside the square in the areas peripheral to the latter, the areas FGHI in figure 5a, the central area consisting of the square being denoted A.

In the case of pure myopia with no astigmatism,  $r_x = r_y$  and  $A_0 = A_x^0 = A_y^0$ .

Thus correction or treatment by means of an object slit scanned in translation along two orthogonal directions produces an optimal effect where the areas scanned by the treatment laser beam FLT in the aforementioned directions intersect, that is over a square in plane projection.

To extend this action beyond the intersection square and to obtain satisfactory correction over a substantially circular area it is possible to extend the lateral scanning of the treatment laser beam FLT while modulating the displacement increment  $\Delta u$  between two adjacent positions, the aforementioned increment  $\Delta u$  remaining constant in the intersection area, of course.

It has been shown that the ablation profile in the first area made up of the three areas A, F and H (that is for  $-R/\sqrt{2} \leq X \leq +R/\sqrt{2}$ ) is achieved by irradiating a slit parallel to the axis OX and moving by increments  $\Delta y_x$  in the direction perpendicular to the OY axis.

Likewise, the ablation profile in the area made up of the area I, A and G (that is for  $-R/\sqrt{2} \leq Y \leq R/\sqrt{2}$ ) is achieved by irradiating a slit parallel to the OY axis moved in increments  $\Delta y_x$  or  $\Delta u$  along the OX axis.

This second operation, correction of the profile along OY, does not modify the profile along an axis parallel to OX, but deepens it uniformly ( $Y = \text{constant}$ ) in particular by an amount  $A_y^0$  over all of the axis OX, that is for  $Y = 0$ .

To complete the resulting total ablation profile along OX and to avoid any discontinuity for  $X = \pm R/\sqrt{2}$  the scanning in translation along OX of the slit which generates the ablation profile along OY can be extended beyond these values, with the translation displacement increment along OX increasing with  $X$  for  $|X| > R/\sqrt{2}$ .

The device in accordance with the invention as shown in figure 4a uses the calculation means 8 to determine the value of the linear displacement increment denoted  $\Delta y_x$ , for example to obtain an exact extension of the parabolic profile for  $Y = 0$ , the translation displacement increment for a corresponding ablation function satisfying the equation:

$$A(X, 0) = A_0 \left( 1 - \frac{X^2}{R_x^2} \right) \quad (36)$$

The translation displacement increment then satisfies over all of the treatment domain comprising areas F, A and H in figure 5a the equation:

$$\Delta Y_x(X) = \begin{cases} E_{\max} \frac{\bar{a}(e)}{A_0 \left(1 - \frac{x^2}{R_x^2}\right)}, & \text{for } \frac{R}{\sqrt{2}} \leq |x| \leq R_x \\ E_{\max} \frac{2 \bar{a}(e)}{A_0^Y}, & \text{for } |x| < \frac{R}{\sqrt{2}} \end{cases} \quad (37)$$

In equations (36) and (37),  $R_x$  defines the total irradiation domain in the X direction. The resulting total ablation function  $A_x(X, Y)$  which defines the resulting total ablation in rectangles F and H in figure 5a, that is to say for

$$\frac{R}{\sqrt{2}} \leq |x| \leq R_x, \quad |y| \leq \frac{R}{\sqrt{2}},$$

satisfies the equation:

$$A_x(X, Y) = \frac{E(Y)}{\Delta X} \bar{a}(e) \quad (38)$$

In this equation  $E(Y)$  represents, of course, the profile of the slit used, the slit having its longitudinal axis  $O'z$  oriented in the Y direction and  $\Delta Y_x$  corresponding to the values of equation (37) for the values of X included in the areas F and H.

The working method previously described with a slit procuring scanning of the treatment laser beam FLT in translation or using a slit with a parabolic profile as explained previously in this description thus yields an ablation profile which over the periphery of the area of an ellipse denoted E in figure 5a, with half-axes  $R_x$  and  $R_y$ , contains eight "perfect" points by which is meant points of zero ablation.

Of course, in the case where there is a requirement not to irradiate the cornea COR beyond an area of radius R it is possible to mask the latter with a mask comprising a circular hole of radius R.

There are shown in figures 5b and 5c respectively a profile characteristic of keratomileusis ablation for myopia with no astigmatism and a profile characteristic of keratomileusis ablation for hypermetroplia.

In figures 5b and 5c units have not been marked on the coordinate axes. In the case of an operation by keratomileusis on myopia, an ablation corresponding to a correction of 15 diopters has a depth of 0.15 mm and extends over an area 5 mm in diameter. The initial radius of curvature is increased to 10.6 mm.

In the case of figure 5c, in which the units have not been shown on the coordinate axes, an ablation corresponding to a correction of 15 diopters has a depth of 0.15 mm and extends over an area 9 mm in diameter. The initial radius of curvature of 7.8 mm is reduced to 5 mm.

The device in accordance with the invention makes it possible to overcome the limitations of prior art devices through the use of an illumination and treatment laser beam the specific shape and displacement of which are computed so that their combination produces the required ablation shape.

When the slit or slits is or are irradiated by a particular pulse from the laser the image of the slit(s) projected

onto the cornea COR is, so to speak, etched on to the surface and causes by photodecomposition the elementary ablation in question. The sum of these elementary ablations distributed over the cornea in accordance with the mathematical laws previously established produces the required modification to the shape of the cornea.

Unlike the prior art devices, in which the concepts of illumination time were involved, the concepts of the laser pulse frequency and of the speed of displacement of the object slit (or its image) are replaced by the concepts of linear or angular increments, as appropriate, between two adjacent positions of the image or of the lobe of the treatment laser beam. Here "adjacent" is to be understood in the geometrical rather than the temporal sense. In other words, the fact that two geometrically adjacent, that is to say geometrically consecutive, elementary ablations are temporally consecutive is not relevant. Generally speaking, they are not.

All the considerations previously mentioned combined with the concept of a threshold relating to each elementary ablation serves through summation of the elementary ablations in question to obtain a corrected or treated surface that is particularly satisfactory and the degree of roughness of which is substantially less than  $1\text{ }\mu\text{m}$ .

In the case of rotational scanning, there is generally projected onto the eye OE a beam whose transverse cross-section is caused to rotate about the projection axis O, which is of course substantially coincident with the optical axis of the eye to be treated. The cross-section of the treatment laser beam FLT is of elongate shape, of course, and in a particularly advantageous way has at least one or several lobes as defined previously. The generatrix at the end of the treatment laser beam or the corresponding lobe coincides with the rotation axis O in figure 2a. The ablation is done by applying the beam to a large number of successive angular positions, spaced by the appropriate angular increment of rotation about the axis O. To obtain the required correction the cross-section of the treatment laser beam FLT, the energy density per unit surface area of which is substantially constant, has the profile as defined previously on the basis of the object slits 211.

In the second embodiment, in particular using the device as shown in figure 4a, the resulting total ablation is obtained by scanning the treatment laser beam FLT in translation by successive linear increments. The displacement takes place in the direction perpendicular to the longitudinal dimension of the largest dimension of the lobe of the laser beam FLT and perpendicular to the optical axis O of the eye OE. Several operations are needed to carry out a complete treatment.

Of course, and in a non-limiting way, it is possible to carry out several operations, for example, the treatment laser beam FLT undergoing after each pass a rotation of a fraction of a circle about the optical axis O. After  $n$  passes ( $n/2$  if the beam is symmetrical), the combination of the aforementioned operations produces an  $n$ th order circular symmetry ablation more or less approximating the required effect.

A particularly advantageous instance, as previously described, is the use of a beam of parabolic cross-section the lobes of which have a parabolic shape as described previously, the laser beam being scanned in two passes along two perpendicular directions.

Compared with rotational scanning of the treatment laser beam FLT, scanning in translation for correction of myopia avoids a problem specific to rotary scanned beams, namely that the centre of the eye where the ablation is strongest coincides with the centre of rotation and that the latter is situated by design at an end of the impact area. In the event of any error in aligning this impact area with respect to the rotation axis, total absence of ablation (or its opposite, excessive ablation) may result in the immediate vicinity of the centre of the cornea. This problem is absent in the case of beams scanned in translation.

Furthermore, in the case of scanning in translation the choice of this scanning mode (along two orthogonal directions) provides a simple means of correcting astigmatism. For this, it is sufficient for the two orientations of the beam along the directions OX and OY to coincide with the principal directions of astigmatism. It then suffices to change the average density of exposure by changing the length of the linear increments between the two orthogonal passes to obtain an ablation of elliptical rather than circular symmetry.

The translational scanning treatment laser beams may of course be used in various ways, the beams with different orientations being applied either successively or simultaneously.

Another particularly advantageous embodiment of an object slit 211 and a diaphragm 21 will be described with reference to figures 6a through 6d.

Referring to figure 6a and figure 6b, the object slits as previously shown in figures 3b, 3c, 3d, 3e, 3f, 4b, 4c and 4d may advantageously be formed on a diaphragm 21 with a curved surface matching the surface of the cornea COR. This embodiment improves the quality of focussing of the image of the object slit on the cornea COR. In the case of figure 6a, the curved surface forming the diaphragm 21 is a spherical dome and the diaphragm may be rotated about its axis of symmetry, as previously described. In the case of object slits scanned in translation, the curved surface forming the diaphragm 21 may advantageously, and as shown in figure 6b, be a semicylindrical surface the longitudinal axis of which is oriented in the translation direction  $d$ , the object slits having their axis  $O''z$  perpendicular to the longitudinal axis of the aforementioned half-cylinder.

A particularly advantageous embodiment of the diaphragm 21 will be described with reference to figures 6c, 6d and 6e.

In the aforementioned figure 6c the diaphragm 21 comprises a semicylindrical surface of radius  $R$  with a longitudinal axis  $O''x$ . The semi-cylindrical surface has an object slit 211 with an aperture or width in the direction  $O''x$  denoted  $E(\varphi)$ . The aperture is, for example, symmetrical to a plane P orthogonal to the longitudinal axis  $O''x$ , this plane containing the directions  $O''y$  and  $O''z$  orthogonal to the direction of the longitudinal axis  $O''x$ . In figure 6c, S represents the middle of the aperture or the width of the slit at a height  $z$

corresponding to a given angle  $\phi$ , the angle  $\phi$  being defined as the angle between the radius vector  $O''S$  of a point  $S$  on the geometrical locus  $LS$ , the curve of symmetry of the object slit 211, and the direction  $Oy$ . The width  $E(\phi)$  of the object slit 211 satisfies the equation:

$$E(\phi) = E \left( \frac{\pi}{2} \right) \sin^3 \phi \quad (39)$$

In this equation,  $E(\pi/2)$  represents the maximum width or aperture of the object slit 211 for  $\phi = \pi/2$ .

It will of course be noted, as will be described in more detail later, that in the case of an operation by keratomileusis to cure myopic astigmatism the radius  $R$  of the semicylindrical surface constituting the diaphragm 21 determines the area within which the practitioner operates on the cornea  $COR$ . To give a non-limiting example, the aforementioned radius is taken as equal to the operating area, the magnification of the focussing optics being taken as equal to unity. It is obvious that any semicylindrical diaphragm of appropriately similar shape could be used, the magnification of the focussing optics being adapted accordingly.

To correct the cornea  $COR$  by keratomileusis for myopic astigmatism, for example, the diaphragm 21 as shown in figure 6c is disposed relative to the cornea  $COR$  so that its concave side faces towards the area of the latter to be treated. The cornea  $COR$  is assumed to have a circular surface of radius  $R'$  and the object slit 211 as shown in figure 6c is illuminated by the laser beam  $FL$ . The longitudinal axis  $O''x$  and the transverse axis  $P''y$  of the diaphragm are oriented in the principal directions of astigmatism  $OX$ ,  $OY$  of the cornea  $COR$ , these principal directions having been determined beforehand by the practitioner.

The device in accordance with the invention further comprises drive means 400 for rotating the diaphragm 21 about the axis  $O''y$ , the rotation drive means 400 advantageously comprising a stepper motor and two rotation half-shafts 401, 402 driven by the latter.

As will be noted on observing figures 6c, 6d and 6e, the width  $E(\phi)$  of the object slit 211 which is also shown in figure 6c by the intersection of the slit and a plane  $Q$  for which the equation is  $Y = R \cos \phi$ , is projected on the axis  $OX$  as an image of width  $E'(\alpha, \phi)$  when the slit 211 is illuminated with parallel light, for example. The width of the slit projected on the axis  $OX$  satisfies the equation:

$$E'(\alpha, \phi) = E(\phi) \cdot \sin \alpha \quad (40)$$

In this equation,  $\alpha$  represents the angle of inclination by which the diaphragm 21 is rotated and in particular of the axis  $O''z$  thereof relative to the direction  $OX$ . The slit 211 turns substantially on a sphere with the same radius as the cylinder and, as the diaphragm 21 is rotated, any middle point  $S$  at a height  $z$  corresponding to a given angle  $\phi$  performs a circle  $CS$  in the aforementioned plane  $Q$ , as shown in figures 6c and 6e.

If it is assumed that the ablation function  $A(\alpha, \phi)$  corresponds to the ablation function  $A(\bar{X}, Y)$  defined by equation (34) and is proportional to the number of pulses received for an elementary displacement less than  $E'(\alpha, \phi)$  and therefore less than the width  $E'(\alpha, \phi)$  of the image of the slit on the axis  $OX$  divided by the elementary displacement  $\Delta X(\alpha)$  (along the  $OX$  axis) for each laser pulse, we may write:

$$X(\alpha) = R \sin \phi \cos \alpha \text{ and } \frac{\delta X}{\delta \alpha} \cdot d\alpha = \frac{\delta}{\delta \alpha} R \sin \phi \cos \alpha d\alpha = -R \sin \phi \sin \alpha d\alpha$$

and  $\Delta X(\alpha) = R \sin \phi \sin \alpha \Delta \alpha$   
whence

$$A(X, Y) = A(\alpha, \phi) = \frac{E'(\alpha, \phi)}{\Delta X(\alpha)}$$

that is

$$A(\alpha, \phi) = \frac{(E) \phi}{R \sin \phi \Delta \alpha} \quad (41)$$

Given the chosen ablation function  $A(X, Y)$  defined by equation (34) above,  $OX$  and  $OY$  are chosen such that  $R_x \leq R_y$  and  $R$  is chosen such that  $R = R_y$  as shown in figures 6d and 6e in particular.

Using the same notation as previously, the ablation function may be written:



$$A(X, Y) = \frac{A_0}{2} \left( 1 - \frac{X^2}{R_x^2} - \frac{Y^2}{R^2} \right) \quad (42)$$

Given the equations:

$$X = R \sin \phi \cos \alpha$$

$$Y = R \cos \alpha$$

the ablation function becomes:

$$A(X, Y) = A(\alpha, \phi) = \frac{A_0}{2} \left( 1 - \frac{R^2}{R_x^2} \cos^2 \alpha \right) \sin^2 \phi \quad (43)$$

Given equations (41) and (43) above, the ablation function may be related to the law of the aperture of the slit  $E(\phi)$  and the rotation increment  $\Delta \alpha$  by the equation:

$$\frac{E(\phi)}{\Delta \alpha} = \frac{RA_0}{2} \cdot \sin^3 \phi \cdot \left( 1 - \frac{R^2}{R_x^2} \cos^2 \alpha \right) \quad (44)$$

It then suffices to choose:

$$E(\phi) = E \left( \frac{\pi}{2} \right) \sin^3 \phi$$

and

$$\Delta \alpha = \Delta_0 \left( 1 - \frac{R^2}{R_x^2} \cos^2 \alpha \right)^{-1}$$

Choosing  $E(\pi/2)$  and  $\Delta_0$  for a given semicylindrical diaphragm produces the required profile.

By modulating the angular rotation increment  $\Delta \alpha$ , the previously described embodiment can correct astigmatism of the cornea and myopia without any problems of edge discontinuities at the periphery of the correction area or excessive ablation at the centre of the cornea. The junction between the corrected area and the uncorrected area is perfect. Also, in the absence of any astigmatism the previous equations hold, given that  $R_x = R_y = R$ . In all cases, the X and Y ablation functions depend only on  $\alpha$  and  $\phi$  respectively.

To facilitate use of the device in accordance with the invention as shown in figure 3a or in figure 4a the calculation means 8 may comprise a microcomputer 80 with its peripheral devices. The memory areas of the microcomputer store programs and/or subroutines for calculating the numbers of laser pulses  $N1_1$ ,  $N1_2$  previously mentioned in the description, the total irradiation times  $T_{1min}$ ,  $T_{2min}$ , and sub-routines for sequencing and synchronising the displacement of the treatment laser beam FLT. These sequencing programs are used, for example, to generate rotation or translation displacement commands sclr and sclt and laser emission commands sce. The program or subroutine can also include a program for modulating the rotation increment  $\Gamma$  as a function of the azimuth angle  $\beta$  or the translation increment  $\Delta u$  as a function of the value of the X or Y

ascissa of the rotation increment  $\Delta\alpha$ .

To facilitate the work of the practitioner the microcomputer 80 may further comprise in its memory area a "menu" type program inviting the practitioner, through an interactive type dialogue, to define at least the principal directions of astigmatism of the eyeball relative to a reference marker, the principal directions having been established by the practitioner as a result of a diagnosis.

The "menu" program may advantageously also invite the practitioner to specify the value of the parameter R defining the optical area for operation and correction of the cornea COR. It may also invite the practitioner to designate the treatment method i.e. scanning the object slits or images of the object slits in rotation or in translation. Finally, the type of operation may be specified according to the particular case under treatment.

The microcomputer 80 can of course be connected by a BUS type link to the means 5 for synchronising the displacement of the image of the lobe or lobes of the treatment laser beam FLT. The means 5 for synchronising the displacement of the image may advantageously comprise an input/output interface circuit generating from rotation or translation displacement commands scdr and scdt and emission commands sce respective commands SCDR, SCDT, SCE for the displacement control means 4 and the laser emission means 1. The input/output interface circuit will not be described in detail, as it may be provided by any conventional type interface with provision for controlling the stepper motor in particular.

Finally, to facilitate the work of the practitioner, following his diagnosis, the device in accordance with the invention may comprise a set of diaphragms each comprising an object slit 211 as defined and described with reference to figures 3b, 3c, 3d, 3e, 3f, 4b, 4c, 4d, 4e, 6a, 6b, and 6c.

There has thus been described a device for performing surgery on the cornea in which rotational or translational scanning of a laser beam having at least one lobe of elongate cross-section produces a precise law of ablation over the area of the cornea COR of the eye to be corrected. Laboratory tests have shown that, compared with prior art devices in which the depth of ablation was controlled by the time of exposure to the treatment laser beam, the corrected surfaces after treatment, that is to say the surfaces of the cornea serving as the input optical surface of the eye of the patient, show a much reduced degree of roughness, thus conferring superior optical qualities on the surfaces of the treated cornea. It has been observed that the degree of roughness of the surfaces after treatment does not exceed  $1\text{ }\mu\text{m}$ . The degree of roughness of the corneal surfaces after treatment with the prior art devices may be explained by the fact that these devices have the disadvantage of applying the laser emission power simultaneously to the major part of the cornea, the effect of which is to create an acoustic shock wave resulting from simultaneous vapourising of material over the anterior surface of the cornea. This kind of phenomenon can also have unwanted physiological consequences, such as ejection of endothelium cells, for example. The device in accordance with the invention makes it possible to eliminate the disadvantages of these devices since the resulting total ablation when the device in accordance with the invention is used results from the summation of elementary ablations distributed over the cornea according to precise mathematical laws, each elementary ablation being carried out with minimal energy density.

Of course, the device in accordance with the invention is not limited to refractive eye surgery. It may also constitute a device for shaping or correcting the shape of an object by laser treatment of the surface of the object. In this case, the device comprises the means 2 for generating a treatment laser beam FLT comprising at least one lobe L1 ... L6 of elongate cross-section and means 3 for focussing the image of the lobe or lobes of the treatment laser beam FLT onto the area of the object OE to be corrected. The means 4 for moving the image of the lobe or lobes of the treatment laser beam FLT over the area of the object to be corrected serve to move the latter over the area of the object to be corrected. The means 5 for synchronising movement of the image of the lobe or lobes of the treatment laser beam FLT over the area of the object OE to be corrected with the treatment laser beam pulses serve to perform the correction or shaping by summing a plurality of elementary discrete ablations. As shown in figure 7, the image of the lobe or lobes of the laser beam is focussed in such a way that the generatrix of one end of the lobe or lobes or the longitudinal axis of symmetry of a lobe or the lobes of the laser beam FLT is coincident with the axis of symmetry OZ of the object to be treated or of an elementary surface of the object to be treated. The means 4 for moving the image of the lobe or lobes of the treatment laser beam FLT over the area of the object to be corrected serve to move the image of the lobe or lobes L1 ... L6 of the laser beam in rotation about the end generatrix or the longitudinal axis of symmetry of the lobes of the treatment laser beam FLT. The rotation is applied in rotation angle increments. The device corresponds substantially to the embodiment of figure 3a.

Furthermore, in an embodiment corresponding to that of figure 4a of a device for shaping or correcting the shape of an object by laser treatment, the means 4 for moving the image of the lobe or lobes of the treatment laser beam FLT over the area of the object to be treated provide for movement in translation in a direction d substantially perpendicular to the largest dimension Oz of the lobe of the treatment laser beam FLT. The movement in translation may be effected in displacement increments  $\Delta u$ , the movement in translation being defined by  $u = X$  or  $u = Y$  defining a plane tangential to the surface of the object OE at the point O on the axis of symmetry of the object or an elementary area of the latter to be treated.

A non-limiting alternative embodiment of the device in accordance with the invention for shaping or correcting the shape of an object or for performing refractive eye surgery will be described with reference to figure 7, this embodiment being based on the embodiment of figure 3a or figure 4a. Referring to figure 7, the device in accordance with the invention further comprises a real time shape recognition system comprising at least two video cameras 1001, 1002 viewing the object or the eye OE to be treated and transmitting image data

to the calculation means 8. The video cameras 1001, 1002 allow for monitoring the progress of the shaping or correction of the object during the treatment process. The shape recognition means may comprise shape recognition means available through normal trade channels and will not be described in detail.

As shown in figure 7, a series of mirrors M1, M2, M3, M4 deflect the treatment laser beam FLT. At least one of these mirrors, the mirror M4, is mounted on a gimbal 2000. The two frames of the gimbal mounting are shown in cross-section in figure 7 to avoid overcomplicating the drawing. Drive and orientation adjustment means for the adjustment mirror comprise DC or stepper motors, for example. These motors are controlled by the shape recognition means 1001, 1002 through the intermediary of the calculating means 8, using a bus type link. The shape recognition system therefore serves to monitor the progress of the correction or treatment during the process and to control the deflection of the treatment laser beam FLT by means of the mirror M4 in the event of uncontrolled movement of the object or of the eye of the patient. In the latter case the practitioner can advantageously make coloured marks on the cornea of the patient before the treatment begins, using methylene blue, for example. Note, however, that if an arrangement of this kind is used with the device in accordance with the invention as shown in figure 4a, the shape recognition means 1001, 1002 can control the focussing lens 430 directly by means of an X-Y movable table 43.

The device in accordance with the invention is therefore usable for shaping or correcting the shape of mechanical objects such as contact lenses or intra-ocular implants and for refractive eye surgery.

## Claims

1. Device for shaping or correcting the shape of an object by laser treatment of the surface of the object comprising:

- means for generating a pulsed treatment laser beam comprising at least one lobe of elongate cross-section,
- means for focussing the image of the lobe or lobes of the treatment laser beam onto the area of the object to be corrected,
- means for displacing the image of the lobe or lobes of the treatment laser beam over the area of the object to be corrected, and
- means for synchronising the displacement of the image of the lobe or lobes of the treatment laser beam over the area of the object to be corrected with the pulses of the treatment laser beam, the total correction or shaping being effected by the summation of a plurality of elementary discrete ablations.

2. Device according to claim 1, wherein said means for focussing the image of the lobe or lobes of the treatment laser beam enable focussing of the image so that the generatrix of an end of the lobe or lobes or the axis of longitudinal symmetry of a lobe or lobes of the treatment laser beam is coincident with the axis of symmetry of the object to be treated.

3. Device according to claim 1 or claim 2, wherein the means for displacing the image of the lobe or lobes of the treatment laser beam over the area of the object to be corrected enable displacement of the image of the lobe or lobes of the laser beam in rotation about the generatrix at the end of or the axis of longitudinal symmetry of the lobes of the treatment laser beam.

4. Device according to claim 3, wherein the rotation is applied in rotation angle increments.

5. Device according to claim 3 or claim 4, wherein the means for displacing the image of the lobe or lobes of the treatment laser beam in rotation comprise:

- a mask or diaphragm comprising an object slit of elongate shape, said slit being illuminated by the laser beam and one end of the slit being disposed at the centre of the diaphragm to generate for the treatment laser beam the aforementioned end generatrix or axis of longitudinal symmetry of the lobes of the treatment laser beam, and
- drive means for rotating the object slit or the image of the object slit.

6. Device according to claim 5, wherein the diaphragm is circular, the drive means for the diaphragm comprising:

- a toothed ring disposed at the periphery of the diaphragm, and
- a stepper motor the drive shaft of which is fitted with at least one toothed wheel meshing with the toothed ring.

7. Device according to any one of claims 3 through 6, wherein, for refractive eye surgery by laser treatment of the cornea, the image of the lobe or lobes of the laser beam and the object slit of the diaphragm for treatment of myopia by keratomileusis have a profile satisfying the equation:

$$\Theta(\rho) = \Gamma \frac{A_0}{\bar{a}(e)} \left(1 - \frac{\rho^2}{R^2}\right) = \Theta(0) \left(1 - \frac{\rho^2}{R^2}\right)$$

5

in which equation:

$\Theta(\rho)$  represents the aperture angle of the slit defined as the angle at the centre of a circle having for its centre the aforementioned end of the slit enabling generation of said end generatrix or the axis of symmetry of the treatment laser beam and for its radius the corresponding value  $\rho$  of the distance from a point on the edge of the slit or on the lobe of the laser beam to the centre,

10

$\Theta(0)$  represents the aperture angle at the origin end  $O'$  of the slit,

$\Gamma$  represents the angular rotation increment,

$A_0$  represents the thickness of ablation or correction at the centre of the area of the cornea to be corrected,

15

$\bar{a}(e)$  represents the average thickness removed by irradiation by each laser pulse, and

$R$  represents the optical area on the cornea on which the cornea is operated on and corrected.

8. Device according to any one of claims 3 through 6, wherein the image of the lobe or lobes of the laser beam and the object slit of the diaphragm for treatment of hypermetropia by keratomileusis or the profile of the slit satisfies the equation:

20

$$\Theta(\rho) = \Gamma \frac{A_0}{\bar{a}(e)} \frac{\rho^2}{R^2}, \quad \rho \in [0, \nu], \quad \nu < 1 \times R$$

$$= \theta_{\max} \frac{\rho^2}{R^2}$$

25

30

in which equation:

35

$\Theta(\rho)$  represents the aperture angle at the origin end  $O'$  of the slit,

$\theta_{\max}$  represents the maximum aperture angle of the object slit,

$\Gamma$  represents the angular rotation increment,

$A_0$  represents the thickness of ablation or correction at the centre of the area of the cornea to be corrected,

40

$\bar{a}(e)$  represents the average thickness removed by irradiation by each laser pulse, and

$R$  represents the optical area on the cornea on which the cornea is operated on and corrected.

9. Device according to claim 7 or claim 8, further comprising means for calculating the angular rotation increment  $\Gamma$  which, for a given object slit, satisfies the equation:

45

$$\Gamma = \theta_{\max} \frac{\bar{a}(e)}{A_0}$$

50

in which  $\theta_{\max}$  is the maximum aperture angle of the object slit or of the lobe of the laser beam.

10. Device according to any one of claims 7 through 9, further comprising means for calculating the number  $NI_1$  of laser pulses and the number of rotation increments  $\Gamma$ , the number  $NI_1$  of pulses satisfying the equation:

55

$$N_{I1} = \frac{2\pi}{\Gamma} = N_{D1} \frac{A_0}{\bar{a}(e)}$$

60

65

in which equation:  $ND_i$  represents the number of totally separate or adjacent slit images.

11. Device according to claim 10, further comprising means for calculating the minimum total irradiation time  $T_{lmin}$  which satisfies the equation:

$$T_{lmin} = N_{Il} \frac{\tau(e)}{N_{Dl}} = \tau(e) \frac{A_0}{\bar{a}(e)}$$

in which equation  $\tau(e)$  represents the minimum time interval between two successive irradiations of the same point on the cornea.

12. Device according to any one of claims 7 through 11, wherein to compensate for astigmatism of the eyeball by re-establishing the symmetry of revolution of the cornea the device comprises means for modulating the angular rotation increment  $\Gamma$  as a function of the azimuth angle  $\beta$  defining the meridian of the cornea of the eyeball, the angle rotation increment  $\Gamma(\beta)$  as a function of the azimuth angle  $\Gamma$  satisfying the equation:

$$\Gamma(\beta) = \theta_{\max} \frac{\bar{a}(e)}{A_0(\beta)}$$

in which equation  $\theta_{\max}$  represents the maximum aperture angle of the object slit and  $A_0(\beta)$  represents the ablation at the origin in the vicinity of the optical axis of the eyeball in the direction with azimuth angle  $\beta$ .

13. Device according to claim 12, wherein for compensating myopic astigmatism of the eyeball or for removing a disc of constant thickness the device comprises at least one auxiliary diaphragm with an object slit of circular sector shape  $\theta(p) = k$  where  $k$  is a constant, the auxiliary slit enabling a constant ablation at the origin  $O$  to be re-established without modifying the radius of curvature of the cornea by further irradiation and displacement in rotation by a rotation increment  $\Gamma(\beta)$  modulated as a function of the azimuth angle  $\beta$ .

14. Device according to any one of claims 7 through 11, wherein for compensating for correction by astigmatism of the eyeball and of the cornea the device comprises on the input side of focussing means on the path of the treatment laser beam an anamorphic optical system the magnification of which depends on the azimuth angle  $\beta$ , the iso-ablation curves on the cornea being ellipses.

15. Device according to any one of claims 7 through 11, wherein for making a circular incision the device comprises at least one auxiliary diaphragm with an object slit of circular arc shape with a specific radius of curvature.

16. Device according to claim 1 or claim 2, wherein the means for displacing the image of the lobe or lobes of the treatment laser beam over the area of the object to be treated enable displacement in translation in a direction substantially perpendicular to the largest dimension of the lobe of the treatment laser beam.

17. Device according to claim 16, wherein the treatment laser beam comprises two lobes or component parts of a single lobe symmetrical relative to a centre of symmetry.

18. Device according to claim 16 or claim 17, wherein the displacement in translation is effected by displacement increments  $\Delta u$  and is defined relative to two reference directions  $OX$  and  $OY$ , with  $u = X$  or  $u = Y$ , defining a plane tangential to the surface of the object at the point  $O$  on the axis of symmetry of the object.

19. Device according to claim 18, wherein the means for displacement in translation of the image of the lobe or lobes of the treatment laser beam enable displacement in translation of the latter in two orthogonal directions  $OX$  and  $OY$ .

20. Device according to any one of claims 16 through 19, wherein the means for displacing the image of the lobe or lobes of the treatment laser beam in translation comprise in succession on the path of the laser beam:

- a fixed diaphragm comprising at least one object slit of elongate shape adapted to be illuminated by the laser beam,
- a first lens, the object slit being placed in the object focal plane of the lens to generate the lobe or lobes of the beam imaging the object slit,
- a rotating prism providing (for a rotation of the prism through an angle  $\alpha$ ) rotation of the emergent light beam, the treatment laser beam, through an angle  $2\alpha$ , and
- a second focussing lens mobile in translation in the directions  $OX$  and  $OY$

21. Device according to any one of claims 16 through 20, wherein, for refractive eye surgery by laser

treatment of the cornea, the image of the lobe or lobes of the treatment laser beam and the object slit of the diaphragm for treatment and correction by keratomileusis for myopia and astigmatism has a substantially parabolic profile satisfying the equation:

$$E(z) = 2 E_{\max} \left( \frac{1}{2} - \frac{z^2}{R^2} \right) = E(u) = \Delta u \frac{A_0}{\bar{a}(e)} \left( \frac{1}{2} - \frac{u^2}{R^2} \right) \quad \text{---}$$

in which equation:

$E(z)$  represents the transverse dimension of the slit or of the lobe of the treatment laser beam at the abscissa  $z$  on an axis of coordinates oriented longitudinally relative to the slit,

$E_{\max}$  represents the maximal transverse dimension of the slit,

$R$  represents the optical area on the cornea in which the cornea is operated on and corrected,

$u$  represents the abscissa or position on the coordinate axis oriented longitudinally relative to the slit itself oriented in the direction OX or the direction OY,

$\Delta u$  represents the translation displacement increment in the direction OY or in the direction OX, and

$A_0$  represents the thickness of ablation or correction at the centre of the area of the cornea to be corrected on displacement in translation of the object slit or of the lobe of the treatment laser beam in the direction OY or in the direction OX,

$\bar{a}(e)$  represents the average thickness removed by irradiation by each laser pulse.

22. Device according to any one of claims 16 through 20, wherein, for refractive eye surgery by laser treatment of the cornea, the image of the lobe or lobes of the laser beam and the object slit of the diaphragm for treatment and correction by keratomileusis of hypermetropia and hypermetropic astigmatism has a substantially parabolic profile satisfying the equation:

$$E(z) = E_{\max} \left( \frac{z^2}{R^2} \right) = E(u) = \Delta u \frac{A_0}{\bar{a}(e)} \left( \frac{u^2}{R^2} \right)$$

in which equation:

$E(z)$  represents the transverse dimension of the slit or of the lobe of the treatment laser beam at the abscissa  $z$  on an axis of coordinates oriented longitudinally relative to the slit,

$E_{\max}$  represents the maximal transverse dimension of the slit,

$R$  represents the optical area on the cornea in which the cornea is operated on and corrected,

$u$  represents the abscissa or position on the coordinate axis oriented longitudinally relative to the slit itself oriented in the direction OX or the direction OY,

$\Delta u$  represents the translation displacement increment in the direction OY or in the direction OX, and

$A_0$  represents the thickness of ablation or correction at the centre of the area of the cornea to be corrected on displacement in translation of the object slit or of the lobe of the treatment laser beam in the direction OY or in the direction OX.

23. Device according to any one of claims 1 or 5 through 8 or 13 or 15 or 21 or 22, wherein the object slits are formed on a diaphragm forming a curved surface.

24. Device according to claim 23, wherein the diaphragm comprises a semicylindrical surface of radius  $R$  with a longitudinal axis, the object slit having an aperture  $E(\varphi)$  or width in the direction  $O''x$  symmetrical with respect to a plane orthogonal to the longitudinal axis  $O''x$ , this plane containing the directions  $O''y$  and  $O''z$  orthogonal to the direction of the longitudinal axis  $O''x$ , the width of the object slit satisfying the equation:

$$E(\varphi) = E\left(\frac{\pi}{2}\right) \sin^3 \varphi$$

in which equation:

-  $\varphi$  represents the angle of the radius vector of a point on the curved geometrical locus of symmetry of the object slit and of the direction  $Oy$ , and

-  $E(\pi/2)$  represents the maximal width or aperture of the object slit for  $\varphi = \pi/2$ .

25. Device according to claim 24, wherein for correcting the cornea by keratomileusis for myopic astigmatism, the diaphragm having its concave side facing towards the cornea and the object slit being illuminated by the laser beam, the longitudinal axis  $O''x$  and the transverse axis  $O''y$  of the diaphragm being oriented in the principal directions of astigmatism OX, OY of the cornea, the device further

comprises drive means for rotating the diaphragm about the axis  $O''y$ .

26. Device according to claim 25, wherein the drive means for rotating the diaphragm about the axis  $O''y$  consist in a stepper motor enabling the diaphragm to be rotated in rotation increments  $\Delta\alpha$  satisfying the equation:

$$\Delta\alpha = \Delta 0 \left( 1 - \frac{R^2}{R_x^2} \cos^2 \alpha \right)^{-1}$$

in which equation:

-  $\alpha$  represents the inclination of the diaphragm and of the axis  $O''z$  relative to the reference direction OX, and

-  $\Delta 0$  represents the minimum angular rotation increment for  $\alpha = \pi/2$ .

27. Device according to claim 21 or claim 22, further comprising means for calculating the translation displacement increment  $\Delta u$  in the direction OY or OX which, for a given object slit, satisfies the equation:

$$\Delta u = E_{\max} \frac{\bar{a}(e)}{A_u}$$

28. Device according to claim 21 or claim 22, further comprising means for calculating the number  $NI_2$  of laser pulses and the number of translation displacement increments  $\Delta u$  in the direction OY or OX, the number  $NI_2$  of pulses satisfying the equation:

$$NI_2 = \frac{2\pi}{\Delta u} = ND_2 \frac{A_u}{\bar{a}(e)}$$

in which equation  $ND_2$  represents the number of totally separate or adjacent images.

29. Device according to claim 28, further comprising means for calculating the minimum total irradiation time  $T_{2\min}$  which satisfies the equation:

$$T_{2\min} = NI_2 \frac{\tau(e)}{ND_2} = \tau(e) \frac{A_u}{a(e)}$$

in which equation  $\tau(e)$  represents the minimum time interval between two successive irradiations of the same point on the cornea.

30. Device according to any one of claims 24 through 26, further comprising means for calculating the rotation translation displacement increment  $\Delta\alpha$  which satisfies the equation:

$$\Delta\alpha = \Delta 0 \left( 1 - \frac{R^2}{R_x^2} \cos^2 \alpha \right)^{-1}$$

31. Device according to claim 3 or claim 5 or claim 16 or claim 20, wherein the object slits are symmetrical with respect to a longitudinal axis of symmetry.

32. Device according to claim 31, wherein the object slits have an edge at the end of curvilinear shape symmetrical with respect to the longitudinal axis of symmetry, the curvilinear shape departing from the variation law  $p = \text{constant}$  to eliminate edge effects from the total ablation.

33. Device according to claim 32, wherein the curvilinear shape is continuously concave with no point of inflection or concave and convex with a point of inflection.

34. Device according to claim 3 or claim 5 or claim 16 or claim 17, wherein the object slit has an adjustable profile to enable compensation of irregular distribution of energy in the cross-section of the treatment laser beam or a lobe thereof.

35. Device according to claim 34, wherein the adjustable slit comprises at least one edge made up of strips mobile in translation in a direction perpendicular to the longitudinal axis of the slit.

36. Device according to any one of claims 9 through 15 or any one of claims 27 through 29, wherein the calculation means comprise a microcomputer with its peripheral devices in the memory areas of which are stored programs and/or subroutines for calculating the numbers  $N_1$ ,  $N_2$  of laser pulses and the total irradiation times  $T_{1min}$ ,  $T_{2min}$ , for sequencing and synchronising the displacement of the treatment laser beam, for generating commands for displacement in rotation or translation and laser emission commands, this last program being stored in a main memory of the computer, and for modulating the rotation increment  $\Gamma(\beta)$  as a function of the azimuth angle  $\beta$  or the translation increment  $\Delta u$ , the rotation increment  $\Delta\alpha$ .

37. Device according to claim 36, wherein the microcomputer further comprises, stored in its memory area, a "menu" type program inviting the practitioner by means of an interactive dialogue to define at least:

- the principal directions of astigmatism of the eyeball, relative to a reference marker,
- the value of the parameter R defining the optical area within which the cornea is operated on and corrected,
- the operating mode of the object slit or object slit image treatment (translation or rotation),
- the type of operation.

38. Device according to claim 35 or claim 36, wherein the means for synchronising displacement of the image of the lobe or lobes of the treatment laser beam comprise an input/output interface circuit producing from rotation and translation displacement commands and emission commands respective commands for the displacement control means and the laser emission means.

39. Device according to any one of the preceding claims, further comprising:

- real time shape recognition means comprising at least two video cameras for viewing the object to be corrected and transmitting image data to the calculation means, the video cameras serving to monitor the progress of the correction or shaping of the object during the process;
- a series of mirrors for deflecting the treatment laser beam one at least of which, referred to as the adjustment mirror, is mounted on a gimbal, and
- drive and orientation adjustment means for the adjustment mirror comprising motors controlled by the shape recognition means through the intermediary of the calculation means.

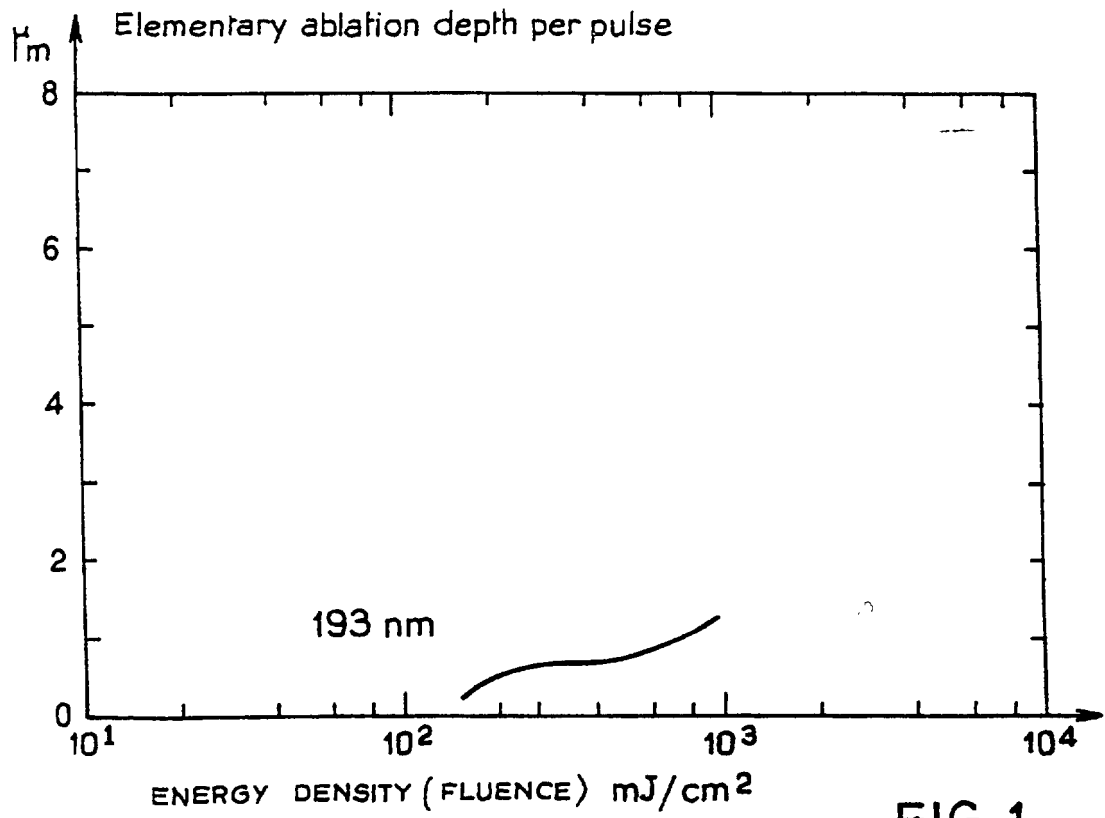
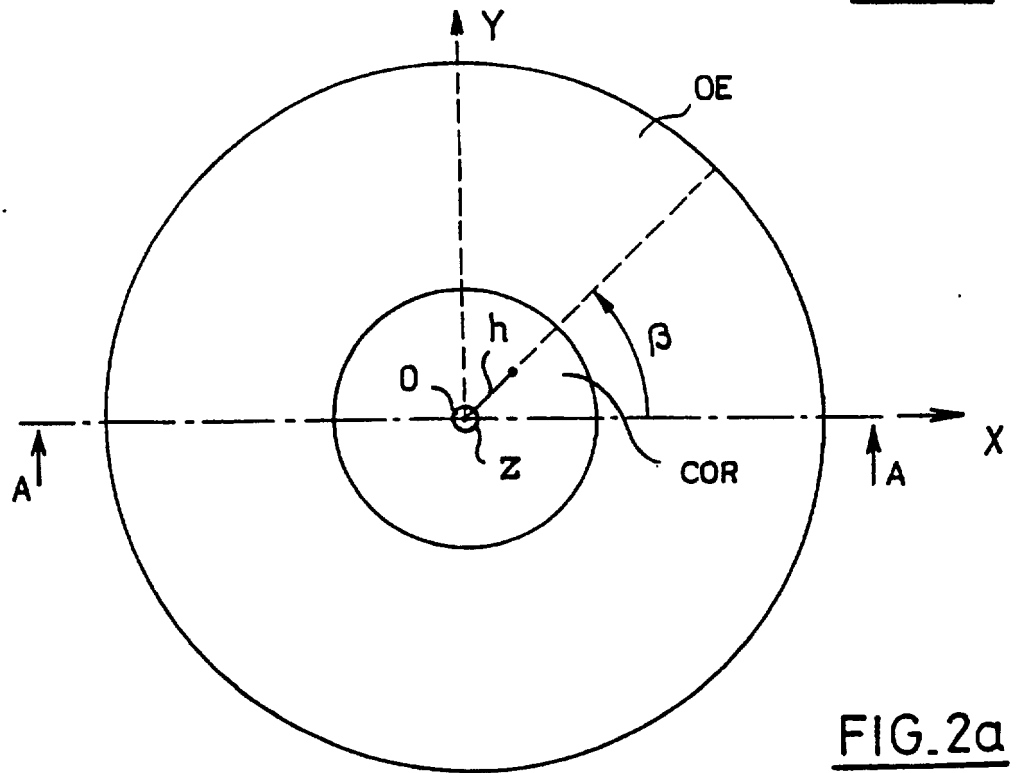
40. Set of diaphragms each comprising an object slit as defined in any one of claims 7, 8, 12, 15, 21, 22 or 23.

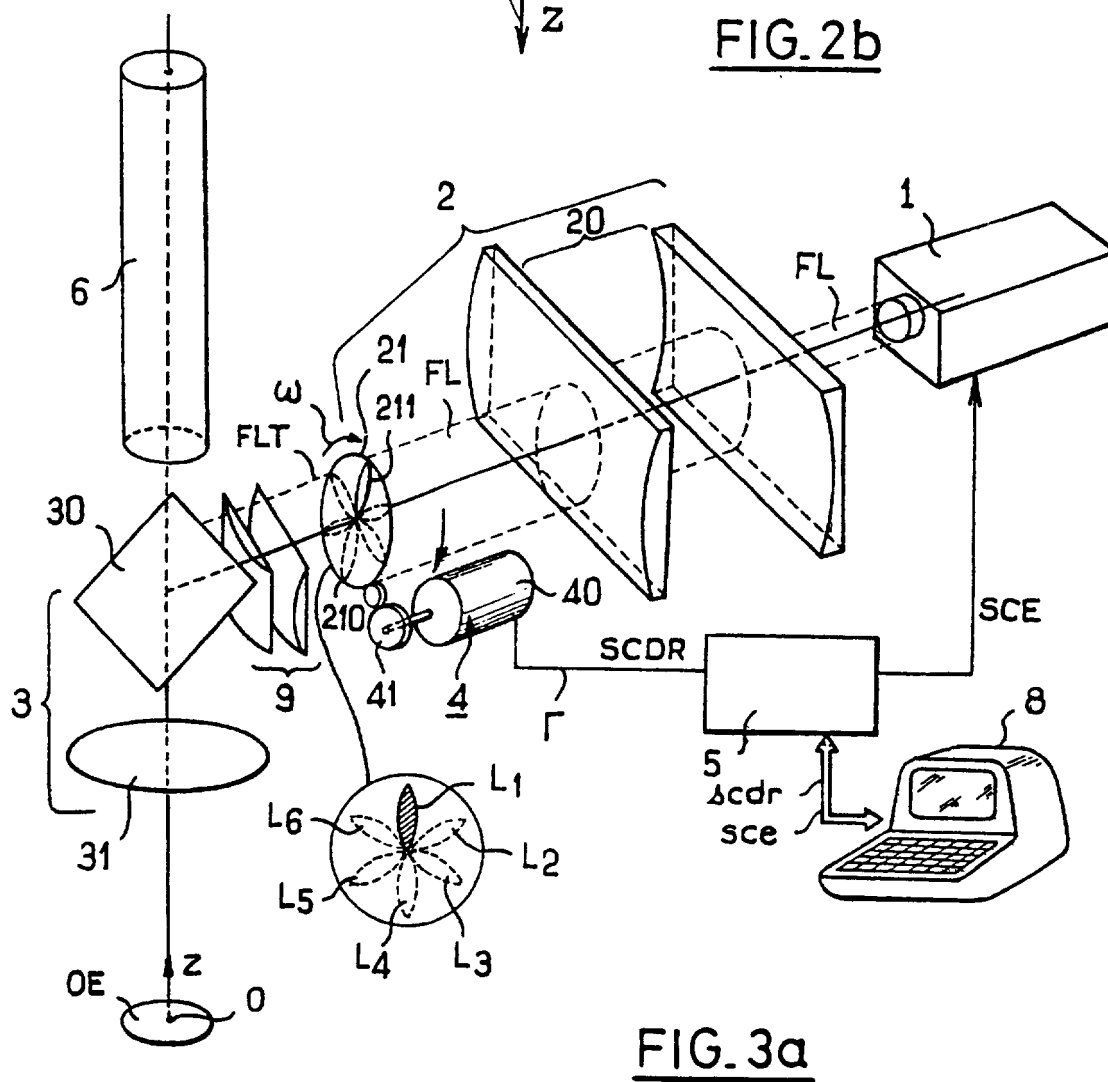
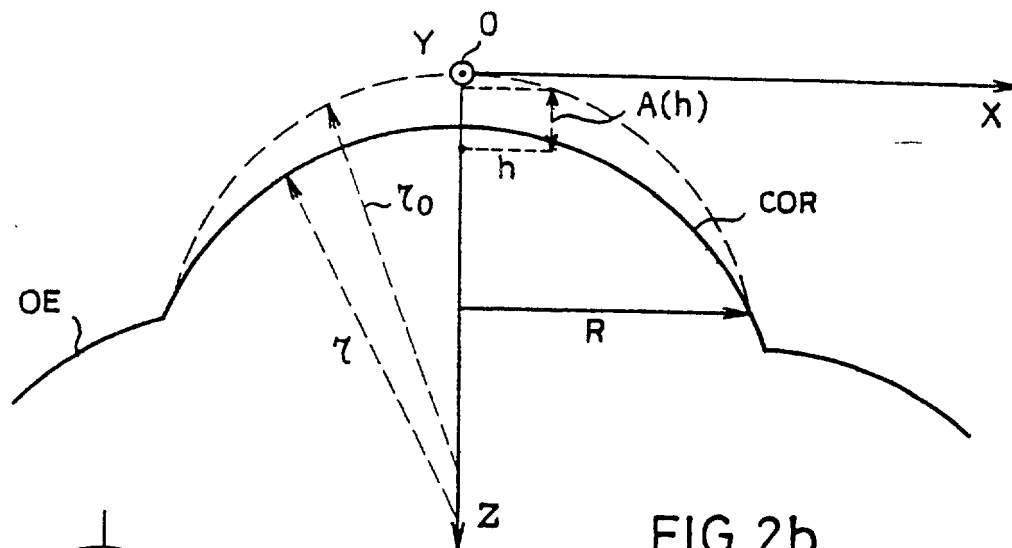
41. Use of the device according to any one of claims 1 through 6 or 16 through 20 for shaping or correcting the shape of mechanical objects such as contact lenses or intra-ocular implants.

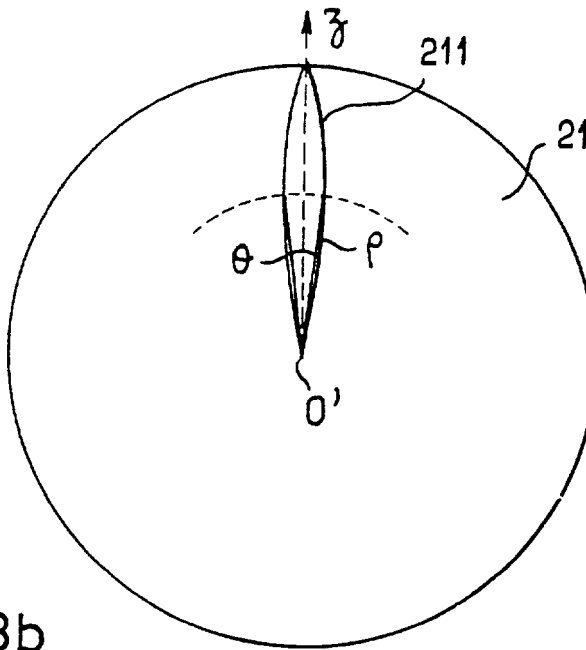
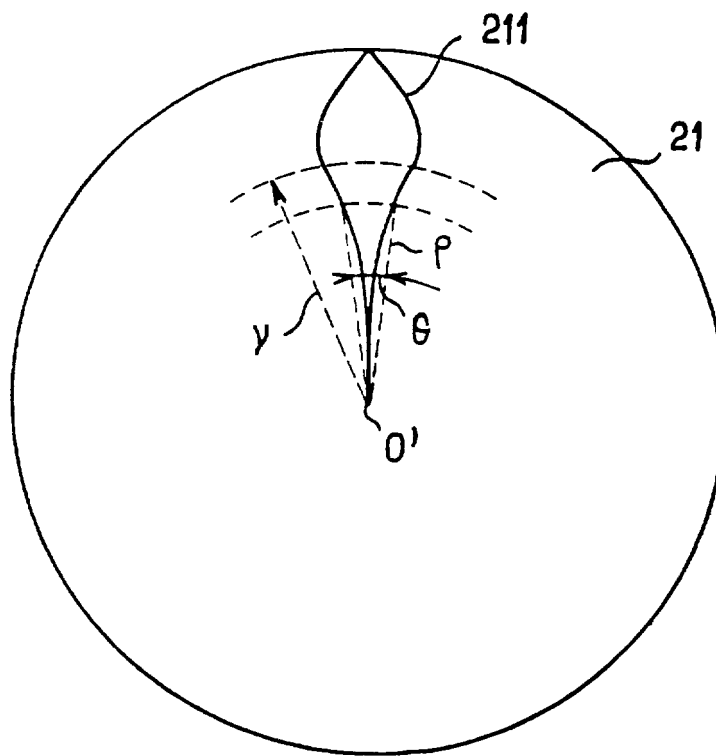
42. Use of the device according to any one of claims 1 through 39 for refractive corneal surgery.

43. Device for shaping or correcting the shape of an object by laser treatment of the surface of the object substantially as hereinbefore described with reference to any of the embodiments shown in the accompanying drawings.



FIG. 1FIG. 2a



FIG. 3bFIG. 3c

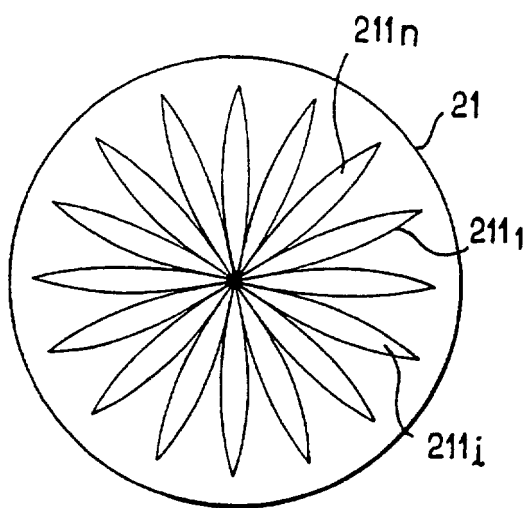


FIG. 3d

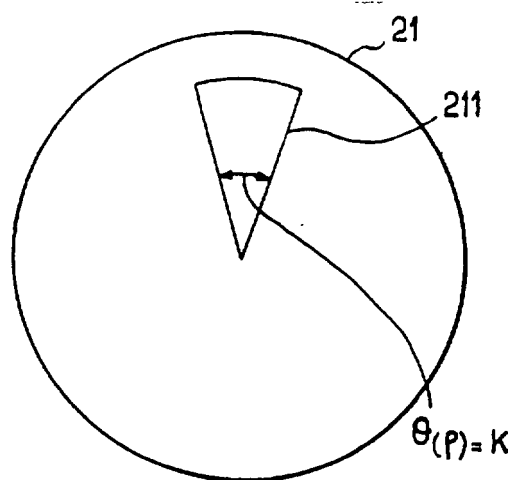


FIG. 3e

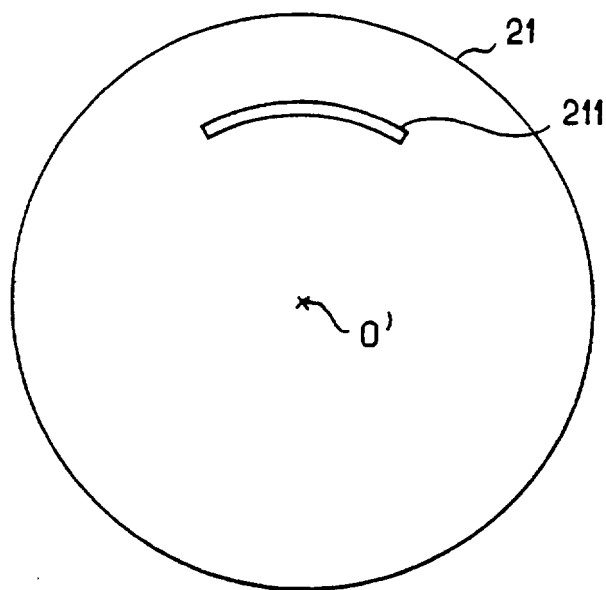


FIG. 3f

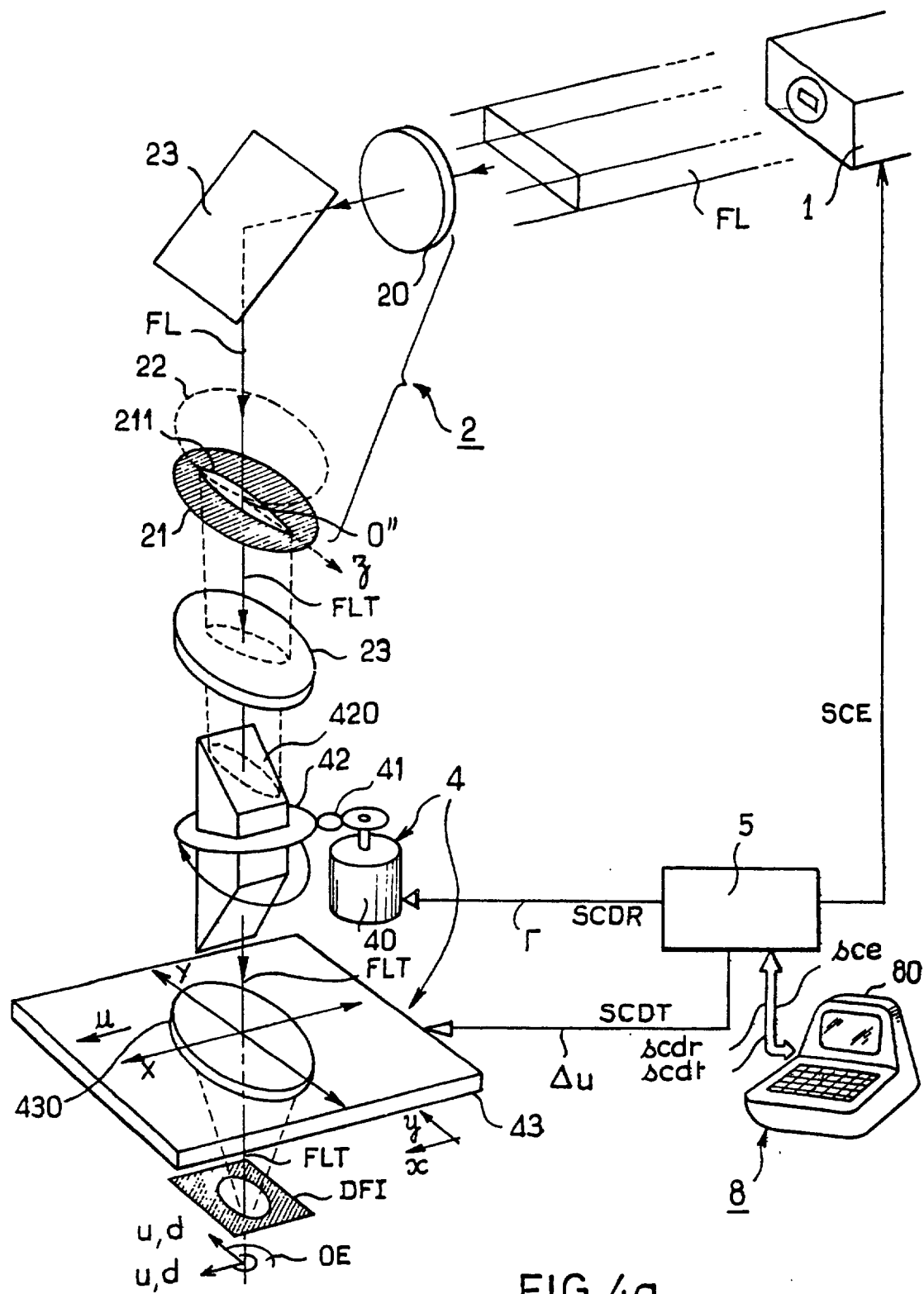
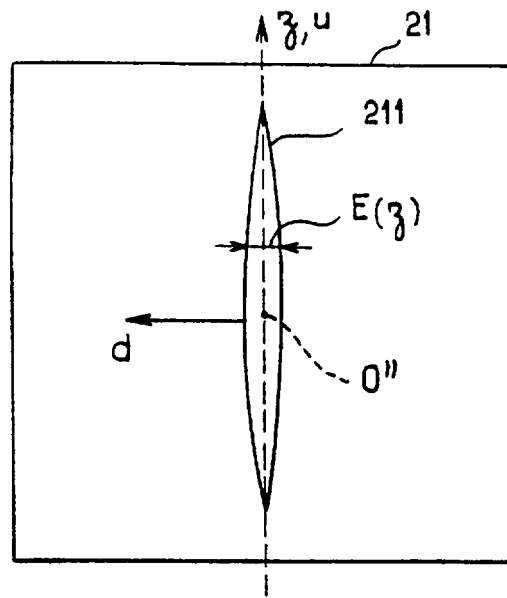
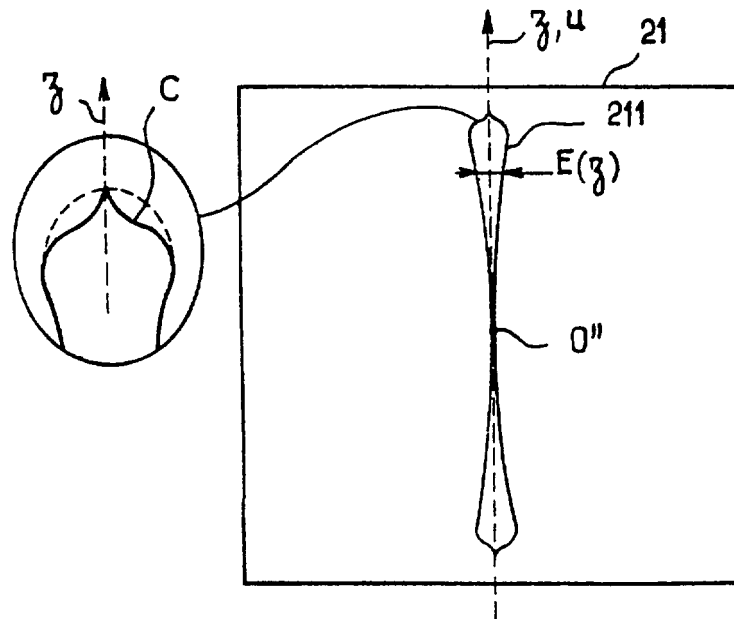


FIG. 4a

FIG. 4bFIG. 4c

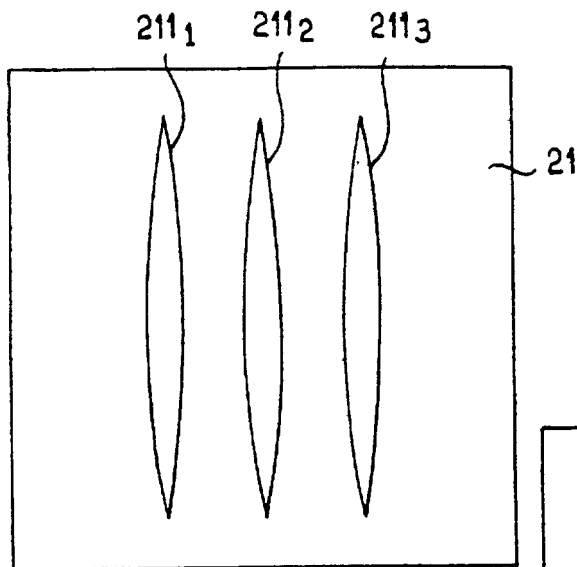


FIG. 4d

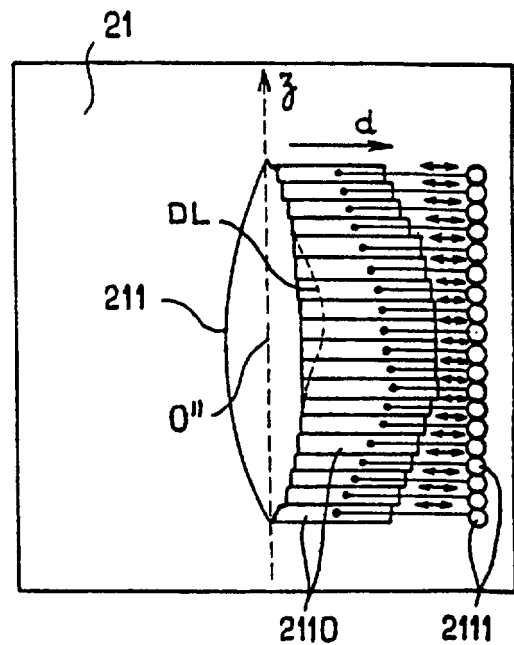


FIG. 4e

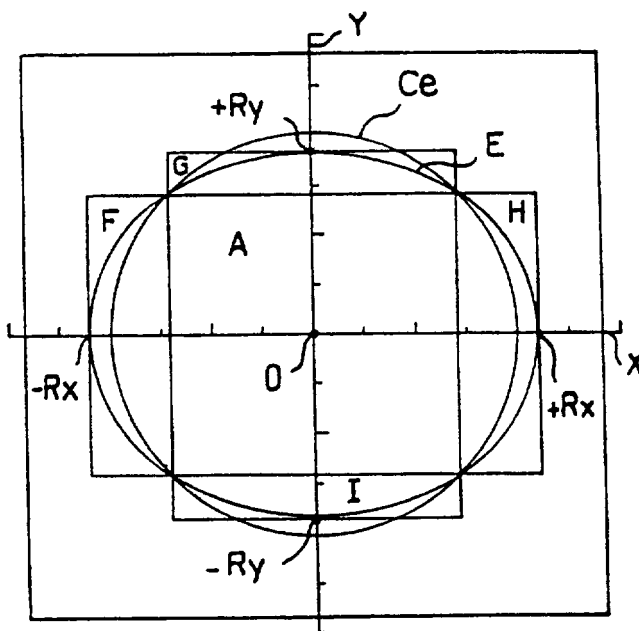
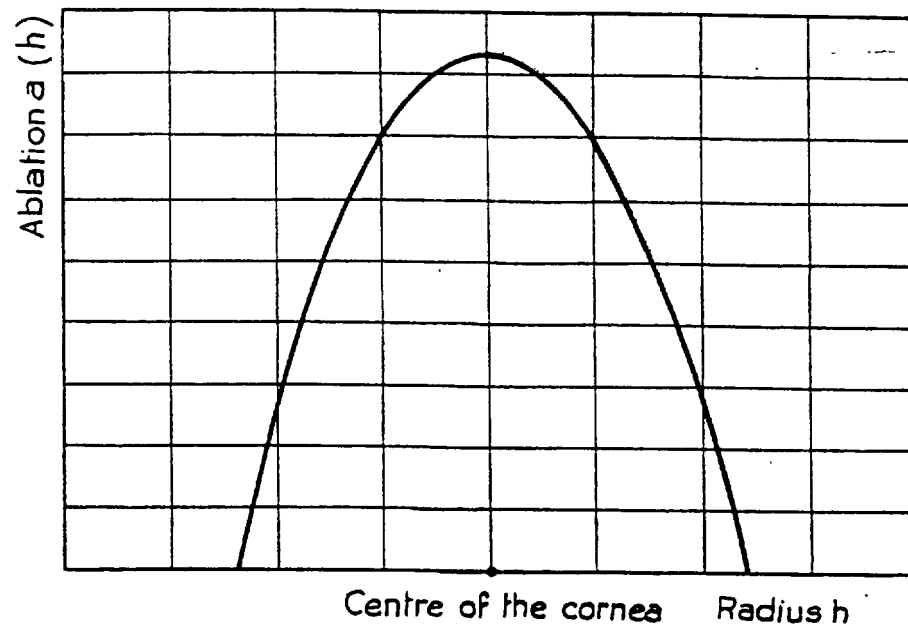
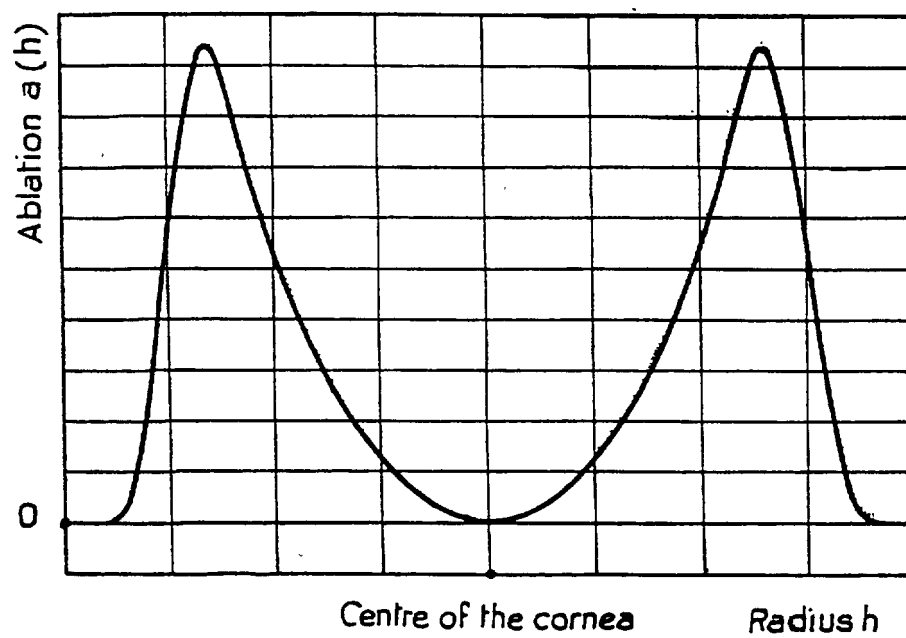


FIG. 5a

FIG. 5bFIG. 5c



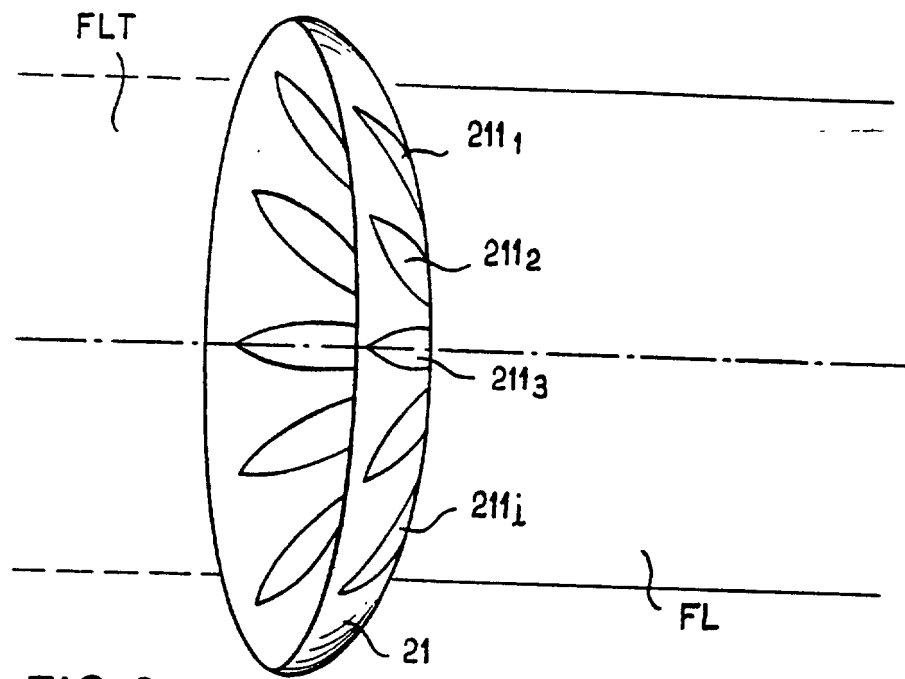


FIG. 6a

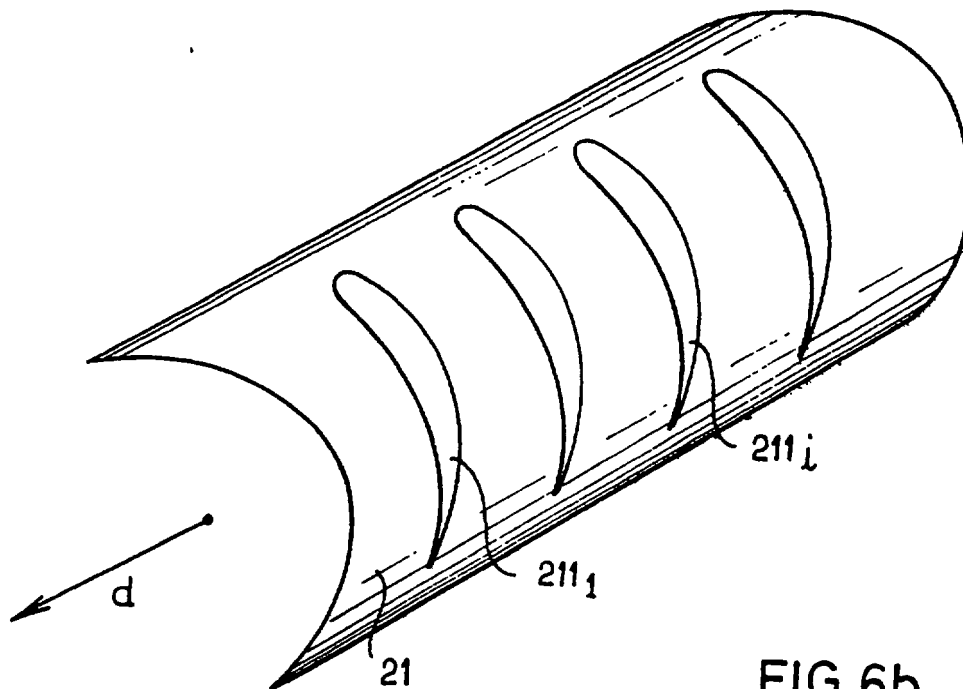
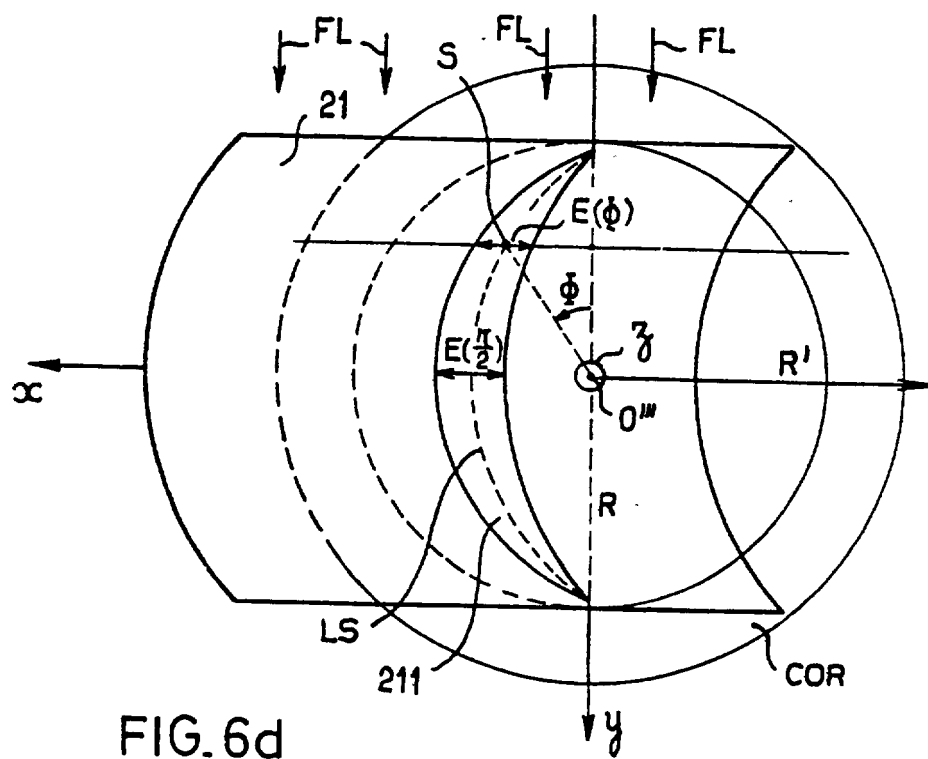
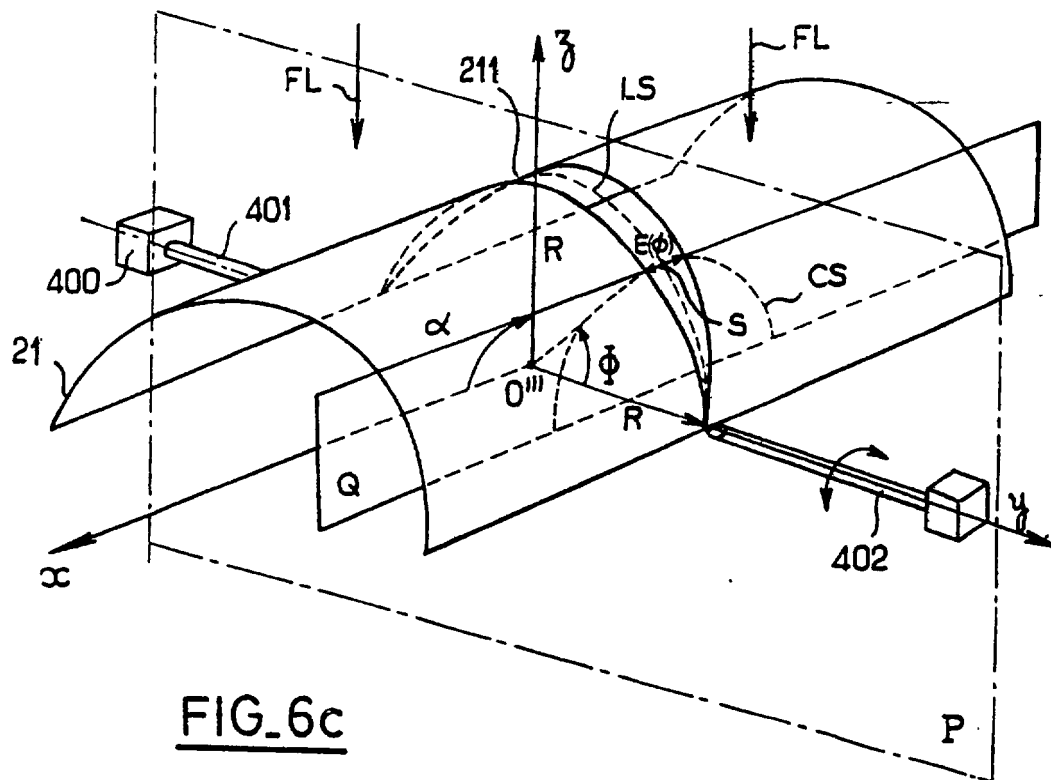
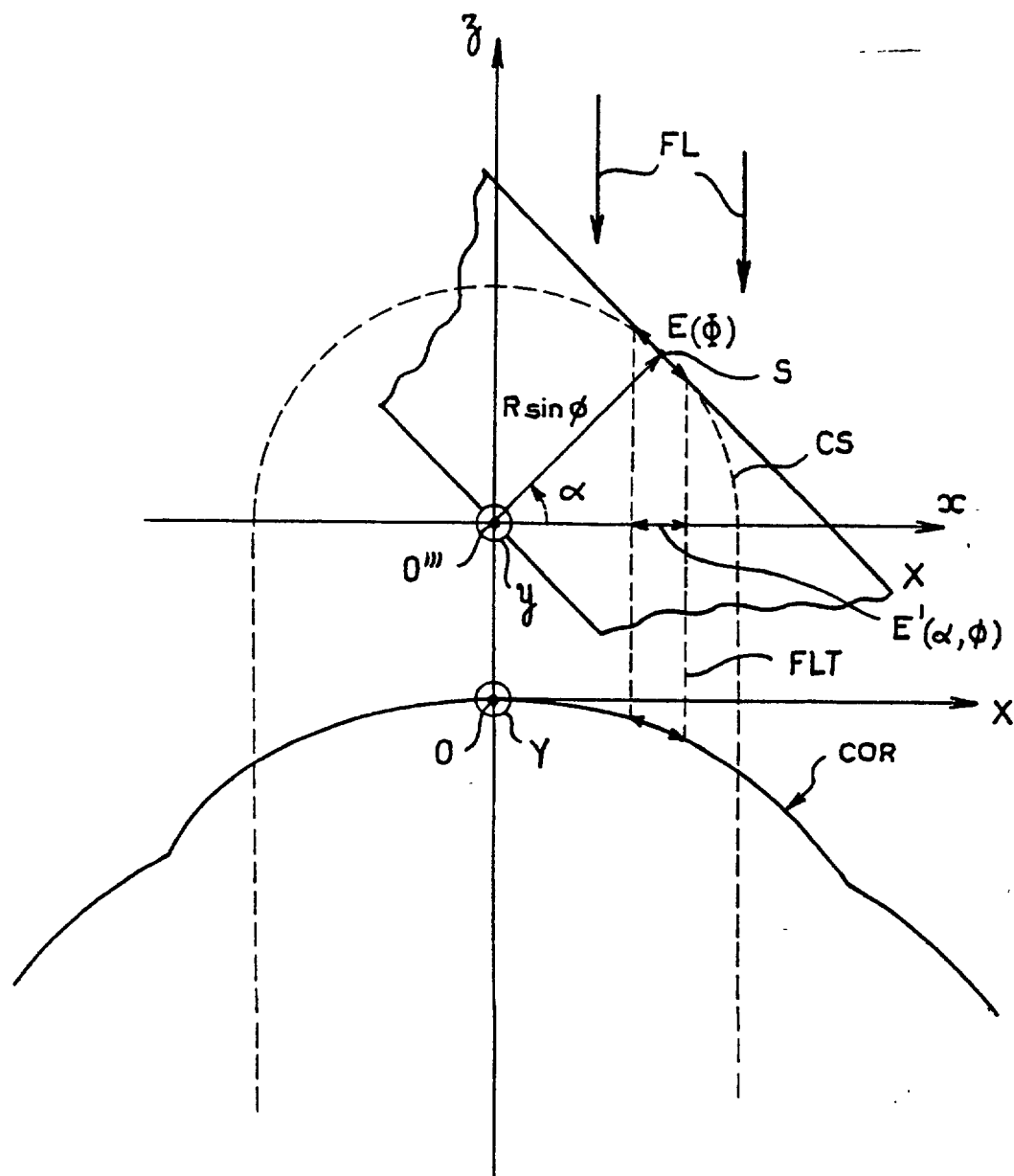


FIG. 6b

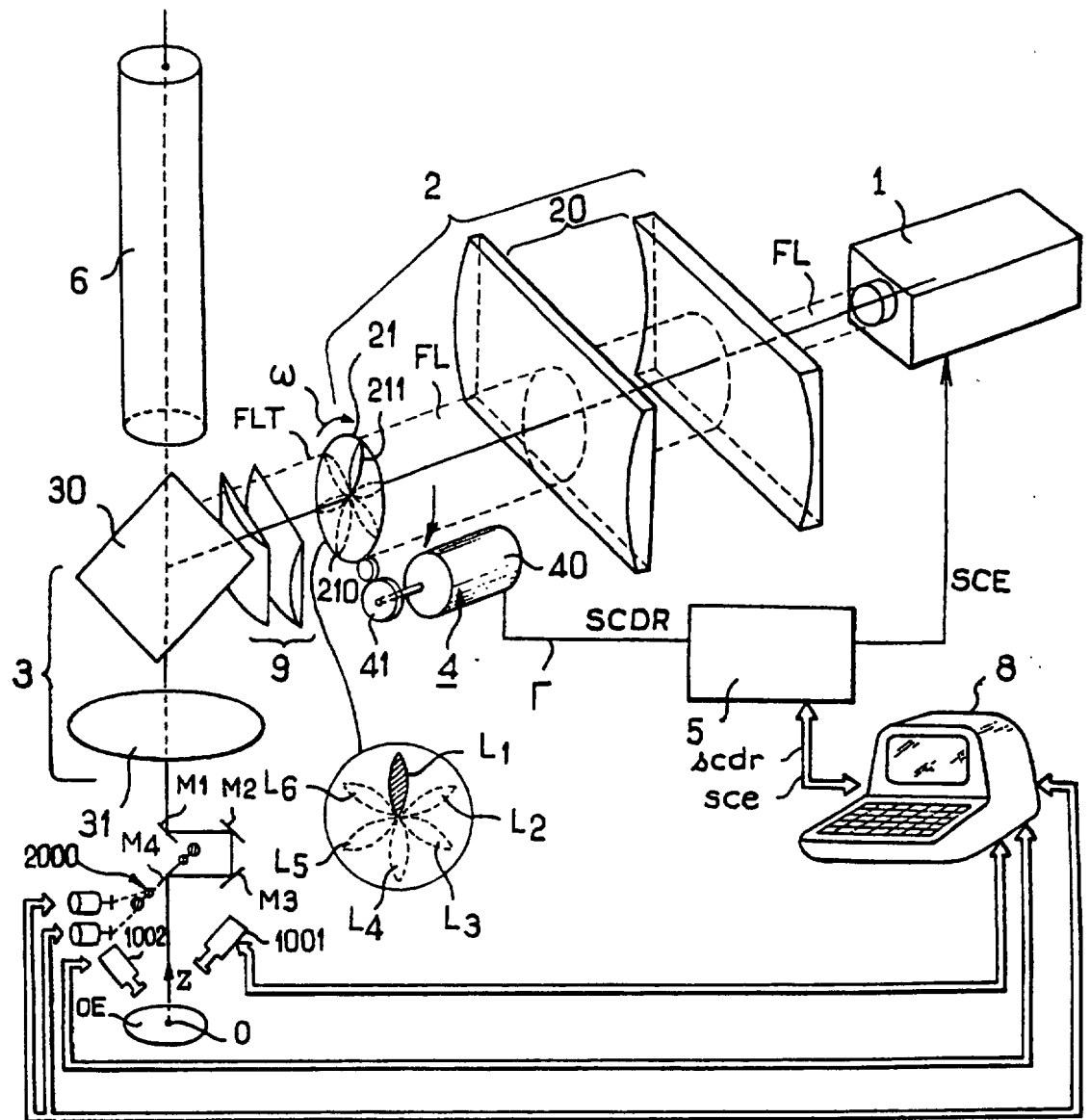


FIG. 6e

```

1  # Loading
2  # =====
3  # =====
4  # =====
5  # =====
6  # =====
7  # =====
8  # =====
9  # =====
10 # =====
11 # =====
12 # =====
13 # =====
14 # =====
15 # =====
16 # =====
17 # =====
18 # =====
19 # =====
20 # =====
21 # =====
22 # =====
23 # =====
24 # =====
25 # =====
26 # =====
27 # =====
28 # =====
29 # =====
30 # =====
31 # =====
32 # =====
33 # =====
34 # =====
35 # =====
36 # =====
37 # =====
38 # =====
39 # =====
40 # =====
41 # =====
42 # =====
43 # =====
44 # =====
45 # =====
46 # =====
47 # =====
48 # =====
49 # =====
50 # =====
51 # =====
52 # =====
53 # =====
54 # =====
55 # =====
56 # =====
57 # =====
58 # =====
59 # =====
60 # =====
61 # =====
62 # =====
63 # =====
64 # =====
65 # =====
66 # =====
67 # =====
68 # =====
69 # =====
70 # =====
71 # =====
72 # =====
73 # =====
74 # =====
75 # =====
76 # =====
77 # =====
78 # =====
79 # =====
80 # =====
81 # =====
82 # =====
83 # =====
84 # =====
85 # =====
86 # =====
87 # =====
88 # =====
89 # =====
90 # =====
91 # =====
92 # =====
93 # =====
94 # =====
95 # =====
96 # =====
97 # =====
98 # =====
99 # =====
100 # =====

```





European Patent  
Office

# EUROPEAN SEARCH REPORT

Application Number

EP 88 40 1607

DOCUMENTS CONSIDERED TO BE RELEVANT			
Category	Citation of document with indication, where appropriate, of relevant passages	Relevant to claim	CLASSIFICATION OF THE APPLICATION (Int. Cl.4)
X	EP-A-0 207 648 (F.A. L'ESPERANCE) * Figures 6,8,9,10,15,16,20; page 9, lines 20-26; page 10, line 3 - page 11, line 1; page 11, line 29 - page 12, line 9; page 12, line 21 - page 14, line 10; page 17, lines 12,13; page 21, lines 10-26; page 22, lines 21-28; page 23, line 7 - page 24, line 16 *	1-4,6,16,18,19,36,38,41-43	A 61 F 9/00
Y	---	5,17,31	
A	---	39,40	
Y	DE-A-3 535 073 (SEILER-GERÄTEBAU) * Whole document *	5,17,31	
A	EP-A-0 224 322 (P.A. CONSULTING SERVICES LTD) * Figure 19; column 18, lines 36-45 *	14	
A	US-A-4 648 400 (SCHNEIDER) * Figures 6-8; column 8, lines 1,2 *	23	
			TECHNICAL FIELDS SEARCHED (Int. Cl.4)
			A 61 F
The present search report has been drawn up for all claims			
Place of search THE HAGUE		Date of completion of the search 22-09-1988	Examiner SEDY, R.
CATEGORY OF CITED DOCUMENTS			
X : particularly relevant if taken alone Y : particularly relevant if combined with another document of the same category A : technological background O : non-written disclosure P : intermediate document		T : theory or principle underlying the invention E : earlier patent document, but published on, or after the filing date D : document cited in the application L : document cited for other reasons & : member of the same patent family, corresponding document	

EPO FORM 1503 01.82 (P0401)



IEEE JOURNAL OF

# QUANTUM ELECTRONICS



DECEMBER 1990

VOLUME 26

NUMBER 12

(ISSN 0018-9197)

A PUBLICATION OF THE IEEE LASERS AND ELECTRO-OPTICS SOCIETY

## SPECIAL ISSUE ON LASERS IN BIOLOGY AND MEDICINE

### QUANTUM ELECTRONICS LETTERS

- Linewidth and Feedback Sensitivity of Semiconductor Diode Lasers..... *O. Nilsson and J. Buus* 2039  
Parametric Oscillation in  $\text{LiB}_3\text{O}_5$  Pumped at  $0.532 \mu\text{m}$ ..... *K. Kato* 2043

### REGULAR PAPERS

#### *Semiconductor Lasers and Amplifiers*

- On the Probabilistic Characterization of Side Mode Fluctuations in Pulsed-Modulated Nearly-Single-Mode Semiconductor Lasers..... *J. C. Cartledge* 2046  
The Effects of Spatial Hole Burning and Energy Diffusion on the Single-Mode Operation of Standing-Wave Lasers..... *J. J. Zayhowski* 2052  
Dependence of the Linewidth of a Semiconductor Laser on the Mode Distribution..... *U. Krüger and K. Petermann* 2058  
Nonlinear Analysis of Surface-Emitting Distributed Feedback Lasers..... *S. H. Macomber* 2065  
Transverse-Mode Competition Effects Observed in the Numerical Simulation of Transients in Gain-Guided Semiconductor Laser Arrays..... *P. Menendez-Valdes, E. Garmire, and M. Ohtaka* 2075  
Gain Saturation Characteristics of Traveling-Wave Semiconductor Laser Amplifiers in Short Optical Pulse Amplification..... *T. Saitoh and T. Mukai* 2086

#### *Fiber Optics*

- Dynamic Optical Soliton Communication..... *M. Nakazawa, K. Suzuki, H. Kubota, E. Yamada, and Y. Kimura* 2095  
Ultralong Dispersion-Shifted Erbium-Doped Fiber Amplifier and Its Application to Soliton Transmission.... *M. Nakazawa, Y. Kimura, and K. Suzuki* 2103  
The Propagation of Bright and Dark Solitons in Lossy Optical Fibers..... *J. A. Giannini and R. I. Joseph* 2109

#### *Nonlinear Optics*

- Propagation and Stability of Optical Pulses in Nonlinear Planar Structures with Instantaneous and Finite Response Times..... *C. S. Mitchell and J. V. Moloney* 2115  
Determination of the Threshold for Instability in Four-Wave Mixing Mediated by Brillouin Scattering..... *D. E. Watkins, A. M. Scott, and K. D. Ridley* 2130

#### *Solid-State Lasers*

- The Output Beam Quality of a Q-Switched Nd:Glass Slab Laser..... *M. K. Reed and R. L. Byer* 2138

### SPECIAL ISSUE PAPERS

- Introduction to the Special Issue..... *R. Birngruber* 2146  
*Cell Biology*  
Laser Trapping in Cell Biology..... *W. H. Wright, G. J. Sonek, Y. Tadir, and M. W. Berns* 2148  
Laser Femtosecond MPI Mass Spectrometry of Dye-Labeled Nucleotides (Invited Paper)... *S. V. Chekalin, V. V. Golovlev, Yu. A. Matveets, A. P. Yartsev, V. S. Letokhov, C. Seidel, J. Wolfrum, and K. O. Greulich* 2158  
Effects of Near-Infrared Laser and Superluminous Diode Irradiation on Escherichia Coli Division Rate ..... *T. Karu, O. Tiphlova, M. Samokhina, C. Diamantopoulos, V. P. Sarantsev, and V. Shveikin* 2162

<i>Optics</i>	
A Review of the Optical Properties of Biological Tissues.....	W. F. Cheong, S. A. Prahl, and A. J. Welch 2166
Optical Reflectance and Transmittance of Tissues: Principles and Applications .....	B. C. Wilson and S. L. Jacques 2186
Optical Properties of Human Arterial Thrombus, Vascular Grafts, and Sutures: Implications for Selective Laser Thrombus Ablation .....	G. M. LaMuraglia, M. R. Prince, N. S. Nishioka, S. Obremski, and R. Birngruber 2200
<i>Diagnostics</i>	
Malignant Tumor and Atherosclerotic Plaque Diagnosis Using Laser-Induced Fluorescence ( <i>Invited Paper</i> ) .....	S. Andersson-Engels, J. Johansson, U. Stenram, K. Svanberg, and S. Svanberg 2207
Time-Resolved Fluorescence Spectroscopy of the Retinal Pigment Epithelium: Age-Related Studies .....	R. Cubeddu, F. Docchio, R. Ramponi, and M. Boulton 2218
Scanning Laser System for Combined Fluorescent Diagnostics and Photodynamic Therapy: Structural Design, Preliminary Trials, and Potentials ( <i>Invited Paper</i> ).....	R. D. Barabash, J. S. McCaughan, Jr., A. S. Kolobanov, G. Wolken, Jr., V. E. Normansky, and J. Walker 2226
Automatic Control of Lesion Size in a Simulated Model of the Eye .....	Y. Yang, M. S. Markow, A. J. Welch, and H. G. Rylander, III 2232
<i>Tissue Interaction</i>	
Intraocular Nd:YAG Laser Surgery: Light-Tissue Interaction, Damage Range, and Reduction of Collateral Effects ( <i>Invited Paper</i> ).....	A. Vogel, P. Schweiger, A. Frieser, M. N. Asiyo, and R. Birngruber 2240
<i>Ablation</i>	
Ablation of Calcified Biological Tissue Using Pulsed Hydrogen Fluoride Laser Radiation .....	J. A. Izatt, N. D. Sankey, F. Partovi, M. Fitzmaurice, R. P. Rava, I. Itzkan, and M. S. Feld 2261
Comparison of Tissue Ablation with Pulsed Holmium and Thulium Lasers .....	N. S. Nishioka and Y. Domankevitz 2271
Measurement of Laser Ablation Threshold with a High-Speed Framing Camera.....	Y. Domankevitz and N. S. Nishioka 2276
Subnanosecond Probing of the Ablation of Soft Plaque from Arterial Wall by 308 nm Laser Pulses Delivered Through a Fiber.....	R. Srinivasan, K. G. Casey, and J. D. Haller 2279
Ablation of the Cornea and Synthetic Polymers Using a UV (213 nm) Solid-State Laser .....	Q. Ren, R. P. Gaulitis, K. P. Thompson, and J. T. Lin 2284
<i>Engineering</i>	
Liquid Core Light Guide for Laser Angioplasty.....	K. W. Gregory and R. R. Anderson 2289
Ball-Tipped Fibers for Laser Angioplasty with the Pulsed-Dye Laser .....	M. R. Prince, G. M. LaMuraglia, C. E. Seidlitz, S. A. Prahl, C. A. Athanasoulis, and R. Birngruber 2297
Acicon: A New Laser Beam Delivery System for Corneal Surgery.....	Q. Ren and R. Birngruber 2305
<b>BOOK REVIEWS</b>	
Optical Computing in Japan—S. Ishihara, Ed.....	Reviewed by H. J. Caulfield 2309
<b>1990 INDEX.....</b>	<i>Follows page</i> 2309



The IEEE JOURNAL OF QUANTUM ELECTRONICS is published by the IEEE Lasers and Electro-Optics Society. All members of the IEEE are eligible for membership in the Society and will receive the JOURNAL upon payment of the annual Society membership fee of \$10.00 plus \$20.00 member subscription fee. For information write to the IEEE Service Center at the address below.

## IEEE LASERS AND ELECTRO-OPTICS SOCIETY

## Officers

C. R. GILLIANO, *President* (1990)  
M. ETTEBERG, *President-Elect* (1990)  
D. A. B. MILLER, *Secretary-Treasurer* (1990)

## Administrative Committee

S. R. J. BRUECK  
L. A. COLDREN  
P. D. DAPKUS

R. D. DUPUIS  
D. T. HODGES  
T. Ikegami

K. M. JOHNSON  
P. KAISER  
D. A. B. MILLER

P. F. MOULTON  
H. R. SCHLOSSBERG  
P. W. SHUMATE

## Executive Office

R. T. WANGEMANN, *Executive Officer*

## Committees

R. DUPUIS, *Awards and Lecturers*  
R. JAIN, *Chapters*  
M. I. COHEN, *Constitution and Bylaws*  
P. KAISER, *Education*  
A. J. DEMARIA, *Fellows Nominations*  
D. A. B. MILLER, *Finance*  
M. I. COHEN, *Long Range Planning*  
S. R. NAGEL, *Meetings*  
S. GUCH, *Membership and Publicity*  
M. I. COHEN, *Nominating*  
P. F. MOULTON, *Publications*  
S. R. J. BRUECK, *Editor, J-QE*  
P. W. SHUMATE, *Editor, PTL*  
M. DAGENAIS, *Division I Magazine*  
D. A. B. MILLER, *Optical Switching and Processing*  
A. J. GLENTHER, *Government Relations*

S. R. NAGEL, *Newsletter*  
P. W. SMITH, *Reprints and Books*  
T. Ikegami, *Director*  
F. KAPRON, *Standards*  
D. R. SCIFRES, *Technical Committee*  
E. KAPON, *Integrated Optics and Optoelectronics*  
D. BOTEZ, *Semiconductor Lasers*  
J. P. HERITAGE, *Ultrafast Optics and Electronics*  
D. CHANNIN, *Optical Communications*  
L. ELIAS, *Free Electron Lasers*  
R. R. JACOBS, *Gas and UV Lasers*  
S. GUCH, *Solid State Lasers*  
T. F. DELTSCH, *Lasers in Biology and Medicine*  
P. A. YEH, *Nonlinear Optics*  
J. CHIVIAN, *M. G. COHEN Engineering*  
T. HOLMES, *Fiber Optic Technology*

## Steering Committees

## CLEO

J. P. HERITAGE '92  
R. R. JACOBS '90  
P. F. LIAO '91  
D. R. SCIFRES '92

## OFC

D. C. HANSON '90  
S. R. NAGEL '90  
R. C. ALFERNES '91  
T. G. GIALLORENZI '92

## OPTCON

G. C. BJORKLUND '90  
S. R. NAGEL '92

## Representatives

M. M. WEISS, *Committee on Man and Radiation*  
M. A. DUGUAY, *Energy Committee*  
D. B. ANDERSON, *Historian*  
D. S. CHEMLA, C. L. TANG, H. R. SCHLOSSBERG  
*Joint Council on Quantum Electronics*

K. IGA, C. E. WEBB, *Overseas Representatives*  
M. A. SANTORO, *PACE Coordinator*  
J. F. McDONALD, T. V. MOU, *Solid State Circuits Council*  
R. C. ALFERNES, P. W. SHUMATE, *J-LT Steering Committee*

C. R. GILLIANO, *Technical Activities Board*

## IEEE JOURNAL OF QUANTUM ELECTRONICS

S. R. J. BRUECK, *Editor* (1989-1991)

(See inside back cover for Information for Authors and listing of Associate Editors.)

## THE INSTITUTE OF ELECTRICAL AND ELECTRONICS ENGINEERS, INC.

## Officers

CARLETON A. BAYLESS, *President*  
ERIC E. SUMNER, *President-Elect*  
MARTHA SLOAN, *Executive Vice President*  
FUMIO HARASHIMA, *Secretary*  
WALLACE S. READ, *Treasurer*

RICHARD S. NICHOLS, *Vice President, Educational Activities*  
MICHAEL J. WHITELAW, *Vice President, Professional Activities*  
RALPH W. WYNDORF, JR., *Vice President, Publication Activities*  
ROBERT T. H. ALDEN, *Vice President, Regional Activities*  
H. TROY NAGLE, *Vice President, Technical Activities*

FREDERICK H. DILL, *Director, Division I—Circuits and Devices*

## Headquarters Staff

ERIC HERZ, *Executive Director and General Manager*  
THOMAS W. BARTLETT, *Associate General Manager—Finance and Administration*  
WILLIAM D. CRAWLEY, *Associate General Manager—Programs*  
JOHN H. POWERS, *Associate General Manager—Volunteer Services*

DONALD CHRISTIANSEN, *Editor, IEEE Spectrum*  
IRVING ENGELSON, *Staff Director, Technical Activities*  
LEO FANNING, *Staff Director, Professional Activities*  
PHYLLIS HALL, *Staff Director, Publishing Services*  
MELVIN I. OLKEN, *Staff Director, Field Services*

EDWARD ROSENBERG, *Controller*  
ANDREW G. SALEM, *Staff Director, Standards*  
RUDOLF A. STAMPEL, *Staff Director, Educational Activities*  
THOMAS C. WHITE, *Staff Director, Public Information*

## Publications Department

Publication Managers: ANN H. BURMEYER, GAIL S. FERENC  
Managing Editor: DAVID A. GEORGE

IEEE JOURNAL OF QUANTUM ELECTRONICS is published monthly by The Institute of Electrical and Electronics Engineers, Inc. Responsibility for the contents rests upon the authors and not upon the IEEE, the Society/Council, or its members. IEEE Headquarters: 345 East 47 Street, New York, NY 10017-2394. NY Telephone: 212-705 + extension: Information -7900; General Manager -7910; Public Information -7867; Publishing Services -7560; Spectrum -7556. Telecopiers: NY (Headquarters) 212-752-4929; NY (Publications) 212-705-7682; NY Telex: 236-411 (international messages only). IEEE Service Center (for orders, subscriptions, address changes, Educational Activities, Region/Section/Student Services, Standards): 445 Hoes Lane, P.O. Box 1331, Piscataway, NJ 08855-1331. NJ Telephone: Information: 908-981-0060; 908-562 + extension: Controller -5365; Technical Activities -3900. IEEE Washington Office (for U.S. professional activities): 1828 L Street, NW, Suite 1202, Washington, DC 20036-5104. Washington Telephone: 202-785-0017. Price/Publication Information: Individual copies: IEEE members \$10.00 (first copy only), nonmembers \$20.00 per copy. (Note: Add \$4.00 postage and handling charge to any order from \$1.00 to \$50.00, including prepaid orders.) Member and nonmember subscription prices available on request. Available in microfiche and microfilm. Copyright and Reprint Permissions: Abstracting is permitted with credit to the source. Libraries are permitted to photocopy beyond the limits of the U.S. Copyright Law for private use of patrons: (1) those post-1977 articles that carry a code at the bottom of the first page, provided the per-copy fee indicated in the code is paid through the Copyright Clearance Center, 29 Congress Street, Salem, MA 01970; (2) pre-1978 articles without fee. Instructors are permitted to photocopy isolated articles for noncommercial classroom use without fee. For all other copying, reprint, or republication permission, write to Copyrights and Permissions Department, IEEE Publishing Services, 445 Hoes Lane, P.O. Box 1331, Piscataway, NJ 08855-1331. Copyright © 1990 by The Institute of Electrical and Electronics Engineers, Inc. All rights reserved. Second-class postage paid at New York, NY, and at additional mailing offices. Postmaster: Send address changes to IEEE JOURNAL OF QUANTUM ELECTRONICS, IEEE, 445 Hoes Lane, P.O. Box 1331, Piscataway, NJ 08855-1331.



# Ablation of the Cornea and Synthetic Polymers Using a UV (213 nm) Solid-State Laser 6

QIUSHI REN, RAYMOND P. GAILITIS, KEITH P. THOMPSON, AND J. T. LIN

**Abstract**—In this paper, we studied photoablation of the porcine cornea and synthetic collagen with 213 nm radiation generated by the fifth harmonic from a Q-switched Nd:YAG laser. The new nonlinear crystals, beta barium borate (BBO), with specific angle cutting were used to optimize the fifth harmonic generation (213 nm). For comparison purposes, the above materials were also ablated by 266 nm (fourth-harmonic) laser radiation. Light and electron microscopy demonstrated that the damage zone created by 213 and 266 nm radiation are  $<1$  and  $15\text{ }\mu\text{m}$ , respectively. The ablation similarity between 193 and 213 nm demonstrated in our paper opens major opportunities for the development of a new corneal sculpting system based on solid-state laser technology which will overcome difficulties associated with excimer laser.

## INTRODUCTION

IN recent years, there has been a growing interest in the possible use of lasers for corneal refractive surgery [1]–[3]. Laser technology may offer more accurate, precise, and controllable procedures than existing techniques for correcting refractive errors. This requires proper selection of laser parameters (such as wavelength, pulse duration, energy density, etc.) and the development of a practical beam delivery system.

For corneal ablation, two spectral regions, far-UV and mid-infrared ( $2.7\text{--}3.0\text{ }\mu\text{m}$ ) have shown potential for corneal surgery by different mechanisms [4], [5]. The argon fluoride excimer (193 nm) has been shown to create particularly clean cuts without adjacent tissue damage. However, this laser is relatively large, expensive, uses substantial quantities of a dangerous gas (fluorine), and is generally limited to low pulse rate operations. Because of the high spatial mode operation of the excimer laser, a complicated beam delivery system must be designed for proper corneal reshaping. Currently available systems have limited flexibility, and they are limited to creating simple spherical or spherocylindrical surfaces.

With the development of new nonlinear crystals [6], [7], it is possible to generate fifth harmonic radiation (213 nm) from a Q-switched Nd:YAG laser with reasonable energy output and with pulse length similar to that

from an excimer laser. From the technical point of view, the fifth harmonic Nd:YAG laser (213 nm) is a solid-state laser and easy to use and maintain. Further research with solid-state lasers will provide additional possibilities for optimizing laser pulse duration. Moreover, the YAG laser can be rapidly pulsed (KHz range) allowing the beam to be scanned onto the target in any pattern desired by using the state-of-art scanning technology. Thus, the demonstration that the fifth harmonic Nd:YAG laser (213 nm) provides precise material removal is important regarding near future technological development of laser system for corneal surgery.

In this paper, we report ablation of the cornea and synthetic collagen epikeratoplasty material using a Q-switched Nd:YAG laser in the fifth (213 nm) and fourth (266 nm) harmonics. Damage zones for the 213 nm and the 266 nm laser radiation are  $<1$  and  $15\text{ }\mu\text{m}$ , respectively. Results suggest that this solid-state laser could replace excimer lasers in performing laser keratomileusis. In addition, we present the features of a new nonlinear crystal, beta barium borate (BBO) which was used in the experiment for the generation of fourth and fifth harmonics.

## MATERIAL AND METHOD

### Generation of 213 nm UV Radiation

A schematic of the experiment is shown in Fig. 1. A flashlamp-pumped Q-switched Nd:YAG laser (Quantel model 580) operating at 10 Hz and 10 ns with a linearly-polarized TEM<sub>00</sub> output energy of 50 mJ per pulse at 1064 nm was used. This fundamental beam was focused into a type-I doubling crystal of CD\*A to perform the second harmonic generation (SHG) at 532 nm. The fourth harmonic generation (4HG) was obtained by doubling the green radiation in a BBO (type I) crystal. The fifth harmonic generation (5HG) was generated by frequency mixing of the fundamental (1064 nm) and the 4HG (266 nm) in another BBO crystal (type I). These BBO crystals were angle-cut at  $47.6^\circ$  and  $51.1^\circ$  for type I 4HG and 5HG, respectively [7]. We note that the combination of type I SHG, 4HG and 5HG provides the simplest setup for the generation of the 5HG from an Nd:YAG laser. Proper polarization of the 4HG and the fundamental beam is necessary to achieve production of the fifth harmonic by the mixing crystal. A  $90^\circ$  shift in polarization occurs in the SHG crystal and another  $90^\circ$  shift occurs in the

Manuscript received August 15, 1990; revised September 15, 1990. This work was supported in part by the National Institutes of Health under Base Grant RR00165. The work of J. T. Lin was supported by the Florida High-Tech Council.

Q. Ren, R. P. Gailitis, and K. P. Thompson are with the Ophthalmic Laser Research Laboratory, Yerkes Regional Primate Research Center, Emory University, Atlanta, GA 30329.

J. T. Lin is with the Center for Research in Electro-Optics and Lasers (CREOL) University of Central Florida, Orlando, FL 32186.

IEEE Log Number 9040430.

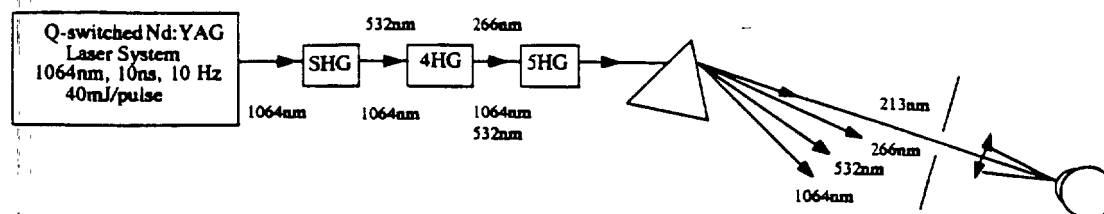


Fig. 1. A schematic of the experiment setup. CD\*A type-I crystal was used for SHG. Two type-I BBO crystals with angles cut at  $47.6^\circ$  and  $51.1^\circ$  were used for 4HG and 5HG, respectively. An energy output  $0.4 \pm 0.05$  mJ/pulse for 213 nm or  $2.3 \pm 0.1$  mJ/pulse for 266 nm was obtained in our experiment.

4HG crystal, such that the fundamental and 4HG beams are parallel polarized. An output energy of  $0.4 \pm 0.05$  and  $2.3 \pm 0.1$  mJ/pulse was achieved at 213 and 266 nm, respectively, using the following crystal specifications (crystal length): CD\*A (20 mm), BBO (for 4HG, cut at  $47.6^\circ$ , 6.5 mm), and BBO (for 5HG, cut at  $51.1^\circ$ , 7 mm). All crystals were supplied by the JTT company (Winter Springs, FL).

### Biomaterial Ablation

Fresh porcine corneas with an average thickness of 600  $\mu$ m, 100  $\mu$ m thick synthetic epikeratoplasty lenticules composed of type I collagen (provided by Bioetica, Portland, ME) were used for ablation study. Before ablation of each cornea, the epithelial layer was mechanically removed.

For the 213 nm study, the laser beam was scanned at 0.1 mm/s across the specimens three times by manually driving a micrometer translation stage. Other samples were focally irradiated by the laser. The spot size energy of 213 nm laser radiation was 0.2 mm in diameter, and  $0.4 \pm 0.05$  mJ/pulse, respectively.

For the fourth harmonic (266 nm) study, the corneas and synthetic lenticules were scanned under the laser beam. The spot size and the energy of the laser beam were 1 mm in diameter, and  $2.3 \pm 0.1$  mJ/pulse. The purpose of this study was to compare the damage to that produced by the excision 213 nm wavelength.

Immediately after ablation, each sample was examined under a dissecting microscope and then fixed in either a solution of 2% paraformaldehyde for light microscopy or 2.2% glutaraldehyde for electron microscopy.

## RESULTS

### 213 nm Ablation

Examination with a dissecting microscope immediately after 213 nm ablation revealed clean surfaces with no adjacent damage evident in any of the three different samples. The gross appearance was similar to ablation performed with the ArF excimer laser at 193 nm from our own experience. 2100 pulses of  $0.4 \pm 0.05$  mJ per pulse (210 s) were needed to perforate the porcine cornea and 100 pulses (10 s) of the same energy were necessary to ablate through the 100  $\mu$ m thick synthetic lenticules.

From our preliminary experiment described above, the ablation rate for 213 nm was estimated to be 0.3  $\mu$ m/pulse



Fig. 2. Photograph for scanning electron microscopy (SEM) on the synthetic collagen. The finger-like microstructure was noted with well-preserved shape.

for porcine cornea and 0.8  $\mu$ m/pulse for synthetic lenticules at  $1.2$  J/cm<sup>2</sup> radiant exposure level. Assuming that the ablation threshold is proportional to the absorption depth, we interpolate the results obtained in [8], and estimate the ablation threshold at 213 nm is 100 mJ/cm<sup>2</sup>.

### 266 nm Ablation

Examination of porcine cornea with the dissecting microscope showed clean ablation similar to those observed with 213 nm. On the synthetic epikeratoplasty lenticules, however there was some slight charring at the edges. A total of 1800 pulses were used during the scan.

### Histopathology

Scanning electron microscopy (SEM) on the synthetic collagen (Fig. 2) revealed an extremely clean ablation, with a finger-like microstructure noted at the edge of the excision.

Light microscopy (Fig. 3) and transmission electron microscopy (TEM) (Fig. 4) of the 213 nm ablation revealed a clean linear excision with no evidence of adjacent tissue damage at the margin of the excision. The structure of the collagen lamellae were preserved. The damage zone is about 0.5  $\mu$ m.

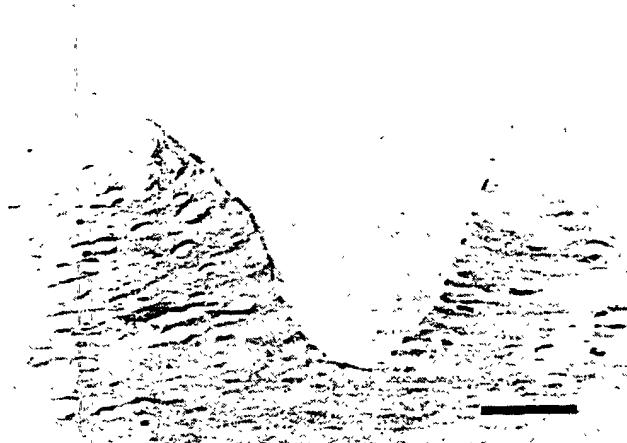


Fig. 3. Light microscopy of the porcine cornea ablated by 213 nm radiation at  $1.2 \text{ mJ/cm}^2$ . The scale bar represents  $100 \mu\text{m}$ .

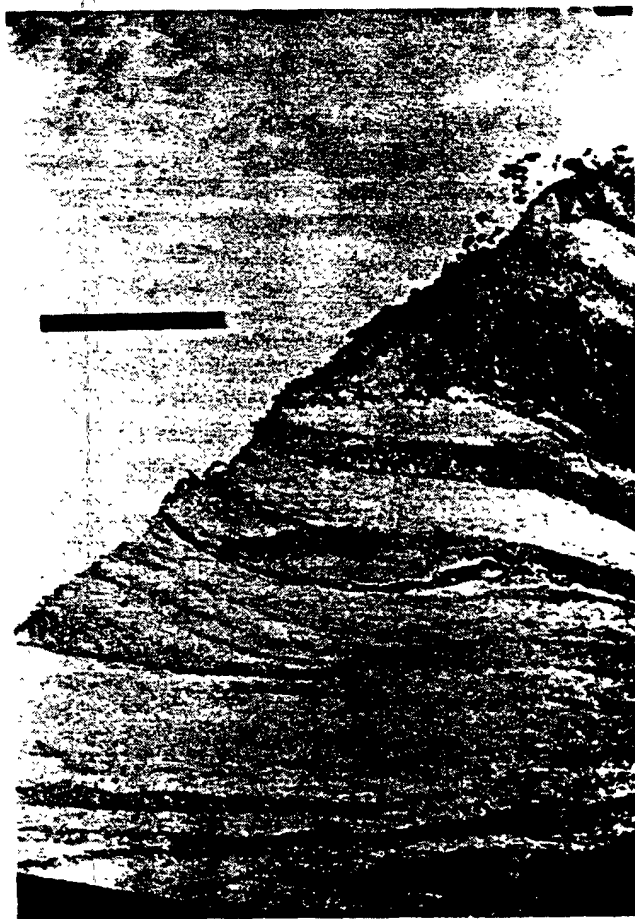


Fig. 4. Transmission electron microscopy of the porcine cornea ablated by 213 nm radiation at  $1.2 \text{ J/cm}^2$ . The scale bar represents  $5 \mu\text{m}$ . The structure of the collagen lamellae was well preserved. The damage zone is about  $0.5 \mu\text{m}$ .

Light microscopy (Fig. 5) and TEM (Fig. 6) of 266 nm ablation showed a  $15 \mu\text{m}$  damage zone of denatured collagen and lamellar disruption.

Similar observation has been reported when compared excimer laser ablation of the cornea at 193 nm (ArF) and 248 nm (KrF) [8], [9].

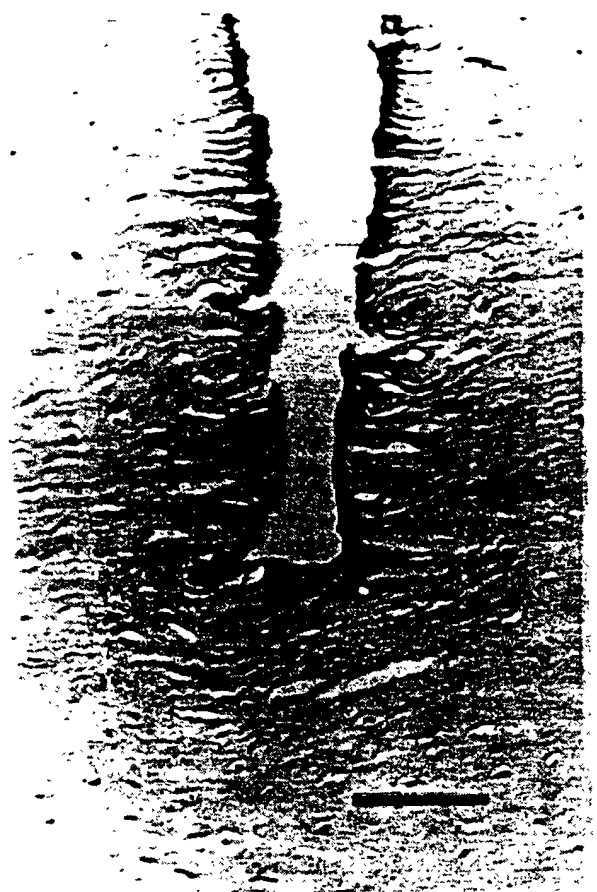


Fig. 5. Light microscopy of the porcine cornea ablated by 266 nm radiation. The scale bar represents  $100 \mu\text{m}$ .

#### DISCUSSION

Our preliminary experiment first demonstrated that the fifth-harmonic Nd:YAG solid-state laser (213 nm) is capable of ablating the cornea and synthetic epikeratoplasty materials with a comparable degree of precision and tissue damage as the 193 nm ArF excimer. This experiment opens major opportunities for the development of a novel corneal sculpting system based on solid-state lasers which may overcome difficulties associated with excimer lasers.

More UV (at 213 nm) energy (1–3 mJ) may be obtained by using longer (8–9 mm) BBO crystals with the appropriate antireflection dielectric coatings on each nonlinear crystal. In this study, the laser was operated at the single-mode (with a maximum fundamental energy of 50 mJ/pulse in our model). Much higher UV (213 nm) energy (20–50 mJ) may be achieved with multimode operation in our system. For better control of our ablation process, however, we prefer a single-mode output of the UV radiation. In an up-graded system with 200 mJ TEM<sub>00</sub> fundamental energy, we should be able to generate 213 nm with energies of (10–20 mJ) when the nonlinear crystals are optimized in lengths and with AR-coated surfaces.

So far, a number of beam delivery systems have been developed based on the ArF excimer laser and are currently undergoing clinical investigation for corneal re-



Fig. 6. Transmission electron microscopy of the porcine cornea ablated by 266 nm. The scale bar represents 5  $\mu\text{m}$ . A 10–15  $\mu\text{m}$  damaged zone with denatured collagen and lamellar disruption was observed.

fractive surgery [10]–[12]. Different methods used by these systems include expanding or constricting diaphragms controlled by a computer, rotating wheels with varying sized apertures and slits, scanning a mathematically defined slit, and ablation of preshaped mask. All of these concepts were developed based on surface ablation using commercially-available excimer laser systems with rectangular beam patterns (usually  $25 \times 7 \text{ mm}$ ) and low operating repetition rates (10–20 Hz). Due to limitations imposed by low repetition rates, these systems must treat relatively large areas with each pulse in order to complete the treatment within a reasonable clinical time frame ( $\sim 60 \text{ s}$ ) and they leave a step-like contour to the cornea surface when using an aperture wheel [12] or discretely expanding and constricting diaphragms [11].

On the other hand, an ultrafast surface scan made possible by the use of a solid-state laser could introduce a new concept of cornea reshaping and allow the smoothness of the corneal surface to be controlled within submicrometer accuracy without lengthening the surgical procedure. With a fast scan mechanism, each pulse etches away a very thin layer of the tissue (submicrometer) within small area. Since the laser beam spot is rapidly scanned away from the ablated area, the interaction between laser

beam and debris generated by ablation process (corneal tissue plume) will be significantly reduced.

The most important feature offered by a rapid pulsed scanning UV laser system is the ability to custom contour a surface to any desired shape without limitation to spherical or cylindrical correction. This will allow correction of all optical aberrations, not just sphere and cylinder, when used for corneal sculpting or laser adjustable synthetic epikeratoplasty (LASE) [2].

#### ACKNOWLEDGMENT

The authors at Emory University would like to thank Dr. M. Penny for his initiative and valuable discussions. We would like to thank J. Montgomery (at CREOL/UCF) for his assistance in the laser system.

#### REFERENCES

- [1] S. L. Trokel, R. Srinivasan, and B. Braren, "Excimer laser surgery of the cornea," *Amer. J. Ophthalmol.*, vol. 96, pp. 710–715, 1983.
- [2] K. P. Thompson, K. Hanna, and G. O. Waring, III, "Emerging technologies for refractive surgery: Laser adjustable synthetic epikeratoplasty," *Refractive Corneal Surg.*, vol. 5, pp. 47–48, 1989.
- [3] S. L. Trokel, "Evolution of excimer laser corneal surgery," *J. Cataract Refract. Surg.*, vol. 15, pp. 373–383, 1989.
- [4] J. Marshall, S. L. Trokel, S. Rothery, and H. Schubert, "An ultrastructural study of corneal incision induced by an excimer laser at 193 nm," *Ophthalmol.*, vol. 92, pp. 749–758, 1985.
- [5] T. Seiler, J. Marshall, S. Rothery, and J. Wollensak, "The potential of an infrared hydrogen fluoride (HF) laser ( $3.0 \mu\text{m}$ ) for cornea surgery," *Lasers Ophthalmol.*, vol. 1, pp. 49–60, 1986.
- [6] J. T. Lin, "Nonlinear crystals for tunable coherent sources," *Opt. Quantum Electron.*, vol. 22, pp. 5283–5313, 1990.
- [7] J. T. Lin and C. Chen, "Choosing a nonlinear crystal," *Lasers Optron.*, vol. 6, p. 59, 1987.
- [8] C. A. Puliafito, R. F. Steinert, T. S. Deutsch, and F. Hillenkamp, "Excimer laser ablation of the cornea and lens," *Ophthalmol.*, vol. 92, pp. 741–748, 1985.
- [9] C. A. Puliafito, K. Wong, and R. F. Steinert, "Quantitative and ultrastructural studies of excimer laser ablation of the cornea at 193 and 248 nanometers," *Laser Surg. Med.*, vol. 1, pp. 155–159, 1978.
- [10] K. D. Hanna, J. C. Chastang, L. Asfar, and J. Samson, "Scanning slit delivery system," *J. Cataract Refract. Surg.*, vol. 15, pp. 390–396, 1989.
- [11] R. G. Caro, and D. F. Muller, "A medical excimer laser system for corneal surgery and laser angioplasty," *Proc. SPIE*, vol. 712, *Lasers in Medicine*, pp. 95–98, 1986.
- [12] P. R. Yoder, W. B. Telfair, J. W. Warner, and C. A. Martin, "Application of the excimer laser to area recontouring of the cornea," *Proc. SPIE*, vol. 1023, *Excimer Lasers and Applications*, pp. 260–267, 1988.



Qiushi Ren received the B.S. degree in optical engineering from the Huazhong University of Science and Technology, Wuhan, China, and the M.S. degree in electrical engineering from the Ohio State University, Columbus, Ohio, in 1984 and 1987, respectively.

He is expecting to receive the Ph.D. degree in electrical engineering from the Ohio State University in December 1990. His Ph.D. research involved investigating the optical interconnection for reconfigurable integrated circuits. During his

Ph.D. training program, he also developed a strong research interest in bioengineering and biophysics. He studied coherent far-UV absorption characteristics on the human cornea, lens, and vitreous. From June 1989 to December 1989, he was a visiting student with Wellman Laboratories of Photomedicine, Harvard University. While with the Wellman Lab, he studied the mechanism of IR-laser interactions with biological tissue, developed a novel beam delivery system for ophthalmic surgery, and investigated the light intensity distribution of optical fiber probes for laser angioplastic surgery. He is currently a technical director of the ophthalmic laser research laboratory at Emory University, working on the LASE (Laser Adjustable Synthetic Epikeratoplasty) project. His current interest is in the area of laser-tissue interactions, biomedical instrumentation, and optoelectronics.

Raymond P. Gailitis, photograph and biography not available at the time of publication.



Keith P. Thompson was a 1984 Alpha Omega Alpha graduate of Southwestern Medical School, Dallas, TX.

Following an internship in internal medicine, he completed a three-year residency in ophthalmology at the Bascom Palmer Eye Institute, Miami, FL. He recently completed a two-year National Institutes of Health Research Training Fellowship in refractive surgery at Emory University. His research concerns the evaluation of new technologies for refractive surgery. His prin-

cipal interest is to develop synthetic biomaterials for corneal lenses, non-invasive methods of attaching them to the cornea, high-resolution imaging systems to determine their shape and refractive power, and excimer laser delivery systems to precisely adjust their shape—a concept termed "Laser Adjustable Synthetic Epikeratoplasty" or LASE. He is the principal investigator of this research effort supported by industry which involves over 25 scientists and physicians at eight institutions. In addition to his research studies, he is currently completing a one-year clinical fellowship in cornea and anterior segment surgery at the Emory Eye Center.

Dr. Thompson is a Diplomat of the American Board of Ophthalmology.

J. T. Lin received the Ph.D. degree from the University of Rochester, Rochester, NY, in 1980.

He is currently an Associate Professor with the Department of Physics and the Center for Research in Electro-Optics and Lasers (CREOL), University of Central Florida, Orlando. Previously he was a senior scientist with JAYCOR/NRL and Litton Laser Systems Division and director of research with Quantum Technology, Inc. His research interests include the development of tunable solid-state and diode-pumped lasers, lasers for surgical treatment, theoretical and experimental studies of nonlinear effects and the growth and characterization of new laser host, and nonlinear optical materials. He has authored over 80 journal papers and technical proceedings. He was the symposia chair for OPTCON'89 on Nonlinear Optical materials and co-chair for SPIE on Nonlinear Optics. He was also the founder of the JTT Company (Florida) and HUATON Optronics Technology, Inc. (China).

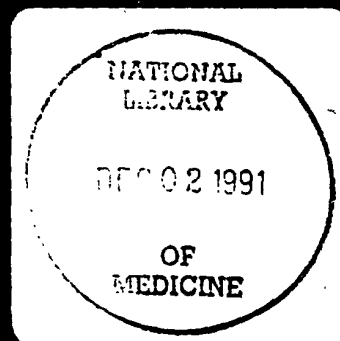
W1 LA784  
NO. 6 1991  
SEQ: L02705000  
LASERS IN SURGERY AND  
MEDICINE

# LASERS IN SURGERY AND MEDICINE

Volume 11,  
Number 6, 1991

- \* Argon and excimer lasers in dentistry
- \* Cellular microsurgery
- \* Port wine stain

 WILEY-LISS



ISSN 0196-8092

## Solid State Ultraviolet Laser (213 nm) Ablation of the Cornea and Synthetic Collagen Lenticules

Ray P. Gaillitis, MD, Qiushi Ren, PhD, Keith P. Thompson, MD, J.T. Lin, PhD,  
and George O. Waring, III, MD, FACS

*Department of Ophthalmology, Emory University, and Yerkes Regional Primate  
Research Center, Atlanta, Georgia 30322 (R.P.G., Q.R., K.P.T., G.O.W.); CREOL,  
University of Central Florida, Orlando (J.T.L.)*

We used a Q-switched Nd:YAG laser with non-linear optical crystals to produce the 5th (213 nm) and the 4th (266 nm) harmonic frequencies. Using these two wavelengths, we ablated fresh porcine corneas and type I collagen synthetic epikeratoplasty lenticules. For the 213-nm ablation, radiant exposure was  $1.3 \text{ J/cm}^2$ . The ablation rate was  $0.23 \mu\text{m}$  per pulse for the epikeratoplasty lenticules. We examined all tissues with light microscopy, transmission electron microscopy, and scanning electron microscopy. Histology for the 213-nm ablation showed a clean ablation crater with minimal collagen lamellae disruption and a damage zone less than  $1 \mu\text{m}$ . In comparison, the 266 nm radiation showed more charring at the edges with a damage zone approximately  $25 \mu\text{m}$  deep with disruption of the stromal lamella.

Our results show that this solid state UV laser is a potential alternative to the excimer laser for cornea surgery.

**Key words:** collagen, excimer lasers, non-linear optical crystals, refractive surgery

### INTRODUCTION

Excimer lasers are being investigated for their potential use in refractive keratoplasty [1], glaucoma filtering procedures [2], and cataract removal [3,4]. Early clinical reports describing the use of argon fluoride (193 nm) excimer lasers to reduce myopia in blind, partially sighted, and sighted eyes have documented general efficacy with minimal subepithelial haze and fair refractive predictability for eyes with less than 6.00 diopters (D) of myopia [5-12]. There are several practical drawbacks to the current generation of argon fluoride excimer lasers. First, they use fluorine gas, which must be carefully contained so as not to escape to the atmosphere and cause harm to patients and operating room personnel, must be changed frequently because of its short half-life, and is corrosive to the laser cavity and resonator optics. The lasers are large and difficult to move. They require frequent maintenance checks and change in optical components in order to function reliably. The lasers are limited to the relatively

slow pulse frequency of 5-10 Hz. Because of the high spatial mode of operation, the laser beam must be manipulated through a complex delivery system in order to obtain a more homogeneous beam of the desired shape before exposing it to the cornea. The cost of the lasers is at this time prohibitive to most individual ophthalmologists.

A solid state laser that produces a wavelength near 193 nm could eliminate many of these disadvantages: eliminating the problems with gases; making the laser more compact, mobile, relatively maintenance free; increasing beam ho-

Accepted for publication August 14, 1991.

Address reprint requests to George O. Waring, M.D., c/o Emory Eye Center, 1327 Clifton Rd, N.E., Atlanta, GA 30322.

This work was supported in part by General Electric Medical Systems, Milwaukee, Wisconsin.

Dr. Lin has a financial interest in the non-linear optical crystals. Dr. Waring is a paid consultant to General Electric. The other authors have no financial interest in the products or procedures presented herein.

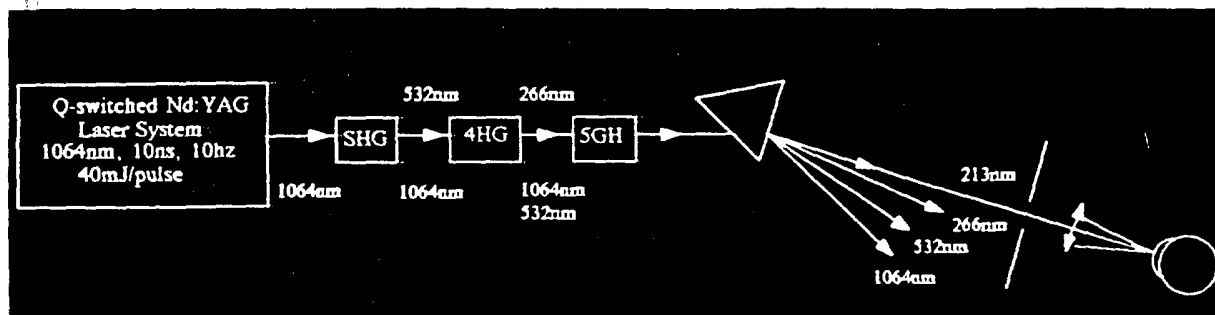


Fig. 1. Schematic of laser arrangement. SHG = second harmonic generator; 4HG = fourth harmonic generator; 5HG = fifth harmonic generator.

mogeneity; reducing cost; and utilizing a fast pulse frequency that would enable a delivery system to scan the corneal surface very rapidly with a small spot for more refined ablation profiles. If such a scanning system were linked to a computerized corneal topography system, this could be effectively used to reshape the cornea or reconstruct synthetic epikeratoplasty lenticules [13].

In this paper, we report using a Q-switched Nd:YAG laser to generate the fifth (213 nm) and the fourth (266 nm) harmonic to ablate the cornea and synthetic collagen materials. With light and scanning electron microscopy, we show that the damage zones for the 213-nm laser are less than 1  $\mu\text{m}$  and for the 266-nm laser less than 10  $\mu\text{m}$ . We also discuss the use of a scanning laser delivery system that may produce correction of spherical and astigmatic refractive errors as well as irregular corneal surfaces.

## MATERIALS AND METHODS

### Laser and Delivery System

A schematic of the experimental setup is shown in Figure 1. A more detailed description of the experimental setup has been published previously [14]. The laser was a flashlamp-pumped, Q-switched Nd:YAG laser (Quantel model 580) operating at 10 Hz and 10-ns per pulse with a TEM<sub>00</sub> output energy of 50 mJ per pulse at 1,064 nm. The fundamental beam was focused into a CD\*A non linear optical crystal to obtain the second harmonic frequency of 532 nm. The 4th harmonic frequency (266 nm) was obtained by doubling the green radiation in a beryllium boroxylate (BBO) crystal. The 5th harmonic frequency (213) was generated by frequency mixing of the fundamental (1,064 nm) and the 4th harmonic (266 nm) frequency in another BBO crystal.

Output energy was measured with a joulemeter (ED200, Gentec, Quebec, Canada). An output energy of  $0.4 \pm .05$  mJ per pulse was achieved for the 213 nm radiation. This was focused to a 200  $\mu\text{m}$  spot size with a biconvex quartz lens giving a radiant exposure of  $1.3 \text{ J/cm}^2$ . The following crystal specifications were used: CD\*A (200 nm long), BBO (for fourth harmonic, cut at  $47.6^\circ$ , 6.5 mm long), and BBO (for fifth harmonic, cut at  $51.1^\circ$ , 7 mm long). At 266 nm, the output energy was  $2.3 \pm 0.1$  mJ per pulse focused into a 200  $\mu\text{m}$  spot size, giving a radiant exposure of  $7.3 \text{ J/cm}^2$ . All crystals were supplied by JTT Company (Winter Springs, Florida).

### Ablation of Tissue and Collagen Lenticules

Six fresh porcine cornea in whole globes and six 100  $\mu\text{m}$  thick dehydrated type I collagen lenticules (Bioetica, Portland, Maine) were ablated. Prior to ablation, the epithelium was scraped from the porcine corneas with a blunt spatula. The globes were mounted on an XY micrometer stage and placed in front of the focused laser beam. The surface of the cornea was exposed to the laser for an average of 70 seconds while the globe was manually moved back and forth three times with the XY stage to obtain a horizontal linear excision approximately 3 mm long and 0.2 mm wide. This was done for both the 213-nm and the 266-nm wavelengths. Three eyes received ablations with the 213-nm wavelength and three eyes with 266-nm wavelengths. The dehydrated synthetic collagen lenticules were mounted to the XY stage, and the above procedure repeated, moving the stage back and forth three times.

The ablation rate was measured with the 213-nm configuration only. This was done by exposing a known-thickness bovine cornea as measured with an ultrasonic pachometer and a



known-thickness synthetic collagen lenticule to the laser and counting the number of pulses needed to perforate the tissue and the biomaterial respectively.

### Tissue Preparation

After ablation, each specimen was examined under a dissecting microscope, and slit-lamp photomicrographs were taken to demonstrate the gross ablation slit. The porcine cornea was dissected off the globe using corneo-scleral scissors and was bisected. One half was fixed in 2% paraformaldehyde and the other half was fixed in 2.2% glutaraldehyde. The synthetic collagen material after ablation was bisected, and placed in the two solutions.

The samples in 2% paraformaldehyde were processed and sectioned into 3- $\mu$ m-thick sections with a microtome. They were stained with hematoxylin and eosin. The samples stored in glutaraldehyde were processed for transmission and scanning electron microscopy as described previously [15]. The depth of the damage zone was then determined by examining the photomicrographs at known magnification and measuring the depth of ablation and the width of the anatomically altered tissue between the edge of the ablation crater and the normal cornea. These were compared with light and electron photomicrographs of corneas and lenticules ablated with the 193 nm ArF excimer laser as reported previously [15].

## RESULTS

### Ablation With the 213 nm Nd:YAG

**Gross Examination.** Examination of the corneas and lenticules with a dissecting microscope immediately after the 213 nm ablation revealed smooth surfaces with no evidence of tissue fragmentation or charring in any of the samples (Fig. 2). The gross examination was similar to ablations obtained with the 193 nm ArF laser.

Two hundred ten seconds were needed to perforate the 483  $\mu$ m thick porcine cornea, and 10 seconds were necessary to perforate the 100- $\mu$ m-thick synthetic lenticule; therefore, the ablation rate at 213 nm was estimated to be 0.23  $\mu$ m per pulse for the porcine corneas and 1.0  $\mu$ m per pulse for synthetic collagen lenticules at 1.3 J/cm<sup>2</sup> radiant exposure.

**Histopathology and Ultrastructure.** Light microscopy of the porcine cornea showed a smooth-walled ablation crater lined with a thin zone of darkly staining material (fig. 3c). Normal collagen

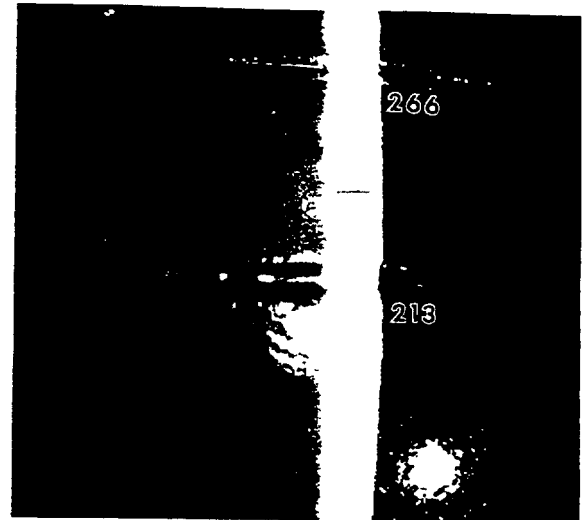


Fig. 2. Slit lamp photo of cornea after UV solid state laser ablation. Upper excision produced by linearly scanning a spot across the cornea with 266-nm radiation. Lower excision produced with 213 nm.

lamellae and keratocytes were present adjacent this zone. Transmission electron micrographs revealed a relatively smooth edged ablation crater with an abnormal dark-stained zone of disorganized and disrupted lamellae ranging from 0 to 0.6  $\mu$ m wide (Fig. 3d). The collagen lamellae adjacent to this zone of damage remained well organized with an occasional vacuolated keratocyte within the lamellae. The average width of the damage zone appeared to be approximately 0.3  $\mu$ m. Scanning electron microscopy revealed an ablation crater with relatively smooth walls. There was no charring noted on the edges (Fig. 4).

Light and transmission electron microscopy of the collagen lenticule showed a darkly staining disorganized zone approximately 1  $\mu$ m wide. Scanning electron microscopy showed a smooth-walled ablation crater with several rows of finger-like projections parallel to the ablated slit (Fig. 5). The tips of these projections were separated from each other by approximately 6  $\mu$ m. They became less prominent further away from the ablation zone.

### Ablation With the 266 nm Nd:YAG

**Gross Examination.** Examination of the porcine corneas with a dissecting microscope showed ablation devoid of charred tissue similar to those observed with the 213 nm laser (Fig. 2). On the synthetic epikeratoplasty lenticules, how-

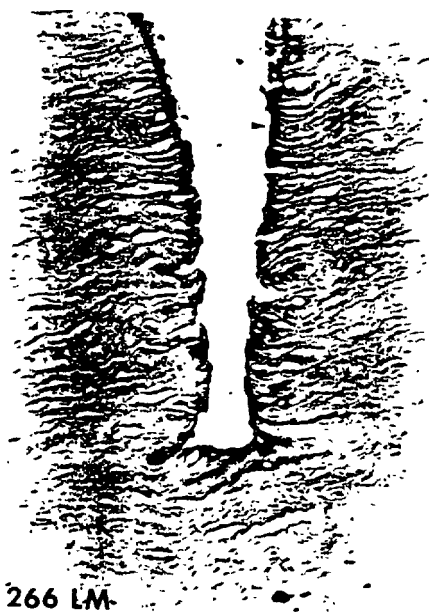
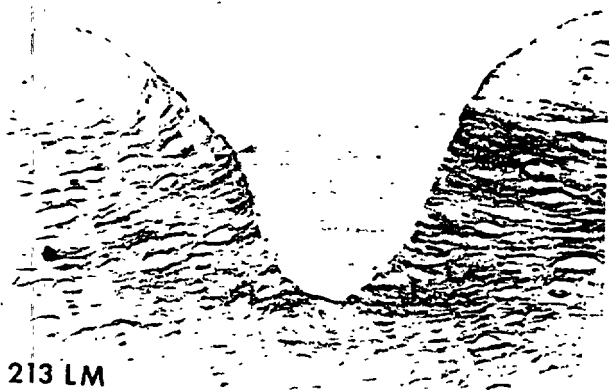
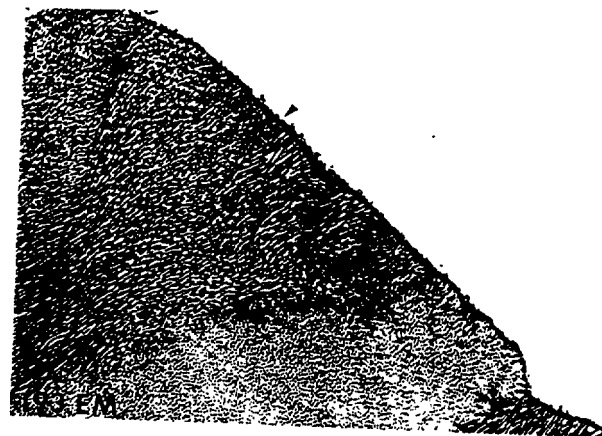
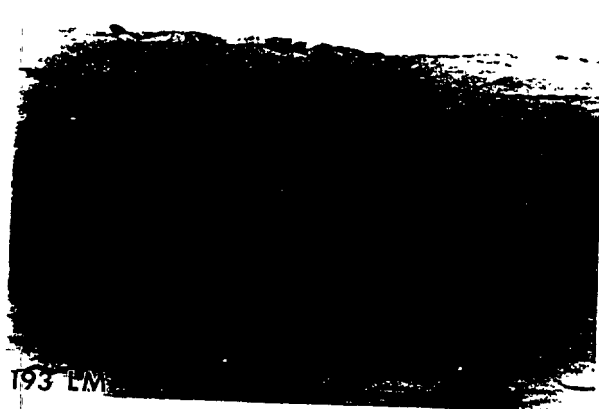


Fig. 3. Light microscopy and ultrastructural comparison of 193 nm, 213-nm and 266-nm corneal ablations. a: Excimer laser (193 nm ArF) ablated rhesus monkey cornea. Hematoxylin and eosin (H&E) stain.  $\times 200$ . Ablated surface appears smooth with minimal collagen disruption. b: Excimer laser (193 nm ArF) ablated rhesus monkey cornea electron micrograph.  $\times 1,490$ . Arrows depict 0.3 nm electron dense condensate. Adjacent stromal collagen lamellae are undisturbed. c: H&E stained light micrograph of a porcine cornea ablated with 213-nm radiation.  $\times 25$ . Smooth ablation crater with a

thin zone of darkly staining material (arrows) adjacent to normal appearing corneal stroma. d: Transmission electron micrograph of a porcine cornea ablated with 213-nm radiation. There is a smooth ablated edge with a darkly colored zone ranging from 0 (single arrows) to 0.6 mm wide (double arrows). The collagen lamellae adjacent to the dark zone appears to be normally organized. Bar = 5  $\mu\text{m}$ . e: H&E stained light micrograph of a porcine cornea ablated with 266 nm radiation.  $\times 25$ . An irregular zone of darkly staining material is adjacent to the ablation center. Normal stroma is seen adjacent to the damage zone. f: Transmission electron micrograph of a porcine cornea ablated with 266-nm radiation. There is a 15- $\mu\text{m}$ -wide zone of collagen damage (arrow). Several vacuoles are seen adjacent to the damage zone. Collagen lamellae adjacent to darkly staining zone appear to be normal. Bar = 10  $\mu\text{m}$ .



Fig. 4. Scanning electron micrograph of porcine cornea ablated with 213-nm radiation. Left,  $\times 52$ . Right,  $\times 304$ . Central portion of slit (box) ablated more than either end. Relatively smooth ablated surfaces are apparent.

ever, there was slight charring at the edges of the ablated area.

**Histopathology and Ultrastructure.** Light microscopy of the porcine cornea showed an irregular ablation crater with several excavated areas (Fig. 3e). A zone of dark staining material of variable thickness was adjacent to the ablation crater which varied in thickness. The underlying stromal cornea lamellae appeared to be normal without disruption. There were many normal appearing keratocytes within the stroma. Transmission electron microscopy showed a dark disorganized zone approximately 15  $\mu\text{m}$  thick containing several vacuolated areas (Fig. 3d). Collagen lamellae and keratocytes adjacent to this dark zone appeared to be normal.

Light and transmission electron microscopy of the synthetic collagen material revealed a dark staining area 8–10  $\mu\text{m}$  thick adjacent to the crater.

## DISCUSSION

### Nd:YAG Laser

In order to generate an ultraviolet frequency from a solid state laser we used nonlinear optical crystals to alter the wavelength from a standard flash pumped Nd:YAG laser (Fig. 1). This has

previously been described in generating the fourth harmonic (266 nm) of the Nd:YAG laser and making corneal incisions [16].

Although we have used the solid state laser to generate an ultraviolet wavelength of 213 nm close to that of the 193-nm ArF excimer laser with a solid state laser, there are several concerns pertaining to the non-linear optical crystals used in this process. Generally, the best crystals are obtained from China, where they are grown under careful supervision. The crystal surfaces have to be cleared carefully so that the incoming laser beam will have a certain incidence angle relative to the crystal lattice. Cost and availability could become a problem if these are needed for commercial production. In order to function properly and not become damaged, all crystals used in the array need to be aligned precisely with regard to the incident laser beam. For long-term function, the crystals need to be kept under strict temperature and humidity control (personal communication, J.T. Lin, May 1990).

### Histopathology and Ultrastructure

Our experiment demonstrated that the 5th harmonic Nd:YAG solid state laser (213 nm) is capable of ablating the cornea and synthetic collagen materials with a comparable amount of tis-

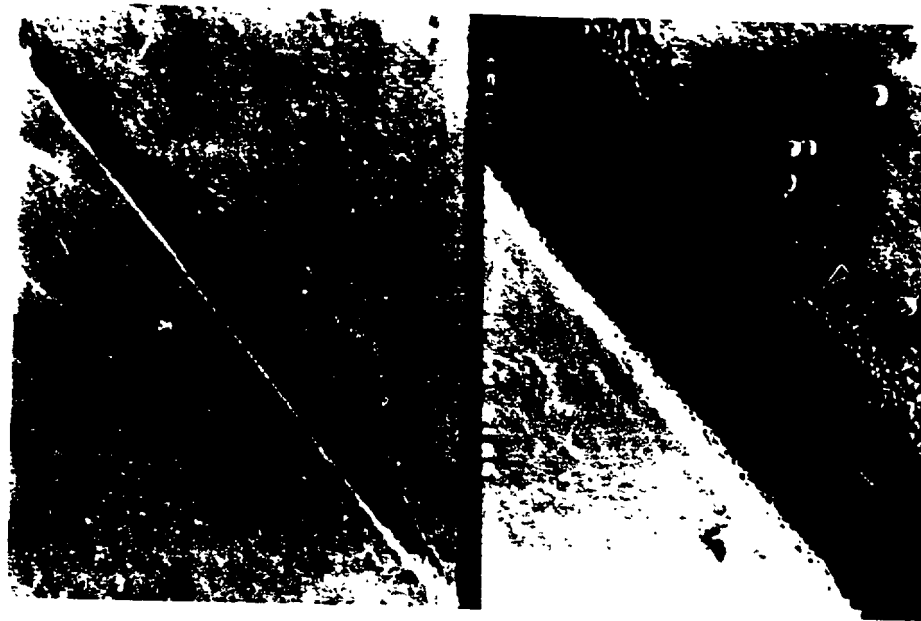


Fig. 5. Scanning electron micrograph of a type I collagen material ablated with 213-nm radiation. The wall of the ablated zone is smooth but the edge shows numerous fingerlike pro-

jections (arrow) separated from each other by 6  $\mu\text{m}$ . These are believed to be caused by the arrangement of the collagen fibrils in the synthetic material. Left,  $\times 49$ ; Right,  $\times 293$ .

sue damage as the 193 ArF excimer laser (Fig. 3a-d).

As reported previously [15], ArF excimer (193 nm) ablation of the cornea produces an electron-dense condensate at the base of the ablated zone which varies from 0.1 to 0.25  $\mu\text{m}$  in thickness (Fig. 3a,b). The depth of the damage zone did not vary with increasing radiant exposure. Others have reported damage zones up to 0.3  $\mu\text{m}$  deep [17].

Our light and electron microscopy sections show a smooth-contoured ablation crater with a damage depth ranging from 0–0.6  $\mu\text{m}$ . There does not appear to be any damage to the collagen lamellae or the keratocytes adjacent to the electron dense zone. The radiant exposure we used (1.3 J/cm<sup>2</sup>) was much higher than that used in the ArF excimer studies. Ablation of the collagen lenticules show a 1  $\mu\text{m}$  damage zone which may have been due to the dehydrated state of the type I collagen.

Although the initial histopathology and ultrastructure are similar for the ArF excimer and the 5th harmonic Nd:YAG lasers, we have not addressed the potential differences in long term wound healing. Recent studies utilizing immunohistopathology have shown extensive wound remodeling in monkey corneas after ablation with the ArF excimer laser [18]. Long-term wound

healing for the 5th harmonic Nd:YAG laser will have to be addressed in future studies.

#### Delivery Systems

There are two separate ways in which energy from this solid state laser could be delivered to the eye. First, if an appropriate energy output from the laser could be obtained, the beam could be expanded with ultraviolet transparent lenses and delivered with conventional excimer laser delivery systems. Such systems include an expanding diaphragm which allows more energy to be deposited in the center of the cornea than the periphery as it expands, an ablatable mask which imparts its general shape on the cornea as it is ablated away, and a scanning mathematically defined elliptical slit which scans across the cornea in two or more orthogonal meridians creating central corneal flattening.

Second, and more innovative, is the concept of ultrafast surface scanning. In this system, a small spot is focused onto the surface of the cornea and ablates the tissue. The spot is scanned quickly to another area which is ablated. With a fast scan mechanism, each pulse etches away a thin layer of tissue within a small area. Since the laser beam spot is scanned rapidly away from the ablated area, the interaction between the laser and the debris generated from the ablation pro-

cess will be reduced significantly and the shielding effect will be eliminated. With the use of solid state lasers, pulse rates of 1,000–10,000 Hz may be obtained.

The most important feature of a rapidly pulsed scanning ultraviolet laser system would be the ability to correct spherical and astigmatic refractive errors and to smooth irregular corneas. Also, this system could make transverse excisions for correction of astigmatism and circular trephinations; aspheric ablations could also be generated. L'Esperance proposed a scanning laser delivering system; however, he limited his discussion to spherical and cylindrical corrections to the cornea only [19]. A scanning spot laser system would be optimal if integrated with a corneal topography system. The exact shape of the cornea would be determined by a topographic system. Next, the surface at the cornea would be divided up into many small unit areas or pixels. Each pixel would then be assigned a number of laser pulses such that the end result would be a smooth surface of predictable curvature no matter how irregular the initial topography was. In this context it would be ideal to use with laser adjustable synthetic epikeratoplasty [13] to image and reprofile a synthetic lenticule that is attached to the corneal surface or to fix a cornea with irregular astigmatism such as after penetrating keratoplasty.

### Mutagenicity

The issue of mutagenicity remains unanswered. Although the 213-nm ultraviolet wavelength is closer to the 260-nm absorption peak of DNA than the ArF excimer, the biological significance of this is not known [16]. Experiments similar to those performed for the 193 excimer laser will have to be done for the 213-nm 5th harmonic Nd:YAG laser to rule out any increased risks of mutagenicity.

### REFERENCES

1. Trokel SL. Development of the excimer laser in ophthalmology: A personal perspective. *Refractive Corneal Surg* 1990; 6:357–362.
2. Stiles M. Experience with partial excimer trabeculectomy. Presented at the Third International Congress on Laser Surgery of the Cornea. Atlanta, GA. November 3, 1990.
3. Nanevitz TM, Prince MR, Gawande AA, et al. Excimer laser ablation of the lens. *Arch Ophthalmol* 1986; 104:1825–1829.
4. Bath PE. Laser phaco: An introduction and review. *Ophthalmic Laser Ther* 1989/89; 3(2):75–82.
5. Seiler T, Bende T, Wollensak J, et al. Excimer laser keratectomy for correction of astigmatism. *Am J Ophthalmol* 1988; 105:117–124.
6. McDonald MB, Kaufman HE, Frantz JM, et al. Excimer laser ablation in a human eye. *Arch Ophthalmol* 1989; 107:641–642.
7. Taylor DM, L'Esperance RA, Jr, Del Pero RA, et al. Human excimer laser lamellar keratectomy: A clinical study. *Ophthalmology* 1989; 96:654–664.
8. Liu J, McDonald MB, Varnell R, et al. Myopic excimer laser photorefractive keratectomy: An analysis of clinical correlations. *Refractive Corneal Surg* 1990; 6:321–328.
9. McDonald MB, Liu JC, Andrade H, et al. Clinical results of 193 nm excimer laser central photorefractive keratectomy for myopia: The partially sighted and sighted eye studies. *Invest Ophthalmol Vis Sci [Suppl]* 1990; 31:245.
10. McDonald MB, Frantz JM, Klyce SD, et al. Central photorefractive keratectomy for myopia. The blind eye study. *Arch Ophthalmol* 1990; 108:799–808.
11. Seiler T, Kahle G, Kriegerowski M. Excimer laser (193 nm) myopic keratomileusis in sighted and blind human eyes. *Refractive Corneal Surg* 1990; 6:165–173.
12. Zabel RW, Sher NA, Ostrov CS, et al. Myopic excimer laser keratectomy: A preliminary report. *Refractive Corneal Surgery* 1990; 6:329–334.
13. Thompson KP, Hanna K, Waring GO. Emerging technologies for refractive surgery: Laser Adjustable Synthetic Epikeratoplasty. *Refractive Corneal Surg* 1989; 5:46–48.
14. Ren Q, Gailitis RP, Thompson KP, Lin JT. Ablation of the cornea and synthetic polymers using a UV (213 nm) solid-state laser. *IEEE Quant Electron* 1990; 26(12):2284–2288.
15. Fantes FE, Waring GO. Effect of excimer laser radiant exposure on uniformity of ablated corneal surface. *Lasers Surg Med* 1989; 9:533–542.
16. Berns MW, Gaster RN. Corneal incisions produced with the fourth harmonic (266 nm) of the YAG laser. *Laser Surg Med* 1985; 5:371–375.
17. Marshall J, Trokel S, Rothery S, et al. A comparative study of corneal incisions induced by diamond and steel knives and two ultraviolet radiations from an excimer laser. *Br J Ophthalmol* 1986; 70:482–501.
18. SundeRaj N, Geiss MJ, Fantes F, et al. Healing of excimer laser ablated monkey corneas: An immunohistochemical evaluation. *Arch Ophthalmol* 1990; 108:1604–1610.
19. U.S. Patent No. 4665913.
20. O'Brien WJ. Measurement of corneal DNA content. *Invest Ophthalmol Vis Sci* 1979; 18:538–543.

VOLUME II  
**OPHTHALMIC  
LASERS**

**FRANCIS A. L'ESPERANCE, JR., M.D.**

Professor of Clinical Ophthalmology,  
Columbia University College of Physicians and Surgeons,  
New York, New York

THIRD EDITION

*With 1401 illustrations, including 4 color plates*

**Tone drawings by Virginia Cantarella**

**The C. V. Mosby Company**

ST. LOUIS · BALTIMORE · TORONTO 1989



*Editor:* Eugenia A. Klein  
*Assistant editor:* Constance C. Spasser  
*Senior secretary:* Robin O. Sutter  
*Project manager:* Kathleen L. Teal  
*Manuscript editor:* Judith Bange  
*Design:* John Rokusek  
*Production:* Ginny Douglas, Judith Bange, Teresa Breckwoldt

### THIRD EDITION

**Copyright © 1989 by The C.V. Mosby Company**

All rights reserved. No part of this publication may be reproduced, stored in a retrieval system, or transmitted, in any form or by any means, electronic, mechanical, photocopying, recording, or otherwise, without prior written permission from the publisher.

Previous editions copyrighted 1975 and 1983

Printed in the United States of America

The C.V. Mosby Company  
 11830 Westline Industrial Drive, St. Louis, Missouri 63146

### Library of Congress Cataloging in Publication Data

L'Esperance, Francis A., 1932-  
 Ophthalmic lasers.

Bibliography: p.

Includes index.

1. Laser coagulation. 2. Eye—Diseases and defects—Radiotherapy. I. Title. [DNLM: 1. Eye—surgery—atlases. 2. Lasers—therapeutic use—atlases. WW 17 L637o]

RE992.P5L47 1989 617.7'1 88-23131

ISBN 0-8016-2965-9

GW/MV/MV 9 8 7 6 5 4 3 2

---

# 26

---

## New Laser Systems, Their Potential Clinical Usefulness, and Investigative Laser Procedures

During the last decade the krypton laser has become commercially available, the carbon dioxide (CO<sub>2</sub>) laser has moved from the experimental to the clinical phase in the treatment spectrum, the dye laser has been introduced as a multiple-color laser with enormous potential in the field of photodynamic and photocoagulation therapy, the Q-switched or mode-locked neodymium: yttrium-aluminum-garnet (Nd:YAG) laser has been introduced for photodisruption of transparent intraocular tissues, and even the argon laser has been reevaluated to determine potential tissue responses to the green or blue wavelengths. The pioneering ingenuity of many investigators to manipulate existing lasers to control glaucoma, to substitute laser procedures for former surgical operations, and to become expert in the use of the advanced technologic precision inherent in ophthalmic lasers has been significant. The purpose of this chapter is to introduce several new laser and delivery systems that should have considerable potential in the treatment of ocular diseases because of their specific wavelength, high power output, or unique photobiologic action. Investigational procedures made possible by these lasers and older systems are also discussed, and they should shortly become part of our therapeutic armamentarium.

---

### FREQUENCY-DOUBLED Nd:YAG LASER Instrumentation

The clinical use of the frequency-doubled Nd:YAG laser as a source for the photocoagulation of ocular tissue was first achieved clinically in human beings in 1970 in our laboratory at the Columbia-Presbyterian Medical Center (Fig. 26-1). Specifically, this highly collimated, intense, monochromatic beam was

□ Portions of this chapter are modified from L. Esperance, FA Jr. "New laser systems and their potential clinical usefulness." In New Orleans Academy of Ophthalmology Symposium on the laser in ophthalmology and glaucoma update, St. Louis, 1985. The CV Mosby Co.



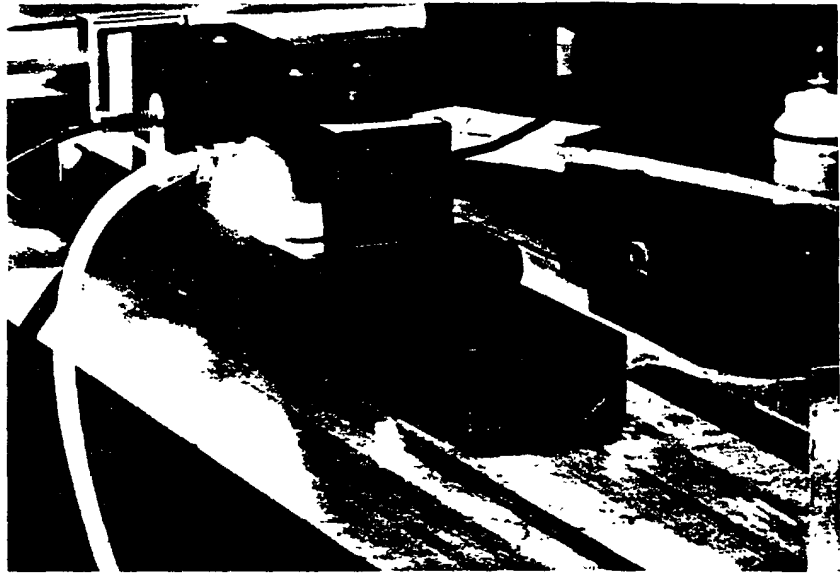


**Fig. 26-1.** Prototype version of the frequency-doubled Nd:YAG laser used during the first clinical human studies in 1970.

employed successfully to therapeutically photocoagulate various chorioretinal abnormalities in seven patients<sup>1</sup> (Fig. 26-2).

At that time the frequency-doubled Nd:YAG laser was loaned to our laboratory by Medical Lasers, Inc., in Burlington, Mass., and consisted of the following parts: (1) a dual elliptic gold-plated cavity; (2) two 3000-W tungsten quartz halogen incandescent lamps; (3) a  $3 \times 75$  mm yttrium-aluminum-garnet host doped with triple-ionized neodymium; (4) two dielectrically coated mirrors; and (5) a barium-sodium-niobate crystal in a temperature-controlled oven.

The fundamental output of the Nd:YAG laser is at 1064 nm. With the addition of the nonlinear crystal in the resonant cavity between the Nd:YAG crystal and the output mirror, the second harmonic is obtained as a bright green beam at 532 nm (Fig. 26-3). The output is obtained through the front mirror, which is dielectrically coated for maximum reflectance at 1064 nm and maximal transmittance of 532 nm.

The pumping source that created the population inversion in the Nd:YAG crystal consisted of two tungsten filament lamps that operated directly from the AC line using a triac power supply. Electric power to the lamps, which were operated in parallel, was continuously variable from 120 V to full power.

The laser power was easily controlled within milliwatts because of the tungsten filament lamps and their inherently long reaction time, which also provided considerable electric output stability. At that time the power supply required an input of either 208 or 220 V with 50- to 60-Hz, single-phase electric requirements. The dimensions of this particular power supply were  $5 \times 5 \times 9$  inches.

in the pea-green portion of the visible spectrum (Fig. 26-4). A potassium-deuterium-phosphate (KDP) crystal has been used with some success during the last several years, but even with this more sophisticated crystal, the potential power in the green portion of the spectrum was still limited. The KTP crystal allows the laser instrument to deliver full power in the frequency-doubled mode.

2. The new frequency-doubled Nd:YAG laser designed by the Laserscope Corporation in conjunction with XMR Laser Company uses a high-intensity flash source pulsing at 25,000 cycles per second (25 kHz) and producing powers in excess of 20-W emission from the laser port. This highly efficient system requires minimal cooling and can be self-contained and used in a portable fashion from the operating room to an outpatient surgical suite or other facility.
3. The entire laser was designed in a modern—if not futuristic—cabinet with the features of automatic self-diagnosis of any problems within the electronic circuitry of the system and with the appropriate method to solve these problems immediately (Fig. 26-5). The entire workings and inter-manipulation of the laser and its energy output is under microprocessor control, and the output wattage, pulse duration, and potential mode of operation are displayed on a cathode ray tube. The system is therefore under complete electronic surveillance at all times, with minimal activation or interchange with the surgeon during the actual photocoagulation or photovaporization procedure.
4. The Laserscope frequency-doubled Nd:YAG laser system has the capability of producing extremely high powers and has been designed for ophthalmic use as a photocoagulator comparable to the argon green laser. It also has the potential of being used with other peripheral devices. These fiberoptic-linked therapeutic devices range from various types of endoscopic cauterization probes to dermatologic tattoo and port-wine stain eradicators and photovaporizers (Figs. 26-6 to 26-8). This multipurpose laser should therefore have considerable medical and surgical advantages, as well as provide an economic medical service.

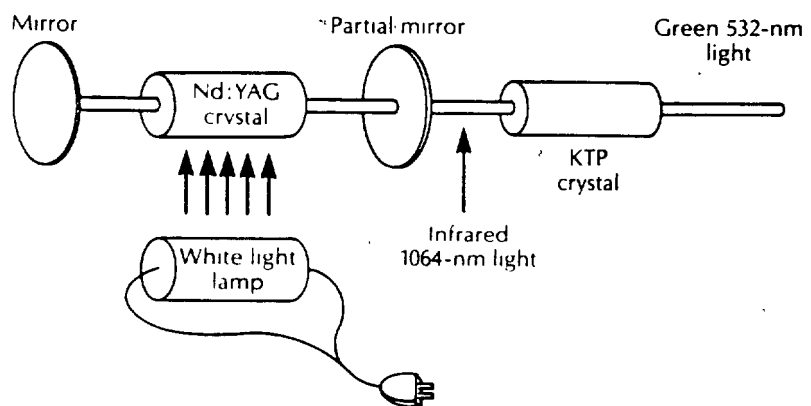


**Fig. 26-4.** Schematic drawing showing a white light pumping lamp that energizes the Nd:YAG crystal to produce an infrared beam, which is then converted by a nonlinear K<sub>2</sub>P crystal to a 532-nm laser beam



**Fig. 26-2.** First patient to be treated by the frequency-doubled Nd:YAG laser (532.0 nm), using 100- to 150- $\mu$ m coagulations at 0.2-sec exposures and power levels ranging from 200 to 350 mW. This patient was treated in 1970 for localized paramacular retinal leakage caused by moderate nonproliferative diabetic retinopathy.

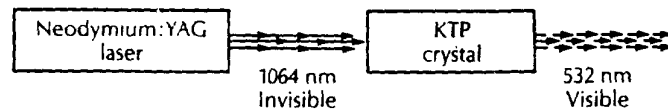


**Fig. 26-3.** Schematic drawing illustrating the Nd:YAG laser producing an invisible beam at 1064 nm that enters the nonlinear potassium-titanium-phosphate (KTP) crystal and emerges with a doubled frequency and a halved wavelength at 532 nm in the pea-green portion of the spectrum.

During the past several years a somewhat similar frequency-doubled Nd:YAG laser has been designed that eliminates many of the disadvantages and drawbacks of the original 1970 laser. The most significant changes with this new instrument are the following:

1. The doubling crystal is no longer a barium-sodium-niobate crystal but rather a potassium-titanium-phosphate (KTP) crystal that has the capability of withstanding the potentially tremendous power generated by the solid-state Nd:YAG crystal and converting this wavelength from 1064 to 532 nm

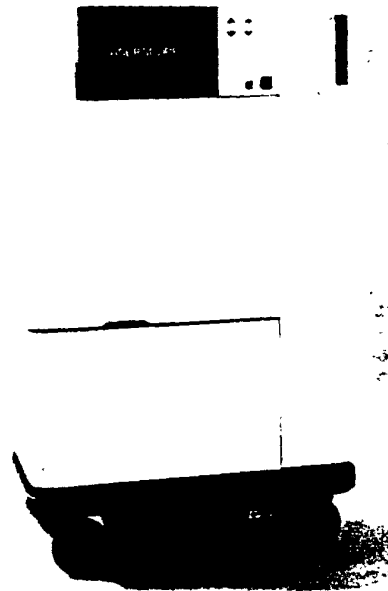


**Fig. 26-5.** Laserscope multispecialty frequency-doubled Nd:YAG laser console showing the cathode ray tube readout area, as well as controls for the microprocessor unit. The unit has self-monitoring electronic surveillance and can produce output powers in the 20-W range at a 532-nm wavelength.

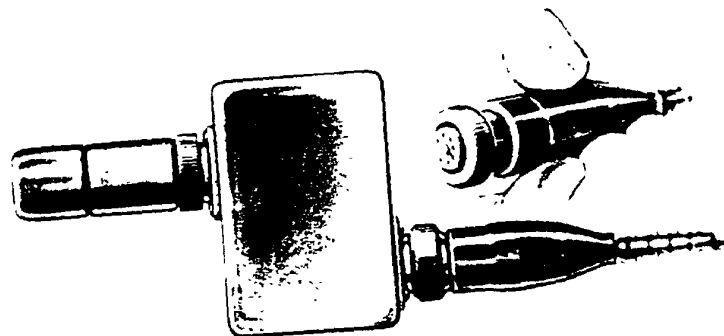


**Fig. 26-6.** Laserscope fiberoptic coupler for various medical uses of the 532-nm beam. Interlock is designed to be recognized by main electronic console, so that each fiberoptic system has its own parameters for precise operation.

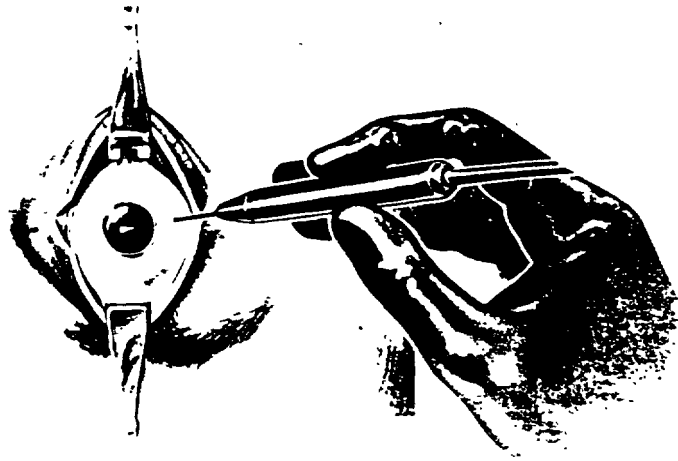


**Fig. 26-7.** Hand-held intraocular probe for endophotocoagulation of chorioretinal structures with 532-nm output. (Courtesy Laserscope, Inc.)

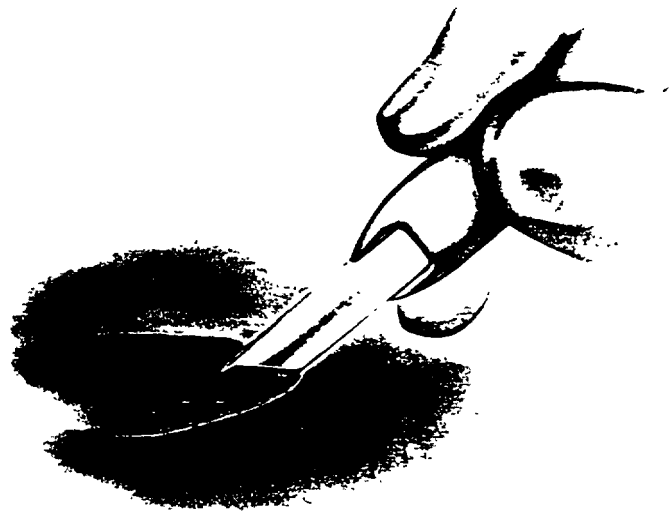


**Fig. 26-8.** Laserscope peripheral hemostatic quartz or diamond (Auth) knife. The 532-nm laser beam is channeled to the cutting tip of the knife to produce hemostasis during the actual incisional process

## Beam Characteristics

Regardless of the nature of the laser or incandescent source, the main concern of the ophthalmologist is the nature of the beam entering the eye and its effectiveness in photocoagulation. This section summarizes the various features of the frequency-doubled Nd:YAG laser beam in terms of photocoagulation ability.

### Collimation

The beam of any laser is extremely collimated or parallel as it travels from its source, and the Nd:YAG laser is no exception. However, the average 3- to 5-milliradian divergence of the beam makes it considerably less parallel than the average argon laser emission and therefore less able to focus to the small retinal spot produced by the argon laser photocoagulation system. This relative lack of collimation is an inherent property of all crystal lasers, such as the Nd:YAG, Nd:glass, ruby, and frequency-doubled Nd:YAG lasers. Gas lasers produce less divergent beams and therefore can be focused more precisely for paramacular or individual vascular coagulations. Optical devices can reduce this divergence disparity, but only at the expense of power output.

It should be emphasized that this small amount of divergence from a crystal laser appears to be insignificant, particularly since the delivery system from the Laserscope frequency-doubled Nd:YAG source is through fiberoptic cables. When a laser beam emanating directly from a laser source enters a fiberoptic system, much of its coherence is broken down, with a significant divergence at the emission end of the fiberoptic cable. This divergent cone of light must be captured in most instances and refocused for the purpose of eventual photocoagulation. This has not posed a significant problem and may be advantageous in certain uses of the frequency-doubled Nd:YAG beam.

It must be noted, however, that this frequency-doubled Nd:YAG laser, produced in the pea-green region of the visible spectrum, will not be used directly after emission from the laser source. In all applications this laser beam will be interfaced with a fiberoptic cable in exactly the same manner as most photocoagulation systems, including the argon laser photocoagulation devices now in use. Because of the use of fiberoptic cable channeling devices from the laser to the photocoagulation instrument, the obvious advantageous property of minimal spot size is disregarded in favor of transmission of the laser beam over longer distances. With the use of fiberoptic coupling from the laser to the surgical instrument, the laser beam loses both its spatial and temporal coherence and becomes simply a monochromatic light source of high potential energy output. In essence, in ophthalmology it is the monochromaticity and the high power output that determine the effectiveness of a laser beam as a photocoagulation, photodynamic, or photovaporization device.

### Monochromaticity

The Nd:YAG laser produces an output beam in the infrared portion of the electromagnetic spectrum at 1064 nm, which, when doubled in frequency (and therefore halved in wavelength) by the proper nonlinear crystal, is converted to a green beam at 532 nm. This single color can then be focused without chromatic aberration onto the retina or other ocular tissue. This factor has always been considered advantageous, and lasers have had the capability of producing retinal coagulations many times smaller than incandescent sources such as the xenon-arc instrument. It is also a law of laser physics that the potential size of

the ocular photocoagulation varies directly with the wavelength, although much of this property is compromised by the use of fiberoptic channeling systems. The frequency-doubled Nd:YAG laser may actually gain some advantage because only one wavelength is being emitted, whereas the argon laser emits eight wavelengths, from 457.9 to 528.7 nm. Only two argon emissions are powerful—488 and 514.5 nm—and they are so closely approximated with regard to focus that they can be considered as one wavelength at 500 nm for calculation purposes. In addition, individual wavelengths can be selected from the argon laser emission spectrum so that the argon system can be considered as either a blue or green photocoagulation device, with focusing potential similar to the frequency-doubled Nd:YAG laser beam.

### Focusing Potential

It is possible to calculate the minimal size of a retinal image of any laser beam by employing a series of formulas described elsewhere.<sup>2</sup> From these figures it can be established that the theoretic minimal retinal image size produced by a frequency-doubled Nd:YAG laser is approximately 10.2  $\mu\text{m}$  in diameter, as compared with a minimal retinal image diameter of 8.4  $\mu\text{m}$  for argon laser radiation and 13.2  $\mu\text{m}$  for krypton red laser radiation. Therefore, by the factor of wavelength only, the frequency-doubled Nd:YAG laser can theoretically produce a retinal coagulation smaller than that of the krypton laser, but not as small as that produced by the argon laser. In addition, the inferior collimation of the Nd:YAG beam may further decrease the focusing ability of this laser for any direct system.

The theoretic minimal retinal image diameter refers to an open, direct system from the laser source to the ocular tissue using optics other than fiberoptic systems. When a fiberoptic system is used, not only the collimation but also the coherence of the laser beam is sacrificed, as previously mentioned, and new optical systems must be introduced to create a minimal spot size (50  $\mu\text{m}$ ) that is essentially the same for all of the visible laser photocoagulation instruments. Therefore, unless focusing becomes an extremely critical matter, all laser beams can be brought to a 50- $\mu\text{m}$  coagulation size and perhaps smaller with fiberoptic channeling couplers. This has proved to be highly satisfactory with all photo-

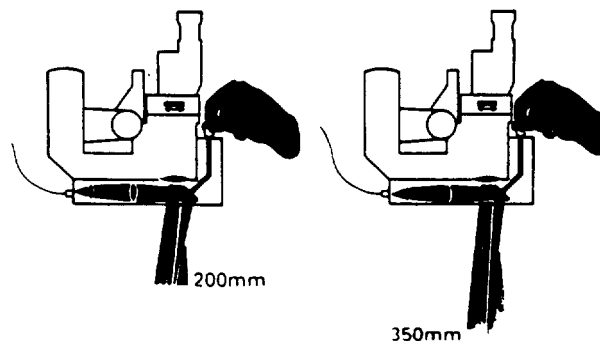


**Fig. 26-9.** Schematic drawing illustrating the fiberoptic input to the operating microscope, with manipulation of the beam by a joystick and the potential of varying focus of a 532-nm beam from 200 to 350 mm from the exit port of the operating microscope. (Courtesy Laserscope, Inc.)

coagulation, photodynamic, and photovaporization surgical procedures (Fig. 26-9).

### Specific Tissue Response

**Histopathology.** The histopathologic response of monochromatic laser energy at 530.8 nm produced by a krypton laser has been described, and the chorio-retinal tissue changes created by a frequency-doubled Nd:YAG laser beam at the closely related wavelength (532 nm) have been shown to be similar.<sup>1</sup> The most apparent histologic damage with the Nd:YAG laser was the coagulation and destruction of the outer nuclear area and the inner portion of the receptor layer in the impact zone. In sagittal sections of rabbit eyes, at 48 hours after irradiation with the green YAG laser emission at 532 nm, there was buckling of the inner retinal layers with some edema of the nerve fiber layer. Little histopathologic damage could be noted in the region of the ganglion cell to the outer plexiform layer. The locus of heat production appeared to be in the area of the outer nuclear rod/cone junction. A moderate pigment epithelial disruptive effect was observed, but there were only minimal choroidal changes. This histopathologic picture is similar to that produced by argon radiation, and both lasers have the potential to destroy the deep vascular plexus in the area of the coagulation (Fig. 26-10).



**Fig. 26-10.** A, Histopathologic microphotograph illustrating the effect of a 532-nm beam on the rabbit retina 48 hours after treatment (see text) B, Histopathologic microphotograph showing the effect of the argon laser beam on the rabbit retina after 48 hours. The effect is very similar to that seen with a 532-nm wavelength (Courtesy Laserscope, Inc.)



**Hemoglobin absorption.** The absorption potential of a 140- $\mu\text{m}$  film of oxy-hemoglobin has been documented spectrophotometrically, and 97% of incident monochromatic laser radiation at 532 nm is absorbed (Fig. 26-11). This figure represents a 15% increase over a comparable monochromatic argon laser beam at 488 nm but is equal to the hemoglobin absorption potential of a 577-nm dye laser emission. These particular laser radiations are all more highly absorbed by blood than is the red krypton (647.1-nm) laser beam (3%) and similarly produce intense coagulation in vascular tissue by the conversion of the absorbed energy to heat.

**Melanin absorption.** The peak of the absorption curve for melanin has been determined to exist at 550 nm,<sup>5</sup> whereas the pigment epithelium absorption peak has been plotted at 530 nm.<sup>1</sup> This would indicate that the frequency-doubled Nd:YAG output would be highly absorbed by pigmented particles in the retina and the pigment epithelium. Therefore an exudative choroiditis could be produced with less transmitted Nd:YAG energy than with any existing laser source. The beam energy would be slightly dissipated at the nuclear retinal layers, where partial absorption takes place, but the existing transmitted energy would be sufficient to create a firm chorioretinal adhesion.

**Xanthophyll absorption.** The absorption peak for xanthophyll has been determined to exist at approximately 460 nm, with a rapid decrease in absorption with the longer wavelengths. The more powerful argon laser wavelengths at 488 and 514.5 nm absorb approximately 70% and 11%, respectively, of the energy that would be absorbed by a tissue pigment with maximal absorption at 460 nm (Fig. 26-12). Therefore the argon blue and the argon green laser wavelengths can be sufficiently absorbed with high input powers to cause sufficient conversion of the light energy to heat energy at the inner and outer plexiform layers of the macula, where the xanthophyll pigment is found. It has been advised by numerous authorities that the argon blue not be used in the macular region because of the high possibility of coagulation of the nerve fiber, outer plexiform, and inner plexiform layers containing the xanthophyll pigment.<sup>6</sup> The argon green (514.5 nm) has been considered to be sufficiently safe—with minimal energy absorption by this pigment—in cauterization of subretinal neovascularization defects of the macular zone.

The frequency-doubled Nd:YAG laser at 532 nm produces a pea-green laser beam that is only 2% absorbed by the xanthophyll layers in the macular region. Therefore it is apparent that this wavelength has a considerable inherent safety margin when used in the macular region with minimal absorption by xanthophyll, while retaining one of the highest absorptions of the commonly used laser emissions, similar to the 577-nm dye laser emission, with oxyhemoglobin or reduced hemoglobin and other hemoglobin-filled vascular abnormalities. The 532-nm wavelength should be considered as one of the ideal wavelengths for the treatment of subretinal neovascularization, macular macroaneurysms, microaneurysms, macular telangiectatic defects, and other pigment-related or structural defects in the macular region.

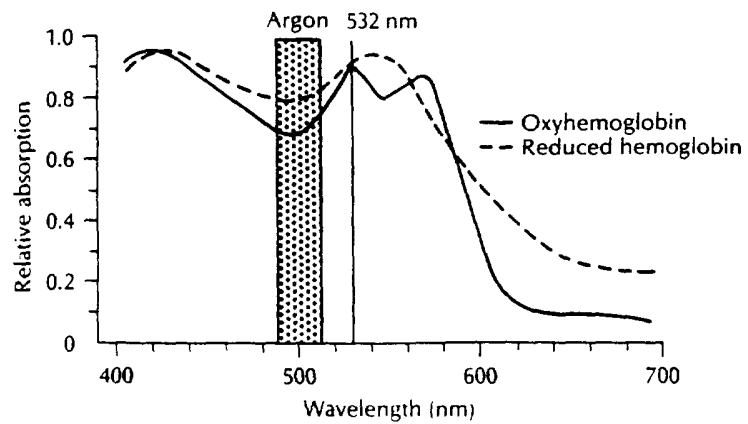


**Fig. 26-11.** Relative absorption for wavelengths emitted from the argon laser and from the frequency-doubled Nd:YAG laser at 532 nm by oxyhemoglobin and reduced hemoglobin. Note that a large differential exists between the absorption potential of the 532-nm wavelength and the basic wavelengths of the argon laser system.

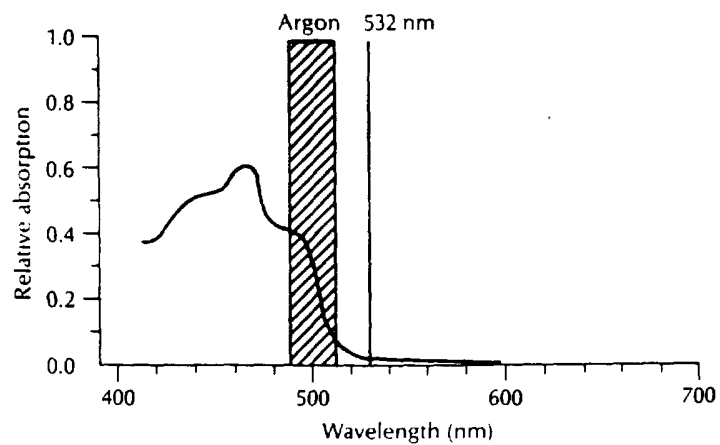


**Fig. 26-12.** Relative absorption of the argon laser and the frequency-doubled Nd:YAG laser (532-nm) beams by macular xanthophyll pigment. The 532-nm wavelength is highly transmitted by xanthophyll pigment, whereas the argon green beam is slightly absorbed and the argon blue beam is highly absorbed.

## Discussion

The technologic advances in physics have allowed ophthalmologists to approach the ideal condition in which various portions of the eye can be selectively photocoagulated by the use of specific monochromatic laser beams. As lasers emitting different-colored beams are developed, the production of a predictable specific target response in an ocular tissue becomes possible. This would mean that a certain chorioretinal layer could be coagulated without disruption of other zones by carefully matching the absorption potential of that layer to the proper laser emission.

The frequency-doubled Nd:YAG laser produces one of the most ideal wavelengths for vascular photocoagulation or production of an adhesive chorioretinitis. The Nd:YAG emission occurs at 1064 nm in the infrared spectral region and after passage through a nonlinear (KTP) crystal is converted to a green wavelength at 532 nm. The green beam exists at a location in the visible spectrum very near one of the peak absorption regions of oxyhemoglobin (542 and 576 nm) and also near the maximum absorption of reduced hemoglobin (552 nm). Therefore less energy is necessary for spasm, occlusion, and obliteration of ocular blood vessels, since the Nd:YAG photocoagulation beam is more highly absorbed, with greater conversion to heat energy. Under ideal conditions, in vitro studies indicate that the frequency-doubled Nd:YAG laser emission would be 15% more highly absorbed by a 140- $\mu$ m film of oxyhemoglobin than the argon laser, 94% more highly absorbed than the red krypton (647.1 nm), and similarly absorbed as the green krypton laser emission (530.8 nm), although 1% less well absorbed than the yellow krypton laser beam (568.2 nm) or the yellow dye laser beam (577.0 nm).

The frequency-doubled Nd:YAG laser should thus offer distinct advantages in photocoagulation therapy of vascular disease over certain other lasers, such as the longer wavelengths of the red dye or the krypton laser (647.1 nm). The Nd:YAG laser should be comparable to certain krypton (568.2- and 530.8-nm) laser emissions, slightly advantageous over the argon (488- and 514.5-nm) laser emissions, and slightly less advantageous when compared with the 577-nm dye laser emission in efficiency and effectiveness for the treatment of vascular diseases such as diabetic retinopathy, angiomas, Coats' disease, sickle cell retinopathy, Eales' disease, and retrolental fibroplasia.

The Nd:YAG green laser may also prove to be more effective than any laser for the creation of a chorioretinal adhesion or for the therapy of diseases related to the pigment epithelium. Minton<sup>5</sup> showed that the peak absorption of melanin from a choroidal melanoma occurred at 550 nm, with decreased absorption at shorter and longer wavelengths. This would indicate that less energy would be required for the coagulation or thermal irritation of the pigment epithelium because of the close approximation of the green Nd:YAG emission wavelength and the melanin absorption maximum.

Less photocoagulation energy passing through the ocular media or retina is always an advantage, especially when corneal, lenticular, or vitreal haze or opacities are present. The use of the green Nd:YAG laser in the treatment of retinal tears, peripheral retinal degeneration, retinoschisis, and postretinal detachment surgery can be anticipated to be highly effective because of the superior absorption characteristics.

Undoubtedly the potential uses of the frequency-doubled Nd:YAG laser operated at 25-kHz pulsing frequency at powers in excess of 20 W will provide a role for this particular laser emission beyond retinal or ocular photocoagulation. A laser source capable of producing powers of this magnitude and at this frequency (532 nm) can be used via fiberoptic transmission to multiple other peripheral devices. This particular laser beam should prove to be extremely valuable in the destruction of tumors of the bronchi and gastrointestinal tract, minisculectomies, dermatologic procedures (including the eradication of port-wine stains and other skin defects), endoscopy, and bronchoscopy (Fig. 26-13). The use of this laser should have enormous potential in all areas of medicine and surgery, as well as in photocoagulation, photodynamic, and photovaporization therapy in ophthalmology.

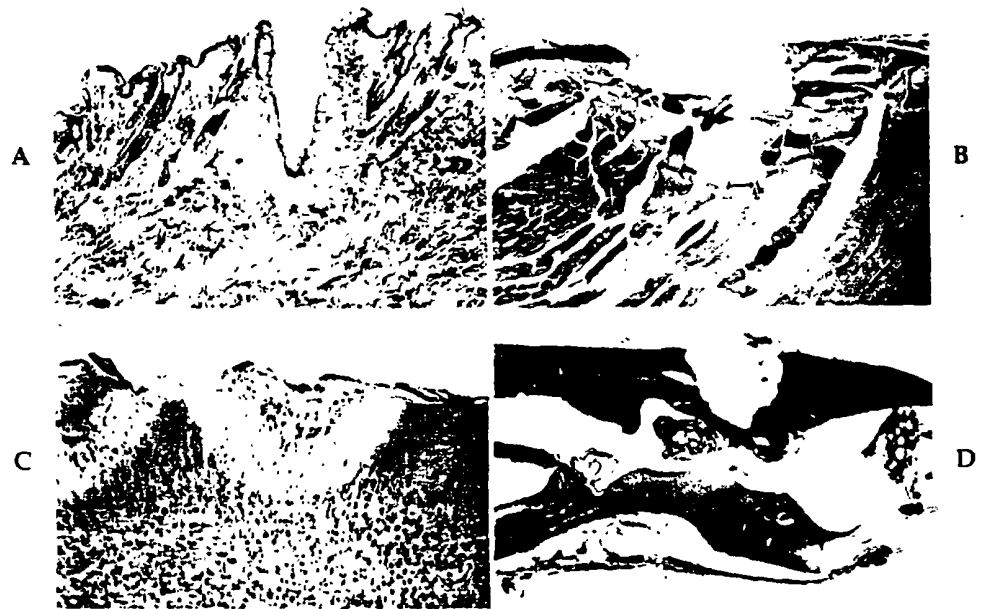


**Fig. 26-13.** A, Histopathologic appearance of skin impacted with sufficient power density to create an incision. Note the thermal destruction of the sides of the incision as well as cauterization of nearby vessels. B, Histopathologic appearance of a section of muscle tissue incised with a 532-nm-focused beam showing slight charring and slight thermal damage to the sides of the incision. C, Histopathologic appearance of brain tissue after minimal incision by a 532-nm-focused beam. Note the slight charring at the incisional site, with the area of coagulation extending deeper into brain tissue. D, Histopathologic appearance of bone tissue incised with higher power densities at 532-nm wavelengths. The power density of the frequency-doubled Nd:YAG laser is sufficient to cut through bone, cartilage, or other biologic structures, with optimal hemostasis and minimal thermal effects to nearby tissue. (Courtesy Laserscope, Inc.)

## EXCIMER LASERS

Excimer lasers are pulsed gas lasers that use a mixture of a rare gas and a halogen as the active medium (Fig. 26-14, A). Excimers are molecules that exist only in the electronically excited state. As these molecules return to the ground state, they emit short-wavelength radiation and dissociate into single atoms because the ground state is nonbonding (Fig. 26-14, B). Thus excimers are an ideal laser medium, since the lower laser level is automatically depleted as a result of dissociation (see Chapter 23).

The high output power and good efficiency agree with theoretic calculations when losses caused by fluorescence or quenching processes are minimized by using a fast excitation. In some excimer lasers a fast electric discharge is used, with its energy first transmitted into a buffer gas such as helium or argon. The output from the excimer molecules can have an efficiency as high as 2%.

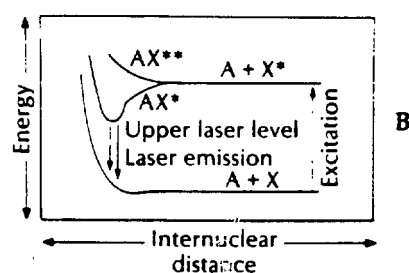
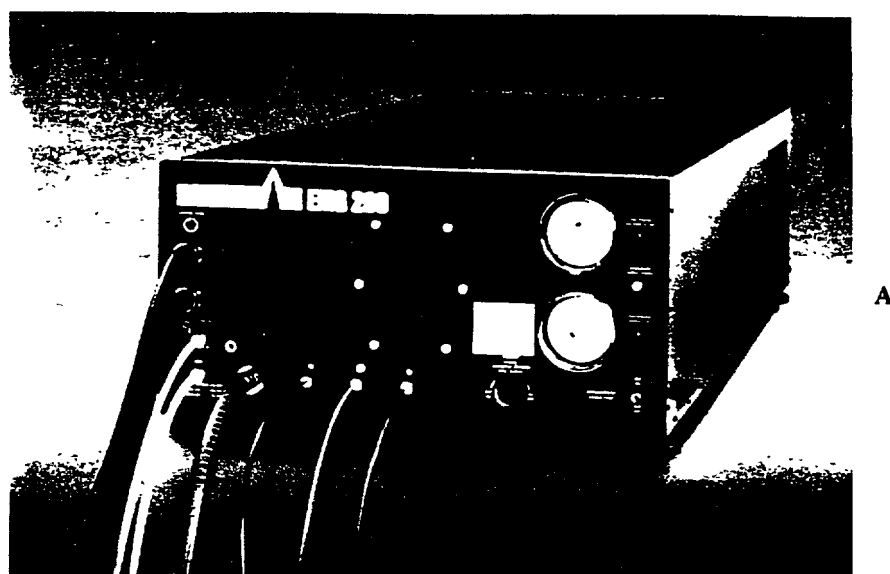
The fast discharge circuit allows the laser to be operated with other gases as well, such as fluorine ( $F_2$ ), operating at 157 nm, or even carbon dioxide ( $CO_2$ ), operating at 10.6  $\mu m$ .

The choice of gas mixture determines the output wavelength. The typical line width of an excimer emission is about 0.3 nm, but tuning the output over a region of about 3 nm is possible at lower output energy.

Certain excimer lasers (Lambda Physik) incorporate a gas processor into the laser to increase the gas-fill lifetime, in some cases approaching as many as 20 million electric discharges. Because the gas processor removes impurities from the gas as the laser operates, power output from the laser deteriorates much more slowly than in conventional excimer lasers. The Lambda Physik technique of cleaning the laser gases is more efficient and reliable than the brute-force technique used in some excimer lasers of automatically increasing discharge power as the laser gas becomes contaminated. Most excimer lasers are multigas lasers in that operation is permitted at a number of wavelengths simply by selecting the appropriate gas mixture. All the common ultraviolet excimer wavelengths shown in Table 26-1 are available (Figs. 26-15 and 26-16). No modification of the laser hardware is required when changing excimer gases, and only the mirrors need be replaced when changing from the ultraviolet to infrared output emissions.

A typical example of an excimer laser (Lambda Physik EMG 103 E) produces 40 W at 249 nm (krypton fluoride), 20 W at 193 nm (argon fluoride), or 20 W at 308 nm (xenon chloride). The standard repetition frequency of the EMG 103 E is 200 Hz, but a slight factory modification allows higher repetition frequencies. Another special configuration, the S-version of the EMG 103 E, allows pulse energy up to 500 mJ at either 249 or 308 nm at a reduced repetition frequency. For the maximum output in the vacuum-ultraviolet mode, an optimized  $F_2$  version of the EMG 103 E produces 1.5 W of average power at 157 nm. These reliable, economically priced lasers can be an attractive alternative to the Nd:YAG lasers in such applications as optical pumping of dye lasers.

The heart of an excimer laser is the gas reservoir, with its integrated laser channel and low-inductance discharge circuit. The gas reservoir is fabricated from a single piece of thick-walled aluminum extrusion in some excimer lasers. It serves not only as a 30/L gas reservoir, complete with gas circulation and cooling mechanisms, but also as a stable optical bench to which the resonator



ENERGY LEVELS OF AN EXCIMER LASER

**Fig. 26-14.** A, Typical appearance of the excimer ultraviolet laser showing various input tubes and the laser exit port. B, Schematic interpretation of the method of population inversion present with the excimer laser. Because of the unstable ground state, most molecules are in an excited or upper laser level and are subject to stimulated emission and laser action. (A courtesy Lambda Physik )

**Table 26-1.** Ultraviolet laser wavelengths (including excimer lasers)

Laser media	Principal wavelength (nm)
Fluorine ( $F_2$ )	157
Frequency-doubled dye	190
Argon fluoride (ArF)	193
Frequency-quintupled Nd:YAG	212
Krypton chloride (KrCl)	222
Krypton fluoride (KrF)	248
Frequency-quadrupled Nd:YAG	266
Xenon chloride (XeCl)	308
Nitrogen ( $N_2$ )	337
Xenon fluoride (XeF)	351

mirrors are attached. A fast transverse flow of laser gas through the electrodes ensures high pulse energy independent of repetition frequency. As noted, with the EMG 103 E frequencies up to 500 Hz are possible.

There are three factors that contribute to the high efficiency of an excimer laser: (1) a properly designed electrode shape, (2) efficient preionization of the laser gas and an ultrafast mode, and (3) a low-inductance electric discharge circuit. In effect, these factors are combined into a single, unique design for the new preionization scheme of the EMG-series lasers as an integral part of the discharge circuit. It is a simple and reliable design that produces a uniform field of ions, and the discharge is completely free of arcs. In some other excimer lasers the peaking capacitors have to be placed very close to the electrodes inside the gas chamber to avoid arcing. The Lambda Physik approach of optimizing the energy transfer from one capacitor to another before the onset of the laser discharge results in a much higher efficiency.

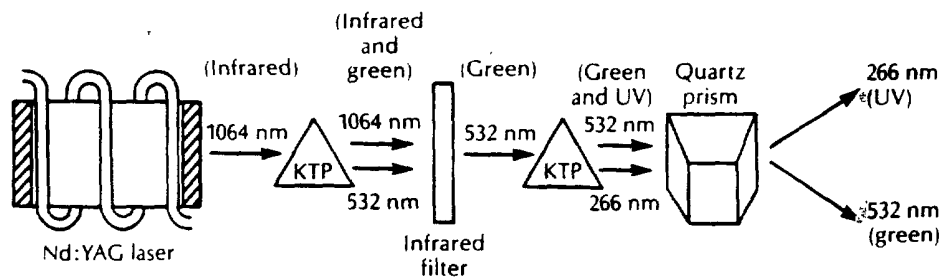


**Fig. 26-15.** Schematic representation of the process of producing second and third harmonic generation by passing a laser beam through the piezoelectric crystal, KTP. The frequency of the Nd:YAG laser is doubled and the wavelength halved as it passes through the KTP crystal. A second transit through the KTP crystal produces a wavelength of 266 nm in the far-ultraviolet portion of the electromagnetic spectrum.

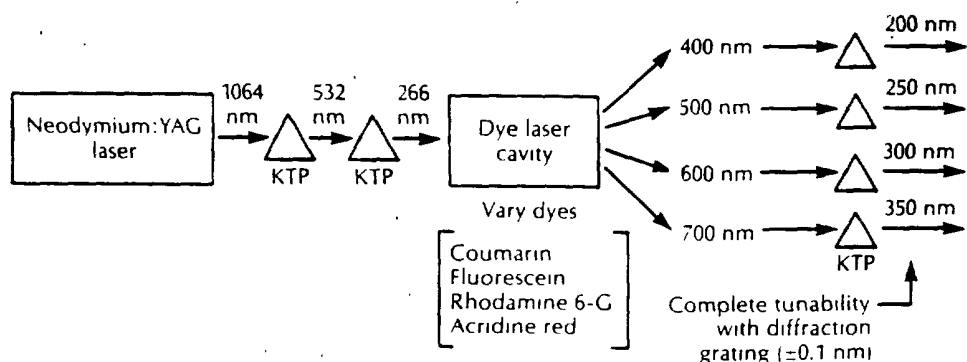


**Fig. 26-16.** Theoretic wavelength versatility by combining a dye laser with harmonic generation or both dye laser wavelengths and a stimulating laser wavelength. In this case the Nd:YAG laser frequency is quadrupled and used to pump the dye laser using various organic dyes for laser action. By selecting the organic dye, wavelengths can be generated throughout most portions of the ultraviolet spectrum.

It is extremely important for excimer lasers to be engineered to allow a maximum life of the laser gases. For the user this means reduced operating cost as well as more reliable laser operation at steady power levels.

Only fluorocarbon insulators and metals such as aluminum and nickel, which passivate quickly in a fluorine or hydrogen-chloride environment, are used in Lambda Physik lasers. All electric circuit components, except the electrodes themselves, are outside the gas system, where they do not need to be passivated.

Significant improvements, both in reduced power deterioration and in-fill lifetime, have been observed when a gas processor is added to a laser. For example, 20 million pulses can usually be obtained from a xenon chloride laser before the power decreases to 50% of its original value. Without the processor, the same laser might only produce 4 million pulses before requiring a gas change. Similar improvements in gas-fill lifetime have been observed for other standard gases, including krypton fluoride, xenon fluoride, and argon fluoride.

Extended lifetime means reduced operating costs for the excimer lasers, particularly in comparison with Nd:YAG lasers, which might alternatively be used as dye laser pumps. The flashlamps of Nd:YAG lasers must be replaced about as frequently as the gas of a xenon chloride laser must be changed, or about every 20 million shots, but a gas change is much less expensive. Based on current prices for research-grade xenon, the gas costs of a xenon chloride laser are 40 cents per hour less if the laser is operated at a 100-Hz repetition frequency. The corresponding operating costs for a Nd:YAG laser are significantly greater.

## Excimer Laser Surgery

Laser applications in ophthalmology include the processes of photocoagulation, photovaporization, photoradiation (photodynamic therapy), photodisruption, and, more recently, photoablative decomposition. Photocoagulation and photovaporization are tissue interactions that involve the thermal effects of laser radiation; photodynamic therapy occurs through a photon interacting with a sensitized chemical bonded to malignant tissue. Photodisruption uses laser-induced optical breakdown to section tissues by forming a plasma and associated shock waves. The excimer laser has provided a fifth form of laser interaction with tissues called photoablative decomposition. The use of this far-ultraviolet laser radiation (150 to 200 nm) creates a specific photochemical reaction and results in the ablation of corneal or other ocular tissues without thermal damage to the remaining adjacent structures (Fig. 26-17). Therefore, incisions of controlled depth and shape can be made in defined areas of the cornea or other ocular tissue, and any amount of tissue can be removed by ablating that tissue to a predetermined depth.

Srinivasan<sup>6,7</sup> reported that the far-ultraviolet radiation acts on organic polymers by a process described as ablative photodecomposition. The irradiated molecules are broken into smaller volatile fragments by direct photochemical interaction without heating the remaining adjacent tissues (Fig. 26-18). Ultraviolet light at this frequency is highly energetic, with each photon having 6.4 eV. This provides the photochemical energy that directly breaks intramolecular bonds.

It is known that the longer-wavelength lasers vaporize tissues but also produce changes in remaining adjacent structures. Histologic studies have demonstrated that irregular edges in various tissues such as bone and muscle are caused by the heat of the cutting thermal laser (Fig. 26-19). Far-ultraviolet laser



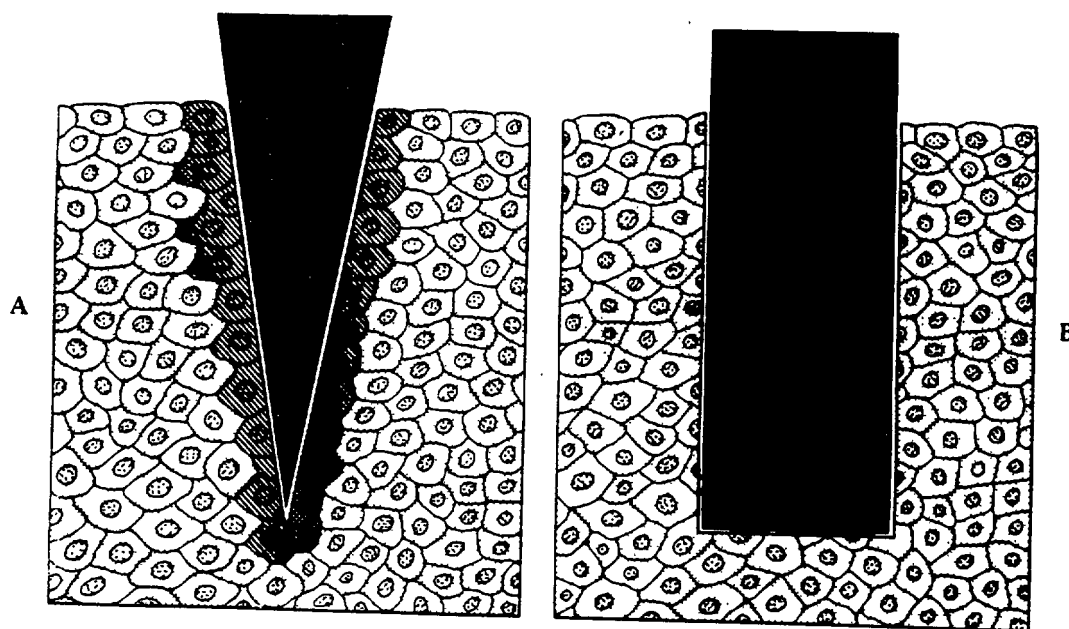


**Fig. 26-17.** Comparison of photovaporization (A) and photodecomposition (B), illustrating the precise cleavage of cells in rectangular fashion without charring with photodecomposition, and minimal charring along the incision site with photovaporization. Photodecomposition is accomplished with far-ultraviolet lasers, and photovaporization can be created with high-photon flux from any visible laser, most commonly with the far-infrared CO<sub>2</sub> laser.

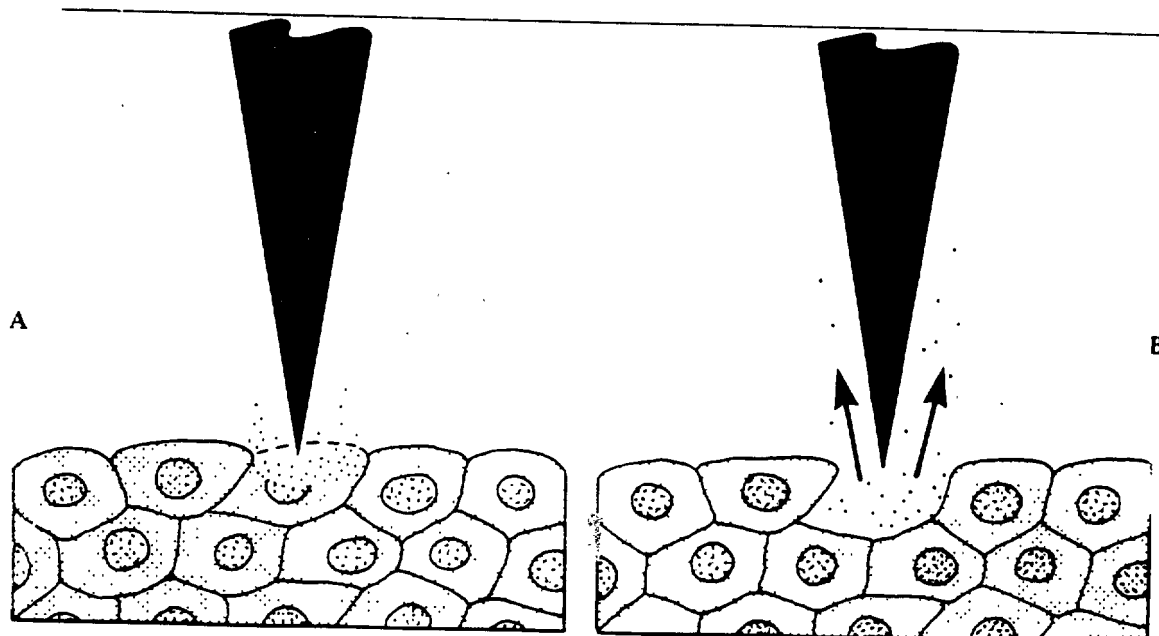


**Fig. 26-18.** Photodecomposition process showing the impact of the far-ultraviolet laser beam on an individual cell or small area of cells (A), causing breakage of intramolecular bonds and disruption and disappearance of cellular matter from the impact site (B).



**Fig. 26-19.** A 0.4-mm crater produced with a 532-nm laser beam showing charring and irregular cauterization of the edges of the incision. (Original magnification  $\times 40$ .) (Courtesy Ralph Linsker, M.D., Ph.D.; R. Srinivasan, Ph.D.; James J. Wynne, Ph.D.; Daniel R. Alonso, M.D.; IBM T.J. Watson Research Center; and Cornell University Medical College.)

irradiation, however, produces a trench with sharp and cleanly defined boundaries, as seen with light microscopy. There are no changes in adjacent tissues; nor are there observable thermal effects (Fig. 26-20).

The implications for the use of the excimer laser with operations such as keratomileusis or corneal transplantation appear to be a logical additional experimental avenue. The applications for refractive keratoplasty would seem to be of great interest, since the cornea can be reshaped in such a manner as to correct most moderate degrees of hyperopia, myopia, and astigmatic defects. This type of laser surgery is highly experimental at this time, but considerable research will be forthcoming.

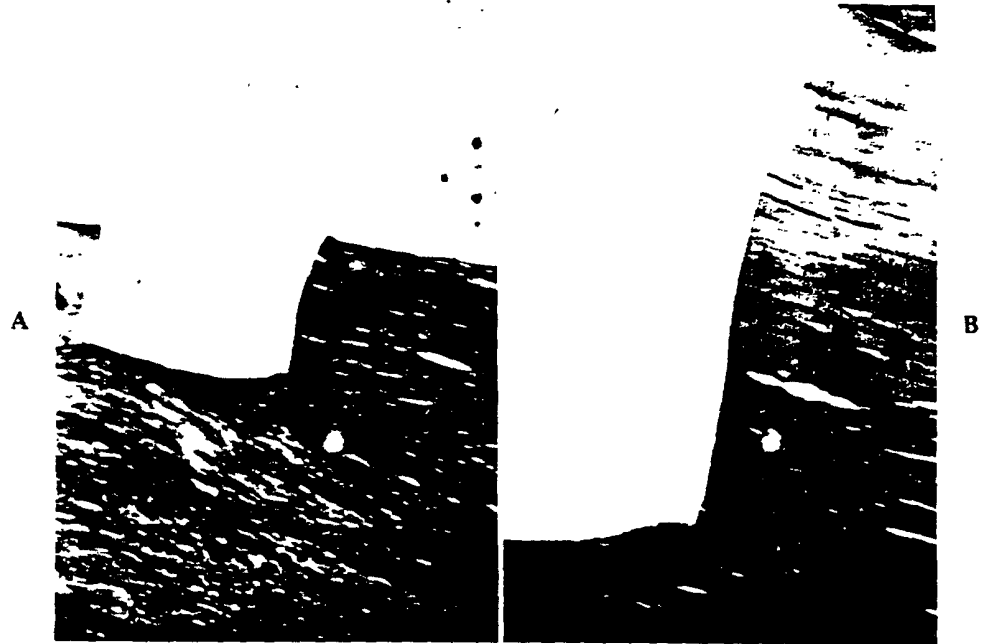


**Fig. 26-20.** A, Trench measuring 0.35 mm produced by excimer laser (193-nm) irradiation of the luminal side of the aortic wall showing exquisite precision and absence of damage to nearby cellular material. (Original magnification  $\times 40$ .) B, Enlarged view ( $\times 160$ ) of the same incision emphasizing the lack of thermal or other damage and precise sculpting of the aortic incision. (Courtesy Ralph Linsker, M.D., Ph.D.; R. Srinivasan, Ph.D.; James J. Wynne, Ph.D.; Daniel R. Alonso, M.D.; IBM T.J. Watson Research Center; and Cornell University Medical College.)

## CONTINUOUS- AND QUASICONTINUOUS-WAVE LASERS

Continuous-wave (CW) laser action will be achieved in almost all laser medias if the material will permit a permanent population inversion to be sustained. Although there are, in general, many competitive processes that may limit CW laser operation, such as heating of the media and "self-quenching" effects, it is often possible to achieve continuous or high-repetition-rate operation even with many materials previously considered as only "pulsed" laser media. The limiting factors are (1) the low efficiency of converting pump energy into laser emission, (2) retention of heat by the laser media, and (3) degradation of the components used for continuous pumping. This does not mean, however, that the same levels of instantaneous power as achieved in the pulsed operation will be achieved in CW operation. The rapid emission and subsequent high power levels achieved with a small ruby laser will be in the multikilowatt range, whereas the quasi-CW (60-Hz) operation of a ruby crystal will only reach a few watts, even in the most ideal system.

The most successful medias for pure CW operation have been gases (or gaseous mixtures) and the many diode lasers. Quasi-CW operation is possible in most of the solid medias common in pulsed operation, in addition to many gases.

## CW Neutral Atom Gas Lasers

CW neutral atom gas lasers operate mainly in the near-infrared range, from about 600 to 3400 nm. Representative lines of such gas media are shown in Table 26-2.

The first CW system was the helium-neon (HeNe) gas mixture. Although the first successful operation was at an infrared wavelength of 1152 nm, an HeNe laser is most well known operating at the red 632.8-nm transition. The more recent HeNe gas laser designs use direct current excitation, and the power output available from the low-efficiency HeNe laser ranges from a fraction of a milliwatt to about 100 mW in the largest available systems. Because the HeNe laser may be easily operated with high-frequency stability and a single-mode operation, many applications have been found in precision measurement holography, but it has not been used in ophthalmology because of the low power output. The HeNe laser has found indirect use as a target beam for the pulsed Nd:YAG systems, as well as for invisible lasers such as the CO<sub>2</sub> photovaporization instruments.

## CW Ion Gas Lasers

CW ion gas lasers operate principally in the ultraviolet and visible range, from 235 to 800 nm. Representative lines of such gas media are shown in Table 26-3.

The gases mercury, argon, krypton, xenon, chlorine, iodine, oxygen, nitrogen, and neon have been successfully operated on the ion laser principle. The combination of gases has generated more than 50 spectral lines in the ultraviolet invisible spectral range. In general, the mechanism of CW ion lasers is one in which an electronic collision—in either single or multiple successive steps—takes place for a double-ionization process to occur, with the power output proportional to the fourth power of the current through the laser tube. This successful series of lasers has made an enormous impact on the field of ophthalmology, particularly using the beneficial wavelengths of the argon and krypton lasers. Because of the precision, monochromaticity, and selective absorption by the ocular pigments, the argon laser is still used as the workhorse in ocular photocoagulation. Recently the krypton red laser (647.1 nm) has added immensely to our understanding and therapy of macular diseases and other conditions complicated by retinal or vitreal hemorrhagic problems.

## CW Molecular Gas Lasers

CW molecular gas lasers operate in the infrared region in a range extending from 5500 to more than 750,000 nm. Representative lines of such gas media are shown in Table 26-4.

There are several molecular gas mixtures that can generate laser emissions. Of these, the CO<sub>2</sub> laser has been found to be the most efficient and consequently the most powerful of all CW laser devices. Continuous powers have been reported above 5000 W in the infrared spectral region at the 10,600-nm wavelength. Unlike the other molecular lasers, the CO<sub>2</sub> laser is chemically stable enough to function with an electric discharge occurring within the gas itself. This function contributes to its high efficiency and its usefulness in many areas other than medicine. This laser has proved to be one of the most useful lasers in all fields of medicine for photovaporization of tumors, as well as an incisional device in areas of potential hemorrhage or with patients with various bleeding disorders. The water vapor laser and the hydrogen cyanide laser have had little practical application in any branch of medicine.

**Table 26-2.** CW neutral atom gas laser wavelengths

Laser media	Principal wavelength (nm)
Helium-neon	593.9
	632.8
	1152.3
	3391.3
Oxygen	844.6
Xenon	2026.2
	2651.1

**Table 26-3.** CW ion gas laser wavelengths

Laser media	Principal wavelengths (nm)
Neon (IV)	235.8
Argon (IV)	262.5
Helium-cadmium	325.0
	441.6
Helium-selenium	460.0
	480.0
	520.0
Neon (II)	332.4
Krypton (II)	467.2
	530.8
	568.2
Argon (II)	647.1
	476.5
	488.0
	514.5
Xenon (II)	526.2
	597.1

**Table 26-4.** CW molecular gas laser wavelength

Laser media	Principal wavelengths (nm)
CO	5,600
CO <sub>2</sub>	10,600
H <sub>2</sub> O	27,974
	47,693
	118,650
	220,340
HCN	310.887
	336.558
ICN	773.500

## Quasi-CW Gas and Solid-State Laser

The quasi-CW gas and solid-state laser classification includes both molecular and ion gas lasers and solid-state systems that cannot be operated except in the rapid pulse (quasi-CW) mode (Fig. 26-21). Representative lines are shown in Table 26-5.

One of the most promising sources at present uses the Nd: neodymium-doped crystal made of YAG. This system is pumped by special tungsten lamps and is capable of an average CW output approaching 100 W at the 1064-nm wavelength. Pulse repetition rates are normally the 60 Hz of the alternating line current. The recent emergence to popularity of the YAG laser has been stimulated by better growth techniques of longer YAG crystals. YAG systems are also ideal for high-repetition-rate, Q-switched operation. Operation at repetition rates of over 20,000 Hz is now commonly reported with and without frequency-doubling of the basic laser emission.

The increasingly common use of the pulsed Nd:YAG laser at its fundamental frequency (1064 nm) in the Q-switched or the mode-locked type of operation produces extremely short pulses of energy at either 10- to 12-ns or 20- to 30-ps duration, respectively. The formation of an optical breakdown at the focal point of the laser, as well as an acoustic and hydrodynamic shock wave, has been instrumental in lysing membranes within the eye, such as the posterior capsule, vitreous strands, and anterior synechiae, and for performing peripheral iridotomies. The expansion of the intravitreal uses of the pulsed Nd:YAG laser, as well as its application in other anterior segment conditions, will undoubtedly be occurring within the near future.

**Table 26-5.** Quasi-CW gas and solid-state laser wavelengths

Laser media	Principal wavelengths (nm)
Nitrogen (molecular)	337.1 540.1
Copper vapor	510.0 578.0
Frequency-doubled Nd:YAG	532.0
Mercury (ion)	614.9
Gold vapor	628.0
Chromium (ruby)	694.3
Chromium (alexandrite)	701.0-818.0
Chromium (emerald)	750.0-759.0
Neodymium (YAG)	1064.0
(glass)	1060.0

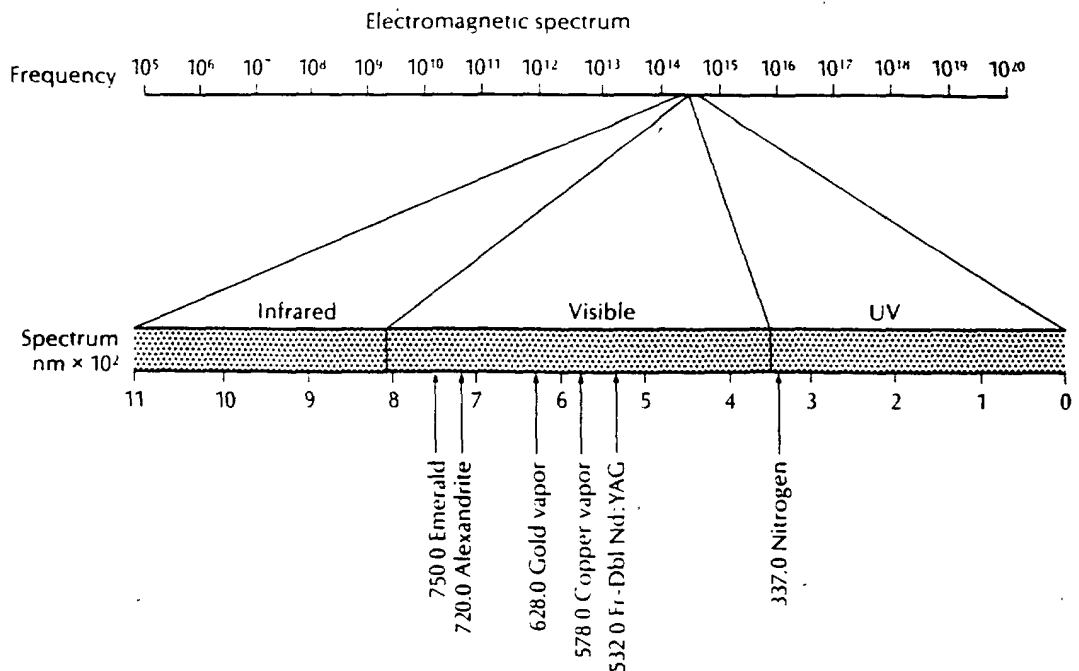


**Fig. 26-21.** Positions in visible portions of the electromagnetic spectrum of the emerald (750.0- to 759.0-nm), alexandrite (701.0- to 818.0-nm), gold vapor (628.0-nm), copper vapor (578.0-nm), frequency-doubled Nd:YAG (532.0-nm), and nitrogen (337.0-nm) laser emissions. These new lasers should have significant impact on the treatment of various diseases in medicine, especially in the field of ophthalmology.

High repetition rates for ruby lasers have been created with pulse rates of up to 100 Hz. To achieve this high repetition rate, special mercury-vapor flash tubes are operated in an ellipsoid cavity in which the flash tube and ruby rod are coaxial. Powers greater than 2 to 3 W in the quasi-CW configuration can be produced at the 694.3-nm wavelength. The red beam from this particular solid-state laser may have significant application in the future, when moderate amounts of blood in the vitreous or inner retina have prevented effective photocoagulation of the pigment epithelium or external chorioretinal structures.

A rapidly pulsed molecular nitrogen laser emits energy in a quasi-CW train of 10-ns pulses, each pulse at 100-kW peak power levels. A maximum average power of several hundred milliwatts is produced at the ultraviolet 337.1-nm wavelength, which may be advantageous for some photodecomposition applications. Other lasers may be more applicable in the field of ophthalmology because of greater stability and higher power output (Fig. 26-22).

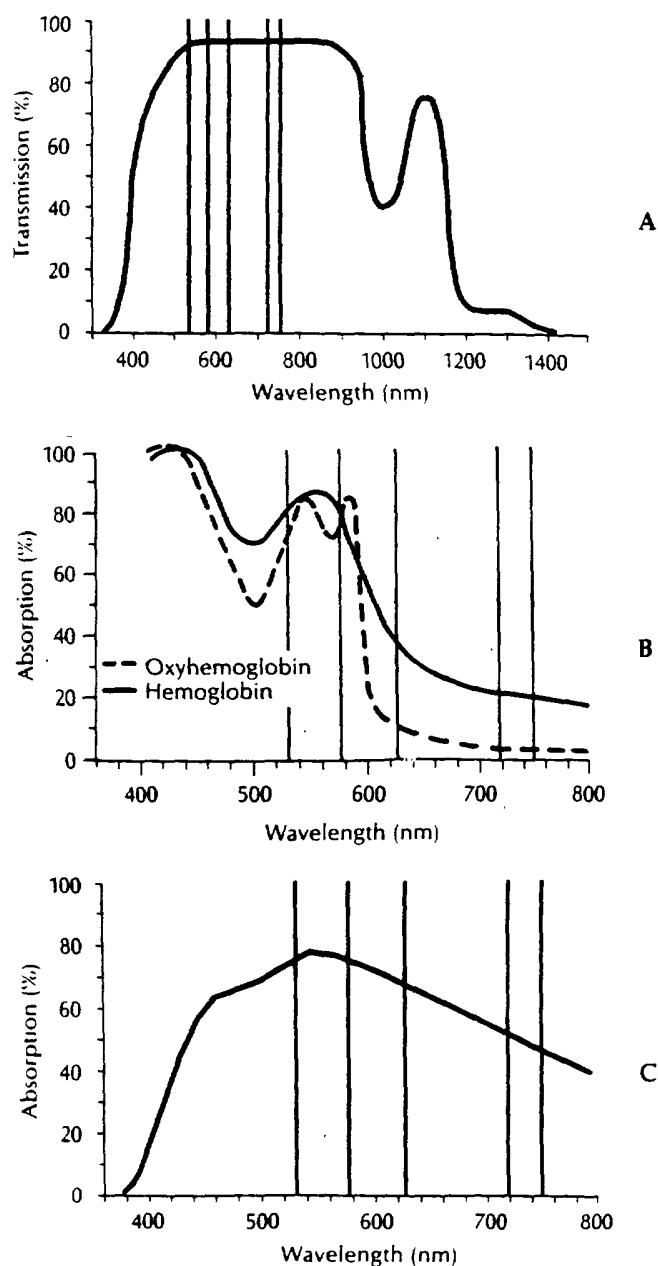


**Fig. 26-22.** A, Ocular media transmission (right to left) for emerald (759.0-nm), alexandrite (720.0-nm), gold vapor (628.0-nm), copper vapor (578.0-nm), and frequency-doubled Nd:YAG (532.0-nm) laser emissions. B, Percent of absorption of oxyhemoglobin and reduced hemoglobin by various wavelengths of the frequency-doubled Nd:YAG (532.0-nm), copper vapor (578.0-nm), gold vapor (628.0-nm), alexandrite (720.0-nm), and emerald (759.0-nm) laser emissions. These interesting new lasers can be used advantageously to create the greatest penetration or absorption by these two blood pigments, depending on the laser wavelength selected. C, Percent absorption of retinal pigment epithelium for various wavelengths represented (right to left) by emerald, alexandrite, gold vapor, copper vapor, and frequency-doubled Nd:YAG laser emissions (per wavelengths in A).

Continued



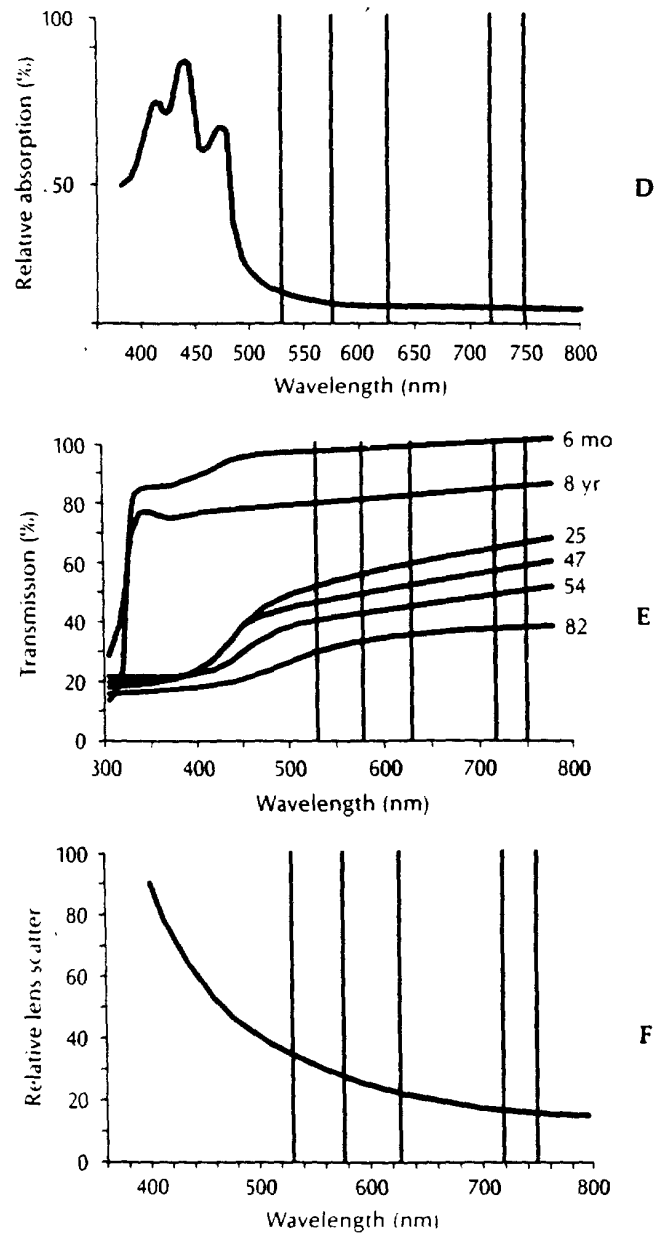


**Fig. 26-22, cont'd.** D, Relative absorption of xanthophyll macular pigment for various wavelengths (right to left) represented by emerald, alexandrite, gold vapor, copper vapor, and frequency-doubled Nd:YAG laser emissions (per wavelengths in A). E, Percent transmission of lens for various wavelengths (right to left) represented by emerald, alexandrite, gold vapor, copper vapor, and frequency-doubled Nd:YAG laser emissions (per wavelengths in A). F, Relative lens scatter for various wavelengths (right to left) represented by emerald, alexandrite, gold vapor, copper vapor, and frequency-doubled Nd:YAG laser emissions (per wavelengths in A).

## DIODE LASERS\*

Although more than 25 years have passed since the invention of the laser, in ophthalmology an ideal laser source emitting visible radiation is still lacking. Ion lasers are currently used to treat many pathologic conditions of the eye. However, they suffer from severe drawbacks as a result of their very low electrical-to-optical efficiency. This is responsible for the extremely high power consumption, large size, high cost, and troublesome maintenance of these lasers.

During the past few years pressing requests arising from the field of optical communications, new optical printing techniques, videodisks, and the great progress in growth technology of semiconductor crystals have led to a fantastic development in semiconductor diode lasers (see Fig. 26-23). Currently these all emit in the far-red or near-infrared spectral range. The new generation of diode lasers has an overall efficiency approaching 50% and output power three orders of magnitude greater than the highest one available a few years ago. The multiwatt output power levels obtained very recently in laboratory systems make these lasers suitable for applications in the medical field, thus replacing the more conventional lasers. Since the size of the light-emitting region in a diode laser is in the submillimeter range, even for the multiwatt devices, very compact laser systems can be developed (Table 26-6). Moreover, the price drop that usually follows large-scale production of solid-state electronic components will lead to much more inexpensive laser systems, thus permitting a wider distribution of medical lasers, especially in those countries with lower economic development.

The lasing wavelengths of the highest-power diode lasers are presently limited to a narrow spectral region, from 750 to 950 nm, because of the use of the most developed gallium-aluminum-arsenide (GaAlAs) crystal technology. Potentially, diode lasers can generate radiation in the whole visible spectrum and in the infrared region up to 30  $\mu\text{m}$ . The extension to diode lasers of the Q-switching and mode-locking techniques will permit the application of diode lasers to all eye pathologic conditions treated by lasers today.

These new diode laser structures represent the most efficient way so far to convert electrical power into light. Therefore they can very conveniently replace flash lamps in optically pumped solid-state lasers. Thus in the very near future, highly efficient solid-state lasers of ophthalmologic interest, such as Nd:YAG and Erbium:YAG (Er:YAG) lasers, will become available. Standard Q-switching and mode-locking techniques will permit the use of these new, compact diode laser-pumped lasers in place of the current systems.

\*The text of this section is modified from Brancato R and Pratesi R. Applications of diode lasers in ophthalmology, *Lasers & Light in Ophthalmology* 1:119, 1987

**Table 26-6.** CW diode laser wavelengths

Laser media	Principle wavelengths (nm)
Zinc sulfide	330
Cadmium sulfide	490
Zinc telluride	540
Gallium arsenide	850
Indium arsenide	3100
Indium antimonide	5400

The highest CW output power at room temperature from a coherent light emitting diode (CLED) reported so far is  $\approx 200$  mW from a standard diode configuration and 1 W from a diode incorporating a special "quantum well" structure, which consists of a sequence of ultrathin alternate semiconductor layers. The maximum power extractable from a CLED is limited mainly by the optical damage to the crystal, particularly in the facet region, produced by the extremely high power density of the laser beam, which easily exceeds several megawatts per square centimeter.

An interesting approach to generating higher laser power is represented by the "phased diode laser array." It consists of several tens of single active diode structures built in the same chip and separated by a very short distance (Fig. 26-23). Coupling between the adjacent active zones makes the overall laser emission spatially coherent. Laser powers close to 3 W CW at room temperature have been obtained with a 40-emitter array. Quick engineering development has led to a rapid succession of commercial models with power outputs of 100 to 200 mW and very recently 500 to 1000 mW (Figs. 26-24 and 26-25).

Recently new potential applications of laser techniques in ophthalmology have been reported. In particular, photoablation of corneal tissues has been demonstrated by using ultraviolet excimer lasers. At  $3\text{ }\mu\text{m}$  a nearly 100% absorption by the cornea occurs (Fig. 26-26). The extremely small penetration depth of a  $3\text{-}\mu\text{m}$  radiation in the cornea has been in fact successfully used to ablate controlled amounts of corneal tissue by using both hydrogen fluoride and Er:YAG lasers emitting at  $2.9$  and  $2.94\text{ }\mu\text{m}$ , respectively.

Diode lasers could be developed with emission wavelengths spanning the spectrum of interest for ophthalmologic applications, namely the visible and



**Fig. 26-23.** Array of ten diode laser emitters in a linear row (*below*) compared with the eye of an ordinary sewing needle. The minute size and potential power of the diode lasers make them applicable for some ophthalmic purposes.

near-infrared (up to  $3\ \mu\text{m}$ ) spectral interval. The availability of the necessary laser power at any given wavelength requires important technologic developments and hence an appropriate pressing demand from the potential users. The medical market is potentially large enough to promote specific developments of laser systems. The ophthalmologic lasers in current use today could be replaced in the short and medium term by the new generation of diode laser-based systems, with extremely important advantages in regard to selection of the optimal wavelength, reliability and easy maintenance, compactness, and low cost.

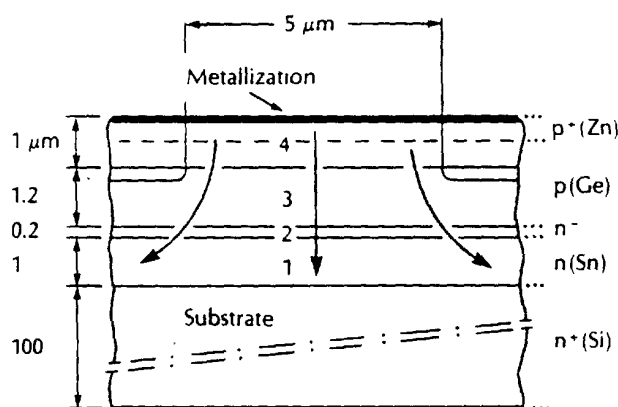


**Fig. 26-24.** Cross section of a typical double-heterostructure diode. Gallium-arsenide (GaAs) layer (2), gallium-aluminum-arsenide (GaAlAs) electrical and optical confinement layers (1,3), layer 4, and substrate: GaAs. (From Brancato R and Pratesi R: Lasers & Light in Ophthalmology 1:119, 1987.)

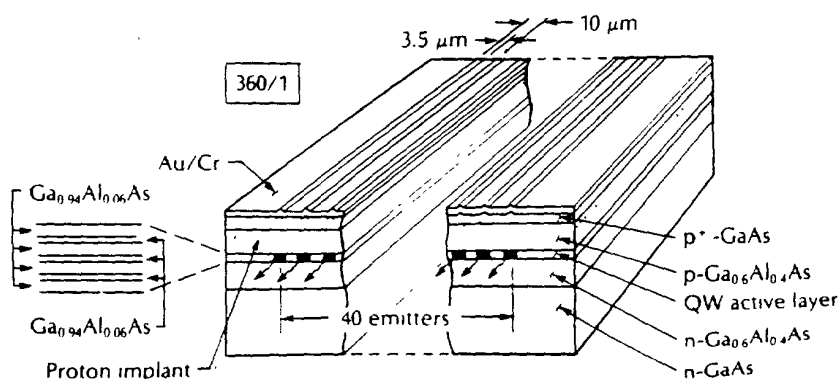


**Fig. 26-25.** Schematic drawing of a typical diode laser 40-emitter array.

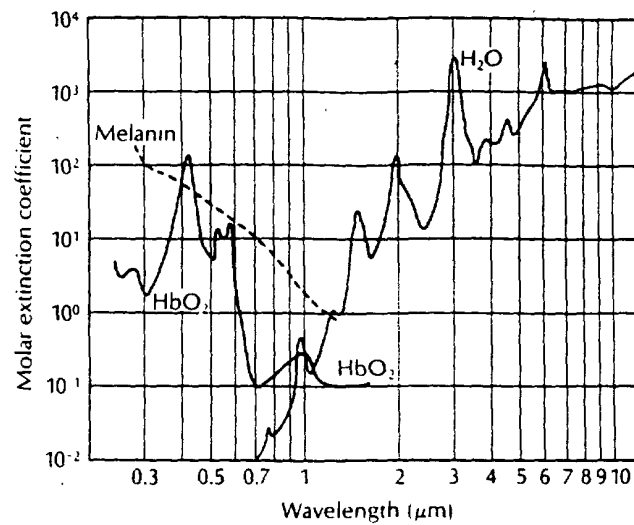


**Fig. 26-26.** Absorption coefficient spectrum of water, oxyhemoglobin, and melanin together with the wavelength positions. (From Brancato R and Pratesi R: *Lasers & Light in Ophthalmology* 1:119, 1987.)

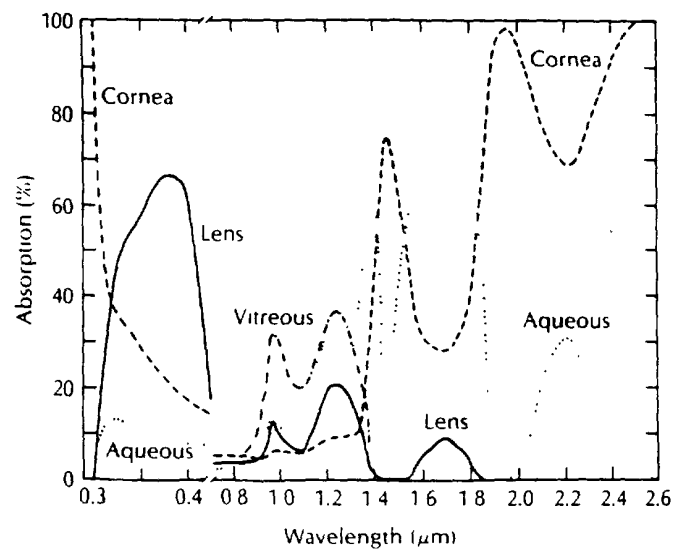


**Fig. 26-27.** Spectral absorption of the ocular media for the human eye. — Cornea. .... aqueous humor; — lens; — · — vitreous humor. (From Brancato R and Pratesi R: *Lasers & Light in Ophthalmology* 1:119, 1987, modified from Sliney D and Wolbarsht M, editors: *Safety with lasers and other optical sources*. New York, 1980, Plenum Publishing Corp.)

## Photocoagulation with GaAlAs Lasers

The highest diode laser powers reported so far for CW or pulsed operation have been achieved by using the most mature technology of crystal growth of a semiconductor alloy, namely the ternary alloy GaAlAs. Wavelength is determined by the band gap of the crystal and ranges from 750 to 950 nm for this particular material. Commercial diode lasers emitting 1 W CW between 780 and 820 nm and an average power of 0.1 W at  $\approx 900$  nm are now available. The 800- to 900-nm radiation is still well transmitted by the ocular media overlying the retina (Fig. 26-27). The absorption of the 750- to 950-nm wavelengths by melanin and oxyhemoglobin is lower than for ion lasers, but substantially higher than for the Nd:YAG laser; in particular, a secondary maximum absorption of oxyhemoglobin is present between 800 and 1000 nm. Moreover, the water absorption is smaller, thus contributing to an increased penetration depth in nonpigmented tissues. In this spectral interval the optical penetration depth is maximum; this is of relevance for transtissue irradiation of vascularized and/or melanized structures. It should be noted that blood vascular absorption may be increased by intravenous injection of suitable dyes. In particular, the indocyanine green dye has an absorption peak matching the diode laser wavelength at 800 nm (Fig. 26-28). Moreover, the use of these lasers appears to be particularly suitable for phototherapy of macular pathologic conditions, since the emission wavelength is away from the xanthophyll absorption spectrum. Therefore the already available GaAlAs diode lasers appear to be suitable for chorioretinal photocoagulations using both noninvasive transpupillary (Fig. 26-29) irradiation with standard slit lamps (Fig. 26-30) and/or contact transscleral irradiation procedures with a suitably shaped fiber end (Fig. 26-31).

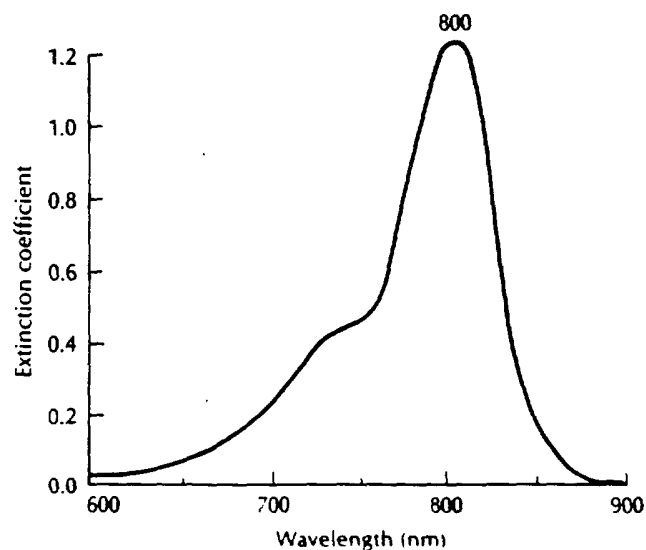


**Fig. 26-28.** Extinction coefficient absorption curve for indocyanine green, showing a maximum absorption for this substance in the region of the 800-nm wavelength.

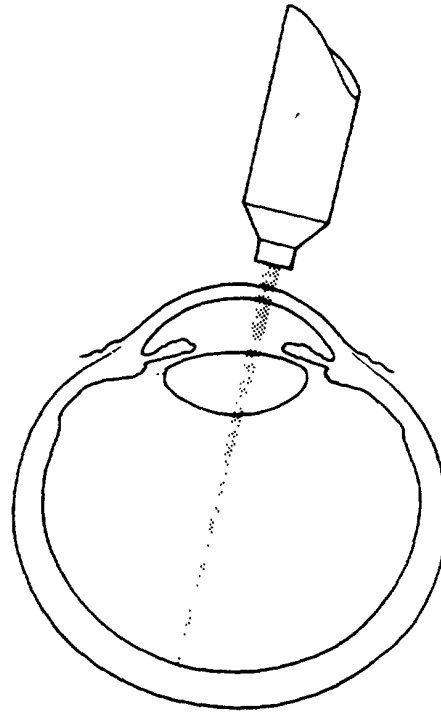


**Fig. 26-29.** Diagrammatic representation of a diode laser beam impinging on the cornea and being transmitted through the ocular media to the chorioretinal structures for the purpose of photocoagulation.

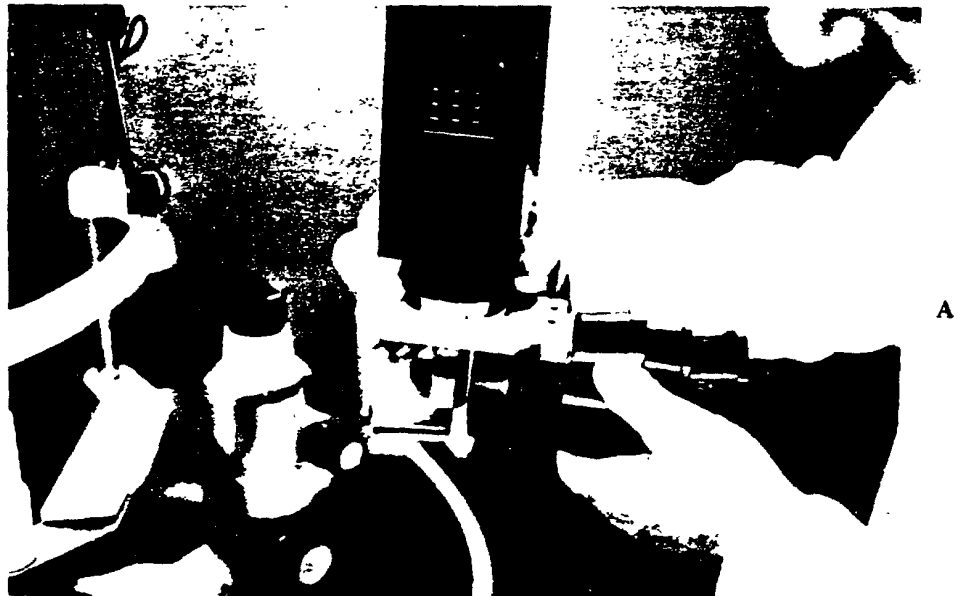


**Fig. 26-30. A,** Prototype with high-power diode laser in its housing (16 × 7 × 8 cm) mounted on the microscope of a commercial slit lamp (From Brancato R and others: *Lasers & Light in Ophthalmology* 2.73, 1988)

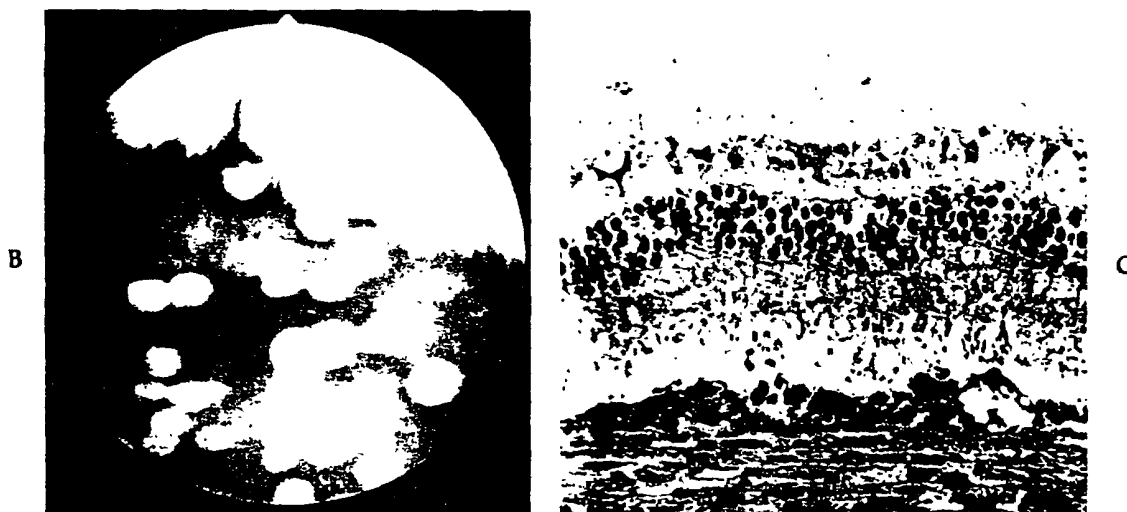


**Fig. 26-30, cont'd.** B, Diode laser photocoagulation. Lesions appear white, disc shaped, and are surrounded by a grayish ring about 500  $\mu\text{m}$  wide. C, Light microscopy: section of acute lesion—area of coagulation necrosis of the pigment epithelium layer. A small vacuole lies over the coagulated area. (Methylene blue  $\times 1125$ .)

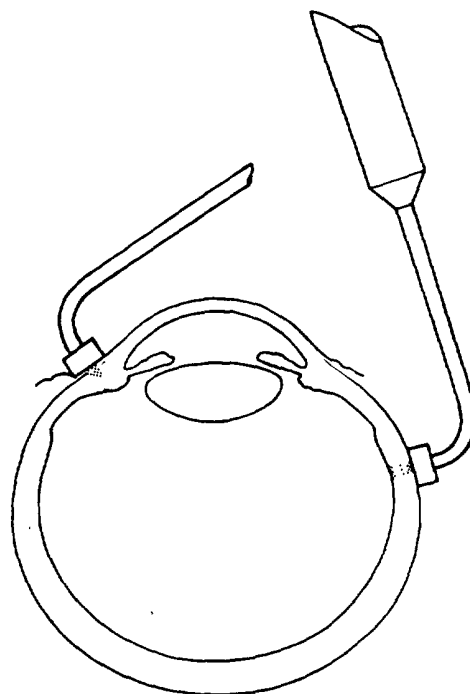


**Fig. 26-31.** Transscleral diode laser applications in the region of the ciliary body (*left*) and the retina (*right*) for the purpose of cyclocautery and retinopexy, respectively.



### Anterior Eye Segment Photodisruption

High-peak powers from mode-locked GaAlAs diode lasers are indicated in the preceding material. Future developments of CLEDs with sufficient energy output in the nanosecond and/or picosecond range will open to these lasers the very fascinating and important area of photodisruptive treatments of transparent ocular structures. Q-switching and/or mode locking of diode laser-pumped solid-state lasers could also represent an improvement with respect to the flash lamp-pumped Nd:YAG lasers in terms of reduction in size and increase in efficiency and reliability.

### Photoablation of the Cornea

The reported success in obtaining controlled removal of corneal tissues with Er:YAG lasers indicates a new potential application for future diode lasers emitting at  $\approx 3 \mu\text{m}$ . This radiation is still well transmitted by flexible zirconium fluoride glass fibers, and compact and handy systems can be foreseen. Diode laser-pumped Er:YAG lasers could also be developed, with an increase in the overall efficiency and a reduction in size.

As foreseen, the capability of diode lasers to produce therapeutically significant photocoagulations has been demonstrated with both CW and pulsed operations. These results are going to open a fascinating new era for laser applications in ophthalmology, offering almost ideal laser systems for a variety of treatments of eye pathology. CW diode lasers operating at 780 to 800 nm are to date the most suitable diode lasers for chorioretinal photocoagulations, since they emit the highest power (up to 2.6 W from laboratory devices and 1 W from most recent commercial systems) at the shortest wavelength. Ultracompact laser photocoagulators are now possible, and the potentially low price of these systems will also allow economically underdeveloped countries to benefit from highly developed medical technologies.

---

## INVESTIGATIONAL LASER PROCEDURES

The use of lasers in the future will be enormously exciting and holds great promise therapeutically. The various areas of therapeutic investigation have been categorized in the following sections, and hopefully will provide the basis for understanding the rationale for the use of a specific laser system to interact with a particular portion of eye tissue in order to correct, remedy, control, or cure a certain ocular defect.

### Laser Refractive Keratoplasty

Laser refractive keratoplasty exemplifies one of the most precise uses of laser energy in the field of medicine. Refractive keratoplasty, of both the incisional and sculpting variety, is possible because of the exquisitely precise interaction of the ultraviolet and possibly the mid-infrared range lasers with the corneal tissue in such a way as to ablate or remove a specific layer of tissue or to incise the cornea in a predetermined manner. In the former situation portions of Bowman's membrane and the stroma are removed in a 5- to 6-mm circular area in such a way as to produce a new curvature on the cornea that would be identical to the anterior surface of a corrective contact lens, in an attempt to produce emmetropia (or any refractive measurement) in that particular eye (Fig. 26-32). Because the ultraviolet lasers, particularly the excimer family of lasers in the

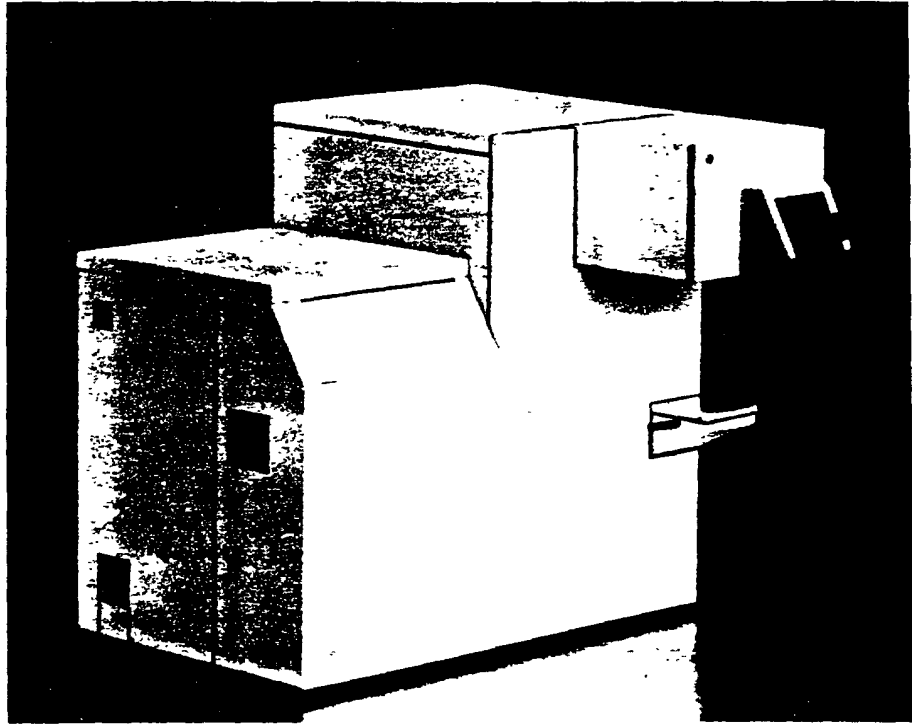


**Fig. 26-32.** Appearance of the prototype computer-controlled excimer laser to be used for various types of corneal surgery, including refractive keratoplasty by anterior corneal recontouring.

region of the argon fluoride 193-nm wavelength, have the ability to remove minute amounts of corneal tissue ( $0.2$  to  $0.3\ \mu\text{m}$ ) with no observable thermal damage and with a precision that is determined by the energy per pulse and the number of pulses applied to a particular portion of the cornea, a precise, extremely smooth spherical surface has been produced for the first time in the stroma of the human cornea in order to correct hyperopia, myopia, or astigmatic refractive errors by our research team.

This same precise laser-tissue interaction of photoablative decomposition, in which intramolecular bonds are broken by the high energy of the impinging photons, can also be used advantageously for incising the cornea in a linear, circular, or any other configuration that could conceivably lead to a change in refractive power of the cornea (Fig. 26-33). Incisions as minute as  $10\ \mu\text{m}$  in width and extending to a depth of 95% thickness of the cornea can be created. These various corneal incisions can be extremely useful for incisional laser refractive keratoplasty as well as for fashioning corneal buttons in which the donor and recipient eye could have corneal buttons of exactly similar size during corneal transplantation. As noted in Chapter 24, an excimer biomicroscopic system has been used by Seiler and Wollensak to produce radial incisions in the cornea. With this device, delicate and precise radial keratotomy incisions can be pro-

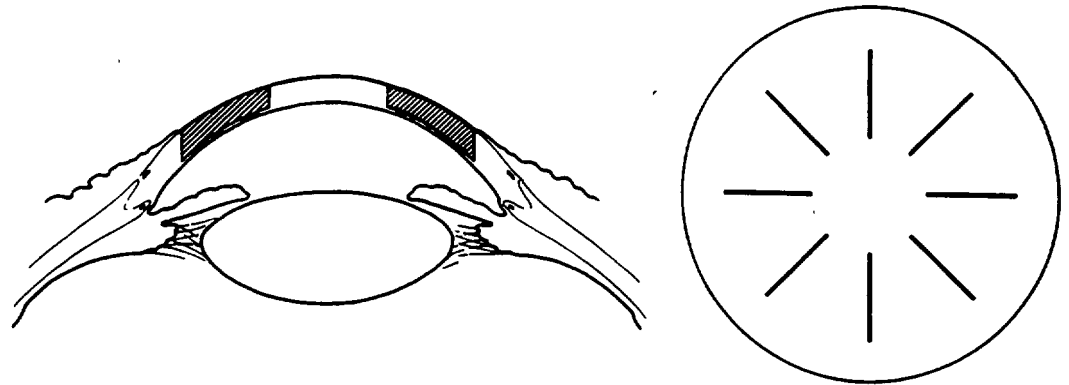


**Fig. 26-33.** Schematic representation of excimer laser radial incisions in the cornea to a depth of 80% to 90% of the corneal thickness in such a manner as to simulate the scalpel-performed radial keratotomy procedure.

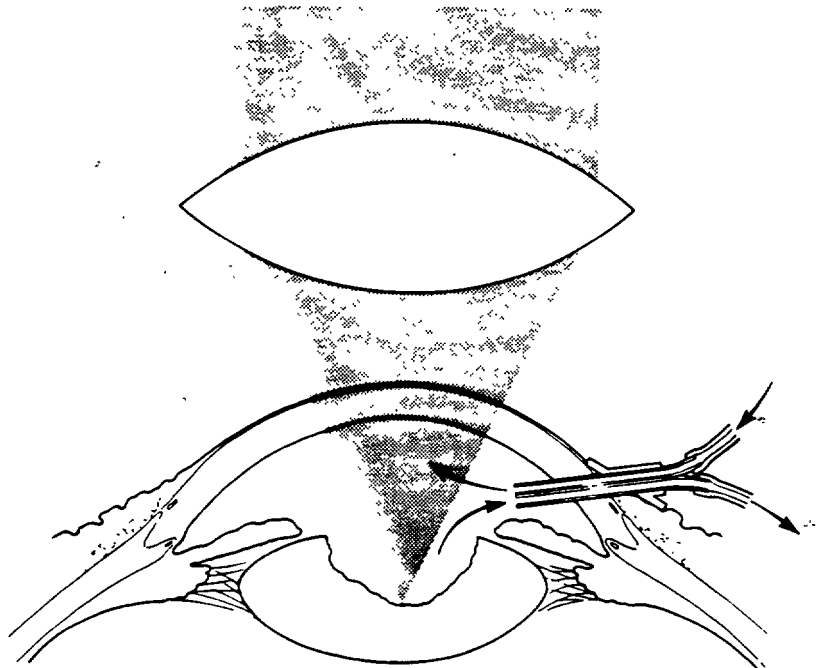


**Fig. 26-34.** Transcorneal photophacoablation depicting the use of excimer or other pulsed laser radiation, usually 308-nm or longer wavelengths, for removal of the cataractous lens by the process of photoablative decomposition directly through the cornea using an extremely wide cone angle to reduce the corneal energy density of the laser beam. Irrigation and aspiration of the decomposed cataractous tissue is accomplished by a small double cannula.

duced that are completely reproducible from patient to patient without the possible inconsistencies of the surgeon's hands. The entire science of strategically placed geometric curvilinear incisions of the cornea and the possibility of recontouring, reshaping, or sculpting the anterior surface of the corneal curvature have opened an enormous range of applications in the field of laser refractive keratoplasty.

### Laser Phacoablation

Another procedure under investigation is the sculpting and ablative decomposition of the cataractous lens in a way that would be minimally invasive except for the removal of debris and other remnants produced by the laser decomposition of the cataractous tissue. With this technique the cataractous lens is approached by one of two methods. First, an extremely large cone of ultraviolet energy (308 nm and longer) is focused on the anterior surface of the cataractous lens and on other areas deeper to the anterior surface as the procedure progresses and the intramolecular bonds of the cataract are broken in a manner similar to that observed with the cornea, liberating molecules of the photodecomposed cataractous tissue into the anterior chamber (Fig. 26-34). This is removed constantly by a lavage of balanced salt solution, producing an effective irrigation and aspiration system. When the cataract has been totally removed centrally, the procedure is terminated except for any additional cortical cleanup that might be necessary beneath the iris by regular microirrigation and aspiration techniques. Therefore the entire procedure is performed with only the irrigation and aspiration cannula invading the anterior chamber during the laser phacoablation procedure.

A second method of cataract removal involves the insertion of a fiberoptic probe within the anterior chamber to impact on the lens with radiation such as that produced by the xenon chloride excimer laser or with longer wavelengths that easily are conducted through a fiberoptic cable (Fig. 26-35). Photoablative

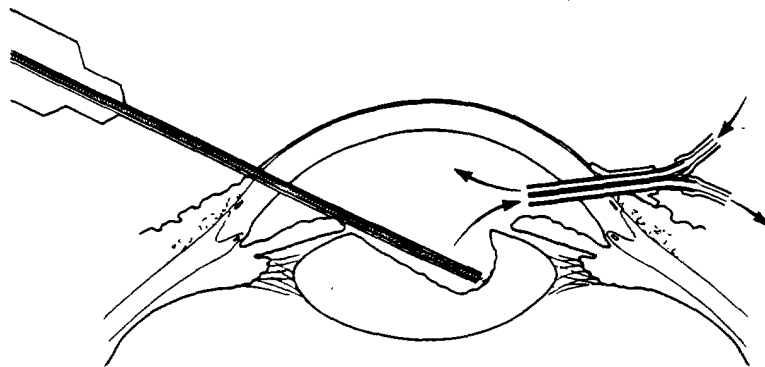


**Fig. 26-35.** Photophacoablation or lensectomy by the process of photoablative decomposition can be produced by channeling an excimer laser of 308-nm (xenon chloride) or longer wavelengths through a fiberoptic probe into the cortex and nucleus of the cataract to be emulsified or ablated. The products of ablation are removed from the anterior chamber and the region undergoing ablative photodecomposition by gentle irrigation and aspiration of the treated region.

decomposition of the cataract is then performed by the impact of the radiation emanating from the tip of the fiberoptic probe against the cataract and tissue in various areas of the lens. The cortical cleanup is produced by the ultraviolet radiation of the lens cataractous material, and the destroyed cataractous tissue is removed by gentle irrigation and aspiration of the anterior chamber. Both systems of fiberoptic conduction of the ultraviolet wavelengths and the direct ablation of the cataractous lens through the cornea are under biomicroscopic control of the surgeon.

### Laser Scalpel

Certain ultraviolet (some excimer, frequency-quadrupled Nd:YAG, frequency-doubled dye laser, etc.) or mid-infrared lasers (holmium, holmium-thallium, Er:YAG, hydrogen fluoride, etc.) can be conducted through a fiberoptic cable to a scalpel-like focusing handle (Fig. 26-36). Ragged incisions such as those made with an argon laser or other thermal laser can be obviated, and incisions can be produced in the cornea that appear as precise as those made by diamond knives or similar devices (Fig. 26-37). Both the infrared and the ultraviolet lasers are of the pulsed variety with extremely short pulses in the nanosecond or picosecond range. The entire technology of the use of these lasers as surgical scalpels with different cutting and shaping capabilities will have enormous impact on ophthalmic and other forms of surgery.

### Photophacofragmentation

Photophacofragmentation has been studied in our laboratory during the past 7 years and involves the photofragmentation and photoemulsification of the nucleus of the cataract 1 day to 3 weeks before cataract extraction in order to permit the removal of the contents between the anterior and posterior capsule through a tiny corneoscleral incision. The use of intracapsular hydrogels or small, foldable silicone intraocular lenses is entirely possible through extremely small incisions with this particular technique. Our apparatus uses a raster, indicated by the overlapping focus of two HeNe laser beams, that is under computer control for accurate spacing and complete fragmentation of an encircled area with individual impacts at the level of the nucleus during the photophacofragmentation procedure. With this technique the area to be impacted on is encircled by manipulating the target HeNe beam in a circular fashion around the nuclear area of the cataract. The vertical (Y axis) and horizontal (X axis) spacing of the impacts to be produced within the circular predetermined zone is established on the computer, and the biomicroscopic system is then adjusted vertically along the Z axis to be focused in a plane through the middle of the nucleus of the cataract of the supine patient. When the photophacofragmentation procedure has been performed, irrigation and aspiration of the fragmented cataract are carried out through an extremely tiny incision at the limbus and at the anterior capsule of the lens. The use of photophacofragmentation has made the routine use of phacoemulsification much easier and has opened an entirely new approach to the withdrawal of cataractous tissue from the eye (Figs. 26-38 to 26-44).

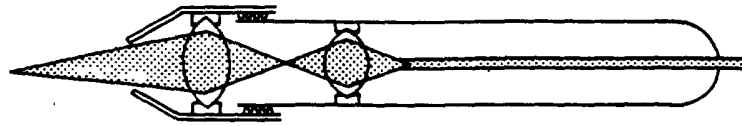


**Fig. 26-36.** Schematic diagram of a typical laser scalpel through which energy from any of the laser sources, typically the longer-wavelength excimer lasers or the more highly powered visible or mid-infrared lasers, would be used and channeled through a fiberoptic cable to be focused by interchangeable laser scalpel tips for the purpose of producing various types of laser scalpel incisions.

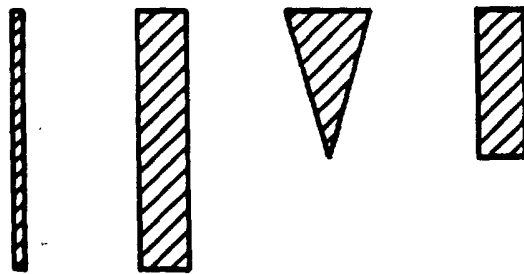


**Fig. 26-37.** Some of the possible laser incisions using various types of scalpel tips in order to produce a square excision of tissue or a fine incision, or any geometric variation of the incision borders.

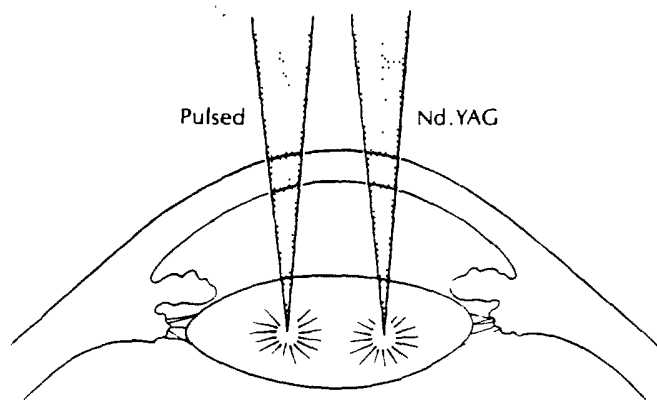


**Fig. 26-38.** Laser photophacotriagmentation with the pulsed Nd:YAG laser at the level of the nucleus of the cataract, producing fragmentation and emulsification of the nuclear material for easier aspiration from the eye

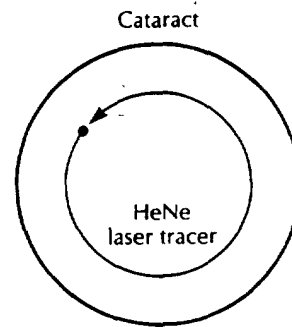


**Fig. 26-39.** A raster for automatic pulsing of the laser is used for proper photofragmentation impacts throughout the nucleus of the lens. The area to be treated by automatic photofragmentation is first delineated by a HeNe laser tracer and later fragmented by the pulsed Nd:YAG laser.

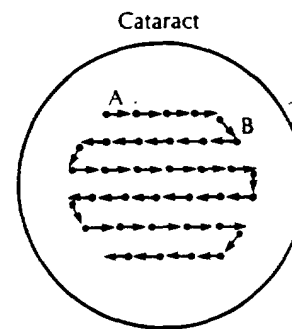


**Fig. 26-40.** The automatic pulsed Nd:YAG laser raster commences following circular delineation of the outer boundaries of the raster zone. The computer has the ability to space the Nd:YAG laser impacts at a precise distance from one another (*A*) and to space each of the rows of linear impacts a designated distance from one another (*B*) in order to obtain complete photophacofragmentation of the nucleus of the cataractous lens before aspiration.

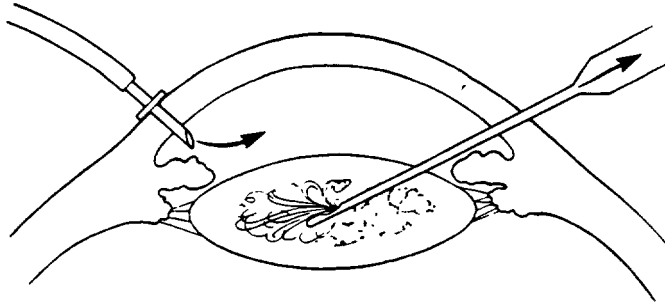


**Fig. 26-41.** Sagittal section showing diagrammatically the infusion port and aspiration cannula that removes the cataractous lenticular material after the process of photophacofragmentation and/or emulsification of the lens by the pulsed Nd:YAG laser impacts.

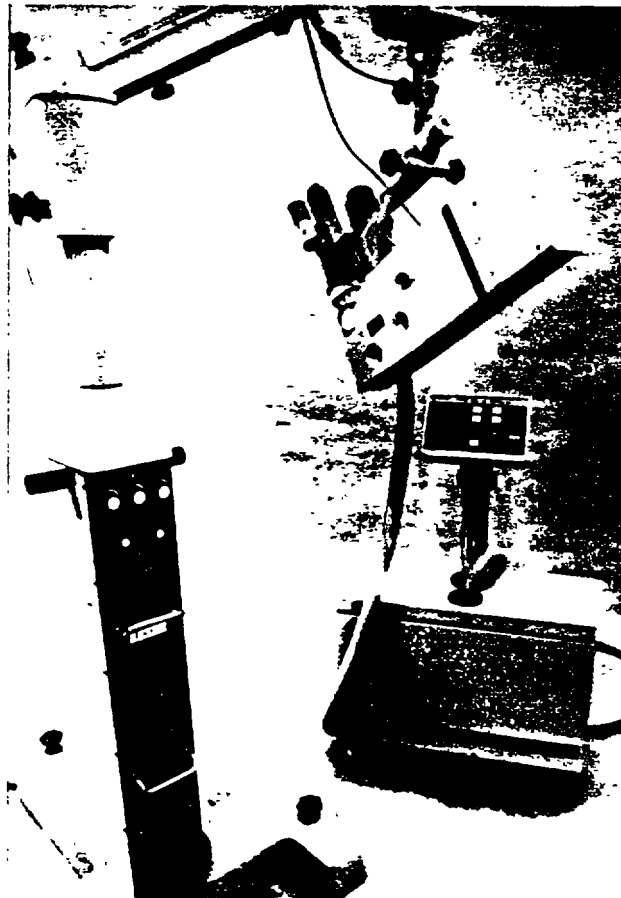


**Fig. 26-42.** Photograph of the vertically mounted photophacofragmentation instrument with its delineating raster apparatus.



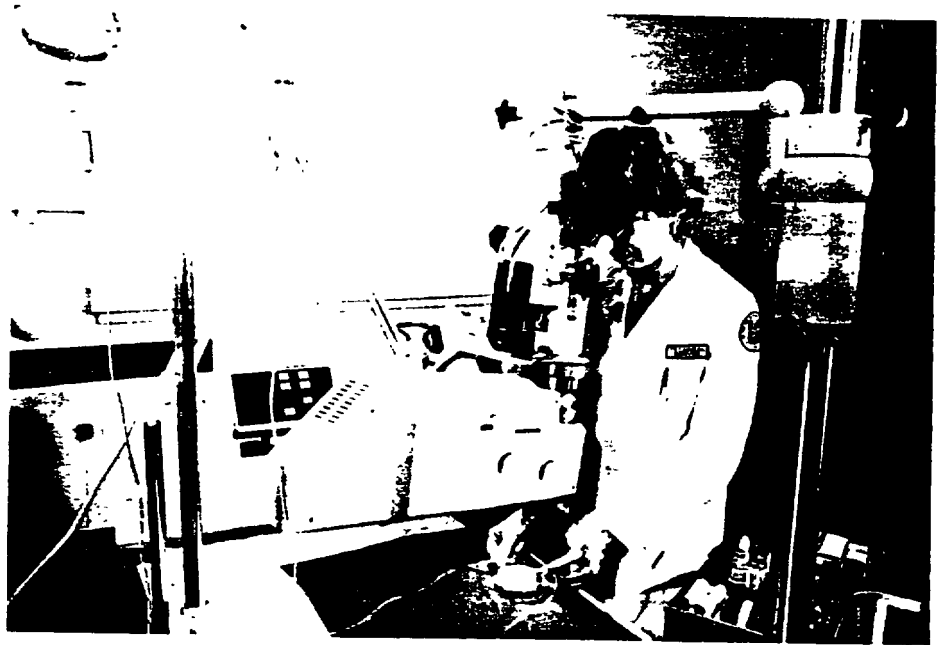


**Fig. 26-43.** Clinical research prototype of the pulsed Nd:YAG laser for photophacofragmentation as developed by the Coherent Medical Group with infusion and aspiration systems to clear the fragmented cataractous material.



**Fig. 26-44.** Initial appearance of the fragmented nucleus of a rabbit's eye showing cavitation bubbles in the areas of photophacofracture. These bubbles disappear rapidly and allow for infusion and aspiration of the fragmented nuclear material.

## Fluorescein-Antibody Laser Asepsis

Fluorescein-antibody laser asepsis is a procedure in which a known organism infecting the cornea is allowed to conjugate with topical drops on the cornea containing an antibody to that organism, which has been tagged with a molecule of sodium fluorescein. The antibodies with the fluorescein tag attach themselves to the organisms in the corneal ulcer, and when they are irradiated with a nonfocused argon laser beam for 2 min, the fluorescein absorbs the argon laser energy, converts it to heat energy, and raises the fluorescein-antibody microorganism complex to a temperature above its thermal death point (Fig. 26-45). This procedure has proved to be useful and effective because of the peak absorption of the fluorescein molecule at 486 nm, which is close to one of the major wavelengths (488 nm) of the argon laser. Therefore the fluorescein and the microorganism-antibody complex can be made to absorb photon energy from the argon beam with an elevation in temperature of the individual microorganism-antibody complex and irradiation of the organisms in the ulceration site (Fig. 26-46). This procedure should prove to be promising with all organisms affecting the cornea because a large number of fluorescein-tagged antibodies for these organisms are readily available.

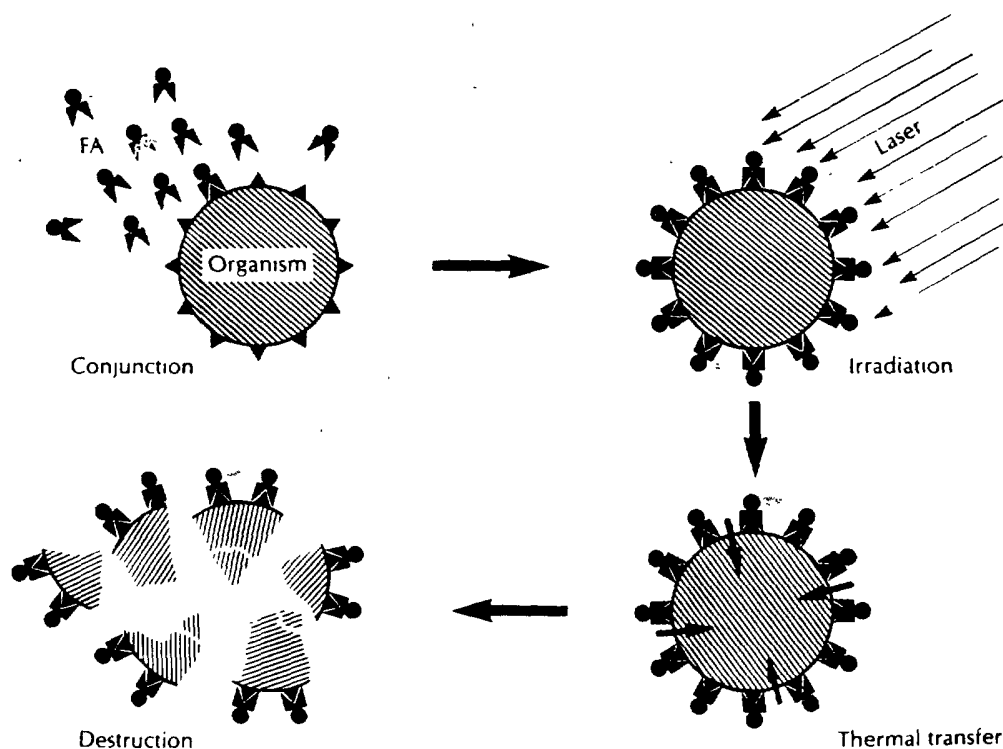


**Fig. 26-45.** Technique of fluorescein-antibody laser asepsis, in which a fluorescein-tagged antibody (FA) to a specific corneal ulcer organism is allowed to conjugate with the organism over a short period followed by irradiation with the argon laser for a 2-min interval in which the fluorescein absorbs the argon laser energy and increases the temperature of the antibody-microorganism complex above the organism's thermal death point, at which time destruction of the organism takes place.

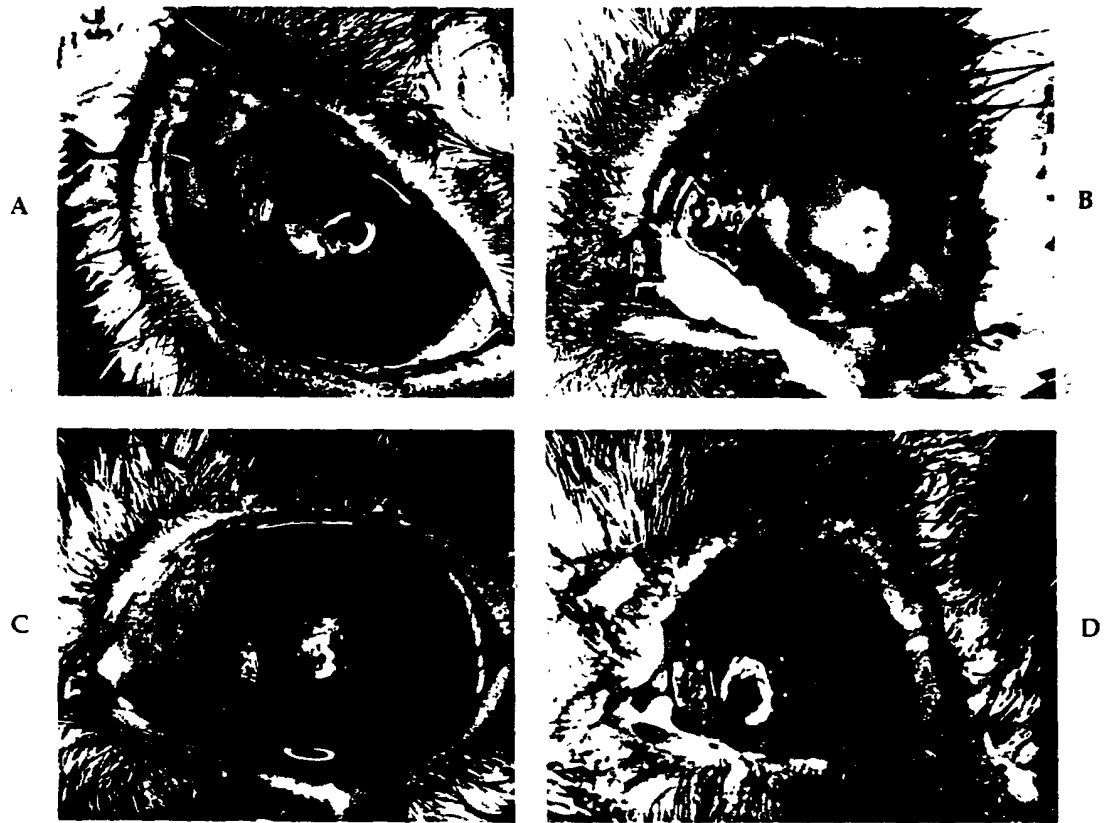


**Fig. 26-46.** A, Typical corneal ulcer caused by the *Pseudomonas* organism 1 day following inoculation of the rabbit cornea. B, Same eye approximately 8 days following inoculation of the cornea with the *Pseudomonas* organism, indicating penetration of the cornea and a marked endophthalmitis and loss of the eye. C, Appearance of a rabbit cornea 24 hours following inoculation of the epithelium of the eye with the *Pseudomonas* organism. Note small but prominent ulceration of the epithelium and anterior stroma. D, Same eye as in C 48 hours following conjugation of the *Pseudomonas* organisms with the tagged antibody-fluorescein complex that absorbed the nonfocused argon beam, thereby raising the temperature of the complex above the thermal death point of the organism, with complete obliteration of the organisms and healing of the corneal ulceration.

## Organic Dye Laser–Chromophore Technique

With the dye laser–chromophore technique the vascular abnormality to be destroyed is treated sufficiently by a photocoagulation laser to injure the vessel wall slightly. Photocoagulation of the target tissue usually produces a spasm and constriction of the telangiectatic or neovascular tissue structure, which then reopens in several minutes. An intravenous dye such as indocyanine green, sodium fluorescein, acridine orange, berberine, or hematoporphyrin derivative or similar dye compound is then injected and allowed to stain the area of previous photocoagulation and spasm of the wall of the abnormal vessel. When this has occurred, usually several minutes after intravenous injection, the dye laser is tuned to the peak absorption of that particular intravenous dye, now absorbed in the wall of the target vessel, and the vascular defect is photocoagulated and destroyed completely as a result of the interaction of the vessel itself, rather than components of the vessel, such as hemoglobin or surrounding melanin. The use of absorbent dyes as chromophores or absorbefacients in conjunction with the tunable dye laser should prove to be valuable in treatment of areas of vascular proliferation or disease that are resistant to conventional photocoagulation therapy (Fig. 26-47).

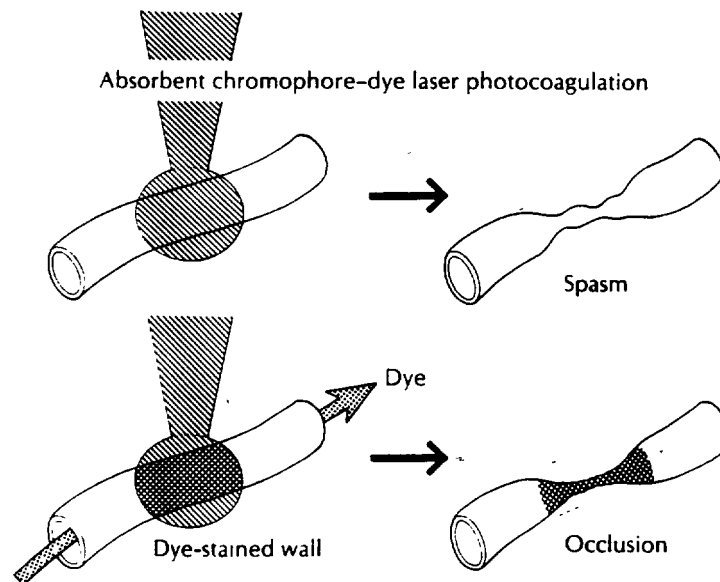


**Fig. 26-47.** Schematic diagram illustrating the technique of absorbent chromophore-dye laser photocoagulation in which an ocular vessel to be occluded is first treated with a laser beam of sufficient power density to cause spasm of that particular vessel. An absorbent dye, such as indocyanine green, sodium fluorescein, rose bengal, or Evans' blue, is injected intravenously and allowed to pass through the injured blood vessel and to stain the photocoagulated portion. After several minutes, when the dye has stained the injured photocoagulated region of the blood vessel, it is treated with a wavelength from the dye laser that would be most highly absorbed by the injected dye residing in the walls of the vessel, thereby causing the vessel to be obliterated and occluded by the thermal action created within the wall of the vessel itself.

## Phototherapy

### Neovascular Stimulation

During the past several years it has been my observation that judicious use of certain types of lasers, particularly those in the red and infrared portions of the spectrum, have had an ill-defined propensity for stimulating the growth of fibroblasts, collagen, endothelial cells, and perhaps other structures. It is well known that melanin and some glial structures undergo proliferation with irradiation by a bright light source, but it is my belief that weak laser interaction with various cells can cause hypertrophy and/or proliferation of those cells. If this is so, it would be possible to create new vascular channels or the opening of old channels within the retina itself in the deep and superficial vascular plexi (Figs. 26-48 and 26-49). In other branches of medicine, the increased blood vessel growth in gums, surgical wounds, poorly vascularized ulcerated areas, or mucous membrane regions should be produced by weak irradiation by a laser system, most probably in the red and infrared portions of the electromagnetic spectrum.

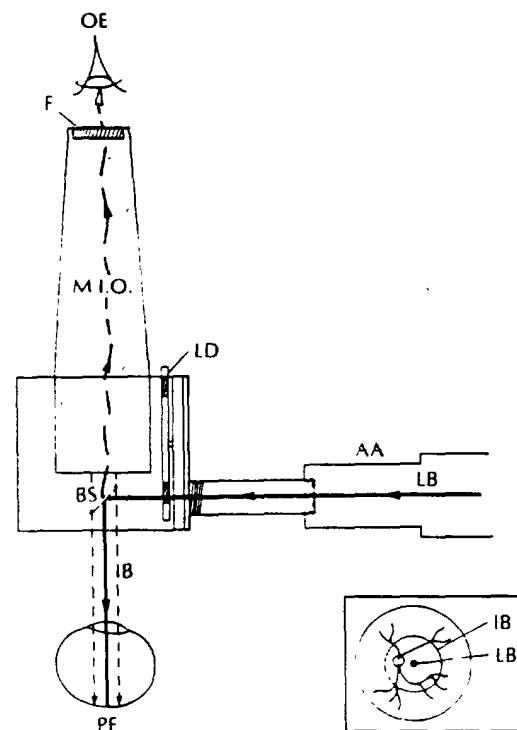


**Fig. 26-48.** Indirect ophthalmoscopic delivery system using a monocular indirect ophthalmoscope with an attached beam splitter and lens disc that can direct the laser beam to the eye for the purpose of phototherapy or photocoagulation. An articulated arm or a fiberoptic cable can be used to channel the laser beam to the indirect monocular laser ophthalmoscopic system. OE, Observer's eye; M.I.O., monocular indirect ophthalmoscope; LD, lens disc; BS, beam splitter; AA, articulated arm; LB, laser beam; IB, illumination beam; PE, patient's eye; F, filter.

### Laser Aseptic Phototherapy

Laser aseptic phototherapy is a procedure that I believe has considerable merit, because most surgical aseptic procedures preceding an operation consist of a chemical and mechanical desquamation of the superficial layers of the epidermis with chemical obliteration of microorganisms on the remaining surface by agents such as iodine, alcohol, and several other chemicals. None of the antiseptic agents is effective deep in the area of hair follicles or crypts that extend deep into the dermis and that harbor considerable amounts of bacteria, which can be massaged to the surface within minutes after the initial preparation of the incision site. Therefore the direct irradiation and penetration deep into the dermal layers by incandescent or laser light of a specific wavelength may have germicidal action that could be used alone or in conjunction with conventional antiseptic techniques. Furthermore the use of an agent such as tetracycline compound or a small intravenous injection of hematoporphyrin derivative (HpD) several hours before the time of surgery might serve to potentiate the action of a particular wavelength, since the chemical substance administered orally or

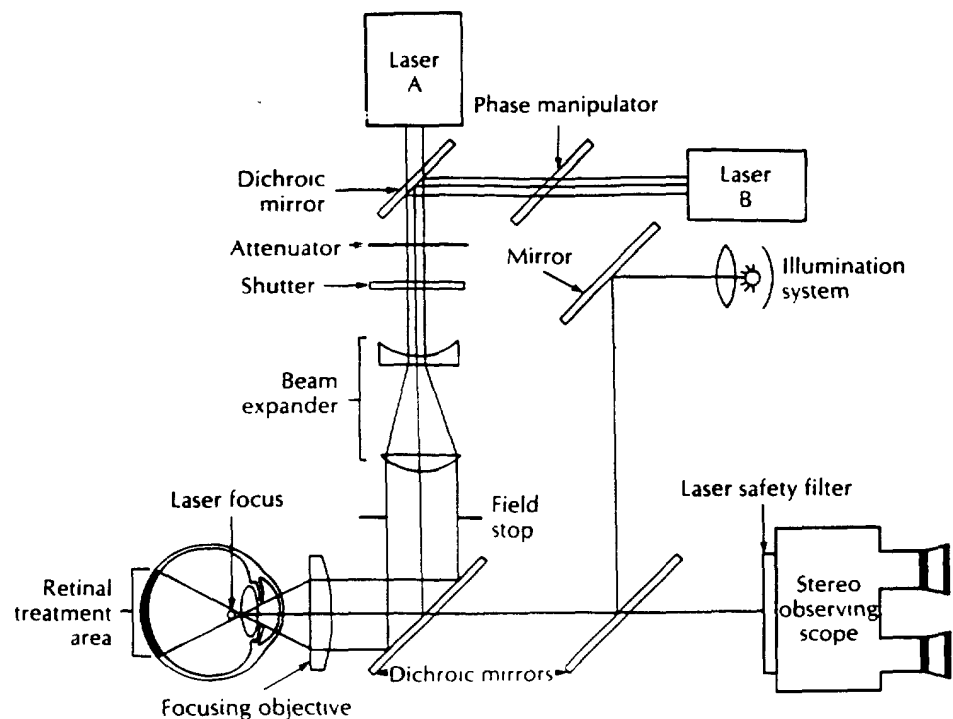


**Fig. 26-49.** Schematic representation of a laser system used for investigational phototherapy of the retinal vasculature. In this particular case laser A and laser B can be identical or produce different wavelengths that are used preferentially to stimulate the growth or reinforcement of the various areas of retinal vasculature

intravenously would be absorbed by the bacteria in the follicles and crypts and then irradiated with the laser wavelength known to be most highly absorbed by that particular substance, which would then cause the thermal or photochemical death of the organisms more deeply situated within the skin (Fig. 26-50).

The technique of laser aseptic phototherapy could also be applied to mucous membranes and other regions of the body such as the gums, where an incandescent or laser light source could be applied to the infected gum region directly or after an oral, intravenous, or mouthwash type of prephotosensitization of the organisms. Following the sensitization, the gum or mucous membrane region thought to be infected could be irradiated for a short period of time with a wavelength highly absorbed by the photosensitizing substance and at a power density sufficient to cause the death of the microorganisms.

---

## GLAUCOMA SURGERY

There are three antiglaucoma surgical interventions under investigation at the present time that may be of considerable usefulness in the future. These procedures include (1) external sclerotrabeculoplasty or external sclerotrabeculostomy, (2) internal sclerotrabeculoplasty or internal sclerotrabeculostomy, and (3) contact laser cyclocautery.

### External Laser Sclerotrabeculoplasty

External laser sclerotrabeculoplasty involves the use of a CW Nd:YAG laser or other mid-infrared laser (ER:YAG or hydrogen fluoride laser) or conceivably the use of an excimer laser with a wavelength of 308 nm or longer channeled through a fiberoptic cable into a stainless steel needlelike probe (Fig. 26-51). The needlelike probe is inserted beneath the conjunctiva, which has been elevated either by saline or by the injection of a small amount of air, and the fiberoptic probe is directed to the area of the trabecular meshwork in the iridocorneal angle. By the process of photovaporization or photoablation, a small hole in the sclera is created and the scleral and trabecular tissue is removed until aqueous fluid is seen to emerge from the sclerostomy hole. In this situation usually a suture is not required in the conjunctiva, and drainage from the anterior chamber into the subconjunctiva and sub-Tenon's space is facilitated. The prior creation of a laser peripheral iridotomy and/or iridectomy in the region of proposed filtration is advised 1 to 3 weeks before the external sclerotrabeculoplasty. In addition, constriction of the pupil and sodium hyaluronate injection into the anterior chamber may be required in some cases.

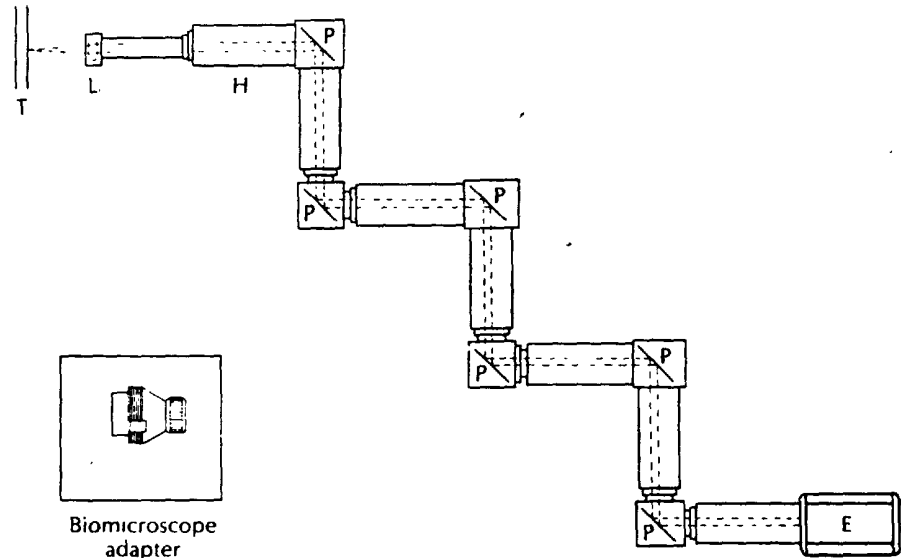


**Fig. 26-50.** Diagram of an articulated arm for channeling laser energy, showing the entrance block for the laser beam at the lower right and the exit of the laser beam at the upper left. The articulated arm can be rotated in any direction because of the free rotation at the joints that contain the prisms. *P*, Prism; *L*, lens; *T*, tissue; *H*, handle; *E*, entrance block.

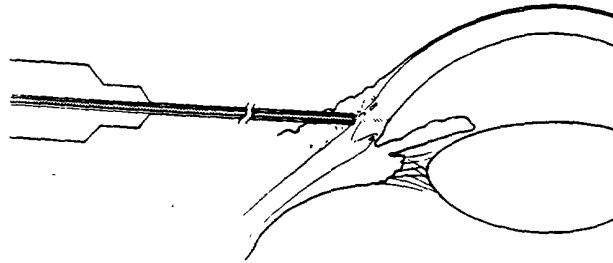


**Fig. 26-51.** Direct external subconjunctival laser sclerotrabeculostomy by means of a CW laser channeled through a fiberoptic cable to a portion of the iridocorneal angle to produce a filtering cicatrix for the relief of open-angle glaucoma.



### Internal Laser Sclerotrabeculoplasty

A procedure similar to that of external laser sclerotrabeculoplasty is followed with the addition that the needlelike probe is brought across the anterior chamber from the point of entrance into the anterior chamber to the exact opposite iridocorneal angle and the trabecular meshwork is subjected to laser irradiation from one of the previously mentioned sources until a fistula is created by the process of photovaporization or photoablation (Fig. 26-52). Photocoagulation has not been entirely successful because of the denatured tissue that forms in the area of the laser irradiation. This tissue may or may not form a filtering cicatrix, and the results of the procedure are inconsistent. After a patent fistula has been created by one of the laser sources mentioned, the aqueous fluid will flow from the anterior chamber to the subconjunctival space with the creation of a large filtering bleb. Both the external and internal laser sclerotrabeculoplasties require a previous laser iridectomy or iridotomy in the area of the proposed filtration in order to minimize the possibility of iris incarceration in the filtering wound.

### Contact Laser Cyclocautery

Contact laser cyclocautery involves the use of a CW or quasi-CW laser source in the near-infrared or mid-infrared portion of the visible spectrum in order to cauterize and coagulate the pars ciliaris of the ciliary body in such a way as to decrease the production of aqueous fluid (Fig. 26-53). With this particular procedure the laser is channeled through a probe to a sapphire or other semiprecious or precious gemlike tip, which then concentrates the laser beam for transmission through the conjunctiva, Tenon's fascia, and sclera to be absorbed or for absorption by the pigmented portions of the ciliary body. The contact sapphire or ruby tip is hard, scratch resistant, and durable, and easily transmits infrared energy without heating or external dispersion. The sapphire tips are artificially grown, and the blank gems are contoured in various ways to manipulate the laser beam for the most precise interaction with the ciliary body or other ocular structure. Placing the contact sapphire tip against the conjunctiva at the time of laser irradiation enables the laser beam to be propagated through the conjunctiva without reflection and without the dramatic losses produced by a noncontact process. This method, like the previous two antiglaucoma procedures, is under considerable investigation and should prove to be valuable in specific cases.

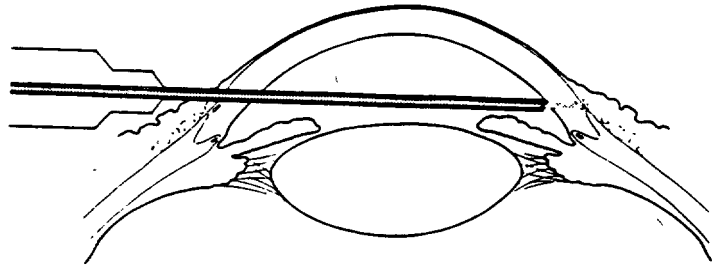


**Fig. 26-52.** Indirect internal subconjunctival laser sclerotrabeculostomy by insertion of a fiberoptic probe across the anterior chamber to the opposite iridocorneal angle, resulting in channeling of the CW laser beam to the trabecular meshwork and scleral area in order to produce an opening and a filtering cicatrix beneath the conjunctiva on the opposite side of the entrance of the fiberoptic probe.

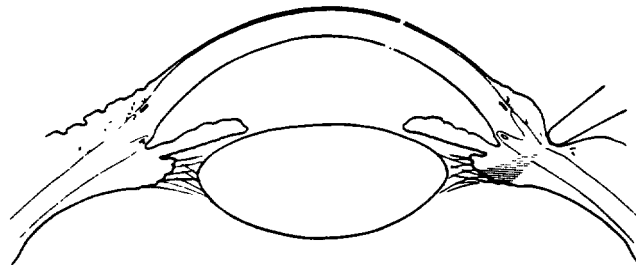


**Fig. 26-53.** Contact laser cyclocautery by means of transconjunctival and transscleral irradiation of the ciliary body to produce coagulation in order to reduce the formation of aqueous fluid.

## REFERENCES

1. Geeraets WJ: The relative absorption of thermal energy in retina and choroid, *Invest Ophthalmol* 1:340, 1962.
2. L'Esperance FA Jr: An ophthalmic argon laser photocoagulation system: design, construction, and laboratory investigations, *Trans Am Ophthalmol Soc* 66:827, 1968.
3. L'Esperance FA Jr: The ocular histopathologic effect of krypton and argon laser radiation, *Am J Ophthalmol* 68:362, 1969.
4. L'Esperance FA Jr: Clinical photocoagulation with the frequency-doubled neodymium yttrium-aluminum-garnet laser, *Am J Ophthalmol* 71:631, 1971.
5. Minton JP: A method to determine laser wavelength absorption capabilities of experimental malignant tumors, *Life Sci* 3:1007, 1964.
6. Srinivasan R: Action of far-ultraviolet light on organic polymer films: applications to semiconductor technology, *J Radiation Curing* 10:12, 1983.
7. Srinivasan R: Kinetics of the ablative photodecomposition of organic polymers in the far-ultraviolet (193 nm), *J Vacuum Sci Technol* B1:923, 1983.
8. Trempe CL: Macular photocoagulation—optimal wavelength selection, *Ophthalmology* 89:7, 1982.
- transscleral photocoagulation, *Ophthalmic Surg* 18(3):183, 1987.
- Gaasterland DE and others: Ab interno and ab externo filtering operations by laser contact surgery, *Ophthalmic Surg* 18(4):254, 1987.
- Horn GD and others: A new "cool" lens capsulotomy laser, *Am Intraocular Implant Soc* 8(4):337, 1982.
- Krauss JM, Puliafito CA, and Steinert RF: Laser interactions with the cornea, *Surv Ophthalmol* 31(1):37, 1986.
- Loertscher H and others: Preliminary report on corneal incisions created by a hydrogen fluoride laser, *Am J Ophthalmol* 102(2):217, 1986.
- Mainster MA and others: Scanning laser ophthalmoscopy: clinical applications, *Ophthalmology* 89(7):852, 1982.
- Marsh RJ and Marshall J: Treatment of lipid keratopathy with the argon laser, *Br J Ophthalmol* 66(2):127, 1982.
- Marshall J and Sliney DH: Endoexcimer laser intraocular ablative photodecomposition, *Am J Ophthalmol* 101(1):130, 1986 (letter).
- Mosier MA and others: Retinal effects of the frequency-doubled (532 nm) YAG laser: histopathological comparison with argon laser, *Laser Surg Med* 5(4):377, 1985.
- Pellin MJ and others: Endoexcimer laser intraocular ablative photodecomposition, *Am J Ophthalmol* 99(4):483, 1985.
- Peyman GA, Conway MD, and House BJ: Effect of CW YAG and argon green lasers on experimentally detached retinas, *Arch Ophthalmol* 62(3):342, 1984.
- Puliafito CA and Steinert RF: Laser surgery of the lens: experimental studies, *Ophthalmology* 90(8):1007, 1983.
- Serdarevic O and others: Excimer laser therapy for experimental *Candida* keratitis, *Am J Ophthalmol* 99(5):534, 1985.
- Summers CG and Hordinsky MD: Argon laser treatment of periocular lesions: an experimental study, *Ophthalmic Surg* 18(2):100, 1987.
- Troutman RC and others: A new laser for collagen wounding in corneal and strabismus surgery: a preliminary report, *Trans Am Ophthalmol Soc* 84:117, 1986.

## ADDITIONAL READINGS

- Bovino JA, Marcus DF, and Nelsen PT: Argon laser choroidotomy for drainage of subretinal fluid, *Arch Ophthalmol* 103(3):443, 1985.
- Bron AJ, Wilson CB, and Hill AR: Laser treatment of primary ring-shaped epithelial iris cyst, *Br J Ophthalmol* 68(12):859, 1984.
- Duvall J and Tso MO: Cellular mechanisms of resolution of drusen after laser coagulation: an experimental study, *Arch Ophthalmol* 103(5):694, 1985.
- Federman JL and others: Contact laser scalpel for ocular wall resection, *Ophthalmic Surg* 18(4):305, 1987.
- Federman JL and others: Contact laser for